

Bioorthogonal Functionalization of Elastin-like Polypeptides

by

Simone A. Costa

Department of Biomedical Engineering
Duke University

Date: _____

Approved:

Ashutosh Chilkoti, Supervisor

Joel Collier

Michael Lynch

Tatiana Segura

Kris Wood

Dissertation submitted in partial fulfillment of
the requirements for the degree of Doctor
of Philosophy in the Department of
Biomedical Engineering in the Graduate School
of Duke University

2019

ABSTRACT

Bioorthogonal Functionalization of Elastin-like Polypeptides

by

Simone A. Costa

Department of Biomedical Engineering
Duke University

Date: _____

Approved:

Ashutosh Chilkoti, Supervisor

Joel Collier

Michael Lynch

Tatiana Segura

Kris Wood

An abstract of a dissertation submitted in partial
fulfillment of the requirements for the degree
of Doctor of Philosophy in the Department of
Biomedical Engineering in the Graduate School of
Duke University

2019

Copyright by
Simone A. Costa
2019

Abstract

Recombinant technology has given us the powerful ability to imagine and create novel biological entities, from potent therapeutics to functionally active materials. By harnessing nature's building blocks and reconfiguring these components, recombinant engineering unlocks the potential to tailor drug specificity and pharmacokinetics, rationally design biomaterials, understand and define protein structure, and probe cellular function with molecular precision. These technological feats are made possible with a few simple biological ingredients: nucleotides, sugars, and amino acids. These components, exquisitely crafted by evolution, are individually combined in useful ratios and precise sequences in living systems to synthesize DNA, RNA, polysaccharides, and proteins. These macromolecules collectively support organismal structure and function and give rise to the incredible diversity in Charles Darwin's "great tree" of life. However, the seemingly infinite potential for new materials built from these components is, in fact, limited. The chemical identity of these building blocks – with a particular focus herein on the twenty naturally-occurring amino acids – limits the scope and functionality of the recombinant materials we can produce. In order to functionalize these products, to fundamentally change their chemical identity while preserving their biological functionality, we require the finesse of bioorthogonal chemistries and modification techniques.

Bioorthogonal reactions modify biological materials within living systems without perturbing function, much as two orthogonal lines intersect only at a single point. That point of intersection can be precisely defined through recombinant technology and gives us access to new classes of biomaterials. The term “bioorthogonal”, coined by Carolyn Bertozzi, importantly defines these unique chemistries, which inertly co-exist with biology until the exact moment when the desired reactions are initiated, to enhance – and even transform – biological systems.

Bioorthogonal modification of proteins will, by definition, require expansion of the biochemical toolbox; there are a variety of techniques used to achieve this goal. In these studies, we explore the use of genetic code expansion for incorporation of unnatural amino acids. This technology permits co-translational incorporation of amino acids with unique and non-canonical R-groups directly into the polypeptide backbone of a protein or biopolymer. These residues introduce unique chemical reactivity for further functionalization with desired moieties or chemical transformation.

We have used this technology to develop novel therapeutic and material platforms comprised of a unique biopolymer, elastin-like polypeptide (ELP). This thermally responsive biopolymer is easily recombinantly synthesized, though more biochemically complex ELPs require successful bioorthogonal modification. We designed the unnatural amino acid-containing ELPs necessary to enable our strategies for developing three distinct biomaterial platforms: 1) photoreactive ELPs which can

generate stable hydrogel particles spanning four orders of magnitude in size; 2) a universal strategy for drug-loaded, targeted ELP nanoparticles by incorporation of a unique site for drug attachment; 3) a sustained-release therapeutic for treatment of brain tumors combining proteins of distinct cellular origin.

We have combined existing tools, technologies, and materials to generate these novel platforms with utility in biomaterials, drug delivery, and cancer therapeutics. The optimizations performed in developing each of these systems will inform future studies with similar goals; similarly, the reactions and strategies employed will contribute to furthering our understanding of the full potential of these important bioorthogonal chemistries.

Dedication

For my parents.

Contents

Abstract	iv
Contents.....	viii
List of Tables.....	xvii
List of Figures	xix
Acknowledgements	xxvi
1. Introduction	1
1.1 Biopolymers	1
1.1.1 Biopolymer-based formulations and materials.....	2
1.1.1.1 Supramolecular particles and hydrogels.....	2
1.1.1.2 Injectable therapeutics: drug delivery vehicles and sustained-release formulations.....	4
1.1.2 Advantages of biopolymer-based systems	5
1.1.3 Limitations of biopolymer-based systems	7
1.2 Elastin-like polypeptides	7
1.2.1 Origin and sequence	8
1.2.1.1 Genetic engineering of repetitive ELPs.....	10
1.2.2 Lower critical solution temperature	12
1.2.2.1 ELP purification by inverse transition cycling.....	14
1.2.3 Recombinant fusions of ELPs	16
1.2.4 Therapeutic ELP formulations.....	16
1.3 Bioorthogonal functionalization of proteins and polypeptides.....	18

1.3.1 Bioorthogonality: definition and importance.....	18
1.3.2 Methods for bioorthogonal functionalization and limitations	20
1.4 Genetic code expansion	23
1.4.1 Unnatural amino acid incorporation in <i>E. coli</i>	25
1.4.2 Chemical diversity of unnatural amino acids	28
1.4.3 Advantages over alternative bioorthogonal modification techniques and potential limitations	29
2. Optimizing unnatural amino acid incorporation into elastin-like polypeptides.....	32
2.1 Introduction and motivation.....	32
2.1.1 Expression hosts.....	32
2.1.2 Translational machinery	37
2.1.3 Growth conditions	38
2.1.4 Construct design	40
2.2 Materials and methods	41
2.2.1 Molecular biology and design of constructs.....	41
2.2.1.1 Design of modified pTac expression vector compatible with recursive ligation cloning.....	41
2.2.1.2 Construct design and stop codon positioning	43
2.2.2 Library of orthogonal translational systems.....	46
2.2.3 Preparation of bacterial expression hosts	47
2.2.4 Protein expression and purification.....	49
2.2.5 Characterizing expressed products	50
2.3 Results and discussion.....	51

2.3.1 Identifying optimal expression host and growth conditions for unnatural amino acid incorporation	51
2.3.1.1 Constructs with one site of incorporation	51
2.3.1.2 Constructs with multiple sites of incorporation	54
2.3.2 Comparing orthogonal translational system incorporation efficiency with mass spectroscopy	57
2.4 Concluding remarks.....	58
3. Bioorthogonal photocrosslinking strategy for synthesizing nano- to microscale hydrogel particles	60
3.1 Introduction and motivation.....	60
3.1.1 Hydrogel particle utility and methods of synthesis	62
3.1.2 Crosslinking strategies for biopolymers	63
3.2 Materials and methods	64
3.2.1 Molecular biology and design of constructs.....	64
3.2.2 Protein expression, purification, and characterization	66
3.2.3 Crosslinking and particle synthesis	68
3.2.3.1 Nanoparticle synthesis	69
3.2.3.2 Mesoparticle synthesis	69
3.2.3.3 Microparticle synthesis	70
3.2.3.4 Particle extraction.....	71
3.2.4 Particle characterization	72
3.2.4.1 Light scattering.....	72
3.2.4.2 Cryogenic transmission electron microscopy	73

3.2.4.3 Atomic force microscopy	74
3.2.4.4 Scanning electron microscopy	74
3.2.4.5 Heating and optical imaging	75
3.2.4.6 <i>In vivo</i> pharmacokinetic analysis	76
3.3 Results and discussion	77
3.3.1 Mass spectrometry analysis	77
3.3.2 Nanoparticle characterization	79
3.3.2.1 Light scattering	79
3.3.2.2 Cryo-transmission electron microscopy	82
3.3.2.3 Atomic force microscopy	83
3.3.2.4 Pharmacokinetic analysis <i>in vivo</i>	83
3.3.3 Mesoparticle characterization	87
3.3.3.1 Light scattering	89
3.3.3.2 Fluorescence imaging	90
3.3.3.3 Scanning electron microscopy	91
3.3.4 Microparticle characterization	92
3.3.4.1 Fluorescence imaging	92
3.3.4.2 Scanning electron microscopy	95
3.4 Conclusions and future directions	96
3.4.1 Summary and significance	96
3.4.2 Future perspectives	98

4. A bioorthogonal strategy for simultaneous drug loading and active targeting of nanoparticles.....	102
4.1 Introduction and motivation.....	102
4.1.1 Nanoscale biopolymer drug carriers	103
4.1.2 Active targeting of drug delivery vehicles	105
4.1.2.1 Criteria for targeting domain selection.....	106
4.1.2.2 EgA1 nanobody.....	107
4.1.2.3 RGD4C cyclic peptide	108
4.1.3 Small molecule drug selection and conjugation to nanoscale carriers	108
4.2 Materials and methods	109
4.2.1 Molecular biology and design of constructs.....	109
4.2.3 Selection of bacterial expression host	113
4.2.4 Protein expression and purification.....	114
4.2.5 Doxorubicin conjugation to <i>pAcF</i>	117
4.2.6 Size exclusion chromatography and pH release	119
4.2.7 Mass spectrometry analysis	120
4.2.8 <i>In vitro</i> characterization of targeted constructs	121
4.2.8.1 Fluorescent protein labeling and flow cytometry	121
4.2.8.2 Cell viability assays	123
4.2.8.3 Intracellular imaging	124
4.3 Results and discussion.....	127
4.3.1 Characterization of purified proteins	127

4.3.1.1	Characterization of targeting domain candidates and selection of EgA1	127
4.3.1.2	Qualitative characterization of EgA1-targeted constructs and <i>pAcF</i> incorporation with gel electrophoresis	131
4.3.1.3	Quantifying <i>pAcF</i> incorporation efficiency with MALDI-TOF-MS and ESI-LC/MS	132
4.3.2	Quantifying EgA1 binding on a panel of cancer cell lines with flow cytometry	135
4.3.3	Confirming and quantifying extent of Doxorubicin conjugation	137
4.3.3.1	Confirming successful reaction with size exclusion chromatography	140
4.3.3.2	Quantifying labeling efficiency with mass spectrometry	141
4.3.3.3	pH-mediated release of Doxorubicin from ELP nanoparticles	145
4.3.4	Biophysical characterization of Doxorubicin conjugates	146
4.3.4.1	Dynamic light scattering of Doxorubicin conjugates	146
4.3.4.2	Static light scattering of Doxorubicin conjugates	148
4.3.4.3	Cryo-transmission electron microscopy imaging of Doxorubicin conjugates	149
4.3.5	<i>In vitro</i> characterization of Doxorubicin conjugate cytotoxicity	150
4.3.6	Intracellular localization of EgA1-targeted constructs	153
4.3.6.1	Confirming EgA1 specificity for EGFR by EGF competition	153
4.3.6.2	Colocalization of Doxorubicin conjugates and endolysosomes	154
4.4	Conclusions and future directions	157
4.4.1	Summary and significance	157
4.4.2	Future perspectives	159

5. Developing a novel immunotoxin formulation for treatment of brain tumors	162
5.1 Introduction and motivation.....	162
5.1.1 Immunotoxins.....	163
5.1.2 Sustained-release formulations with ELPs	166
5.1.3 Strategies for immunotoxin-ELP synthesis.....	167
5.1.3.1 Click chemistry attachment enabled by genetic code expansion.....	168
5.1.3.2 Enzymatic protein-protein ligation with Sortase A	170
5.1.3.3 Recombinant fusion.....	171
5.2 Materials and methods	172
5.2.1 Construct design and synthesis.....	172
5.2.1.1 Monoclonal antibody.....	172
5.2.1.2 Gly ₃ -DBCO for Sortase A modification of mAb	173
5.2.1.3 <i>p</i> AzF-ELP-toxin for click chemistry attachment.....	174
5.2.1.4 Gly ₃ -ELP-toxin for Sortase A-mediated attachment	175
5.2.1.5 Affibody-ELP-toxin (AffETox)	175
5.2.2 Protein expression and purification.....	177
5.2.2.1 HEK293 transient expression of monoclonal antibodies.....	177
5.2.2.2 Bacterial expression of Sortase A and toxin fusion proteins.....	178
5.2.2.3 Endotoxin purification	182
5.2.2.4 AbETox conjugation and purification strategies.....	184
5.2.3 Immunotoxin characterization	188
5.2.3.1 Mass spectroscopy	188

5.2.3.2 Phase transition behavior	189
5.2.3.3 Cell-free protein translation inhibition assay.....	190
5.2.3.4 Cell viability assays and flow cytometry.....	191
5.2.4 <i>In vivo</i> studies.....	195
5.3 Results and discussion.....	197
5.3.1 Adapting strategies for immunotoxin-ELP synthesis	197
5.3.1.1 Click chemistry attachment for synthesis of antibody-ELP-toxin (AbETox)	197
5.3.1.2 Sortase A-mediated fusion for synthesis of antibody-ELP-toxin (AbETox)	204
5.3.1.3 Recombinant fusion of affibody-ELP-toxin (AffETox)	207
5.3.2 Characterization of AffETox library	208
5.3.2.1 Thermal responsivity of AffETox	208
5.3.2.2 Protein translation inhibition by toxin.....	211
5.3.2.3 <i>In vitro</i> characterization of AffETox	212
5.3.3 <i>In vivo</i> efficacy of AffETox.....	219
5.4 Conclusions and future directions.....	228
5.4.1 Summary and significance.....	228
5.4.2 Future perspectives	231
6. Conclusions.....	235
6.1 Summary of technologies developed	235
6.2 Combining platforms in future work	238
Appendix A.....	242

Appendix B	246
Appendix C.....	248
Appendix D.....	251
References	257
Biography.....	299

List of Tables

Table 1: Growth temperatures of <i>E. coli</i> lines for recombinant unnatural amino acid incorporation	50
Table 2: Static light scattering characterization of xPCD and nxPCD above the critical micellization temperature	81
Table 3: Pharmacokinetic data of xPCD and nxPCD.	87
Table 4: Summary of <i>E. coli</i> strains, growth conditions, and yield of constructs for drug-loaded, targeted nanoparticle platform.	133
Table 5: Percent composition of <i>pAcF</i> -containing constructs by ESI-LC/MS	134
Table 6: Reaction conditions and labeling efficiency of Dox reactions.	139
Table 7: Percent composition of Dox reaction products	145
Table 8: Static light scattering of Dox conjugates.	148
Table 9: ELP nomenclature used for immunotoxin fusion proteins	176
Table 10: Expression yields of immunotoxin proteins and controls	181
Table 11: Treatment groups for GBM maximum tolerated dose study #1	221
Table 12: Median survival of treatment groups in AffETox MTD study #1	223
Table 13: Treatment groups for GBM maximum tolerated dose study #2	224
Table 14: Median survival of treatment groups in AffETox MTD study #2	226
Table 15: Library of orthogonal translation systems explored.	242
Table 16: Growth media composition for recombinant unnatural amino acid incorporation.	244
Table 17: Amino acid sequences and molecular weights of constructs used in crosslinked hydrogel platform	246

Table 18: Amino acid sequences and molecular weights of constructs used in targeted, drug-loaded nanoparticle platform.....	248
Table 19: Amino acid sequences of constructs used in sustained-release immunotoxin platform.....	251

List of Figures

Figure 1: Plasmid reconstruction by recursive directional ligation (PRE-RDL).....	11
Figure 2: Theoretical phase diagram of LCST and UCST polymers.....	13
Figure 3: Schematic of ELP purification via inverse transition cycling (ITC).....	15
Figure 4: Bioorthogonality provides chemical precision for biological systems.	19
Figure 5: Methods for bioorthogonal modification of proteins and polypeptides.	21
Figure 6: Unnatural amino acids transform biomaterials and proteins.	24
Figure 7: Recombinant unnatural amino acid incorporation in <i>E. coli</i>	26
Figure 8: Example residues illustrate the structural and functional diversity of unnatural amino acids.	28
Figure 9: BL21(DE3) incorporation of unnatural amino acids.....	33
Figure 10: Release factors and UAA-tRNA compete at stop codons.....	34
Figure 11: Genomically recoded <i>E.coli</i> for unnatural amino acid incorporation (C321.ΔA.1).	35
Figure 12: Genomically recoded <i>E.coli</i> for unnatural amino acid incorporation (C321.ΔA.2).	36
Figure 13: Phenylalanine auxotroph <i>E.coli</i> for unnatural amino acid incorporation (AF-IQ).....	37
Figure 14: pEvol orthogonal translation system vector map.....	38
Figure 15: Culture media investigated for recombinant unnatural amino acid incorporation, classified by complexity and definition.....	40
Figure 16: Vector maps of m-pET24 and m-pTac plasmids.....	42
Figure 17: ELP architectures explored for unnatural amino acid incorporation.	44
Figure 18: Western blot confirming T7 lysogenization of C321.ΔA.1 <i>E. coli</i>	48

Figure 19: SDS-PAGE of ELP constructs incorporating a single unnatural amino acid at the N-terminus.	52
Figure 20: SDS-PAGE of ELP constructs incorporating a single unnatural amino acid positioned within the chain.	53
Figure 21: Incorporation of four regularly-spaced unnatural residues into ELPs.	55
Figure 22: Incorporation of eight regularly-spaced unnatural residues into ELPs.	56
Figure 23: Incorporation of four and eight clustered unnatural residues into ELPs.	57
Figure 24: ESI-LC/MS analysis comparing the incorporation efficiency of <i>pAzF</i> by two generations of pEvol orthogonal translation systems.	58
Figure 25: Structure of <i>p</i> -azidophenylalanine (<i>pAzF</i>), the unnatural residue used for photocrosslinking.	61
Figure 26: Schematic of two constructs, PCE and PCD, used in crosslinked particle platform.	65
Figure 27: Strategy for crosslinked hydrogel particle synthesis with programmable size	68
Figure 28: Schematic for formation of crosslinked ELP nanoparticles.	69
Figure 29: Schematic for formation of crosslinked ELP mesoparticles.	70
Figure 30: Schematic for formation of crosslinked ELP microparticles.	71
Figure 31: Crosslinked particle extraction from microfluidic droplets.	72
Figure 32: SDS-PAGE of PCE and PCD.	77
Figure 33: ESI-LC/MS analysis of PCE and PCD.	78
Figure 34: Thermal ramp dynamic light scattering of xPCD and nxPCD nano-scale micelles.	80
Figure 35: Hydrodynamic radius of xPCD nano-gels as a function of temperature for multiple heating-cooling cycles indicates no hysteresis in particle size.	81

Figure 36: Cryo-TEM images taken above the critical micellization temperature of xPCD.	82
Figure 37: Tapping mode atomic force microscopy (AFM) images of xPCD nano-gels... 83	83
Figure 38: Dynamic light scattering of fluorescently-labeled PCD confirms particle assembly is unaffected by dye labeling.	84
Figure 39: Pharmacokinetic data for xPCD and nxPCD micelles <i>in vivo</i>	86
Figure 40: PCE exhibits LCST phase behavior in aqueous solution.	88
Figure 41: Dynamic light scattering of crosslinked mesoparticles.....	89
Figure 42: Visualizing mesoscale particles within microfluidic droplets.	90
Figure 43: Scanning electron microscopy imaging of mesoparticles and size distribution.	91
Figure 44: PCE undergoes phase separation upon heating to form liquid coacervates within microdroplets.	92
Figure 45: Fluorescence microscopy images of microgels within water-in-oil emulsion droplets.....	93
Figure 46: Volumetric change of crosslinked microparticles upon heating.	94
Figure 47: Scanning electron microscopy imaging of microparticles and size distribution.	95
Figure 48: Stability of microparticles in a variety of storage conditions.	96
Figure 49: Crosslinked hydrogel particles span four orders of magnitude in size.....	97
Figure 50: Design of targeted ELP _{BC} candidates displaying the RGD4C cyclic peptide or the EgA1 nanobody.	110
Figure 51: Structure of <i>p</i> -acetylphenylalanine (<i>p</i> AcF), the unnatural residue used for Dox conjugation.....	110
Figure 52: Design and assembly of Dox- <i>p</i> AcF-ELP _{BC} -EgA1 nanoparticles.....	111

Figure 53: Characterization of ELP _{BC} -EgA1 and ELP _{BC} -RGD4C self-assembly via dynamic light scattering.....	128
Figure 54: Fluorescence microscopy imaging of ELP _{BC} -RGD4C and ELP _{BC} -EgA1 nanoparticle uptake.....	130
Figure 55: SDS-PAGE of purified constructs for targeted nanoparticle study.....	131
Figure 56: Confirming <i>pAcF</i> incorporation with fluorescent SDS-PAGE.....	132
Figure 57: Tryptic digest of <i>pAcF</i> -ELP _{BC} -EgA1 followed by MALDI-TOF-MS mass spectrometry in both <i>E. coli</i> expression hosts.....	133
Figure 58: Confirming <i>pAcF</i> incorporation into <i>pAcF</i> -ELP _{BC} and <i>pAcF</i> -ELP _{BC} -EgA1 with ESI-LC/MS.....	134
Figure 59: Analysis of fluorescently labeled ELP _{BC} -EgA1 or ELP _{BC} by flow cytometry in EGFR-expressing cell lines.....	136
Figure 60: Flow cytometry of fluorescently labeled ELP _{BC} -EgA1 and ELP _{BC} in additional cell lines with diverse EGFR expression levels.....	137
Figure 61: Linker candidates explored for Dox conjugation reactions.....	138
Figure 62: Schematic of the two-step Dox conjugation to <i>pAcF</i>	140
Figure 63: Attachment of Dox to <i>pAcF</i> -ELP _{BC} -EgA1 and confirmation of purity of the final conjugate using size exclusion chromatography (SEC).....	140
Figure 64: Confirmation of Dox conjugation to Dox- <i>pAcF</i> -ELP _{BC} using size exclusion chromatography (SEC).....	141
Figure 65: Schematic of tryptic digest of <i>pAcF</i> -ELP _{BC}	142
Figure 66: MALDI-TOF-MS spectra of Dox reaction steps following tryptic digest.....	143
Figure 67: Evaluating efficiency of Dox reaction steps with ESI-LC/MS.....	144
Figure 68: pH-mediated release of Dox from Dox- <i>pAcF</i> -ELP _{BC} -EgA1.....	146
Figure 69: Characterization of Dox- <i>pAcF</i> -ELP _{BC} -EgA1 self-assembly by dynamic light scattering.....	147

Figure 70: Approximating critical micellization concentration (CMC) of Dox- <i>p</i> AcF-ELP _{BC} -EgA1 by analyzing dilution series with dynamic light scattering.	147
Figure 71: Static light scattering characterization of Dox conjugates.	149
Figure 72: Visualization of Dox- <i>p</i> AcF-ELP _{BC} -EgA1 and Dox- <i>p</i> AcF-ELP _{BC} micelles by cryogenic transmission electron microscopy (cryo-TEM).	150
Figure 73: EgA1-targeted Dox- <i>p</i> AcF-ELP _{BC} -EgA1 is significantly more potent in cancer cells.	151
Figure 74: Control cell viability assays for Dox conjugates.	153
Figure 75: Confirming EGFR specificity of EgA1 nanobody by EGF competitive uptake assay.	154
Figure 76: Spinning disk confocal imaging of A431 cells incubated with Dox- <i>p</i> AcF-ELP _{BC} -EgA1 or Dox- <i>p</i> AcF-ELP _{BC}	155
Figure 77: Quantifying colocalization of Dox conjugates and endolysosomal compartments.	156
Figure 78: Universal platform for orthogonal drug loading and active targeting of ELP nanoparticles.	158
Figure 79: Bioorthogonal chemistries and corresponding unnatural amino acid residues.	161
Figure 80: Components of an immunotoxin-ELP fusion.	164
Figure 81: Sustained-release immunotoxin platform for treatment of GBM.	166
Figure 82: Sortase A-mediated attachment of clickable DBCO handle to antibody.	169
Figure 83: Spontaneous strain-promoted alkyne-azide cycloaddition (SPAAC) between the modified antibody-DBCO and <i>p</i> AzF-ELP-toxin for AbETox synthesis.	170
Figure 84: Direct Sortase A-mediated ligation for AbETox synthesis.	170
Figure 85: AffETox recombinant fusion proteins with one, two, or four Affibody domains.	172

Figure 86: Synthetic route for Gly ₃ -DBCO.....	173
Figure 87: AbETox two-step purification scheme #1.	186
Figure 88: AbETox two-step purification scheme #2.	187
Figure 89: AbETox two-step purification scheme #3.	188
Figure 90: Cell-free protein translation inhibition assay.	190
Figure 91: SDS-PAGE of purified mAb.....	197
Figure 92: SDS-PAGE of purified Sortase A variants.	198
Figure 93: ESI-LC/MS analysis of Gly ₃ -DBCO synthesis.....	199
Figure 94: Confirming DBCO functionalization of mAb with fluorescent SDS-PAGE. .	200
Figure 95: Confirming specificity of mAb for EGFR and EGFRvIII using flow cytometry.	201
Figure 96: Confirming <i>pAzF</i> incorporation in <i>pAzF</i> -ELP-toxin with fluorescent SDS- PAGE.	202
Figure 97: SDS-PAGE demonstrating click attachment of mAb-DBCO and <i>pAzF</i> -ELP. 203	
Figure 98: SDS-PAGE demonstrating click attachment of mAb-DBCO and <i>pAzF</i> -ELP- toxin.	203
Figure 99: SDS-PAGE of purified Gly ₃ -ELP-toxin.....	204
Figure 100: SDS-PAGE of Sortase A reaction products and non-specific activity.....	205
Figure 101: SDS-PAGE of purified AbETox.	206
Figure 102: MALDI-TOF/MS analysis of AbETox to confirm ELP-toxin attachment.	206
Figure 103: SDS-PAGE of AffETox library and control proteins.	208
Figure 104: Phase transition behavior of AffETox and control proteins as assessed by thermal ramp UV/Vis spectroscopy.	209

Figure 105: Relationship between T_t and concentration for AffETox library.	210
Figure 106: Cell-free translation inhibition of luciferase expression by immunotoxins and control proteins.	211
Figure 107: Cytotoxicity of AffETox constructs in transfected murine fibroblasts expressing human EGFR or EGFRvIII.	213
Figure 108: Summary of IC_{50} values for AffETox library in murine fibroblasts expressing EGFR or EGFRvIII.	214
Figure 109: Untransfected murine fibroblasts which do not express EGFR or EGFRvIII are not sensitive to treatment with AffETox.	215
Figure 110: AffETox constructs demonstrate picomolar efficacy in A431 squamous cell carcinoma lines.	215
Figure 111: Efficacy of AffETox in two patient-derived GBM lines.	216
Figure 112: Potency of AffETox in two murine GBM lines.	218
Figure 113: Flow cytometry confirms binding of ZEGFR affibody to EGFR-expressing fibroblasts and xenograft GBM line.	219
Figure 114: Study design for AffETox efficacy in an orthotopic, syngeneic mouse GBM tumor model.	220
Figure 115: AffETox efficacy in CT-2A orthotopic model (MTD study #1).	222
Figure 116: AffETox efficacy in CT-2A orthotopic model (MTD study #2).	225
Figure 117: Bioorthogonality unlocks new potential for ELPs.	237

Acknowledgements

I owe a debt of gratitude to those in my personal and professional life for their support, mentorship, and encouragement throughout my academic career; no one achieves anything alone.

First and foremost, I thank my parents: for not only investing wholeheartedly in my education, but in my dreams. My dad, a true philosopher, taught me how to wonder, how to appreciate beauty in art and science alike, and has never stopped laying down railroad tracks for us. My mom, the strongest, most selfless woman I know and my biggest role model, taught me how to navigate the world, to be organized and effective, and above all, the importance of being kind. If I have accomplished anything in my life, it is because of them.

To my husband, Matt: from high school to graduate school, your enthusiasm, reassurance, and sense of humor has made all the difference. This thesis would not have been possible without your support. I love you and thank you – may we always revel in the magic of science together.

To my sister, Julia, thank you for believing in me, always being silly with me, and leading by example – it is because of you that I have ever pushed myself; your encouragement means the world. To my oldest, most cherished friends, Sandra, Sarah,

and Justine: thank you for your never-ending words of support and being a constant source of inspiration. The friendship and kindness you have shown me is incomparable.

To my colleagues in the Chilkoti lab, thank you for filling these past years with fond memories and for fostering an environment which nurtures profound growth. I am grateful for each reagent shared, every piece of sound advice, and all the laughter. In particular, I am grateful for the unfailing support and friendship of Dr. Mandana Manzari, Dr. Stefan Roberts, Michael Dzuricky, and Samagya Banskota. To Jonathan Su, it has been a privilege to train you and I am excited to see all you will achieve.

I must acknowledge all of the outstanding mentors I have had throughout my academic career. It was under her mentorship of Prof. Ora Weisz, along with that of Jennifer Bruns and Dr. Christina Szalinski, that I found my love of scientific research and navigated my way, with their help, to graduate school. I am also immensely grateful for Dr. Sarah MacEwan, who trained me as a first-year graduate student in the Chilkoti group, Prof. Davoud Mozhdehi, and Dr. Joseph Bellucci. These individuals redefined for me what it means to be a scientist, and I am very fortunate to have researched alongside of and learned from them.

I have had the privilege of working with exceptional collaborators who have enriched my projects and my professional development. I thank Dr. Eric Brustad for his thoughtful guidance and consistent support from the beginning. I am grateful for the collaboration of Dr. Darrell Bigner, Dr. Vidya Chandramohan, Charlotte McDowall, and

Scott Parker, and I thank them for all their efforts. I am appreciative of my committee members' generous time and constructive feedback throughout my degree milestones.

It is difficult to adequately encapsulate and recognize the effort and time invested by my advisor, Prof. Ashutosh Chilkoti, throughout the course of my graduate career. I thank him for his enthusiastic guidance, allowing me the freedom and space to explore the fascinating – though diametric – worlds of unnatural amino acids and brain tumors, and for demonstrating the importance of continuously evaluating one's science with uncompromising rigor. I have become a stronger communicator and critical thinker, and a more confident scientist with a clear vision of my professional goals as a result of his mentorship. For that, I am and will always be unequivocally grateful.

One final note of gratitude, though she cannot quite read – I will relay this message in the form of her favorite snack – for my dog, Gracie. My constant companion and an unfailing source of joy throughout graduate school; seeing her ever-wagging tail at the end of every day made the difficult moments easier and the good times a cause for celebration.

1. Introduction

This thesis work has broadly focused on the development of novel biomaterials through bioorthogonal manipulation of elastin-like polypeptide (ELP) biopolymers. We first optimized the incorporation of unnatural amino acids (UAAs) into ELPs to maximize potential for functionalization of this biopolymer (Chapter 2). These studies directly enabled our subsequent work employing these unique residues first for photo-mediated crosslinking of these biopolymers to synthesize hydrogel particles spanning four orders of magnitude in size (Chapter 3). We then employed an UAA as a site of attachment to develop a novel strategy for conjugating a small molecule chemotherapeutic to a targeted ELP nanoparticle (Chapter 4). We then investigated these residues for macromolecular attachment of proteins to ELPs to generate a novel drug for brain tumors. This project evolved from its origins in bioorthogonal attachment to an entirely recombinant strategy which has enabled its successful study *in vivo* (Chapter 5). We describe here the foundational research and concepts upon which we built the experimental work in the chapters that follow.

1.1 Biopolymers

Biopolymers are covalently-linked, repeating chains of chemically similar biological monomers produced by living systems and include nucleic acids, polysaccharides, and polypeptides.¹ Recombinant biopolymers are comprised of these same building blocks, but have been reconfigured by molecular engineers to exhibit and

embody specifically desired properties. While nucleic acids, sugars, and esters have been explored to generate unique biomaterials, we focus here specifically on those recombinant biopolymers comprised of amino acids, or polypeptides. These engineered biopolymers are not only composed of the same building blocks, but frequently derive their component sequence motifs from structurally unique proteins, such as silk, collagen, resilin, and elastin.² The recombinant biopolymers can recapitulate specific properties of these, such as the extensibility of elastin or robustness of silk, and provide insight into the biophysical properties of the parent protein. Polypeptides such as elastin-like polypeptides (ELPs) can be engineered into different formulations such as nanoparticles or injectable gels on the basis of their sequence and preparation. The advantages of biopolymers over their synthetic counterparts, ranging from biocompatibility to precise sequence control, as well as inherent limitations as biologically-derived materials, are covered in greater detail below.

1.1.1 Biopolymer-based formulations and materials

1.1.1.1 Supramolecular particles and hydrogels

One of the most functionally useful preparations of biopolymers is as a particle; particles ranging from the nano- to microscale have utility in a variety of applications from therapeutics and tissue engineering to cosmetics and photonics.³⁻⁷ Particles can uniquely be manipulated both in solution as a bulk material and individually during synthesis, providing a high degree of control and tunability.

The size of these biopolymer particles dictates much about their functional utility and intrinsic properties. Nanoparticles composed of biopolymers can be easily prepared using block copolymers, which can be tuned to self-assemble in response to an external trigger.⁸ Nano-scale biopolymer micelles provide many of the advantages of traditional nanoparticles: ease of preparation and administration,⁹ high surface area-to-volume ratio for surface functionalization,¹⁰ and ideal size for penetrating tissues,¹¹ making them useful delivery vehicles *in vivo*. Supramolecular aggregates and assemblies of biopolymers which extend beyond the nanoscale can be used in transporting larger cargoes, cell capture and release, as actuators, and in personal care and food-grade products.¹² These soft matter materials become even better suited for these applications when stabilized as crosslinked hydrogel particles.

Hydrogels are networks of polymers stabilized by covalent crosslinking which rapidly undergo changes in network solubility and hydration state in response to external stimuli, such as local changes in pH and temperature. When hydrogels are confined to a particle geometry, these large-scale volumetric changes can then be directly employed for cargo capture and release, coatings, biosensing, and optics.¹³⁻¹⁹ Biopolymer-based hydrogel particles provide an additional level of tunability with the potential for genetically encoding bioactive domains.

1.1.1.2 Injectable therapeutics: drug delivery vehicles and sustained-release formulations

Beyond having noteworthy biophysical properties, biopolymer-based materials are exceptionally useful for injectable delivery of therapeutics as monomers, particles, and as *in situ* degradable gels loaded with small molecule drugs and biologics. The goal of drug delivery is to improve both the site-specific penetrance and systemic retention of a drug, as many potent small molecule drugs and biologics are cleared rapidly from the system by glomerular filtration or are neutralized by anti-drug antibodies.²⁰⁻²¹ Cargo can benefit from ligation to a polymer carrier through reduction of renal clearance, improved solubility and reduced aggregation, and introduction of “stealth” properties to minimize immune-mediated clearance.²¹ When loaded into polymeric particles, hydrophobic drugs safely sequestered in the core can be both passively and actively targeted to tumors and tissues. Nanoparticles in particular take advantage of the enhanced permeability and retention (EPR) effect, whereby particles on this size scale preferentially hone to and accumulate in tumors owing to the leaky vasculature and lack of proper lymphatic drainage.²² As injectable gels, thermally responsive biopolymers can support sustained-release of cargo to enhance its pharmacokinetic profile and maximize the therapeutic effect. These viscous, insoluble coacervates or drug “depots” provide controlled, tunable release via interstitial flow-driven dilution of the depot perimeter and diffusion of depot components into surrounding tissue and circulation. The

biopolymers that comprise these formulations have many advantages over their synthetic counterparts.

1.1.2 Advantages of biopolymer-based systems

Biopolymers are emerging as the material of choice for injectable therapeutics in large part due to their superior biocompatibility as compared to synthetic polymers. Biologically-inspired biopolymers such as ELP, which is derived from human tropoelastin, are non-toxic, non-immunogenic, biodegradable, and bio-inert.²³ These biopolymers have significant proportions of oxygen and nitrogen in their backbone, along with carbon and hydrogen, and are therefore readily broken down into biological building blocks.²⁴ This ensures a seamless integration with and minimal perturbation to biological systems in a variety of applications.

The bio-inspired sequences comprising biopolymers largely prevent their immune recognition, as compared to the increasingly apparent immunogenicity of synthetic polymers.²⁵⁻²⁷ An immune response against a drug carrier will immediately opsonize the carrier and neutralize the cytotoxic cargo.²⁸⁻³⁰ Conjugating cargo to a biopolymer carrier therefore provides two layers of protection against immune-mediated clearance: prevention of non-specific adsorption of immune-activating proteins as well as minimal immunogenicity of the carrier itself.

As many biopolymers are bioinspired, these materials often recapitulate many of the unique properties of their parent material such as self-assembly into fibrils,

responsivity to changes in temperature, pH, or osmolarity, as well as many useful bulk properties such as high tensile strength, elasticity, and resiliency.¹ The various highly advantageous properties evolved by biological systems to maintain structure, define shape, provide natural defenses, and support movement can be easily controlled by simple genetic manipulation of these biopolymers.

Biopolymers encoded at the gene level allow for extensive customizability via introduction of bioactive domains and biological motifs. Biopolymers can support an incredible diversity of functionalities through introduction of targeting ligands for active delivery, protease recognition sites for programmable degradation, functional enzymes for controlled metabolic processing, and any number of cytotoxic protein payloads. While synthetic polymer networks require chemical conjugation or immobilization of these motifs and moieties, biopolymers can be seamlessly fused with these groups allowing for precise stoichiometric control of their occurrence and population bioactivity.

One of the greatest advantages of using genetically encoded biopolymers is their perfect monodispersity – every chain expressed has identical chemical identity and chain length. This is of critical importance for therapeutic applications, which demand homogeneity to control and predict therapeutic response.

1.1.3 Limitations of biopolymer-based systems

While biopolymers have many advantages over their synthetic counterparts, the latter does possess the advantage of being more easily chemically manipulated and functionalized with a variety of moieties. The limited chemical diversity available with the twenty naturally-occurring amino acid side chains in turn has traditionally limited the potential for functionalization of biopolymers. The wide diversity of the proteome is largely supported through post-translational modifications and a few key residues provide *bona fide* chemical handles for functionalization: lysine, cysteine, and, to a lesser extent, tyrosine, tryptophan, and histidine.³¹⁻³³ However, these residues are equally as important for protein function as they are reactive; lysine is often required for bioactivity and cysteine for stability and folding.³⁴⁻³⁶ Recent advancements in bioorthogonal chemistries have expanded the functionalities available for biopolymers and heightened their chemical tunability to the level of synthetic polymers.

1.2 Elastin-like polypeptides

Elastin-like polypeptides (ELPs) are thermally responsive peptide polymers used extensively in biomedical research. Their biological origin and stimuli-responsive properties have positioned ELPs as a valuable bridge between the fields of polymer chemistry and medicine. Advances in genetic engineering of repetitive peptide polymers allow the *de novo* design of self-assembled structures, including nanoparticles and bio-active hydrogels. The ability to design ELPs as soluble unimers, viscous coacervates, or

to self-assemble into higher order structures showcases their structural versatility. Their biocompatibility, extensive genetic tunability, and unique biophysical properties have led to the establishment of ELPs as a cutting-edge tool across a spectrum of materials science and biomedical applications, ranging from polymer physics to tissue engineering and drug delivery.

1.2.1 Origin and sequence

Elastin is an essential component of the vertebrate extracellular matrix.³⁷ Elastin proteins provide the repetitive stretch and elastic recoil necessary for the operation of extensible tissues such as blood vessels, skin, vocal folds, bladder, and elastic ligaments.³⁸⁻³⁹ In arteries, for example, elastin couples with collagen, wherein collagen prevents rupture at high extension while elastin minimizes the energy demands on the heart by providing consistent recoil and high resilience.^{37, 40-41} Considered one of the most elastic biomaterials known, elastin can deform at least 60% in the elastic region, has a Young's modulus of ~1MPa, and a resilience of ~90%.⁴²⁻⁴⁴ The extensibility of elastin has been reported to range between 100-200%.⁴⁴ Elastin is not only highly elastic, but also a highly durable material with a half-life on the order of the lifetime of the parent organism.⁴²⁻⁴⁵ The durability of elastin is evidenced by the billions of stretch/relaxation cycles experienced by elastic fibers in the aortic arch without showing fatigue.⁴⁶ The force for elastic recoil arises from the decrease in entropy upon stretching rather than by direct strain of the material.⁴⁷ In addition to its unique mechanical properties, elastin has

been shown to self-assemble and coacervate in response to a variety of stimuli, notably local fluctuations in temperature.⁴⁸⁻⁴⁹ For example, α -elastin has been shown to self-assemble into 5-nm-wide fibers upon sustained heating.⁵⁰

The precursor protein to these insoluble elastin networks is the soluble protein tropoelastin. Early analysis of the amino acid sequence (involving the tryptic digest of solubilized elastin from porcine aortas) revealed the presence of disordered hydrophobic domains and structured hydrophilic domains.⁵¹⁻⁵³ The tropoelastin amino acid sequence alternates between repetitive hydrophobic domains rich in proline, glycine, alanine, and valine residues and ordered hydrophilic domains which contain lysine residues for covalent crosslinking.⁵⁴ The final macromolecular elastin complex is biologically synthesized through enzyme-mediated, irreversible crosslinking of aggregated tropoelastin proteins into insoluble, mature elastin fibers.⁵⁵ The conserved sequence features of tropoelastin provided the basis of elastin-derived biopolymers.

Motivated by the repetitive nature of elastin, Urry pioneered the development of biopolymers inspired by elastin by chemically synthesizing polypeptides. His initial efforts centered around the synthesis and study of polymers containing the pentamer “VPGVG” and studying the resulting unique reversible phase behavior in aqueous solvents.^{51, 56} These elastin-like polypeptides (ELPs) constitute the most reductionist approach to the design of biomaterials inspired by elastin. His group further generalized this approach to polymers composed of the recurrent pentapeptide motif found in

tropoelastin, VPGXG, where X is any amino acid except proline. This pentameric motif is repeated '*n*' times in an ELP chain to give rise to a unique, intrinsically disordered, thermally responsive biopolymer with the simple sequence (VPGXG)_{*n*}.⁵⁷ The ability to translate environmental changes into pronounced changes in the physical properties of a material constitutes the basis for the "smart" behavior of elastin biopolymers.

1.2.1.1 Genetic engineering of repetitive ELPs

The greatest challenge in the recombinant synthesis of ELPs and other highly repetitive polypeptides is that they are also highly repetitive at the gene level. Standard gene assembly methods involving polymerase chain reaction (PCR) and hybridization of overlapping sequences cannot be used for assembly of highly repetitive genes; therefore, ELPs require specialized genetic assembly methods to produce polymers of various lengths. There is a suite of gene oligomerization methods for rapidly producing and building ELP genes: concatemerization,⁵⁸ overlap extension rolling circle amplification (OERCA),⁵⁹ and two seamless cloning strategies: recursive directional ligation (RDL),⁶⁰ and plasmid reconstruction by recursive directional ligation (Pre-RDL).⁶¹ The latter is the main technique used for construction of genes in this thesis.

Pre-RDL involves ligating two halves of a parent plasmid, each containing an oligomer to build the final ELP gene product with a specified oligomer order.⁶¹ This technique relies on Type II restriction enzymes which cleave at a defined number of nucleotides away from their recognition sequence. This effectively eliminates any

restriction on the biopolymer sequence, as the recognition sites are designed to be outside of the coding region of the gene itself. Two separate plasmids are used as substrates for the reaction – both are digested with one common enzyme and a second unique enzyme. While the unique enzymes have distinct recognition sequences, the overlaps generated after digestion are complementary. Ligation of the two halves seamlessly joins the two starting gene sections in a defined orientation in the final complete vector, which can be readily digested for another round of PRe-RDL cloning. The plasmid backbone, including the antibiotic resistance marker, is only reconstructed upon successful ligation, thereby nearly guaranteeing any vector products contain both desired genes (Figure 1).

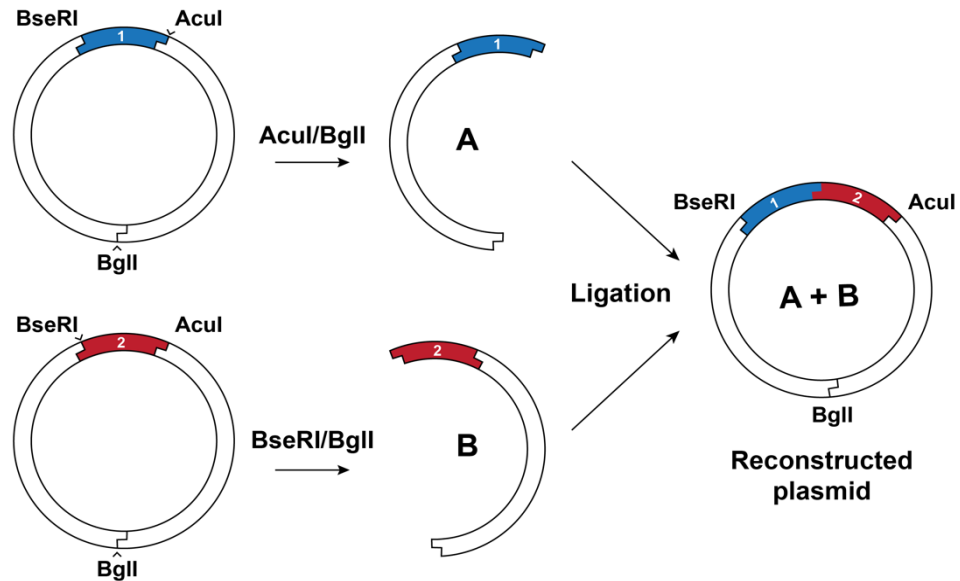


Figure 1: Plasmid reconstruction by recursive directional ligation (PRe-RDL).

PRe-RDL is highly successful in constructing genes up to approximately 2400 base pairs in length; longer inserts compromise ligation efficiency. This method enables

the rapid synthesis of ELP monomers, construction of block copolymers, as well as introduction of N-terminal leader and C-terminal trailer sequences.

1.2.2 Lower critical solution temperature

ELPs belong to a broad class of stimuli-responsive polymers which possess a lower critical solution temperature transition (LCST). These polymers exhibit a unique inverse transition temperature – at temperatures below a characteristic transition temperature, a polymer mixture contains a single, continuous phase but upon heating will phase separate into two distinct phases. This behavior can be directly attributed to the significant proportion of hydrophobic amino acids comprising the ELP pentameric motif; these residues readily undergo hydrophobic collapse and aggregate upon heating.

The phase transition behavior of ELPs can be described with a representative phase diagram.⁶² The region below the binodal line indicates the temperatures and concentrations for which polymer chains in an aqueous mixture are well-solvated and soluble. A metastable phase lies between the spinodal and binodal boundaries, in which two separated phases are each stable against small fluctuations in composition or temperature and will not fully phase separate unless initiated by a large nucleation event. Above the spinodal boundary, the solution will spontaneously phase separate into two distinct phases: a polymer-rich and polymer-poor phase. The critical point (LCST), or inverse transition temperature (T_i) is the point of intersection of the spinodal and binodal curves, which indicates the lowest possible temperature that will elicit a

phase change. In contrast to this behavior, polymers that display upper critical solution transition (UCST) phase behavior have a phase diagram that is a mirror image of LCST phase behavior (Figure 2).⁶³

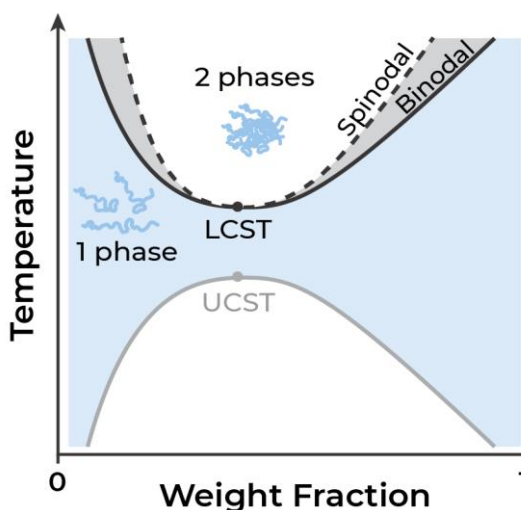


Figure 2: Theoretical phase diagram of LCST and UCST polymers. Shaded region between the spinodal and binodal boundaries denotes the metastable phase.

The precise tunability of this LCST behavior at the sequence level has led to the widespread use of ELPs as a biomaterial and as a biomolecular tool. Urry and coworkers first demonstrated that the phase transition temperature (T_t) of ELPs could be controlled by the hydrophobicity of the guest residue 'X' in the VPGXG pentapeptide motif.⁵⁷ Meyer and Chilkoti subsequently elucidated two additional variables that significantly impact the T_t : the chain length of an ELP and its solution concentration.⁶⁴

The reliance of T_t on guest residue enables the synthesis of self-assembling ELP diblock copolymers. Amphiphilic ELPs can be designed with two distinct blocks containing guest residues that differ significantly in their hydrophobicity, (i.e.

(VPGVG)_n(VPGSG)_n).⁶⁵ Below a critical micellization temperature (CMT), both blocks are soluble, and the polymer chains exist as well-solvated unimers in solution. Upon heating past the T_t of the hydrophobic block, this block will selectively desolvate, collapsing into the core of a self-assembled nanoscale micelle, while the hydrophilic block remains solvated on the corona. Upon heating further, the hydrophilic block will transition, and the micelles will aggregate into micron-scale, insoluble coacervates.

Importantly, this phase transition behavior is entirely reversible. ELPs form nearly perfect elastomeric materials that do not dissipate energy during stretching, thus displaying very little thermal hysteresis. ELPs rapidly resolubilize upon cooling, often at the same temperature required for phase separation upon heating. This reversible LCST behavior enables a useful strategy for non-chromatographic purification of ELPs.

1.2.2.1 ELP purification by inverse transition cycling

Production of ELPs is cost-efficient and scalable due to a simple purification strategy, known as inverse transition cycling (ITC) (Figure 3). This non-chromatographic purification scheme exploits the inverse phase separation of solutions of ELP in response to increased heat and ionic strength.⁶⁶⁻⁶⁷ ELPs are expressed recombinantly in the soluble fraction of *E. coli* bacteria; shaker flask cultures can produce 50 mg L⁻¹ to 1.5 g L⁻¹ of pure ELP under optimal conditions.⁵⁵

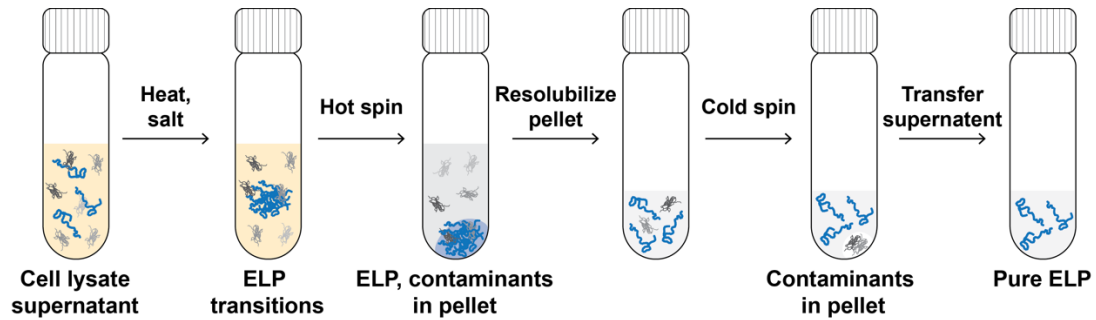


Figure 3: Schematic of ELP purification via inverse transition cycling (ITC)

The first step in the purification process is to lyse the bacteria; the cell lysate is then centrifuged below the T_t of the polymer to remove insoluble cell fragments. This step may also include the addition of the polycationic polyethyleneimine (PEI) to precipitate nucleic acids. The supernatant is then heated ($T > T_t$) to trigger the ELP phase transition. Changing the ionic strength of a solution by adding kosmotropic salts from the Hofmeister series (i.e. sodium chloride, ammonium sulfate) is another strategy to encourage ELP transition.⁶⁸ This suspension is then centrifuged leading to the formation of an ELP-rich pellet at the bottom of the centrifuge tube, along with entrapped, aggregated contaminant proteins. This centrifuge is performed at a temperature above the T_t and is therefore termed a “hot spin”. The pellet is then dissolved by reversing the phase transition by the addition of low salt buffer at a temperature below the T_t of the ELP. The remaining contaminant proteins which irreversibly aggregated during the hot spin will not resolubilize; after centrifuging this resuspension these insoluble proteins will pellet and can be removed by transfer of the ELP-rich supernatant to a new tube. This spin is performed below the T_t of the ELP and is therefore termed a “cold spin”.

These centrifugation steps can be repeated several times until a product is obtained with the desired purity level; typically, ELPs can be purified to > 95% purity after four rounds of purification with this method.⁶⁹⁻⁷⁰

1.2.3 Recombinant fusions of ELPs

Given that ELPs are genetically encoded, they can easily be fused to recombinant protein partners at their N- or C-termini, or both, without loss of LCST behavior.

Furthermore, the fusion partners will then be imbued with the ability to phase transition while maintaining their structure and bioactivity. The transition temperature of the parent ELP will likely be affected by introduction of a fusion partner, the extent to which is determined by the relative hydrophobicity and surface charge of the appended protein or peptide.⁷¹⁻⁷² ELPs have previously been fused to peptides,⁷³ fibronectin domains,⁷⁴ nanobodies,⁷⁵⁻⁷⁶ TRAIL,⁷⁷ glycoproteins,⁷⁸ enzymes,⁷⁹ and fluorescent proteins⁸⁰ at their N- or C-termini, or both. Not only can the appended ELP provide a useful purification handle for these fusion partners, the resulting chimeric protein can form the basis of a powerful therapeutic or unique biomaterial.

1.2.4 Therapeutic ELP formulations

ELPs have been formulated into a variety of delivery systems for therapeutic payloads, ranging from small molecule drugs to peptides and proteins, for applications in tissue engineering, heart disease, cancer, and diabetes.⁸¹ These formulations all take

advantage of the unique phase transition behavior of ELP to modulate delivery, optimize pharmacokinetics, and tune drug release.

Amphiphilic ELP diblocks which self-assemble into nanoscale micelles can act as drug delivery vehicles for conjugated small molecule drugs. Chemotherapeutic drugs are often hydrophobic ($1 < \log P < 5$) which results in poor bioavailability and poses a barrier to optimal pharmacokinetics.⁸² These hydrophobic drugs can be used to drive self-assembly of ELP monoblocks into micelles simply via site-specific conjugation.⁸³ When sequestered in the hydrophobic core of these micelles and delivered intravenously, this ELP-based delivery system increases drug half-life several orders of magnitude and provides a means for passive targeting and accumulation in tumor tissue via the EPR effect, both of which significantly improve bioavailability (see Section 1.1.1.2). Drugs such as doxorubicin, paclitaxel, and gemcitabine have been conjugated to ELP mono- and diblock carriers for successful treatment of tumors *in vivo*.⁸⁴⁻⁸⁶

Another injectable formulation for ELP-based therapeutics is as a “depot” for sustained drug release. The transition temperature of an ELP or ELP fusion can be tuned such that a solution of this material is a soluble liquid in the syringe, but transitions to a viscous gel, or coacervate, upon injection *in vivo*, a process driven solely by body heat. This depot will slowly dissolve over time, releasing soluble fusion molecules at a steady rate. This sustained release is a product of the inverse-log relationship between T_t and concentration.⁸⁷ As the perimeter of the depot is diluted by interstitial flow, the ELP

fusion concentration in this region decreases, causing the T_i to increase above body temperature. Unimers residing at the depot margins thereby resolubilize and diffuse into the surrounding tissue or into circulation.^{73, 88-89} These ELP depots can be used to prolong the release of drugs for over one week *in vivo*; an injectable peptide-ELP depot was previously developed that released soluble fusion molecules for up to ten days in mice with zero-order kinetics, and up to twenty days in non-human primates.⁸⁸ Both particle- and depot-forming ELPs provide an avenue to genetically encode and molecularly engineer sophisticated drug delivery systems.

1.3 Bioorthogonal functionalization of proteins and polypeptides

We have exquisite control over the design of our ELP at the sequence level, with the ability to precisely specify molecular weight, tune phase transition properties, and include fusion partners. However, we are limited by the chemical diversity of the twenty naturally-occurring amino acids without additional functionalization. We rely on bioorthogonal chemistries to shape the biochemical landscape of proteins and biopolymers with precision and minimal perturbation of essential biological properties.

1.3.1 Bioorthogonality: definition and importance

Bioorthogonality introduces an indispensable level of control for next-generation protein engineering and recombinant biotechnology: the ability to manipulate biological systems with the precision, selectivity, and the deftness of chemistry. Bertozzi and co-workers were the first to identify and classify bioorthogonal reactions as those “chemical

reactions that neither interact with nor interfere with a biological system".⁹⁰⁻⁹¹ For our purposes, we explore those reactions which involve precise manipulation of biological material (proteins and polypeptides), but do not take place within a living system and therefore have a marginally different set of constraints and requirements than the classically defined reactions. Regardless of context, the goal remains the same: a chemical reaction which selectively modifies biological material with pinpoint precision, and which has minimal impact on the other components in the system (Figure 4).

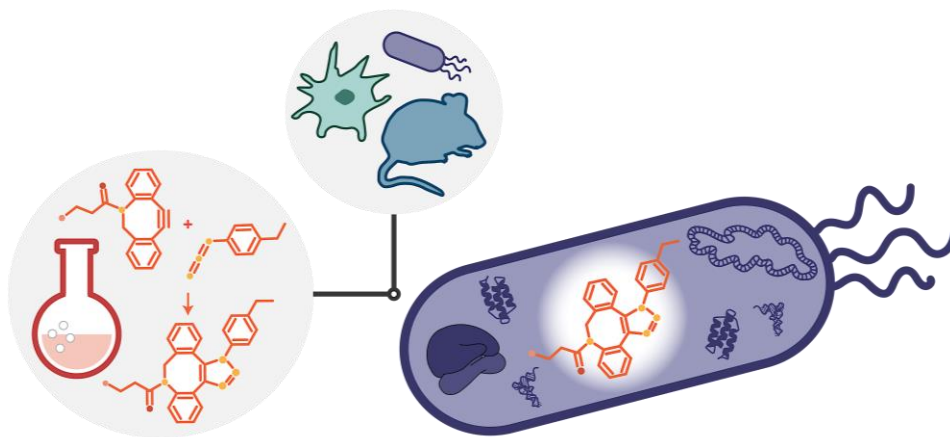


Figure 4: Bioorthogonality provides chemical precision for biological systems.

In order for a reaction to achieve bioorthogonality, the reaction partners and the reaction product must fulfill several key parameters. The reaction partners employed for bioorthogonal reactions must be kinetically, thermodynamically, and metabolically stable prior to the reaction, to ensure absolute inertness with the surrounding biological material.⁹² These innocuous reactive groups are typically small in molecular weight and identified by studying the reactivity space outside of those chemical reactions already

employed by nature (i.e. alkyne-azide cycloaddition).⁹¹ It is the defining element of a bioorthogonal reaction that the reaction partners are specific for each other, and only each other, with minimal possibility of undesirable side reactions under physiological conditions. The resulting covalent linkage formed after reaction must be stable, with either no or non-toxic byproducts (i.e. nitrogen gas, water).⁹²

The investment in developing these valuable reactions has been richly rewarded by the diversity of sophisticated new biomaterials – and even entire biological systems – enabled by these chemistries. Potent antibody-drug conjugates, synthetic glycoproteins, high-resolution tracking of zebrafish development, and single-cell imaging in live mice have all been made possible through the advent of bioorthogonal reactions.⁹³ These reactions have ushered in a new era of biotechnology: the powerful ability to control the bountiful, rugged landscape of biology with the exactness and dexterity of chemistry.

1.3.2 Methods for bioorthogonal functionalization and limitations

There is a suite of bioorthogonal modification techniques widely employed in recombinant biotechnology to convert otherwise inert proteins and polypeptides into reactive species through the introduction of unique chemical handles. There are alternative functionalization strategies, such as post-translational modifications, which introduce unique chemical groups, but these are frequently non-reactive; our focus here is on those chemistries which provide a handle for covalent bond formation (i.e.

conjugation or crosslinking). These methods have their merit and demonstrated utility, but present some limitations, as well (Figure 5).

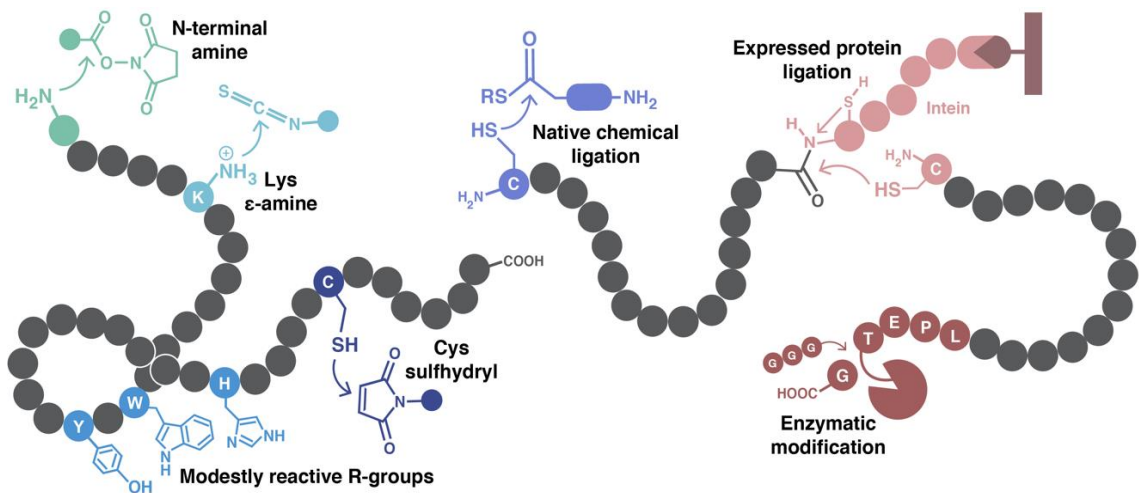


Figure 5: Methods for bioorthogonal modification of proteins and polypeptides.

Chemical modification of proteins without genetic code expansion largely relies on reaction at the N-terminus, residues with reactive side chains, or enzymatic ligation. Reaction at the N-terminal amine is commonly achieved by reaction with N-hydroxysuccinimide (NHS) ester- or imidoester-functionalized probes.⁹⁴ However, this only provides one restricted site of conjugation and there is potential for cross-reactivity with the nucleophilic primary amines of lysine R-groups. The ϵ -amine of these residues can be modified with the same electrophilic reagents, with selectivity between these two sites achieved by specifying the pH of the solution during labeling. However, not all proteins are tolerant to the elevated pH (≥ 10.5) required for selective labeling of lysine

residues.⁹⁵ Furthermore, the introduction of multiple charged lysine residues can undesirably impact the biophysical properties, especially for polypeptides such as ELPs.

The side groups of other reactive amino acids can also be used for functionalization, though all residue-specific strategies restrict the location or bioactivity of the parent biomolecule, or both. Modestly reactive tyrosine, tryptophan, and histidine residues can be labeled with specialized reagents, though the low reactivity of these side chains limits the utility of these methods.⁹⁶ The sulfhydryl side chain of cysteine residues is used frequently for labeling with thiol-reactive reagents such as maleimide- and iodoacetamide-functionalized probes.⁹⁷ Cysteine is the most robustly nucleophilic amino acid and is readily labeled with these chemistries. Though typically rare in protein sequences, these residues are critical for structure and bioactivity when present. Introducing engineered sites for labeling can form undesirable inter- or intrachain disulfide bonds. Furthermore, the bonds formed through labeling are reversible upon changes in oxidation state, limiting their utility in biological settings.

Native chemical ligation (NCL) is one method for synthetic construction of polypeptide backbones and involves the formation of a native peptide bond between the N-terminal cysteine residue of a protein and a thioester-containing peptide.⁹⁸ However, this method is location-restricted to the N-terminus and an engineered cysteine is required, along with solid phase synthesis of the substrate peptide. Expressed protein-ligation is a variation on NCL in which recombinant proteins can be ligated by the same

chemistry, with a self-cleaving intein sequence used to generate the C-terminal thioester; this method is useful for building composite proteins, but only in a linear fashion.⁹⁹⁻¹⁰⁰

Lastly, chemical groups, peptides, and proteins can be conjugated enzymatically with Sortase A, formylglycine-generating enzyme (FGE), SpyTag/SpyCatcher, and others.¹⁰¹⁻¹⁰³ However, these enzymes require a recognition motif positioned in solvent-accessible sites, and often specifically at the N- or C-terminus; these can be disruptive to protein structure and function. Furthermore, reactive amino acids positioned outside of the recognition sequence can encourage non-specific enzyme activity, severely limiting the ability to employ these techniques when selectivity is required.

The existing methods of bioorthogonal functionalization restrict both the location and number of sites available for chemical modification and rely heavily on the use of amino acid side chains or sequence-specific motifs. An alternative approach, in which all naturally occurring amino acids and sequences are available for unrestricted protein design and synthesis, is to introduce a bioorthogonal residue into the polypeptide backbone through genetic code expansion.

1.4 Genetic code expansion

Genetic code expansion is the platform technology through which the universal genetic code is effectively amplified and reorganized to include additional amino acids beyond the twenty naturally-occurring residues, termed non-canonical, non-standard, or unnatural amino acids. Unnatural amino acids are versatile and powerful tools to

expand the chemical repertoire of biopolymers and proteins and to introduce an incredible diversity of chemical handles, while maintaining the bioactivity and biophysical properties of the parent protein. The efficiency and fidelity of this technology supports a wide variety of recombinant biotechnologies: probing of protein structure and function, identifying the role of post-translational modifications in the proteome, regulating and modifying protein function including immunogenicity, conjugating functional payloads to proteins both post-purification and *in vivo*, and, in general, producing more sophisticated, superior biomaterials (Figure 6).

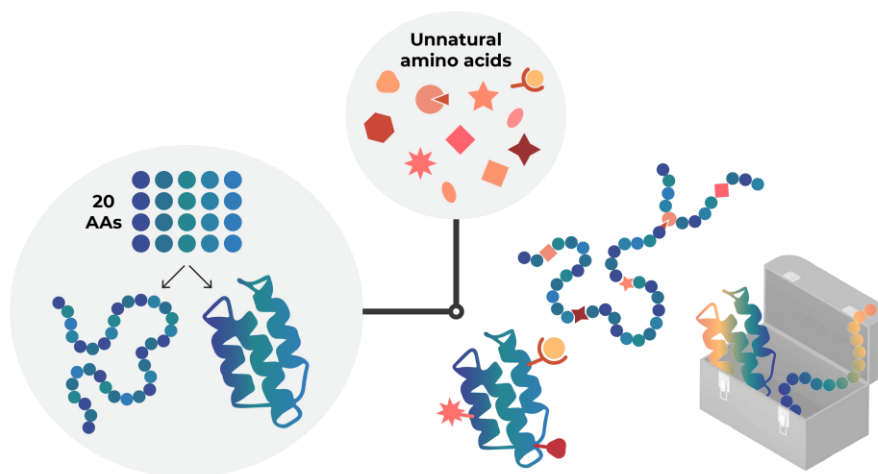


Figure 6: Unnatural amino acids transform biomaterials and proteins.

There are a few methods for incorporation of unnatural amino acids into recombinant proteins. The approach employed in this thesis work, site-specific stop codon suppression, was first developed over two decades ago by Peter Schultz and co-workers.¹⁰⁴ His approach to circumvent the lack of unassigned codons in the universal genetic code was to reassign the least frequently used stop codon – the amber stop

codon – in the *E. coli* genome to be used for unnatural residue incorporation. The first residue incorporated with this method was *o*-methyltyrosine into *E. coli* using an orthogonal translation system (OTS) imported from *Methanococcus jannaschii*. Methanogens are sufficiently evolutionarily divergent from prokaryotes to be orthogonal, and this particular species was the first archaeon to have its genome sequenced, revealing its use of the amber codon to code for tyrosine.¹⁰⁵⁻¹⁰⁶ It was a logical progression, then, to use the *M. jannaschii* tyrosine machinery to develop an OTS which could incorporate tyrosine structural analogs at amber stop codons in *E. coli*. The technology has since exploded from its origins in prokaryotes to viruses, yeast, and mammalian cells, to entire organisms ranging from silk worms to zebrafish to mice.¹⁰⁷⁻¹¹¹

1.4.1 Unnatural amino acid incorporation in *E. coli*

There are four general requirements for recombinant unnatural amino acid incorporation in *E. coli*: 1) the unnatural residue of interest, to be added to the growth media; 2) the vector encoding the orthogonal translation system (OTS), including the aminoacyl tRNA synthetase and tRNA; 3) the vector encoding the gene of interest with amber codons designating the incorporation site(s); and 4) the inducing agents and selection antibiotics corresponding to these two vectors (Figure 7).

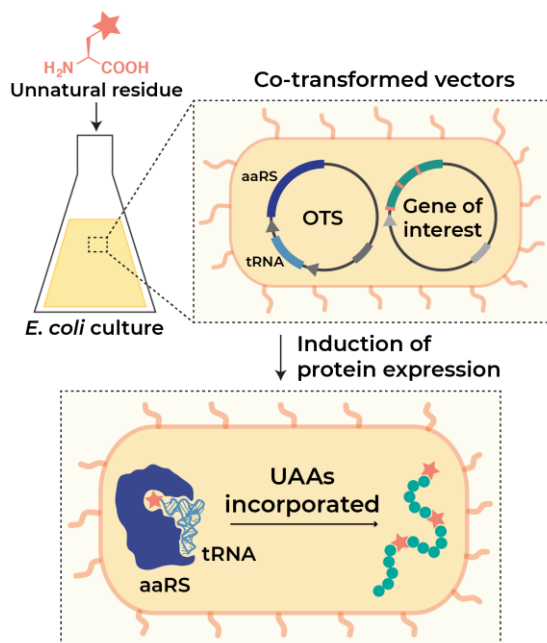


Figure 7: Recombinant unnatural amino acid incorporation in *E. coli*.

The unnatural residue is added directly to the media, either as a hydrochloride salt or solubilized with a strong base, and many unnatural residues are commercially available or can be easily synthesized using inexpensive starting materials. These residues are typically added at a final concentration of 1 mM, though previous studies have increased this as much as five-fold in an effort to maximize incorporation efficiency and yield.¹¹¹⁻¹¹² Few groups have systematically tested the effect of instead lowering UAA concentration on yield; however, Isaacs and co-workers identified that in the context of their optimized OTS, 0.5 mM of several UAAs tested had comparable or superior protein yield as expressions with 1 mM residue.¹¹³ It is prudent, therefore, to identify the minimal concentration of UAA necessary for protein production during optimization studies. The addition of an unnatural residue which is structurally

analogous to Tyr or Phe increases the potential for misincorporation into critical endogenous proteins, and the added energetic burden of the unnatural machinery can be toxic to the cells.

In addition to the unnatural residue, the two vectors to be co-transformed into the *E. coli* expression host must have compatible origins of replication, promoters, and selection markers to ensure co-expression of all the necessary components. The OTS (aminoacyl tRNA synthetase/aaRS and tRNA) is derived from an evolutionarily distant species (including *M. jannaschii*, *M. barkeri*, *M. mazei*) to ensure orthogonality prior to the necessary directed evolution to tailor this system for unnatural residue incorporation.¹⁰⁵

¹¹⁴⁻¹¹⁵ The evolution of the OTS involves multiple rounds of positive and negative selection to stringently identify the mutant aaRS/tRNA pair which is mutually exclusive for only one another and the unnatural residue in the presence of endogenous *E. coli* machinery and materials.

While the expression of the gene of interest is induced during log phase growth, there are different schools of thought as to the optimal time for induction of the OTS. Often, this decision is simply a matter of preference of the individual experimenter. Some groups induce the OTS immediately after inoculation of the culture, guided by the hypothesis that expression of the aaRS and associated charging of tRNA is a prerequisite for expression of the gene of interest. Conversely, other researchers surmise that it is more important for all induction to take place only when the bacteria have reached log

phase growth and induce expression of both the OTS and gene of interest simultaneously at that point. There have yet to be any systematic studies to determine which approach is optimal, and even then, with many other variables ranging from growth media to residue to OTS itself, the optimal time for induction may vary according each individual expression.

1.4.2 Chemical diversity of unnatural amino acids

There is incredible structural and functional diversity among the unnatural amino acids that have been incorporated into proteins in both prokaryotic and eukaryotic expression hosts. For *E. coli*, there are well over 100 residues with corresponding orthogonal translation systems (OTS), with functionalities ranging from sites for bioorthogonal ligation, polymerization initiation, imaging probes, and post-translational modification mimics, among others (Figure 8).¹¹⁶

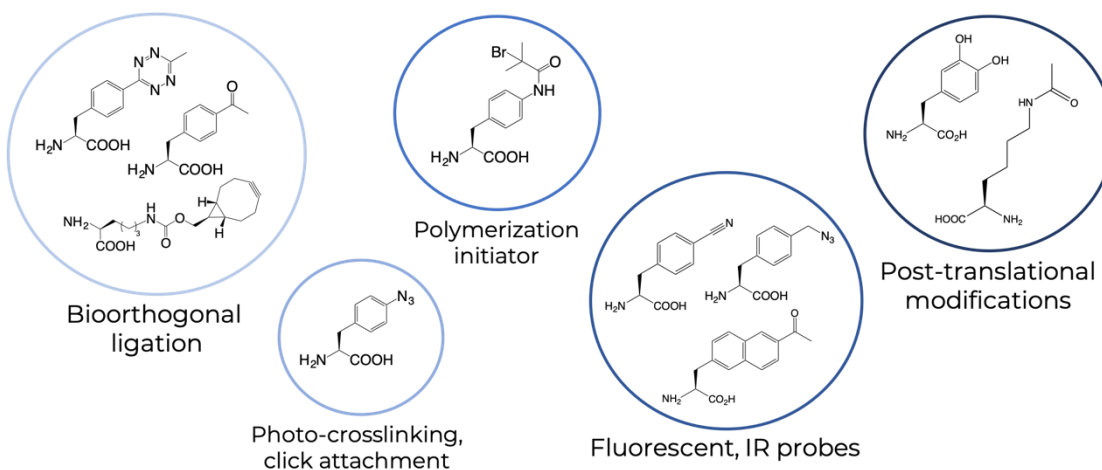


Figure 8: Example residues illustrate the structural and functional diversity of unnatural amino acids.

Importantly, this number was reported in a review article compiled almost a decade ago; there are undoubtedly dozens or even hundreds of novel residues available currently. With over 150 research articles published involving genetic code expansion per year, this rapidly growing field continues to innovate with novel residues and OTS being regularly developed and reported.

1.4.3 Advantages over alternative bioorthogonal modification techniques and potential limitations

The potential for site-specific and highly efficient bioorthogonal ligation is one exciting avenue for unnatural amino acid utility, and the most pertinent to this dissertation. There are several advantages of using these residues over alternative methods, as well as a few areas for improvement as the field continues to grow.

Genetic code expansion effectively addresses the limitations inherent to other bioorthogonal ligation methods, as outlined in Section 1.3.2. These residues represent the most ideal orthogonal handle for functionalization, as they co-translationally introduce a moiety with minimal or no cross-reactivity to endogenous chemistries. The location of UAA incorporation and therefore functionalization can be precisely determined, and these genetically encoded sites ensure the homogeneity of the recombinant protein population. This level of stringent bioorthogonality provides a previously unattainable level of control for functionalization of recombinant proteins. Furthermore, selection of the specific unnatural residue allows for control of the type and reversibility of the bond formed with any attached ligands. These reactive proteins

are immediately available for the next step of processing after purification or can even be purified using these reactive handles. Genetic code expansion eliminates the reliance on the “middleman” reactions required of many bioorthogonal reactions to convert inert residues into reactive sites.

While genetic code expansion is strongly positioned at the forefront of bioorthogonal chemistry, there are clear areas where future development in the field can be focused to improve this technology even further. While there are theoretically no restrictions on the location of UAA insertion or the number of sites, there are practical limitations on placement within structured proteins and on maximum yield with multi-site incorporations. However, the limitations on yield can be addressed by evolving orthogonal translation systems which can catalytically match the translational rate of endogenous machinery, as was accomplished by Isaacs and co-workers.¹¹⁷ Another limitation is that not all unnatural residues are tolerated for incorporation by cellular systems as the chemical groups themselves introduce toxicity. For these, cell-free systems can be used, albeit with a moderate reduction in yield. Similarly, it has historically been marginally more complicated to incorporate multiple different residues into a single protein for multi-level bioorthogonal functionalization. However, recent developments have made this feasible through the use of the ochre stop codon, four-letter codons, alternative ribosomes, or co-opting other infrequently used sense codons, such as tryptophan, phenylalanine, methionine, isoleucine, leucine, and proline.^{92, 118-120}

These methods can be used in combination along with other bioorthogonal strategies to produce highly sophisticated conjugates. Finally, while not necessarily limited to genetic code expansion, as users of this technology we are beholden to the interest of the developers in terms of which residues are investigated and disseminated. Fortunately, with the impressive diversity of residues and functionalities already described and as more collaborations are forged between users and developers, this potential limitation is minimized as the field continues to grow.

2. Optimizing unnatural amino acid incorporation into elastin-like polypeptides

2.1 Introduction and motivation

The incorporation of unnatural amino acids (UAAs) into recombinant proteins can result in low yields and undesirable truncation products. Proteins with UAAs incorporated have expression yields ranging from two- to six-fold lower than the corresponding wild type proteins, when reported, and are typically fewer than ten milligrams per liter of culture. We therefore anticipated the need for optimization of several expression parameters to produce enough protein for our biomaterial studies, which require nearly gram-scale quantities. Through this optimization, we have empirically identified four key factors influencing UAA incorporation and yield in *E. coli*: 1) expression host; 2) efficiency of translational machinery; 3) growth conditions, especially culture media; and 4) construct design with regards to number and placement of incorporation sites.

2.1.1 Expression hosts

A critical factor in recombinant incorporation of UAAs is in selection of the bacterial expression host. In the field of genetic code expansion, the development of specialized, genomically recoded *E. coli* lines has fittingly accompanied the exploding diversity of translational machineries being reported. There are now several choices for

UAA expression host, ranging from genomically recoded options to the mainstay protein expression bacterial lines, with distinct advantages and limitations of each.

Our initial expressions were performed in the standard *E. coli* line for ELP and recombinant protein production, BL21(DE3). This line has the advantages of being highly optimized for recombinant protein expression through genomic deletions of injurious proteases and endonucleases, enhanced phage resistance, and remarkable tolerance to high density culture.¹²¹ Although not discussed in detail here as it was not a part of our initial optimizations, we have also determined the SHuffle T7 Express *E. coli* line, a BL21(DE3) derivative tailored for cytoplasmic disulfide bond formation, is a viable option for UAA incorporation (see Section 4.2.3). However, these lines have intact release factor 1, the direct competitor with UAA translational machinery and main cause of low yield in this context (Figure 9).

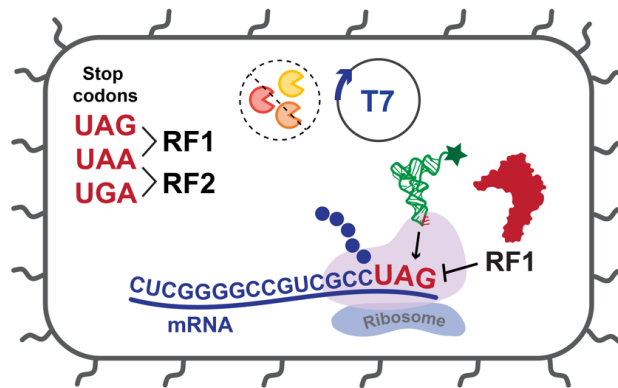


Figure 9: BL21(DE3) incorporation of unnatural amino acids.

There are several genomically recoded strains of *E. coli* that have been developed specifically for UAA incorporation; we have investigated two derivative strains of a line

with a stop codon exclusively for UAA incorporation as well as a phenylalanine auxotroph. First, we investigated the use of a highly specialized genomically recoded strain of *E. coli* touted as the ideal background for unnatural amino acid incorporation.¹²²⁻¹²³ This strain has all 321 amber stop codons in the genome recoded to the ochre stop codon and corresponding release factor 1 deleted, and is appropriately designated C321.ΔA. These genomic modifications effectively liberate the amber stop codon for reassignment as an exclusively “unnatural” codon by eliminating release factor competition (Figure 10).

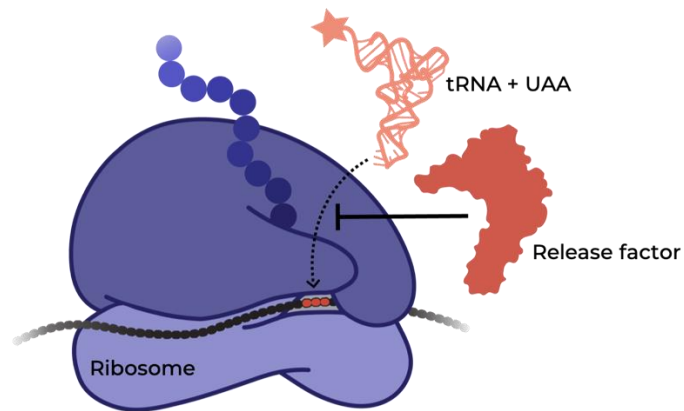


Figure 10: Release factors and UAA-tRNA compete at stop codons.

C321.ΔA has been used to successfully express proteins with multiple instances of UAA incorporation in high yield and with > 95% efficiency.¹¹⁷ We have evaluated two variations of this strain which are both derivatives of the same *E. coli* MG1655 parent strain as BL21(DE3). These genomically recoded organisms were developed by large-scale, multiplexed, hierarchical assembly of ochre-substituted genome fragments.¹²²⁻¹²⁴ The first (designated here as C321.ΔA.1) we further modified to be compatible with pET

vector expression through lysogenization of the T7 RNA polymerase gene into the genome (Figure 11).

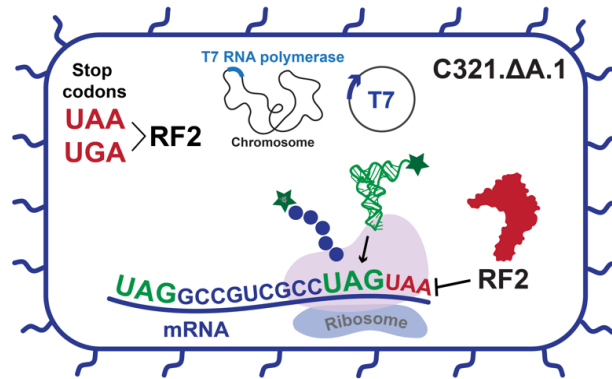


Figure 11: Genomically recoded *E.coli* for unnatural amino acid incorporation (C321.ΔA.1). This strain has all 321 UAG stop codons recoded to UAA and corresponding release factor 1 deleted, allowing exclusive use of the UAG codon for site of unnatural residue incorporation. We have lysogenized this strain with the T7 RNA polymerase gene to provide compatibility with pET expression.

The second derivative of the C321.ΔA strain (designated here as C321.ΔA.2) has proteases and endonucleases genomically deleted, similar to BL21(DE3), and was generously provided by Farren Isaacs, Yale University (Figure 12). We chose not to lysogenize this strain with the T7 RNA polymerase gene in an effort to maximize strain fitness and diminish truncation products. The latter are hypothesized to be a consequence of the significant kinetic disparity between the highly processive T7 RNA polymerase and unnatural translational machinery, which results in ribosomal stalling and premature translation termination.¹²⁵ Use of this strain, therefore, required the development of an alternative expression plasmid (see Section 2.2.1.2).

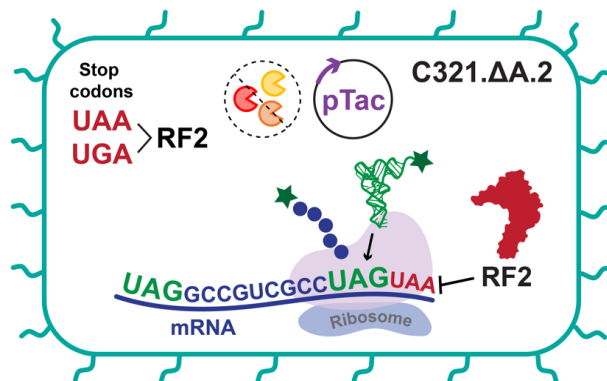


Figure 12: Genomically recoded *E.coli* for unnatural amino acid incorporation (C321.ΔA.2). This strain has additional proteases and endonucleases deleted but is not pET-compatible; we developed a pTac expression vector for use with this cell line.

While these genomically recoded strains have the distinct advantage of offering an exclusive codon for UAA incorporation, the genomic modifications increase the reliance on a single release factor and reported doubling times for this line are greater than the parent *E. coli*.¹²³ However, the slightly lower growth rate is offset by the benefits of enhanced incorporation efficiency and minimization of truncation products.

Lastly, although not the major focus of these optimizations, we also investigated an alternative approach to UAA incorporation altogether, with a phenylalanine auxotrophic line. AF-IQ is a BL21(DE3) derivative developed by Tirrell and co-workers which has the genes necessary for phenylalanine synthesis deleted, ensuring the cells' reliance on exogenously supplied phenylalanine.¹²⁶ These cells are also modified to express a mutated phenylalanine synthetase (PheRS*) with relaxed substrate specificity, which will accept structural analogs of this residue for co-translational insertion at

locations specified by phenylalanine codons. This can be exploited for proteome-wide replacement of phenylalanine with a structurally analogous UAA (Figure 13).

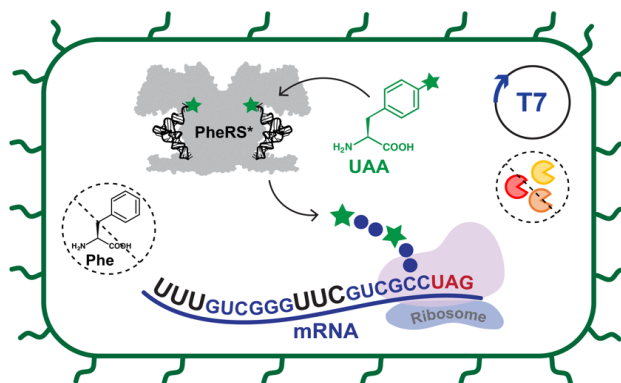


Figure 13: Phenylalanine auxotroph *E.coli* for unnatural amino acid incorporation (AF-IQ). PheRS and tRNA structures adapted from PDB entries 1EIY and 4TNA.

While this level of universal substitution may perturb the structure and function of many proteins, ELPs do not canonically include phenylalanine in their sequences, making this cell line a viable choice for UAA-ELP expression.

2.1.2 Translational machinery

Through the course of these studies, we have endeavored to incorporate a variety of structurally diverse residues and have accordingly populated our library of plasmids encoding the corresponding orthogonal translation systems (OTS), which includes the aminoacyl tRNA synthetase (aaRS) and tRNA (see Appendix A). The two most frequently used aaRS/tRNA orthogonal pairs are derived from those of *M. jannaschii* tyrosine (MjTyr) and *M. barkeri* pyrrolysine (MbPyl). We focused our optimization efforts on the MjTyr system encoded by the pEvol vector developed by

Schultz and co-workers and the evolved, high efficiency pEvol-pAcFRS.1.t1 vector evolved by Isaacs and co-workers (Figure 14).¹²⁷

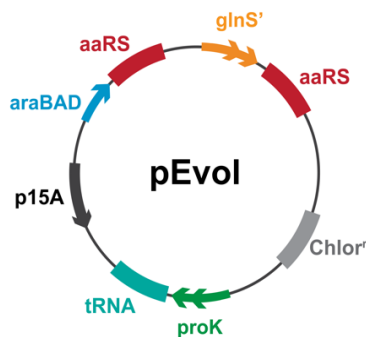


Figure 14: pEvol orthogonal translation system vector map. Adapted from Addgene (plasmid #31186).

Several alternatives to pEvol have been developed, including pUltra, pDule, pSupAR, and pTECH vectors, which all have genetic modifications that promote higher incorporation efficiencies, increased expression yields, and support the possibility of multi-UAA incorporation when used in combination.^{120, 128-130} To ensure compatibility with the co-transformed expression vector, particular attention must be paid to the copy number and origins of replication of these various OTS vectors.

2.1.3 Growth conditions

The combination of bacterial growth conditions – culture media, temperature, duration of growth, and timing and amount of inducing agent – intricately cooperate to affect recombinant protein expression, particularly with the incorporation of UAAs. We empirically determined that culture media was the key parameter affecting yield and truncation in the context of our specific expressions. The growth medias we explored

can be classified into one of three categories: 1) complex and undefined; 2) minimal and defined; and 3) complex and defined (Figure 15). Complex, undefined media that does not adequately control for leaky expression of toxic or demanding proteins can reduce yield by inducing expression before bacteria have reached peak log-phase growth.¹³¹ While minimal, defined medias such as M9 or MOPS provide stringent control over protein induction, the modest nutrient level does not support high levels of protein expression. Conversely, while complex medias such as LB, 2xYT, and TB can support high density growth, these undefined mixtures of tryptone and yeast extract often contain trace lactose which, again, prematurely induces protein expression. Defined, yet complex medias such as auto-induction media with precisely specified composition provide sufficient nutrients to support high density growth with minimal premature induction. Unfortunately, for reasons yet unknown, this media did not support the growth of the two genomically recoded C321.ΔA lines we investigated. Each of the culture medias investigated has their own merit and limitations, which must all be taken into consideration when optimizing UAA incorporation (see Appendix A, Table 16 for growth media compositions).

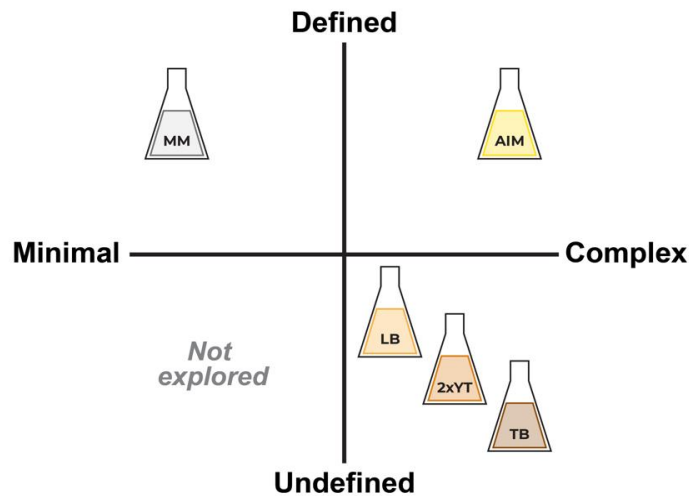


Figure 15: Culture media investigated for recombinant unnatural amino acid incorporation, classified by complexity and definition. MM, minimal media; AIM, auto-induction media; LB, Luria-Bertani broth; 2xYT, 2x yeast-tryptone broth; TB, terrific broth.

2.1.4 Construct design

While the growing conditions have substantial impact on yield, the design of the expressed construct itself – specifically with respect to stop codon placement – is the ultimate determinant of material utility. With ELPs, we advantageously have more freedom in terms of the frequency and positioning of stop codons than with structured recombinant proteins. With respect to the latter, UAAs are often incorporated within flexible loops or at protein termini to preserve important structural and functional elements or are restricted to mimicking residue-specific post-translational modifications. The flexibility afforded with intrinsically disordered ELPs provides an exceptional background for UAA incorporation; we can precisely specify the location of the unnatural residue with minimal expected consequences for biopolymer properties. Stop

codons can be positioned as guest residues or outside the context of an ELP repeat, and multiple stop codons can be clustered or spaced regularly throughout the chain. While we have empirically determined some locations are optimal to maximize yield and reduce truncation products, there is indisputably a vast sequence space to explore.

2.2 Materials and methods

2.2.1 Molecular biology and design of constructs

2.2.1.1 Design of modified pTac expression vector compatible with recursive ligation cloning

Our ELP library has been established in modified pET-24 vectors which are not compatible with the C321.ΔA.2 *E. coli* line in the absence of T7 translational machinery. We therefore designed a new vector, m-pTac, for protein expression in this cell line. Use of m-pTac is by no means restricted to this cell line or UAA incorporation; exploring an alternative to the highly processive T7 polymerase is a useful strategy to mitigate the expression-level challenges facing many complex recombinant proteins.

To synthesize the m-pTac vector, we replaced the T7 promoter and terminator sequences of m-pET-24+ with a pTac promoter and *rrnB* terminator, to maintain the restriction enzyme sites and origin of replication in the modified vector, m-pTac (Figure 16). We are grateful for cloning design assistance by Nicholas C. Tang and vector reconstruction was performed by GenScript USA Inc. (Piscataway, NJ).

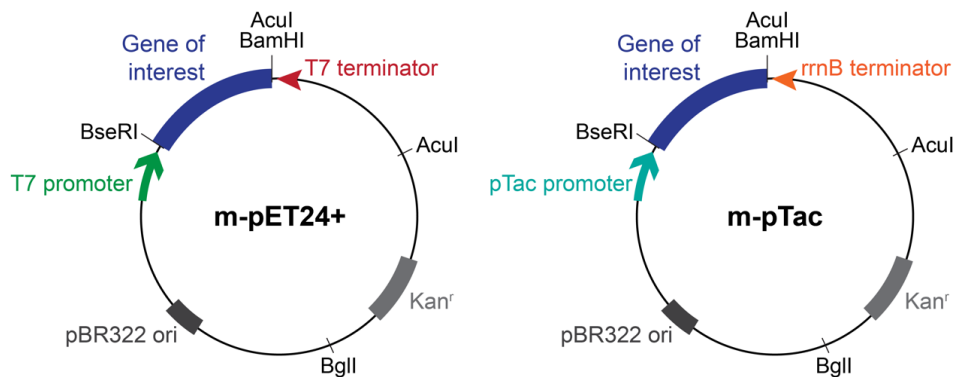


Figure 16: Vector maps of m-pET24 and m-pTac plasmids.

To replace the T7 promoter, we selected the pTac promoter, a hybrid between the well-studied *E. coli* trp and lac promoters. The trp promoter is a component of the well-studied trp operon, which is responsible for regulation of tryptophan synthesis genes and is an vital genomic element in *E. coli*.¹³² Similarly, the lac promoter is derived from the lac operon, an essential regulator for the transport and metabolism of lactose in *E. coli*.¹³³ The pTac promoter is highly efficient, offers controlled expression with repression by the lac promoter and de-repression with isopropyl beta-D-thiogalactoside (IPTG), and is compatible with endogenous *E. coli* transcriptional machinery.¹³⁴ We selected the rrnB terminator, the endogenous terminator for the *E. coli* ribosomal RNA gene, as this hairpin-dependent terminator is frequently employed as an efficient alternative to the T7 termination sequence.^{125, 135}

This vector, termed “m-pTac”, is compatible with protein expression and UAA incorporation in the genomically recoded *E. coli* when co-transformed with the appropriate orthogonal translation system, especially pEvol, which has a compatible

p15A origin of replication, araBAD promoter, and chloramphenicol resistance marker. We designed the m-pTac vector to ensure the ease of gene transfer between the m-pET-24+ vector and m-pTac for expression. Gene-encoding m-pET-24+ vectors are digested with BseRI/BamHI, the insert is extracted using agarose gel separation and purification, and the insert gene seamlessly ligated with similarly digested m-pTac.

2.2.1.2 Construct design and stop codon positioning

We explored several ELP construct architectures with respect to stop codon number and placement to achieve the various goals of this thesis work. For single insertion sites, we positioned the amber stop codon both directly at the N-terminus, as the first codon following the methionine start codon, and in the middle of the construct, to provide a metric of incorporation success by molecular weight. For multiple insertion sites, we investigated incorporation at both four and eight stop codons. For incorporating four residues, we have investigated constructs with both N-terminally clustered and regularly spaced residues. For inserting eight residues, we focused on stop codons regularly spaced throughout the chain. We have also interchangeably positioned the stop codon outside the context of an ELP repeat and as a guest residue with no discernible difference in outcome (Figure 17).

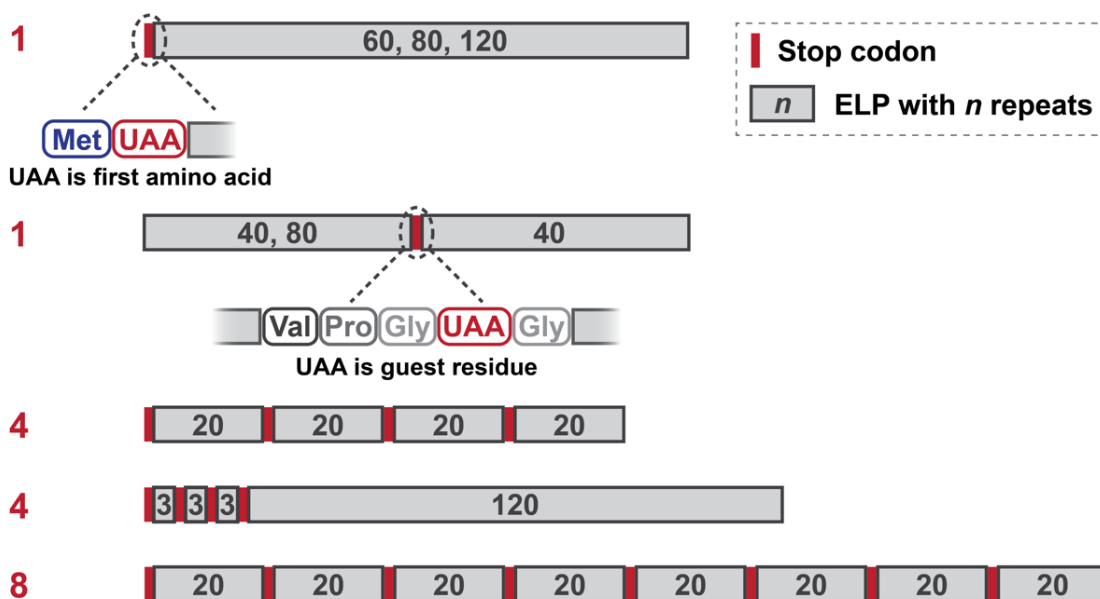


Figure 17: ELP architectures explored for unnatural amino acid incorporation.

The genes for each of these constructs were synthesized using recursive directional ligation by plasmid reconstruction.¹³⁶ In brief, we modified a pET-24+ cloning vector (m-pET-24+) to contain endonuclease recognition sites for *AcuI*, *BseRI*, and *BglI*. We digested m-pET-24+ with *BseRI* and ligated the desired ELP repeat sequences into the vector. The ELP sequences used in this library were previously constructed by first concatemering complementary ssDNA strands that encode for the desired ELP repeat motif along with “sticky end” overhangs, permitting the subsequent insertion into m-pET-24+.⁵⁹ Longer ELP sequences were constructed by digesting two populations of ELP-encoding m-pET-24+ with either *AcuI/BglI* or *BseRI/BglI* to create compatible plasmid fragments which, upon ligation, seamlessly encode the new gene product. In this case, the amber stop codon was introduced in the form of one of three peptides with

amino acid sequence 1) M*G; 2) GVPG*G; or 3) GVGVPG*GRG, where the asterisk indicates the location of the stop codon. We purchased ssDNA oligonucleotides encoding these sequences (IDT Technologies, Skokie, IL) and first annealed these together, digesting the m-pET-24+ plasmid with BseRI, and inserting these dsDNA fragments via the “sticky end” overhangs. This vector was then digested with AcuI and BglI to create an “A” population and the ELP-containing vector was digested with BseRI and BglI to create a “B” population. These two populations were then ligated to create a vector containing the gene encoding an amber stop codon-bearing ELP gene with the desired sequence architecture.

For the constructs to be expressed in the C321.ΔA.2 line, which is not T7 compatible, we transferred the ELP genes of interest from the m-pET-24+ vector to the m-pTac plasmid by digesting both vectors with BseRI/BamHI, extracting the insert using agarose gel separation and purification, and ligating with similarly digested m-pTac.

Incorporating UAAs at the amber stop codon ensures the versatility of the library of constructs we have developed; these genes can be used for future incorporation of any unnatural residue when provided with the corresponding orthogonal translation system. Conversely, the Phe auxotroph expression system required us to construct similar genes as those described above with a Phe codon (DNA sequence TTT) in the place of the amber stop codon. While this does not largely restrict the functionality of the ELP itself, this approach does preclude future use of any Phe-containing fusion partners.

2.2.2 Library of orthogonal translational systems

We explored the incorporation of a diverse range of unnatural residue functionalities and structures, enabled by the corresponding orthogonal translation systems (OTS). Please see Appendix A for a comprehensive list of the vectors, parent synthetase/tRNA pairs, and corresponding unnatural amino acid residue(s) which we have investigated. We have used these OTS – all based on one of the three available parent MjTyr, MmPyl, and MbPyl aaRS/tRNA pairs – in order to incorporate residues with functionality ranging from bioorthogonal reactivity including SPAAC reaction partners, photocrosslinking, polymerization initiation, and vibrational reporters.

Prior to expression with BL21(DE3) or C321.ΔA cell lines, we co-transformed the OTS vectors and the plasmid containing the gene of interest into the bacterial host of choice. To do this, we simultaneously mixed 100 ng of each plasmid DNA with competent cells. The cells were incubated on ice for 10 min, followed by a 30 s heat shock at 42°C, and a short recovery on ice for an additional 2 min. We then incubated the cells in complete SOC media (ThermoFisher Scientific, Pittsburgh, PA) for 1 h at 37°C prior to plating on dual-selection agar plates. For the genomically recoded AF-IQ line, we transformed with only the expression plasmid containing a gene of interest harboring phenylalanine codons as the sites of insertion.

2.2.3 Preparation of bacterial expression hosts

As described in Section 2.1.1.1, we have investigated five different expression hosts for unnatural amino acid incorporation, some of which required additional modification prior to expression. For example, we made the T7-compatible C321.ΔA.1 line via λDE3 lysogenization, as the C321.ΔA.exp line originally purchased from Addgene (Watertown, MA) had only endogenous *E. coli* expression machinery. To do this, we used the commercially available λDE3 Lysogenization Kit (MilliporeSigma, Burlington, MA). This kit contains a λDE3 prophage strain carrying the T7 phage RNA polymerase gene, which will be site-specifically inserted in the genome at the *attB* sequence in the bacterial chromosome.¹³⁷ We inoculated cultures of C321.ΔA.exp in LB media supplemented with 0.2% maltose, 10 mM MgSO₄, 25 μg L⁻¹ D-biotin, and 25 μg mL⁻¹ zeocin (InvivoGen, San Diego, CA) and incubated with shaking at 30°C until an OD₆₀₀ of 0.5 was reached. At that point, we mixed 10⁸ PFU (plaque-forming units) λDE3, 10⁸ PFU helper phage, and 10⁸ PFU selection phage with 5 μL of the C321.ΔA.exp culture. We incubated this mixture for 20 min at 37°C and then plated by spreading onto zeocin-supplemented LB plates. We incubated these plates inverted at 37°C for 18 h and selected lysogens (colonies) from these plates to inoculate overnight cultures for long-term storage as 50% glycerol stocks at -80°C.

We confirmed successful lysogenization of the resulting C321.ΔA.1 colonies by Western blot. The C321.ΔA strain is resistant to T7 phage infection; therefore, we needed

an alternative strategy to the T7 Tester Phage provided with the kit for validating lysogens. For the Western blot, we grew 5 mL LB cultures of C321.ΔA.1 as well as control BL21(DE3) and EB5α *E. coli*, to an OD₆₀₀ of 0.8. At that point we induced with 1 mM isopropyl β-D-1 thiogalactopyranoside (IPTG), while maintaining one culture of C321.ΔA.1 as an uninduced control. We grew these cultures for an additional 16 h, at which point we lysed by sonication for 1 min. We ran 10 μL of cell lysate for each sample on sodium dodecyl sulfate polyacrylamide gel electrophoresis (SDS-PAGE) and transferred to a polyvinylidene difluoride (PVDF) membrane using the Trans-Blot Turbo Transfer System (BioRad, Hercules, CA). We then blotted for T7 RNA polymerase expression by incubating the membrane with a polyclonal anti-T7 RNA polymerase antibody (MilliporeSigma, Burlington, MA) at a 1:10,000 dilution. We developed the resulting blot on CL-Xposure film (ThermoFisher, Pittsburgh, PA) to qualitatively confirm IPTG-inducible expression of T7 RNA polymerase (Figure 18).

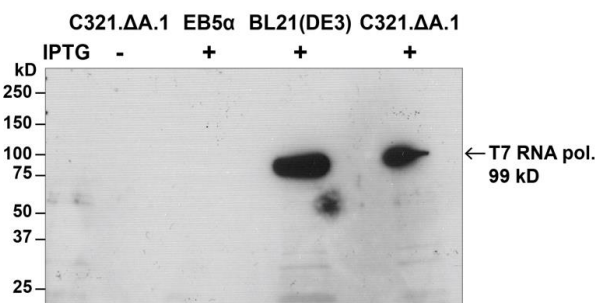


Figure 18: Western blot confirming T7 lysogenization of C321.ΔA.1 *E. coli*.

To use the genomically recoded lines (C321.ΔA.1, C321.ΔA.2, AF-IQ) for protein expression, we had to prepare chemically competent stocks for co-transformation of the

necessary vectors. To do this, we grew a 2 mL culture of LB media supplemented with the appropriate selection markers (25 $\mu\text{g mL}^{-1}$ zeocin for the C321. Δ A lines, 25 $\mu\text{g mL}^{-1}$ chloramphenicol for AF-IQ) for 12 h at 37°C. We inoculated a fresh 10 mL LB culture at a dilution ratio of 1:100 with the overnight culture and grew until the OD_{600} reached 0.4. At this point, we collected the cells by centrifuging at 3,500xg at 4°C for 10 min. We resuspended the pellet in 10 mL sterile, cold 0.1 M CaCl_2 and incubated on ice for 20 min. We centrifuged again as before and resuspended the pellet in 1 mL sterile, cold 0.1 M CaCl_2 , 10% glycerol. Following an additional 20 min incubation on ice, we aliquoted the competent cells into 50 μL stocks to be stored at -80°C for a maximum of six months.

2.2.4 Protein expression and purification

Recombinant protein expression for these studies followed a similar protocol for all of the expression hosts tested, with minor variations in growth temperature and growth media composition. In general, we first inoculated liquid cultures (50 mL) of co-transformed strains from frozen glycerol stocks and grew this to confluence overnight. We then inoculated growth cultures (1 L) at a 1:20 dilution in media supplemented with the appropriate dual-selection markers. We induced aaRS expression by the addition of arabinose (0.2%) and the unnatural residue of interest (1 mM), both added at the same time as the inoculation. Cells were grown at in a shaking incubator at 200 r.p.m. for 6 h, at which time ELP expression was induced by the addition of IPTG (1 mM), and the

cultures incubated at an additional 18 h, with both incubations at the cell-line dependent growth temperature (Table 1).

Table 1: Growth temperatures of *E. coli* lines for recombinant unnatural amino acid incorporation

<i>E. coli</i>	Temperature (°C)	<i>E. coli</i>	Temperature (°C)
BL21(DE3)	37	C321.ΔA.1	30
SHuffle T7 Express	25/16	C321.ΔA.2	34
		AF-IQ	37

We harvested cell pellets by centrifugation at 3,500xg and resuspended these in 1xPBS (20 mL). Cells were then lysed by sonication for a total of 3 min (Misonix; Farmingdale, NY) and DNA was precipitated by addition of polyethyleneimine (10%; MP Biomedicals, Santa Ana, CA). Precipitated DNA and cellular debris were removed by centrifugation at 20,000xg at 4°C. Soluble ELPs were then purified using four rounds of inverse transition cycling as described previously and in Section 1.2.2.1.⁶⁹

2.2.5 Characterizing expressed products

To characterize the recombinantly expressed proteins, we employed both qualitative SDS-PAGE analysis as well as mass spectroscopy. We ran purified proteins on 4–20% gradient Tris-HCl (Biorad, Hercules, CA) SDS-PAGE and visualized with both 0.5 M CuCl₂ staining and fluorescent imaging of fluorescently labeled proteins.

Incorporation efficiency was quantified with deconvolution of ESI-LC/MS spectra performed on intact proteins. Solutions of ELP (20 μM) were prepared in 5% acetonitrile/0.2% formic acid/water and mass spectra acquired on an Agilent 1100

LC/MSD Trap SL (Agilent Technologies, Santa Clara, CA) in positive mode. Samples were injected into a Phenomenex Luna C18 column (50 x 1 mm, 3 μ m; 0.2% formic acid in water as buffer A, 0.2% formic acid in acetonitrile as buffer B) and then into the mass spectrometer using a fully automated system. Deconvolution was performed using LC/MSD Trap Data Analysis software.

2.3 Results and discussion

2.3.1 Identifying optimal expression host and growth conditions for unnatural amino acid incorporation

The task of identifying a single optimized protocol for recombinant incorporation of UAAs into ELPs is complicated by the variety of possible growth conditions and combinations thereof. As discussed, the many factors which influence recombinant expression in this context are inextricably linked. In our experience, the primary determining factor for protocol selection was construct architecture, which subsequently influenced choice of expression host and growth media. We have accordingly organized the following discussion by construct design with respect to number of incorporation sites. Furthermore, we have focused the discussion here on our expressions with the pEvol OTS and incorporation of either *p*-azidophenylalanine (*pAzF*, Figure 25), or *p*-acetylphenylalanine (*pAcF*, Figure 51).

2.3.1.1 Constructs with one site of incorporation

The highest yielding constructs we tested had a single site of UAA incorporation immediately following the start codon at the N-terminus. We expressed these in

BL21(DE3) *E. coli* in TB, AIM, and 2xYT medias, as well as in both of the genomically recoded C321.ΔA lines. We obtained higher yields with the BL21 expressions, particularly in AIM (ca. 100 mg L⁻¹ with either *pAcF* or *pAzF*). The single N-terminal position allows for rapid assessment of successful stop codon suppression by confirming expected protein molecular weight with SDS-PAGE (Figure 19).

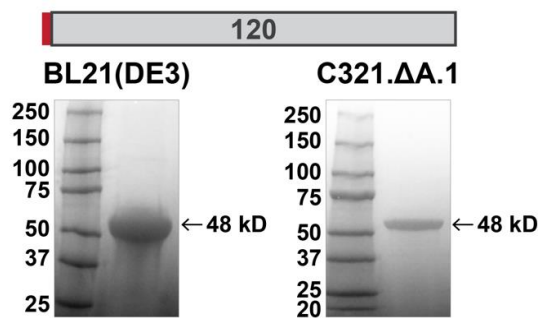


Figure 19: SDS-PAGE of ELP constructs incorporating a single unnatural amino acid at the N-terminus.

Our expressions involving a single incorporation site positioned in the middle of the ELP sequence resulted in truncation products, a commonly encountered challenge with UAA incorporation. Our initial expressions with BL21(DE3) in rich media (TB, 2xYT, or AIM) resulted in products corresponding to the ELP block upstream of the stop codon in ostensibly equivalent yields as the full-length construct. The same was true for expressions in the genomically recoded C321.ΔA.1 line in either TB or 2xYT media, despite the deletion of release factor 1 in this line. We also investigated expressions with C321.ΔA.1 in minimal media in an attempt to slow the global metabolic rate of all the processes in these cells, including transcription and translation. While these conditions

seemingly eliminated these truncation products, the yields from these expressions were unacceptably low for material characterization (ca. 2 mg L⁻¹ with *pAcF*) (Figure 20).

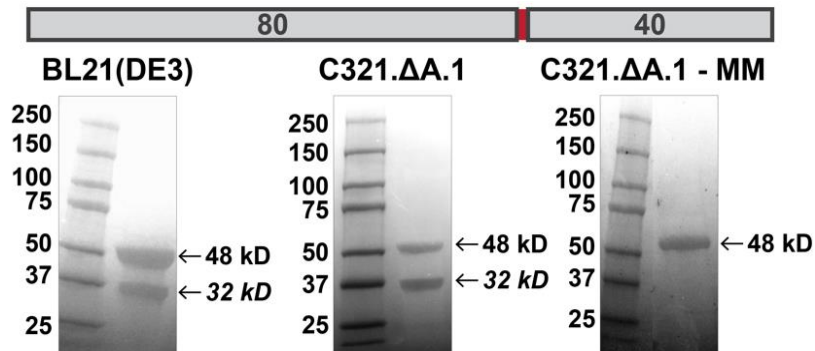


Figure 20: SDS-PAGE of ELP constructs incorporating a single unnatural amino acid positioned within the chain. Italicized text indicates molecular weight of truncation product corresponding to ELP block preceding the stop codon.

The truncation products observed with the genomically recoded line support the hypothesis that this phenomenon can be attributed to ribosomal stalling, as premature truncation can occur even in the absence of release factor competition. If the unoptimized and/or insufficiently induced UAA translational machinery cannot match the transcription rate of the highly prolific T7 RNA polymerase (which can produce target gene mRNA in quantities comparable to of the total ribosomal RNA in a cell), the ribosomes will prematurely release the nascent peptide chain; similar truncation phenomenon have been observed for expression of challenging recombinant proteins in other contexts.^{131, 138}

These expressions were informative as to both the strengths and limitations of genetic code expansion in our hands, providing us with a realistic threshold for success as we investigated more complex sequences with multiple stop codons.

2.3.1.2 Constructs with multiple sites of incorporation

While we successfully incorporated a single unnatural residue into ELPs at the N-terminus, the potential utility of these constructs is limited. We next focused on optimizing the incorporation of multiple residues, which greatly enriches the chemical identity of these functionalized ELPs. The maximum reported number of unnatural residues successfully incorporated into an ELP is thirty; we have investigated the incorporation of both four and eight residues.¹¹³

We first designed constructs with four amber stop codons regularly spaced throughout an ELP chain, separated by twenty ELP repeats. Our initial expressions incorporating *pAzF* in either BL21(DE3) or C321.ΔA.1 *E. coli* in rich media (TB, 2xYT), resulted in regular truncation products corresponding to termination after the second, third, and fourth stop codon, in addition to full-length protein. The accompanying fluorescent gel images, with reactive dyes labeling the *pAzF* residues, indicate the successful incorporation of two, three, or all four *pAzF* residues. We eliminated these truncation products by genetically introducing a His tag at the C-terminus of this chain, in order to purify only the full-length product with affinity chromatography. This is a viable approach and produced approximately 30 mg L⁻¹ of pure material. Until this point

in our studies, we had been using the first generation of pEvol *pAcFRS*, which had remained largely unoptimized since its development in 2003 and was the only OTS available for incorporating *pAcF* or *pAzF*. With the advent of the highly optimized pEvol *pAcFRS.t1.1* OTS and the specialized C321.ΔA.2 line, we found expressions of the same constructs in 2xYT media produced approximately 55 mg L⁻¹ of pure product, without any truncation products (Figure 21).

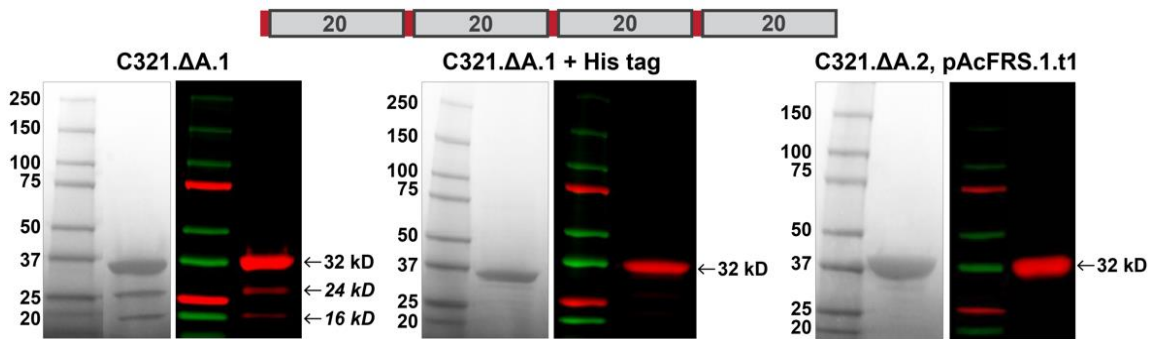


Figure 21: Incorporation of four regularly-spaced unnatural residues into ELPs. *pAzF* residues are labeled and visualized with a reactive DBCO-Cy5 dye.

When testing the same conditions with a similarly design construct with eight stop codons regularly spaced throughout the chain, however, we again encountered truncation products when incorporating *pAzF* (Figure 22). These can be easily eliminated using a C-terminal His tag to obtain only the full-length construct, though likely with a detriment to yield.

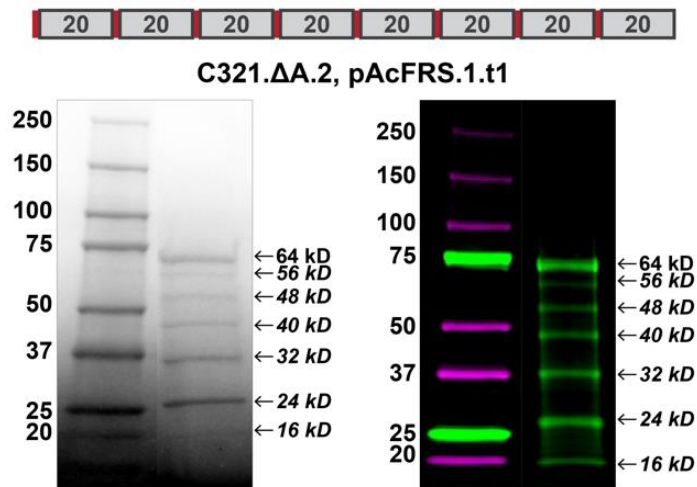


Figure 22: Incorporation of eight regularly-spaced unnatural residues into ELPs. *pAzF* residues are labeled and visualized with a reactive DBCO-Cy5 dye.

We also investigated insertion of *pAcF* into constructs with four or eight insertion sites clustered at the N-terminus, each separated by three ELP repeats and followed by a 120-mer ELP chain. While both expressions were successful in producing full-length material, the construct with eight insertion sites also produced a low molecular weight truncation product, which we predict to be the leader segment containing eight stop codons. This block is approximately 14 kDa, and hydrophobic ELPs tend to migrate 20% higher on SDS-PAGE than their apparent molecular weight.¹³⁹⁻

¹⁴⁰ However, more stringent mass spectroscopy analysis is needed to validate this hypothesis. (Figure 23).

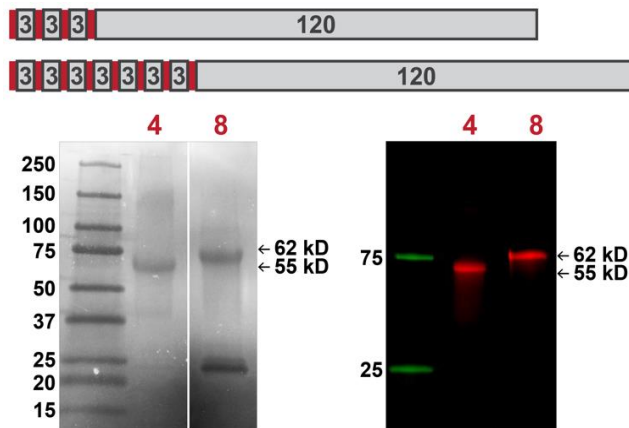


Figure 23: Incorporation of four and eight clustered unnatural residues into ELPs. *pAcF* residues are labeled and visualized with a reactive AlexaFluor647-hydroxylamine dye.

Through these expressions, we have identified the limit of efficiency for our system lies between four and eight residues. A systematic investigation into constructs with incorporation sites spanning this interval will reveal the threshold for successful full-length suppression. We hypothesize that the increased number of stop codons stresses the translational load beyond the point at which the unnatural amino acid machinery can compensate – particularly in the case when these residues are clustered together – which leads to ribosomal stalling and truncation.

2.3.2 Comparing orthogonal translational system incorporation efficiency with mass spectroscopy

To quantify the extent to which the evolved pEvol *pAcFRS.1.t1* is superior to the original pEvol *pAcFRS*, we compared the incorporation efficiency of these with electron spray ionization liquid chromatography mass spectroscopy (ESI-LC/MS). We confirmed a higher incorporation efficiency with the evolved pEvol *pAcFRS.1.t1* (> 99%) as we

identified a significant population of protein with misincorporated residues with the first generation pEvol *pAcFRS* (Figure 24). Based on the molecular weight of this population, the misincorporated residues likely include a mixture of Tyr, Phe, Lys, and Pro, which is consistent with literature reports.¹¹³

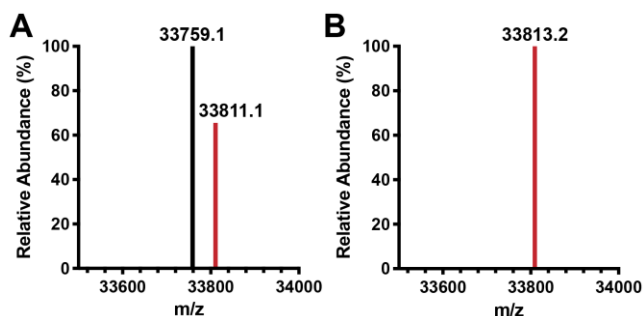


Figure 24: ESI-LC/MS analysis comparing the incorporation efficiency of *pAzF* by two generations of pEvol orthogonal translation systems. Spectra collect for proteins expressed with (A) pEvol *pAcFRS*, (B) pEvol *pAcFRS.1.t1*. Red bars correspond to expected product molecular weight (33814.9 Da), black bar represents population with misincorporation.

2.4 Concluding remarks

These optimizations directly enabled the work in the chapters that follow, which required ample material for functionalization and characterization. We have used these findings as guides for our successful incorporations of several other residues including 4-(2-bromoisobutyramido)-phenylalanine (BiBaF), *para*-azidomethyl-L-phenylalanine (*pAMF*), and a tetrazine-containing residue, Tet2.0 (see Table 15, Appendix A). A useful alternative which we also explored for incorporating Phe-based structures, such as *pAcF*, is the use of a Phe auxotroph and permissive PheRS, developed and generously provided to us by Tirrell and co-workers.¹²⁶ The diversity of published expression

conditions and configurations continues to exponentially grow, keeping pace with the rapidly expanding field of genetic code expansion. These optimizations have enabled us to identify the distilled requirements for successful UAA incorporation with our system.

We have designed a general protocol for future recombinant UAA incorporations with respect to expression host, growth media, and the promoter for the gene of interest. With most constructs, and particularly those requiring multiple incorporation sites, the optimal expression host is the genomically recoded C321.ΔA.2 *E. coli*, cultured in 2xYT media. Along with the gene of interest under the control of the pTac promoter and an optimized OTS, the combination of these conditions provides the greatest confidence in our ability to simultaneously maximize yield, incorporation efficiency, and minimize truncation products. If the construct of interest only requires a single site of incorporation and there is flexibility as to its positioning, the immediate N-terminal position is ideal. This position provides the most rapid read-out of success by confirming full-length expression with SDS-PAGE and mass spectroscopy. When the primary concern with these constructs is in maximizing yield, we recommend testing incorporation with BL21(DE3) *E. coli* in 2xYT or TB media with the construct still under control of the pTac promoter. As we have determined, the driving principle for successful recombinant UAA incorporation is to delicately balance maximizing the translational load against the potential for easily overloading the system, which causes undesirable truncation products and low yield.

3. Bioorthogonal photocrosslinking strategy for synthesizing nano- to microscale hydrogel particles

3.1 Introduction and motivation

We have exquisite control over elastin-like polypeptide (ELP) self-assembly, with the ability to design unique multi-layered architectures and tune particle size ranging from the nano- to microscale. However, because of the limited chemical diversity of natural amino acids, we have yet to effectively stabilize and transform these assemblies from merely observed phenomena into functional materials. For example, while amphiphilic ELP polymers drive self-assembly of unimers into nanoscale micelles, these particles can disassemble in the complex physiological milieu of the circulation as the unimer-to-micelle equilibrium is in constant dynamic flux.¹⁴¹⁻¹⁴² Similarly, nanoparticles confirmed to be stable in buffer have been shown to disassemble in serum and multi-component media.¹⁴² Stabilization of these polymeric nanoscale micelles by crosslinking has been proven to enhance their systemic exposure and reduce renal clearance.¹⁴³⁻¹⁴⁴

We have developed a simple yet powerful system to easily stabilize ELP-based, thermoresponsive hydrogel particles, from the nano- to microscale, using a bioorthogonal, photoreactive unnatural amino acid. Particle size is controlled by the self-assembly and unique phase transition behavior of ELPs in bulk and within microfluidic-generated droplets. These particles are then stabilized through ultraviolet (UV) irradiation of a photocrosslinkable residue, *p*-azidophenylalanine (*p*AzF, Figure 25), cotranslationally incorporated into the parent ELP.

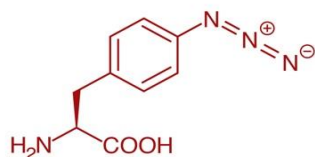


Figure 25: Structure of *p*-azidophenylalanine (*pAzF*), the unnatural residue used for photocrosslinking.

The aryl azide group on this residue forms a reactive nitrene upon irradiation with UV light, which readily inserts into nearby N-H or C-H bonds to form an irreversible covalent linkage.¹⁴⁵⁻¹⁴⁶ Use of this residue accomplishes several key goals: 1) the relative location and number of crosslinking sites can be determined by site-specifically genetically encoding the *pAzF* residues along the polymer chain, 2) crosslinking can be performed at a specific temperature with irradiation of UV light, allowing for stabilization of fully assembled particles, and 3) this residue will ensure bioorthogonality of the crosslinking strategy.

The platform we describe in this chapter represents a fundamental advance in the generation of crosslinked biopolymer networks and is one of the first demonstrations of successful use of unnatural amino acids in generating a novel material. The work presented here resulted in a publication in *Advanced Materials* (license number 4517780048529) and was completed in collaboration with my colleague, Joseph Simon.¹⁴⁷ I am grateful for his assistance in completing these studies and have noted which of the data were specifically collected and analyzed by Joseph in the following sections.

3.1.1 Hydrogel particle utility and methods of synthesis

Hydrogel particles are versatile materials used extensively in a wide variety of fields, ranging from photonics, optics, cell capture, biosensing, drug delivery, and tissue engineering to the food industry and cosmetics.^{7, 13-15, 148-154} These particles, made of crosslinked networks of polymers, respond to local changes in temperature by reversibly shrinking and swelling in solution due to changes in network solubility. These large-scale volumetric changes provide exquisite, tunable control over the sequestration and delivery of materials and cargo, with demonstrated utility in diverse applications.

Both biological and synthetic polymers have been used to synthesize hydrogel particles, with the latter being more frequently employed owing to the higher degree of chemical flexibility. Synthetic starting materials range from polyesters (e.g. poly(N-isopropylacrylamide), poly(ethylene glycol)diacrylate), to polyethers, such as polyethylene glycol, to co-polymers such as poly(lactic-co-glycolic) acid. These polymers are then formulated into stable hydrogel particles through the introduction of chemical crosslinking sites and using a range of fabrication strategies.¹⁵⁵

The favorable properties of hydrogel particles are chiefly dictated by particle structure, composition, and size. Particles ranging from nanometers to micrometers are used in different applications depending on particle geometry, refractive index, cargo loading capacity, release kinetics, and deformability parameters. Traditionally, these particles have been fabricated using a variety of advanced techniques and starting

materials, and only within one size regime. While particle size and geometry can be controlled using such techniques as layer-by-layer deposition, molecular self-assembly, electrohydrodynamic co-jetting, lithography, imprinting, micromolding, and droplet microfluidics, these approaches restrict particle size, for example, to either the nanoscale by self-assembly or the microscale by fluidic templating.¹⁵⁶⁻¹⁶³ Despite the importance of this parameter, an overarching challenge in synthesizing biopolymer-based hydrogel particles is the ability to control particle size via on-demand, orthogonal crosslinking.

3.1.2 Crosslinking strategies for biopolymers

Crosslinking of biopolymers has been accomplished with engineered disulfide bonds, enzymatic processing, radiation, or through the use of extrinsic chemical crosslinking agents and reaction at lysine residues. Disulfide bonds can spontaneously and randomly form intramolecular crosslinks between cysteine-containing polymers in reducing conditions.¹⁵⁰ High-energy, ionizing radiation can be used to initiate covalent, intrachain dimerization of phenylalanine and tyrosine residues, provided these residues are included in a biopolymer sequence.¹⁶⁴ Enzymatic strategies for crosslinking, such as with tissue transglutaminase, Sortase A, or the SpyTag/SpyCatcher system, require specific recognition and substrate motifs to be incorporated into the polymer sequence, as well as addition of the necessary enzyme to the system and its subsequent removal after crosslinking.^{102, 165-166} The primary amine of lysine residues can undergo condensation reactions with extrinsic chemical crosslinkers to form a random network.³³

Alternatively, non-covalent crosslinking can be achieved through self-associating and self-assembling protein domains such as helices and leucine zipper motifs.¹⁶⁷

These strategies, while useful in certain contexts, present limitations for developing biopolymer-based hydrogel particles. Protein-protein interactions and disulfide bond formation are both reversible, which leads to inefficient crosslinking, particularly when temporal and spatial control is required.¹⁵⁰ Extrinsic crosslinkers are often cytotoxic, and both this approach and that of enzymatic processing require extensive purification before use *in vitro* and *in vivo*.¹⁶⁸⁻¹⁷⁰ All of these strategies require either specific amino acids to be included in the biopolymer sequence, or in the case of enzymes, entire motifs or even protein domains. A bioorthogonal strategy is needed to crosslink and stabilize biopolymers with spatiotemporal control, in the presence of bioactive residues, and with limited restriction on amino acid sequence.

3.2 Materials and methods

3.2.1 Molecular biology and design of constructs

We designed two ELPs containing photocrosslinkable *pAzF* residues to serve as the constituent polypeptides of our system (Figure 26). One polypeptide, termed photocrosslinkable ELP (PCE), is composed of eighty pentameric repeats of the VPGVG motif with four regularly-spaced *pAzF* residues, a sufficient number to form a crosslinked network.³² The second ELP in our system is a self-assembling photocrosslinkable diblock (PCD) comprised of two distinct repetitive blocks: an N-

terminal hydrophobic PCE block and a C-terminal hydrophilic ELP block, composed of eighty pentameric repeats of the VPGSG motif.

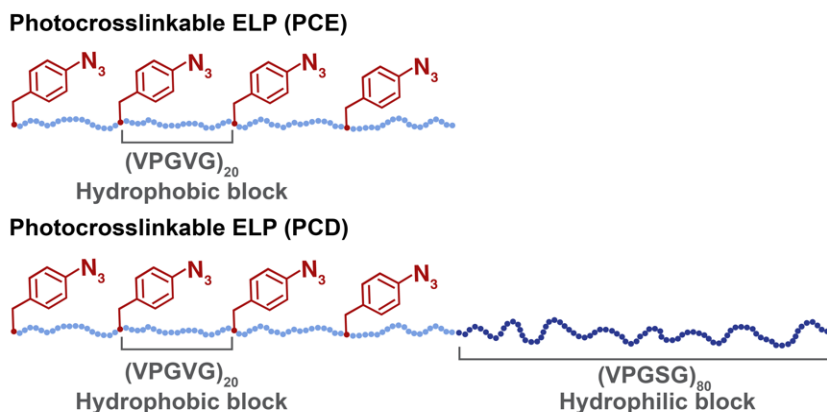


Figure 26: Schematic of two constructs, PCE and PCD, used in crosslinked particle platform.

Genes encoding PCE and PCD were first synthesized using recursive directional ligation by plasmid reconstruction in a modified pET24+ vector. We made use of a modified pET-24+ cloning vector (m-pET-24+) with unique restriction enzyme recognition sites for *AcuI*, *BseRI*, and *BglI*. We digested m-pET-24+ with *BseRI* to ligate the base repeat of PCE into the vector: $pAzF(VPGVG)_{20}$. The amber stop codon and insertion site for $pAzF$ (DNA sequence “TAG”) was introduced as an oligonucleotide by digesting a m-pET-24+ containing the gene encoding $(VPGVG)_{20}$ with *BseRI*. This base repeat was used to construct the final PCE and PCD sequences through sequential rounds of plasmid reconstruction, as described previously.⁶¹ The amino acid sequences of these constructs are shown in Appendix B, Table 17.

We then transferred the PCE and PCD genes from the m-pET-24+ plasmids to the m-pTac vector (see Section 2.2.1.2). These vectors were then co-transformed with an evolved pEvol tRNA/aaRS vector into the genomically recoded *E. coli*, both generously provided by Prof. Farren J. Isaacs at Yale University.

3.2.2 Protein expression, purification, and characterization

To express the proteins for these studies, starter cultures (50 mL) of co-transformed strains harboring pEvol and ELP plasmids were inoculated from frozen glycerol stocks and grown for 18 h. The starter cultures were then inoculated at 1:20 dilution in 2xYT media (1 L) supplemented with kanamycin (45 $\mu\text{g ml}^{-1}$) and chloramphenicol (25 $\mu\text{g ml}^{-1}$). aaRS expression was simultaneously induced by the addition of arabinose (0.2%) and *pAzF* (1 mM). Cells were grown at 34°C in a shaking incubator at 200 r.p.m. for 6 h, at which time ELP expression was induced by the addition of IPTG (1 mM), and the cultures incubated at 34°C for an additional 18 h. Cell pellets were harvested by centrifugation at 3500xg and resuspended in 1xPBS (20 mL). Cells were lysed by sonication for a total of 3 min (Misonix; Farmingdale, NY) and DNA was precipitated by addition of polyethyleneimine (10%; MP Biomedicals, Santa Ana, CA). Precipitated DNA and cellular debris were removed by centrifugation at 20,000xg at 4°C. Proteins were then purified using four rounds of inverse transition cycling, as described previously and in Section 1.2.2.1.⁶⁹ Briefly, solutions of proteins were heated and salt (NaCl) was added to induce the phase transition of the ELP, followed by

centrifugation to collect all insoluble material at 20,000xg, 35°C, and the resulting pellet was re-suspended in cold 1xPBS. Upon cooling, the ELP resolubilizes, while contaminants remain insoluble and can be removed by centrifugation at 20,000xg, 4°C. These centrifugation steps are repeated sequentially until the desired purity is achieved. All protein samples containing *pAzF* were handled in the dark to protect this photosensitive residue from ambient light.

Purified PCE and PCD were characterized for purity by sodium dodecyl sulfate polyacrylamide gel electrophoresis (SDS-PAGE). Incorporation of *pAzF* was qualitatively confirmed by strain-promoted alkyne-azide cycloaddition (SPAAC) reaction with excess dibenzocyclooctyne-Cy5 (DBCO-Cy5) dye followed by separation on SDS-PAGE and imaging on a Typhoon 9410 Variable Mode Imager (GE Healthcare, Pittsburgh, PA). Incorporation efficiency of *pAzF* was quantified with deconvolution of ESI-LC/MS spectra performed on intact proteins. Solutions of PCE and PCD (20 μM) were prepared in 5% acetonitrile/0.2% formic acid/water and mass spectra acquired on an Agilent 1100 LC/MSD Trap SL (Agilent Technologies, Santa Clara, CA) in positive mode. Samples were injected into a Phenomenex Luna C18 column (50 x 1 mm, 3 μm; 0.2% formic acid in water as buffer A, 0.2% formic acid in acetonitrile as buffer B) and then into the mass spectrometer using a fully automated system. Deconvolution was performed using LC/MSD Trap Data Analysis software.

The transition temperatures (T_i) of PCE and PCD were determined by temperature-controlled spectrophotometry using a Cary 300 (Agilent Technologies, Santa Clara, CA). Samples containing various concentrations of PCE or PCD in 1xPBS were heated at 1°C min^{-1} and the optical turbidity at 650 nm was recorded every 0.1°C . The transition temperature was determined for each sample as the maximum of the first derivative of the turbidity as a function of temperature.

3.2.3 Crosslinking and particle synthesis

We devised a simple two-step strategy to fabricate uniform thermoresponsive gel particles spanning multiple length scales (Figure 27).

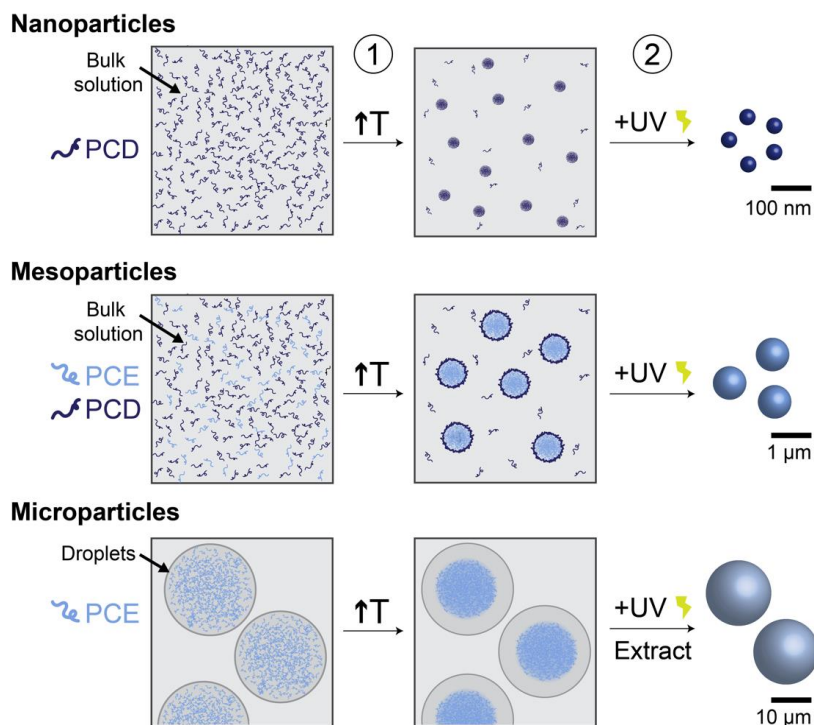


Figure 27: Strategy for crosslinked hydrogel particle synthesis with programmable size

We first tuned the temperature of solutions containing PCD, PCE, or a mixture of both to form particles, and then stabilized the resulting particles by crosslinking with broad spectrum UV light for a minimum of 10 s (250-450 nm filter set, Omnicure® Series 1000 lamp, Ontario, Canada).

3.2.3.1 Nanoparticle synthesis

For nanoscale particle synthesis we use PCD, a thermally responsive amphiphile. Raising the temperature above its critical micellization temperature (CMT) in bulk solution triggers self-assembly into spherical micelles and subsequent UV-irradiation crosslinks the micelle cores, stabilizing these nano-gel particles (Figure 28).

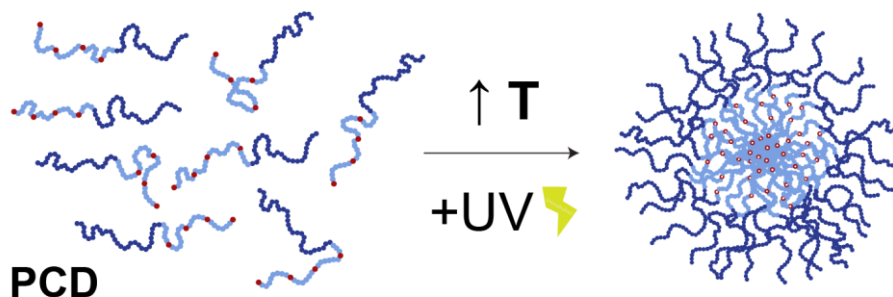


Figure 28: Schematic for formation of crosslinked ELP nanoparticles.

3.2.3.2 Mesoparticle synthesis

To create hydrogel particles that span the mesoscale, from 100 nm – 1 μ m, we combine diblock PCD and monoblock PCE in solution. By tuning the temperature above both the CMT of the PCD and the T_i of PCE, but below the T_i of PCD, we can generate mesoscopic coacervates of PCE whose size is limited by the PCD. It is a well-established phenomenon of polymer physics that diblock copolymers, such as PCD, behave as

macromolecular analogues of surfactants in solution with homopolymers, such as PCE. PCD limits coarsening of the PCE coacervates through solubilization of the PCE-block of PCD with PCE unimers.¹⁷¹ By modulating the ratio of PCE to PCD, we can tune particle size within the mesoscale regime. UV-irradiation then stabilizes these mesoscale assemblies into spherical particles (Figure 29).

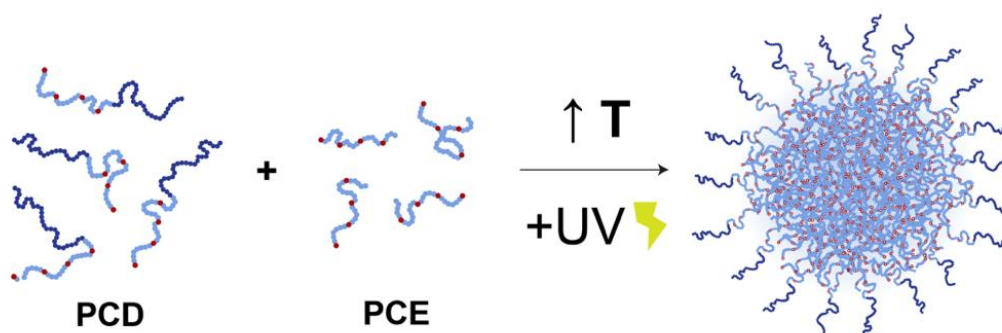


Figure 29: Schematic for formation of crosslinked ELP mesoparticles.

3.2.3.3 Microparticle synthesis

To synthesize microparticles, we utilized microfluidic droplet-generating chips to create monodisperse water-in-oil emulsion droplets containing PCE. Tuning the temperature either above or below the T_1 of PCE and subsequent UV-irradiation crosslinks the PCE coacervates into microscopic particles. Gel particle size can be easily tuned by modulating the starting concentration of PCE and the temperature at which crosslinking occurs (Figure 30).

To create water-in-oil emulsion droplets, two liquid phases – an aqueous phase of ELPs in 1xPBS and an organic phase comprised of TEGOSOFT® DEC/ABIL® EM 90/mineral oil (75%/5%/20% vol/vol) – were injected into the microfluidic droplet

generator at constant flow rates using syringe pumps. The flow rates of the two phases were tuned to ensure droplet formation in the dripping regime; this was achieved using a constant flow rate of $250 \mu\text{L hr}^{-1}$ for the organic phase and $75\text{-}100 \mu\text{L hr}^{-1}$ for the aqueous phase. The production of droplets was monitored using a $5\times$ objective on an inverted microscope (Leica) equipped with a digital camera (Lumenera Infinity 3-1 CCD).

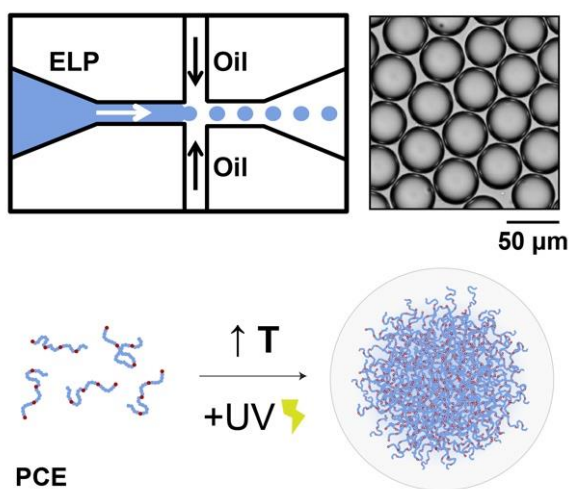


Figure 30: Schematic for formation of crosslinked ELP microparticles.

3.2.3.4 Particle extraction

Microscale particles were extracted from droplets immediately following droplet synthesis using isobutanol to disrupt the water/oil phase boundary and create two continuous phases.¹⁷² Isobutanol was added at a ratio of 10:1 with droplets in solution and vortexed gently to mix. Droplet rupture was evidenced by a change in the solution from turbid and yellow-white to clear and colorless. This solution was then centrifuged for 1 min at $20,000\times g$ and the supernatant removed. The remaining pellet contained the

crosslinked particles and was resuspended in 1xPBS for storage. Particle integrity, shape, and size were confirmed to be intact and unchanged before and after droplet extraction via light microscopy (Figure 31).

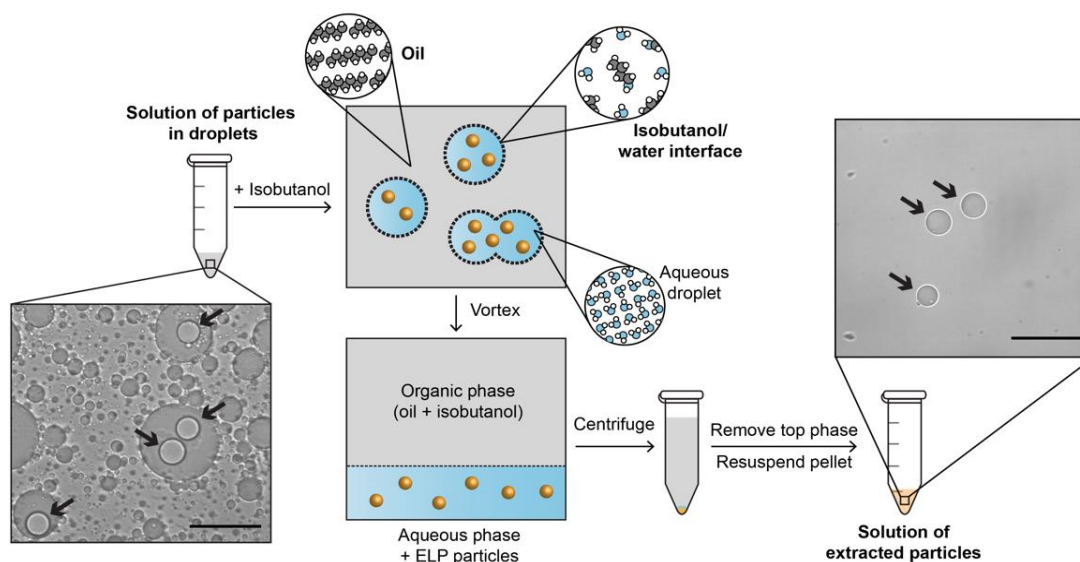


Figure 31: Crosslinked particle extraction from microfluidic droplets. Isobutanol is mixed with the solution of microdroplets to create two continuous phases. The less dense organic phase is easily removed after centrifugation and aspiration. The resulting pellet of particles can then be resuspended in the aqueous solvent of choice. Scale bars, 50 μm .

3.2.4 Particle characterization

3.2.4.1 Light scattering

Temperature ramp dynamic light scattering (DLS) measurements of nano- and mesoparticles were performed from 15–50°C using a Wyatt DynaPro temperature-controlled instrument (Wyatt Technology, Santa Barbara, CA), with five acquisitions collected every 1°C. Samples for the DLS system were prepared in 1xPBS and filtered through Whatman Anotop sterile syringe filters (0.2 μm ; GE Healthcare Life Sciences,

Pittsburgh, PA), into a quartz crystal cuvette (12 μ L; Wyatt Technology, Santa Barbara, CA). The data points presented for these characterizations represent the mean R_h or D_h of the sample at each temperature, with error bars illustrating the polydispersity.

Static light scattering (SLS) measurements were performed using an ALV/CGS-3 goniometer system (Langen, Germany). Samples for the ALV/CGS-3 goniometer system were prepared in 1xPBS and filtered through Whatman Anotop sterile syringe filters (0.2 μ m) into a disposable borosilicate glass tube (10 mm; Fischer Scientific, Pittsburgh, PA). Simultaneous SLS measurements at 37°C were obtained at angles between 30°-150° at 5° increments, with each angle consisting of 3 runs for 15 s. The differential refractive index ($dn\ dc^{-1}$) was determined by measuring refractive index at 37°C at five different concentrations using an Abbemat 500 refractometer (Anton Paar, Graz, Austria). Static light scattering data were analyzed by partial Zimm plots using the ALVSTAT software to determine the radius of gyration (R_g) and molecular weight. N_{agg} was determined by dividing the particle molecular weight by molecular weight of an individual PCD chain.

3.2.4.2 Cryogenic transmission electron microscopy

Cryo-EM imaging was performed on a Tecnai G² Spirit BioTWIN (FEI-Company, Eindhoven, the Netherlands, and Hillsboro, OR) operated at 120 kV. Samples containing crosslinked PCD nanoparticles were adsorbed onto holey carbon grids. Either 2.0 μ m holes, 2.0 μ m spacing, Quantifoil grids (Quantifoil Micro Tools GmbH, Großlöbichau, Germany) or Lacey carbon grids (Ted Pella, Redding, CA) covered with a thin

continuous carbon film were used. Samples were vitrified using a FEI Vitrobot Mark IV device and loaded onto the grid in the Vitrobot chamber at RT (22°C) with the relative humidity set to 100%. Samples were blotted for 2 s with a force set to 3, plunged directly into liquid ethane and transferred into liquid nitrogen. Grids were then transferred into a Gatan 626 cryo-holder (GATAN Inc. Pleasanton, CA) and inserted into the TEM. 2D micrographs were acquired using a FEI Eagle 4kx4K CCD camera in low-dose condition at varying magnifications with a dose not exceeding $15 \text{ e } \text{Å}^{-2} \text{ s}^{-1}$. The cryo-TEM data were collected by Cedric Bouchet-Marquis at FEI-Company (Hillsboro, OR).

3.2.4.3 Atomic force microscopy

Samples for atomic force microscopy (AFM) imaging were prepared by placing a drop (~20 μl) of sample solution (6 mg ml^{-1} PCD in water) onto a freshly cleaved mica surface. The samples were then incubated for 15 min and subsequently gently rinsed with Milli-Q H_2O and dried with N_2 gas. AFM images were acquired in Tapping Mode at 25°C using a Nanoscope MultiMode AFM (Bruker). Tapping Mode silicon cantilevers were used for all the AFM images ($k_F = 40 \text{ N mol}^{-1}$, $f_{res} = 300 \text{ kHz}$). The particle sizes were determined using ImageJ open source software.

3.2.4.4 Scanning electron microscopy

Microparticles were extracted from droplets as described in Section 3.2.3.4 and resuspended in water for scanning electron microscopy (SEM) imaging. An aliquot of extracted particles (5 μL) was drop-cast onto a silicon wafer attached to an aluminum

stub with double-sided adhesive carbon tape and allowed to air dry for at least 4 h. The dried samples were sputter-coated with gold for 250 s (Denton Desk IV, Moorestown, NJ) and then imaged with a FEI XL30 SEM-FEG at 7 kV. Mesoparticles were crosslinked in bulk and diluted 1:100 in water prior to sample preparation and imaging.

3.2.4.5 Heating and optical imaging

Prior to particle synthesis, a sample of PCE was fluorescently labeled by Alexa488-NHS ester coupling to the N-terminal amine of these chains. Briefly, purified PCE was reacted with an excess of AlexaFluor488-NHS ester dissolved in dimethylsulfoxide (DMSO) for 16 h at 4°C in 1xPBS. Unreacted dye was removed by washing with 15% acetonitrile/PBS in Amicon-0.5 Ultra Centrifugal Filters (MilliporeSigma, Burlington, MA). Labeling efficiency was determined by quantifying the absorbance at 495 nm following lyophilization and gravimetric determination of labeled PCE weight. A labeling efficiency of 40-50% was typically achieved with this approach.

Mesoparticle or microparticle samples in emulsion droplets were prepared with 25% molar fraction AlexaFluor488-labeled PCE, and unlabeled PCD in the case of the mesoparticles. Droplets were then collected on a glass microscope slide and heated using a precision Peltier heating and cooling stage (Linkam LTS120) equipped with a Linkam PE95 digital temperature control unit. The spatial distribution of fluorescent PCE was characterized via fluorescence microscopy using an upright Zeiss Axio Imager

A2 microscope with a 20× objective and the appropriate filter set (ex. 470/40, em. 525/50). Image acquisition and particle sizing of visible particles was done by Joseph Simon using MATLAB.

3.2.4.6 *In vivo* pharmacokinetic analysis

To compare the circulation half-life and pharmacokinetic profiles of crosslinked and non-crosslinked nano-gels, we fluorescently labeled PCD with AlexaFluor488-NHS ester as described in Section 3.2.4.5. We prepared crosslinked, fluorescently labeled particles as described in Section 3.2.3. These were administered intravenously via the tail vein of BALB/c mice, with a separate group of control mice receiving non-crosslinked, fluorescently labeled samples, with both samples pre-warmed above the critical micellization temperature to 37°C to ensure particle assembly. At select time points (1 min, 15 min, 45 min, 1.5 h, 4 h, 8 h, 24 h, 48 h), 10 µL of blood was sampled from a tail vein prick. The blood sample was diluted in 100 µL of heparinized PBS (1 KU mL⁻¹) and red blood cells were removed by centrifugation at 5,000xg for 5 min. The supernatant was loaded onto black 96-well microplates and the fluorescence of AlexaFluor488 was measured on a microplate reader (WallaC, PerkinElmer, Waltham, MA) and corrected for background signal from the plasma of untreated mice. The fluorescent signal was either normalized to the first time point or it was converted to absolute concentration using fluorescent standard curves created for each of the administered samples. Notably, the fluorescence of the Alexa488 dye sequestered in the core of the micelles,

was affected by crosslinking and standard curves were prepared specifically for either the crosslinked or non-crosslinked samples. SAAM II software was used to fit the data to a two-compartment model and determine the distribution half-life ($\alpha t_{1/2}$), elimination half-life ($\beta t_{1/2}$), and area under the curve (AUC).

3.3 Results and discussion

3.3.1 Mass spectrometry analysis

After expression of PCE and PCD, we confirmed > 95% purity of these samples and qualitatively confirmed the molecular weight using SDS-PAGE (Figure 32A). Hydrophobic ELPs routinely migrate 20% higher than their expected molecular weight on SDS-PAGE. We confirmed the incorporation and reactivity of the *pAzF* residues with fluorescent labeling and fluorescent SDS-PAGE imaging (Figure 32B).

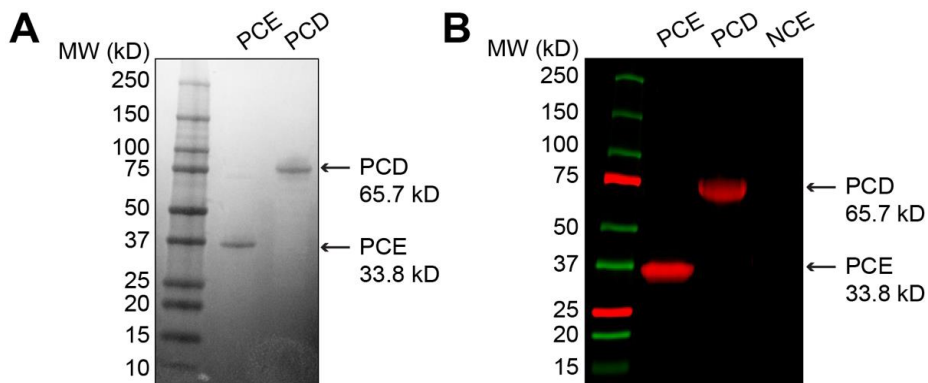


Figure 32: SDS-PAGE of PCE and PCD. (A) Confirming purity and molecular weight of PCE and PCD on SDS-PAGE, stained by copper chloride. (B) Fluorescent SDS-PAGE gel of PCE, PCD, and NCE (non-crosslinkable ELP, (VPGVG)₈₀) labeled with DBCO-Cy5. PCE and PCD contain *pAzF* residues which react with DBCO-Cy5, while the negative control NCE is not fluorescently labeled via click.

We then quantified the incorporation efficiency of *pAzF* in these biopolymers using electron spray ionization liquid chromatography mass spectrometry (ESI-LC/MS) (Figure 33). We analyzed intact proteins and deconvoluted the resulting spectra to obtain the average theoretical mass; the major peaks were consistent with the expected molecular weights for these polypeptides and we did not observe any additional populations of significant intensity which would correspond to misincorporated residues. The > 99% incorporation efficiency of *pAzF* we achieved is consistent with previous reports and indicates these biopolymers are capable of robust photocrosslinking immediately post-purification.¹¹⁷

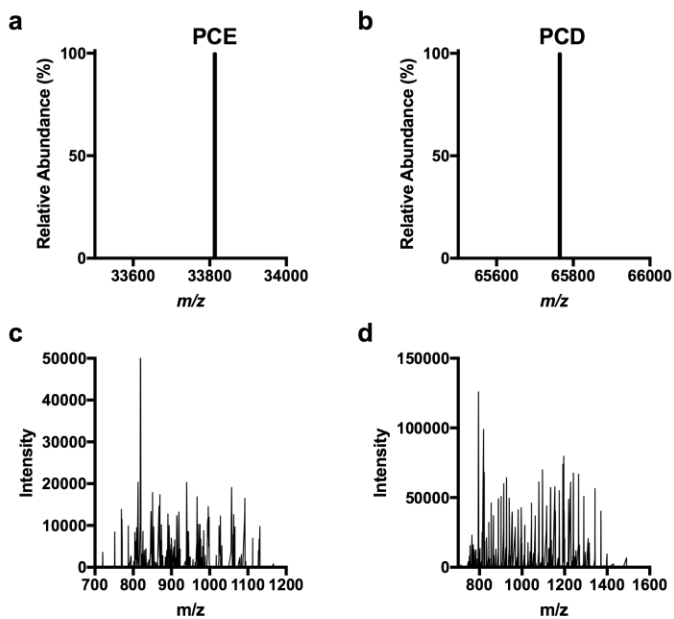


Figure 33: ESI-LC/MS analysis of PCE and PCD. (A) Deconvoluted mass spectra of PCE indicates no natural amino acid misincorporation with observed molecular weight of 33813.2 ± 3.2 Da, expected 33814.9 Da. (B) Deconvoluted mass spectra of PCD with observed molecular weight of 65764.9 ± 4.7 Da, expected 65772.6 Da. Intact mass spectra of (C) PCE and (D) PCD.

3.3.2 Nanoparticle characterization

We first synthesized crosslinked nanoscale hydrogel particles by thermally triggering PCD self-assembly into micelles in bulk solution and then crosslinking with UV light. Amphiphilic block copolymers readily self-assemble when heated to a temperature, T , above the T_t of the hydrophobic block, but below the T_t of the hydrophilic block. Upon heating, the hydrophobic block will phase separate, collapsing into the core of the resulting nano-scale micelles, with the hydrophilic block forming the solvated corona. Given the precisely defined molecular weight of our genetically encoded polymers, and the physical constraints on chain packing per particle, the resulting hydrogel particle population is highly monodisperse.¹⁷³⁻¹⁷⁴ We use the terms “xPCD” for these micelles after they are crosslinked into nano-gels by UV irradiation and “nxPCD” to denote the control, non-crosslinked micelles. We characterized the nanoscale assemblies of PCD before and after crosslinking in bulk solution with light scattering and microscopy.

3.3.2.1 Light scattering

Thermal ramp dynamic light scattering (DLS) of xPCD in solution confirmed the stabilization of self-assembled nano-sized gel particles (Figure 34). Notably, these xPCD particles retain the reversible thermal responsiveness of their component ELP chains, as evidenced by xPCD shrinking upon heating as the hydrophobic core further desolvates

and swelling upon cooling. In contrast, the nxPCD particles assemble upon heating into nano-scale micelles but disassemble completely into single chains upon cooling.

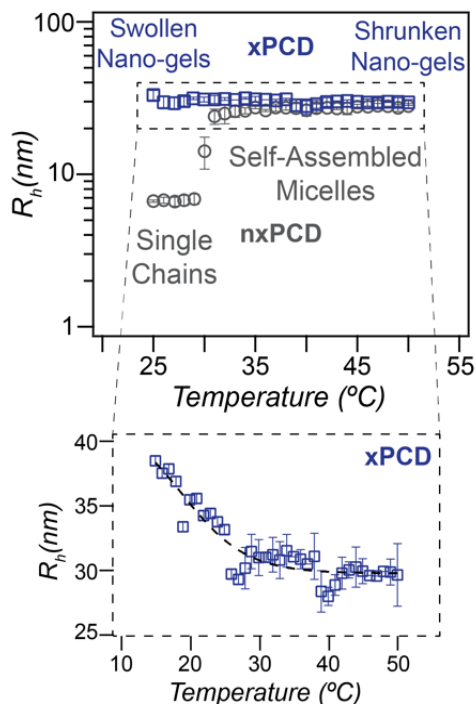


Figure 34: Thermal ramp dynamic light scattering of xPCD and nxPCD nano-scale micelles. Hydrodynamic radius (R_h) of nxPCD (grey; non-crosslinked) and xPCD (blue; crosslinked) as a function of temperature. nxPCD self-assembles from single chains into monodisperse micelles above the critical micellization temperature, whereas xPCD does not disassemble into single chains when the temperature is lowered below the CMT. Inset demonstrates the significant de-swelling of xPCD nano-gels with increasing temperature. Black dashed line represents the best sigmoidal curve fit for visualization. Error bars represent the polydispersity percentages ($n = 5$).

Given our observation that xPCD particles considerably shrink and swell upon heating and cooling, we were interested in determining the robustness of this phenomenon. We collected DLS data for repeated heating and cooling cycles and did not observe any hysteresis in the size of the xPCD particles. We performed five

successive rounds of heating/cooling on a single sample of dilute xPCD, with the first and last cycles shown in Figure 35.

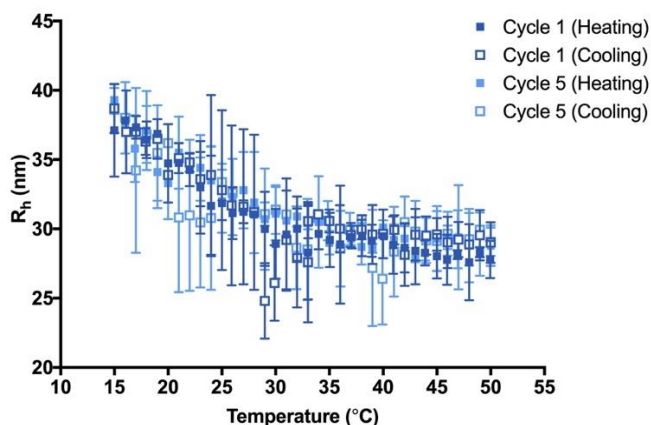


Figure 35: Hydrodynamic radius of xPCD nano-gels as a function of temperature for multiple heating-cooling cycles indicates no hysteresis in particle size. Each color represents a different heat/cool cycle and error bars represent the polydispersity percentage ($n = 5$).

We performed static light scattering (SLS) on both xPCD and nxPCD performed above the *CMT* at 37°C to assess the radius of gyration (R_g), radius of hydration (R_h), form factor (ρ), molecular weight per micelle, and the number of chains per particle (N_{agg}) (Table 2).

Table 2: Static light scattering characterization of xPCD and nxPCD above the critical micellization temperature.

	R_g [nm]	R_h [nm]	ρ	$MW_{micelle}$ [g mol ⁻¹]	N_{agg}
nxPCD	16.4	27.4	0.60	1.1×10^7	162
xPCD	19.2	29.1	0.66	1.3×10^7	200

This analysis confirms the formation of spherical particles approximately 60 nm in diameter and corroborates the R_h values for both xPCD and nxPCD as measured by

DLS. While the size and shape of the xPCD and nxPCD particles are similar, interestingly, the xPCD particles have more chains packed per particle, likely due to the constant flux of chains between the unimer and micelle state in the non-crosslinked sample. These SLS data were collected and analyzed by Joseph Simon.

3.3.2.2 Cryo-transmission electron microscopy

We visualized the xPCD particles using cryo-transmission electron microscopy (cryo-TEM), with samples vitrified at 25°C, below the critical micellization temperature (Figure 36). These images illustrate the monodispersity and stability of these nano-gels. These images were collected and processed by Cedric Bouchet-Marquis (FEI-Company, Hillsboro, OR).

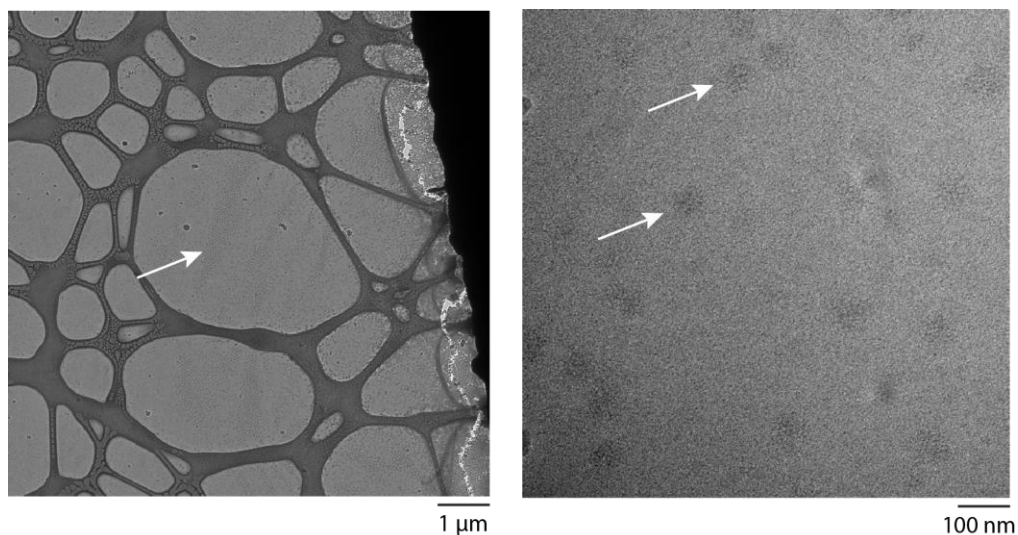


Figure 36: Cryo-TEM images taken above the critical micellization temperature of xPCD. The arrows indicate the location of monodisperse micelles, while the darker particles are hexagonal ice.

3.3.2.3 Atomic force microscopy

We further confirmed the stability of the xPCD particles by performing tapping mode atomic force microscopy (AFM) below the critical micellization temperature at ambient temperature. These images capture the highly monodisperse xPCD particles and confirmed their spherical shape (Figure 37A). Particle sizing analysis of these AFM images revealed the nominal radius of the xPCD nano-gels to be 30.2 ± 11.7 nm, further confirming the size measured with light scattering. At the same temperature, nxPCD does not form any visible nanoscale assemblies in the absence of crosslinks to stabilize the chains against dissociation (Figure 37B). These images were collected and processed by Lei Tang.

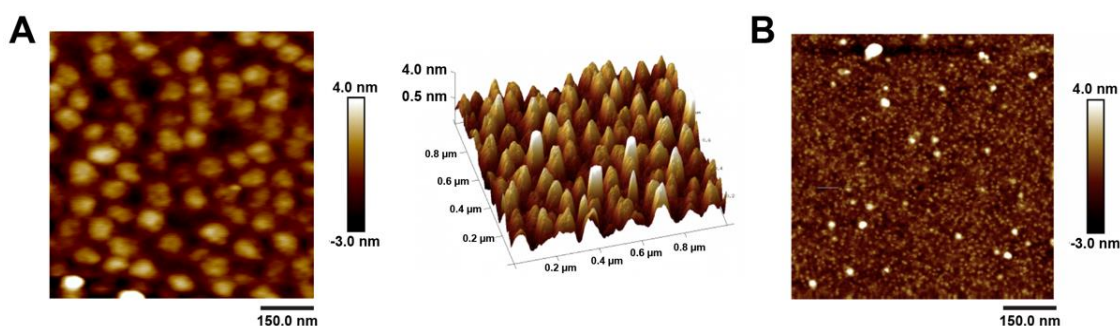


Figure 37: Tapping mode atomic force microscopy (AFM) images of xPCD nano-gels.

3.3.2.4 Pharmacokinetic analysis *in vivo*

These uniform, spherical xPCD nano-gels are ideally suited as drug delivery vehicles as they can be generated in solution after cargo loading and exist as stable micelles across a range of temperatures, an important consideration when preparing and storing samples at lower temperatures than physiological temperature. Their size and

solvation, both of which decrease with increasing temperature, are useful tunable attributes that can provide an active mechanism to release encapsulated cargo as compared to typical passive diffusion from most hydrogels. As such, we were interested in comparing the fate of the stabilized, crosslinked particles to non-crosslinked, self-assembled particles with respect to half-life and total exposure in circulation. We hypothesized that the crosslinked particles would persist longer in circulation, as the non-crosslinked micelles will expectedly disassemble and be cleared by glomerular filtration.²¹ Stabilized drug carriers with a consistent size above the renal filtration cut-off but below the pores of leaky tumor vasculature are best positioned to take advantage of the enhanced permeability and retention effect, the well-established phenomenon whereby nanocarriers passively and preferentially accumulate in tumors.²²

To assess the pharmacokinetics of these particles, we first fluorescently labeled PCD with AlexaFluor488-NHS ester and ensured particle assembly and size were unaffected by labeling for both the xPCD and nxPCD (Figure 38).

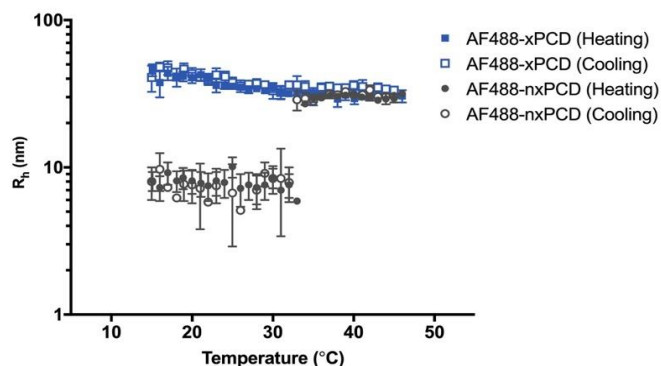


Figure 38: Dynamic light scattering of fluorescently-labeled PCD confirms particle assembly is unaffected by dye labeling.

We measured the pharmacokinetics of fluorescently-labeled xPCD and nxPCD in five-week-old female BALB/c mice following intravenous injection. We heated both samples to 37°C, above the critical micellization temperature, to ensure self-assembly prior to injection. Many of the non-crosslinked nanoscale micelles we have studied *in vivo* self-assemble after conjugation of hydrophobic cargo, such as small molecule drugs.⁸³ Therefore, we wanted to ensure the non-crosslinked samples were introduced into circulation as micelles to then track their systemic fate. After injection, we sampled the blood concentration of our fluorescently-labeled micelles with tail vein blood draws at various time points and measuring fluorescence with a plate reader. The fluorescent signal of these samples was converted to PCD concentration using standard curves we prepared for both the AlexaFluor488-xPCD and AlexaFluor488-nxPCD. For this, we diluted known quantities of each in mouse serum and measured the absorbance at 488 nm. The PCD concentrations were plotted as a function of time and a two-compartment model fit to this data to determine the distribution and elimination half-lives, as well as the area under the curve (AUC) (Figure 39).

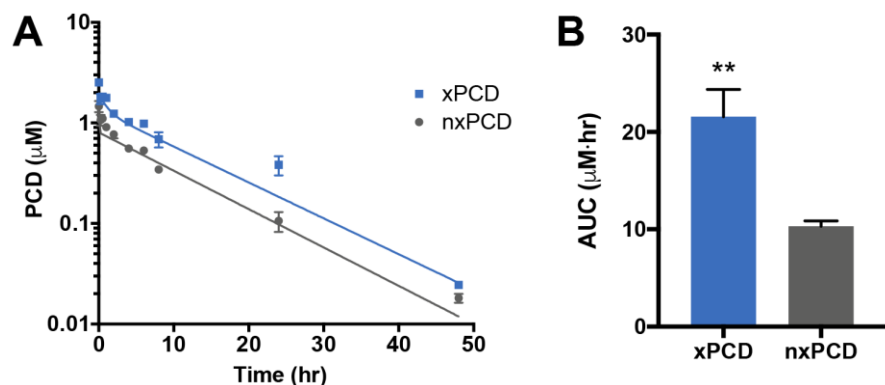


Figure 39: Pharmacokinetic data for xPCD and nxPCD micelles *in vivo*. (A) Concentration of PCD in circulation versus time (B) Area under the curve (AUC) demonstrates total systemic exposure over the experimental time frame, and that of xPCD is significantly higher than nxPCD ($p < 0.05$).

We found the initial clearance of nxPCD particles to be more rapid than xPCD, particularly when comparing the concentrations of both by 24 hours post-injection. By 48 hours, the concentrations of both samples approach the limit of detection (LOD) for the plate reader instrument used to quantify fluorescence of these samples. Notably, the effective exposure of xPCD for the entire time course of the study was significantly higher than that of nxPCD (Figure 39B).

We fit the data to a two-compartment model and, in addition to the area under the curve, determined the distribution and elimination half-lives ($\alpha t_{1/2}$, $\beta t_{1/2}$) and y-intercepts (α_0 , β_0) for this data (Table 3). While the distribution and elimination half-lives were similar for both samples, intriguingly, the elimination y-intercept was significantly higher for xPCD. This parameter represents the plasma concentration of drug after equilibration given the rate constant governing the elimination phase (β); a greater value

for this parameter indicates the bioavailability of xPCD is greater than that of nxPCD during this phase, which represents the majority of the interval for systemic exposure.

Table 3: Pharmacokinetic data of xPCD and nxPCD.

	Distribution α $t_{1/2}$ (hr)	Elimination β $t_{1/2}$ (hr)	α_0 (μM)	β_0 (μM)	AUC ($\mu\text{M}\cdot\text{hr}$)
xPCD	1.1 ± 0.5	8.4 ± 0.3	1.2 ± 0.6	1.6 ± 0.7	21.6 ± 2.8
nxPCD	0.9 ± 0.1	8.7 ± 0.3	0.6 ± 0.3	0.4 ± 0.02	10.3 ± 0.5

Taken together, these results suggest disparate biodistribution of the crosslinked and non-crosslinked particles, which would directly contribute to the differences in pharmacokinetic parameters observed. Future work will investigate the tissue-specific fate of these particles to identify the mechanistic underpinnings of these data.

3.3.3 Mesoparticle characterization

We next developed crosslinked particles with sizes spanning the mesoscopic range (100 nm - 1 μm), a challenging size regime for the synthesis of stable biopolymer-based particles. We have previously established that we can produce mesoscopic coacervates of uniform size by emulsifying and heating mixtures of ELP diblocks and monoblocks to initiate phase separation of the hydrophobic homopolymer blocks.¹⁷⁵ In our system, we mix the photocrosslinkable diblock, PCD, and the photocrosslinkable monoblock, PCE. Upon heating these mixtures to a precise temperature, we can initiate the assembly of PCE into spherical mesoscopic coacervates where the surfactant-like PCD chains prevent further coalescence of the coacervate droplets.

To determine the appropriate temperature, T , for mesoscale particle formation, we first confirmed that the phase separation of PCE in bulk solution is not impeded by the presence of the $pAzF$ residues. Although the $pAzF$ does depress the transition temperature compared to the same ELP sequence without these residues (NCE), the non-crosslinked samples of PCE solutions still exhibit the canonical reversible liquid-liquid phase separation of ELPs (Figure 40).

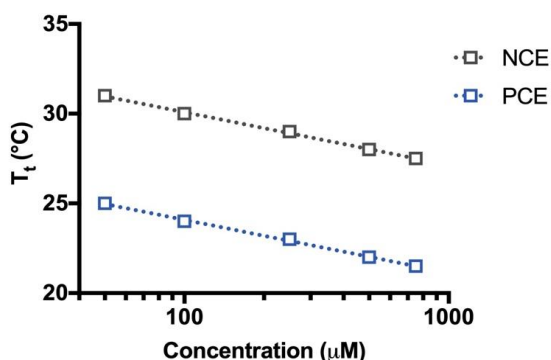


Figure 40: PCE exhibits LCST phase behavior in aqueous solution. Transition temperatures of PCE (blue) and NCE (grey) as a function of concentration. The dashed lines represent the best logarithmic fit for each data set.

The light scattering analysis we performed on PCD (Section 3.3.2.1) informed us of the critical micellization temperature (CMT) and transition temperature (T_t) of this polymer. These experiments allowed us to identify a range of temperatures, T , for given concentrations of PCE and PCD such that $CMT_{PCD} < T < T_{t-PCD}$ and $T > T_{t-PCE}$. Heating a solution of PCE and PCD to any temperature within this range will form mesoscale particles owing to the distinct phase separation of this mixture. For example, at 100 μM , CMT_{PCD} is 27°C, T_{t-PCD} is 65°C, and T_{t-PCE} is 23°C; therefore, heating to any temperature in

the range of $27^{\circ}\text{C} < T < 65^{\circ}\text{C}$ will result in mesoscale particle formation. Exposing the mesoscopic PCE-PCD assemblies to UV light efficiently crosslinks them into particles that do not re-solubilize upon cooling below $T_{t\text{-PCE}}$.

3.3.3.1 Light scattering

We determined that the size of the mesoscale coacervates can be easily tuned; it is possible to create hydrogel particles spanning the entire mesoscale regime by simply varying the ratio of PCE: PCD in these mixtures. Increasing the concentration of PCE relative to PCD, and thereby reducing the molar fraction of “surfactant” in solution, produces coacervate droplets with increasing size upon heating which can be photocrosslinked into stable meso-gels. As we observed with the crosslinked nano-gels, the meso-gels do not disassemble upon cooling, and shrink upon heating (Figure 41).

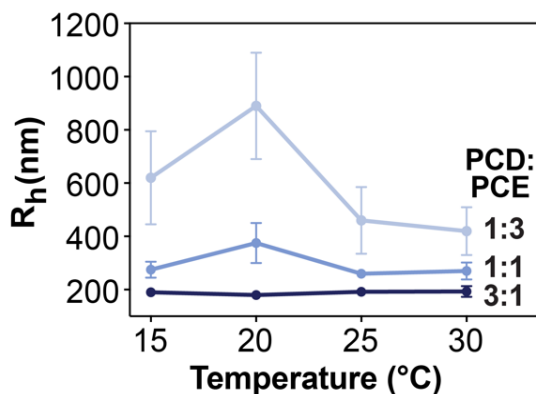


Figure 41: Dynamic light scattering of crosslinked mesoparticles. Data points represent the mean R_h and the error bars represent the polydispersity percentage.

3.3.3.2 Fluorescence imaging

To visualize these mesoparticles in solution, we used a microfluidic chip to produce water-in-oil emulsion microdroplets containing our particles. The fluorescent microscope we used to visualize these particles is equipped with a precision thermal stage, allowing us to specify the temperature of the solution containing these droplets. For the accompanying images, we prepared the aqueous phase of our microfluidic device with equimolar concentrations of fluorescently-labeled PCE and unlabeled PCD (Figure 42A). Heating these droplets to 30°C induces the assembly of mesoscale coacervates approximately 500 nm in diameter that do not coarsen over time but rather exhibit Brownian motion due to the surfactant-like PCD chains at the interface between the PCE-rich and PCE-poor phases (Figure 42B, C). Exposing the mesoscopic PCE-PCD coacervates to UV light efficiently crosslinks them into particles that do not re-solubilize upon cooling (Figure 42D). These images were collected and processed by Joseph Simon.

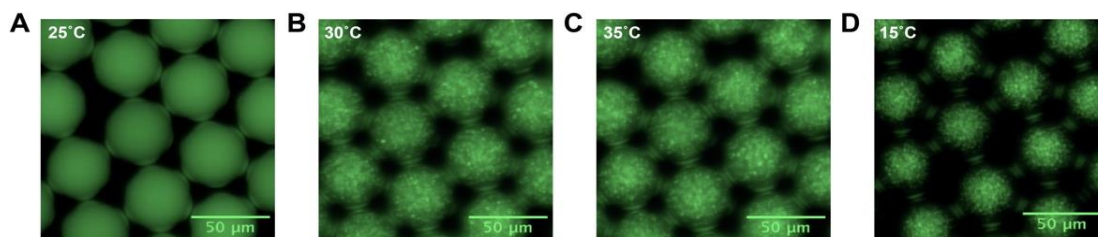


Figure 42: Visualizing mesoscale particles within microfluidic droplets. (A) Prior to heating, the solutions within the droplets are a homogenous mixture of AlexaFluor488-PCE and PCD. (B) Meso-coacervates assemble upon heating above the T_i of PCE and the CMT of PCD. (C) Mesoparticles are stabilized with UV crosslinking. (D) Crosslinked meso-gels do not disassemble upon cooling.

3.3.3.3 Scanning electron microscopy

We confirmed the size, shape, and stability of the mesoparticles using scanning electron microscopy (SEM). We prepared mesoparticles of different sizes by varying the ratio of PCD: PCE in solution, heating, and crosslinking the resulting assemblies. The particles in solution are densely concentrated, and we empirically determined it was necessary to dilute the samples 1:100 or 1:1000 in water prior to SEM imaging. We imaged mesoparticles ranging from approximately 250 nm to 1500 nm, corroborating our light scattering sizing of these particles and confirming our ability to easily tune particle size within the mesoscale range (Figure 43).

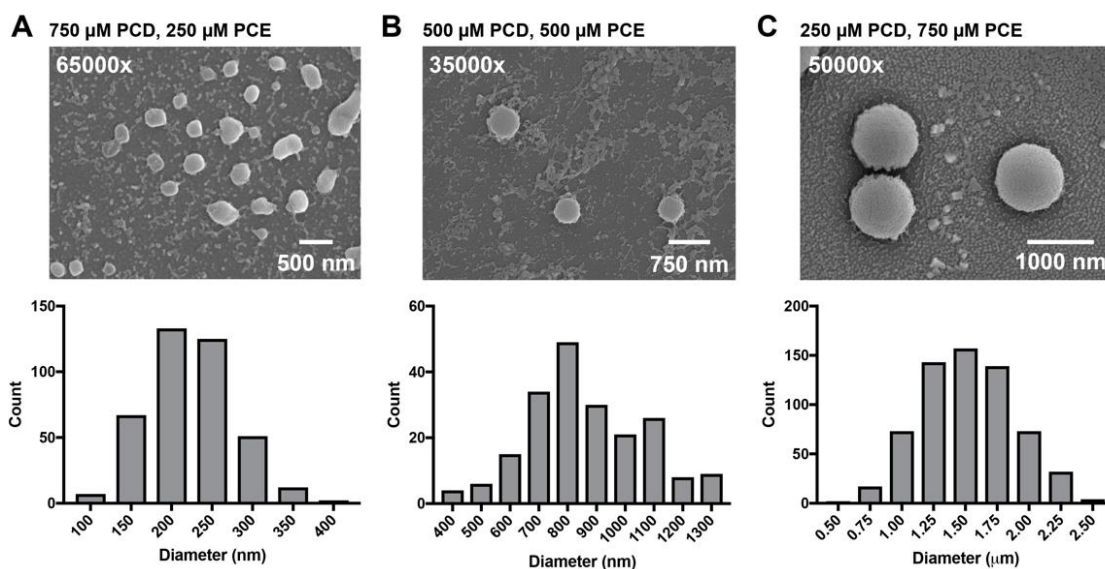


Figure 43: Scanning electron microscopy imaging of mesoparticles and size distribution. SEM image and corresponding histogram plot of the diameter of mesogels with mean diameter (A) 220 ± 52 nm ($n = 397$), (B) 865 ± 199 nm ($n = 202$), (C) 1510 ± 360 nm ($n = 639$).

3.3.4 Microparticle characterization

To extend the size of the particles further into the microscale, we used water-in-oil emulsion microfluidic droplets with the aqueous phase containing only PCE. Without PCD chains present in solution, PCE undergoes the canonical ELP liquid-liquid phase separation (Figure 44). The resulting coacervates are formed into microscale spheres with dimensions dictated by the template droplet size; theoretically, any such “mold” could be used to generate stable coacervates of PCE with various sizes and shapes. The PCE chains will re-solubilize upon cooling unless they are crosslinked with UV light into stabilized microparticles.

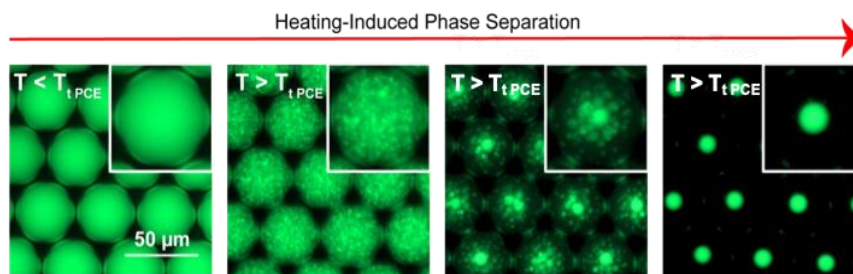


Figure 44: PCE undergoes phase separation upon heating to form liquid coacervates within microdroplets. Time-lapse fluorescence microscopy images of heating-triggered phase separation of Alexa 488-labeled PCE. PCE chains are soluble at temperatures below the T_t , whereas at temperatures above the T_t , PCE collapses to form spherical PCE-rich liquid droplets. These images were collected by Joseph Simon.

3.3.4.1 Fluorescence imaging

We can tune the size of these microparticles by modulating the initial concentration of PCE and then crosslinking at a temperature either above or below the transition temperature (T_t). We used this approach to generate microparticles of two

uniform sizes – either 12 μm or 25 μm in diameter – though particle size can be easily tuned with different starting conditions. To generate 25 μm micro-gels, we crosslinked droplets containing soluble PCE at a concentration above chain overlap to enable network formation. To create the 12 μm micro-gels, we heated PCE droplets to form one uniform coacervate per droplet and then irradiated the droplets with UV light to crosslink the coacervates into particles.

We investigated the thermal responsivity of our microparticles by monitoring their size as a function of temperature using temperature-controlled fluorescence microscopy. As we observed with the nano- and mesoparticles, after crosslinking these micro-gels expel water and shrink upon heating from 15°C to 30°C due to enhanced chain-chain interactions and desolvation (Figure 45).

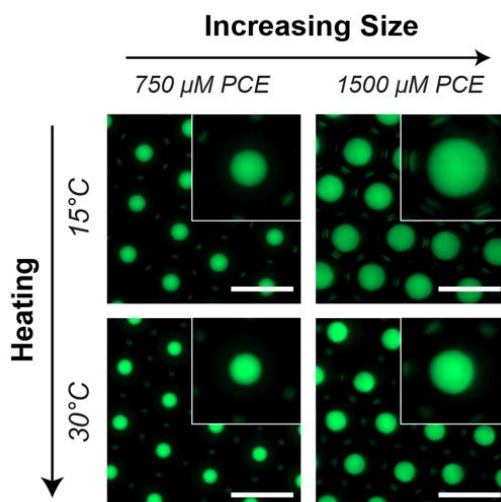


Figure 45: Fluorescence microscopy images of microgels within water-in-oil emulsion droplets. 12 μm micro-gels (left) and 25 μm micro-gels (right) with starting concentration of PCE shown above; upon heating the particles swell (top panels) and the particles shrink upon cooling (bottom panels).

We tracked the volumetric changes of these particles over this heating ramp using visible particle sizing of the fluorescent microscopy images to better quantify the extent of “de-swelling” with our two microparticle preparations. We normalized the apparent volume at each temperature to the starting volume of the particles at 15°C, below the T_i of PCE. The de-swelling effect is more prominent for the 25 μm microgels, with these particles shrinking down to 40% of their original volume, likely due to a less densely packed network (Figure 46).

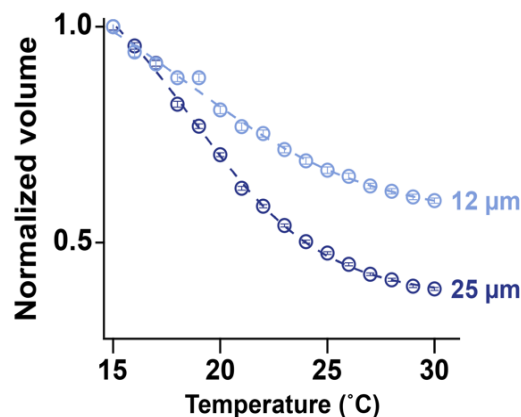


Figure 46: Volumetric change of crosslinked microparticles upon heating. The volumes of the 12 μm particles (light blue) and 25 μm particles (dark blue) at each temperature are normalized to the initial volume at 15°C. The dashed lines represent the best sigmoidal fit and the error bars represent the SEM ($n = 150$ droplets).

These results demonstrate that by simply changing the conditions at which crosslinking is performed (i.e., upon solutions of soluble or insoluble PCE), it is possible to control the extent of volumetric change in response to heating and cooling. These images were collected and processed by Joseph Simon.

3.3.4.2 Scanning electron microscopy

The microparticles were extracted from their parent droplets using isobutanol extraction, which disrupts the water/oil interface of the droplets to produce two continuous phases. The aqueous phase containing the particles can easily be separated from the less dense organic phase through centrifugation and aspiration of the supernatant. We optimized the extraction protocol to maintain the integrity of the particles after extraction, allowing us to capture these highly monodisperse, spherical particles with scanning electron microscopy (SEM) imaging (Figure 47).

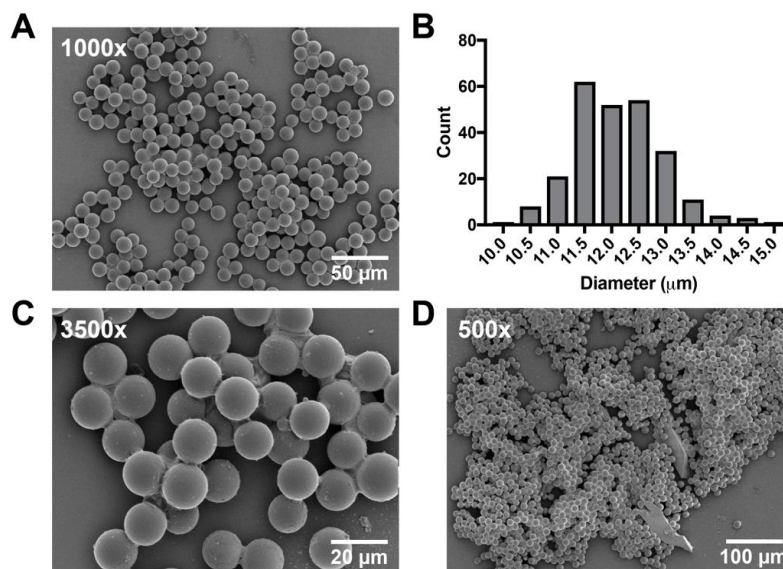


Figure 47: Scanning electron microscopy imaging of microparticles and size distribution. (A) SEM imaging and (B) sizing of particles with mean particle diameter $12.1 \mu\text{m} \pm 0.8 \mu\text{m}$ ($n \geq 200$). (C) and (D) show additional magnifications of these particles.

As evidenced by the lower magnification image (Figure 47D), our microfluidic chip is able to produce a high volume of these particles; our set-up produces

approximately 1000 droplets per second. A typical experiment with three hours of collection time therefore provides on the order of 10^7 total microparticles. After extraction, the density of these particles in solution can be adjusted by resuspending the extracted pellet in the desired volume.

These particles are also highly stable; after extraction they can be reconstituted in water or phosphate-buffered saline (PBS), lyophilized and reconstituted in solution, and stored at temperatures ranging from -80°C to 37°C for at least one week without loss of structural integrity or change in size (Figure 48).

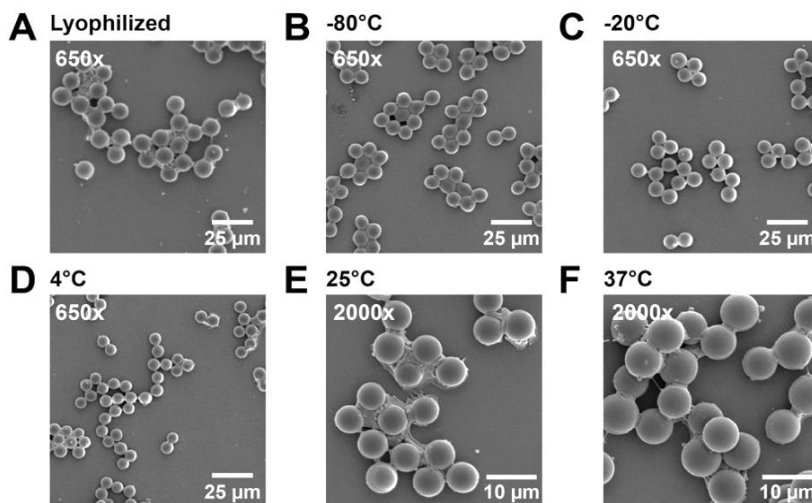


Figure 48: Stability of microparticles in a variety of storage conditions. (A) Lyophilized particles reconstituted in PBS, and particles stored at (B) -80°C , (C) -20°C , (D) 4°C , (E) 25°C , or (F) 37°C for one week in buffered solution.

3.4 Conclusions and future directions

3.4.1 Summary and significance

In conclusion, we have developed simple and convenient strategies to fabricate thermoresponsive gel particles that are tunable from the nanoscale to microscale in size

using genetically encoded polypeptides. We tune particle size from the nano- to mesoscale by increasing the ratio of the *pAzF*-containing ELP monoblock (PCE) to diblock ELP (PCD). To extend into the microscale regime, microfluidic droplets provide a necessary level of control for templating PCE coacervates, with droplet dimensions directly dictating particle size (Figure 49).

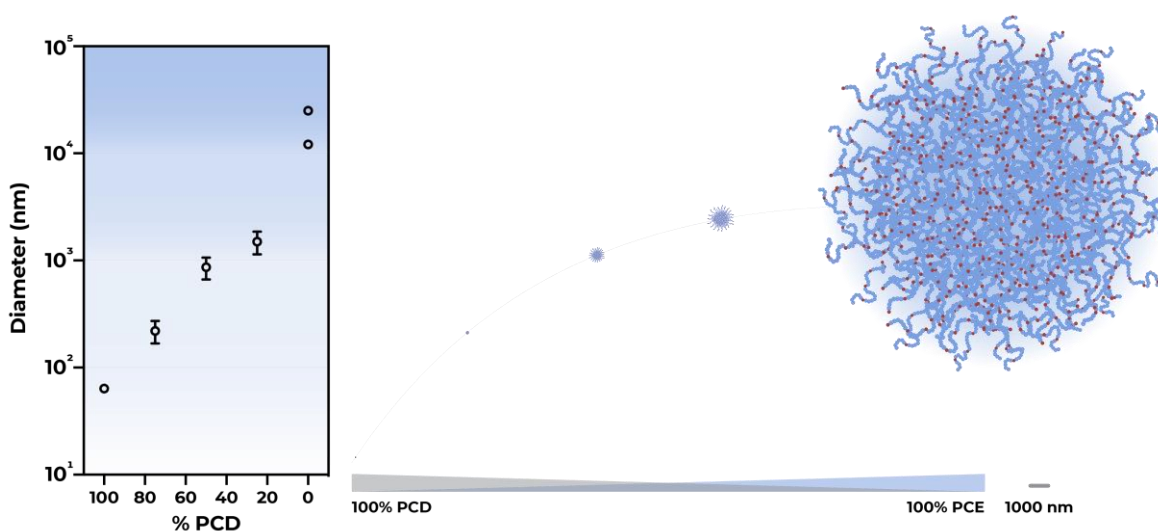


Figure 49: Crosslinked hydrogel particles span four orders of magnitude in size. Gel particle diameter as a function of PCD content (PCE percentage = 100 – PCD). Error bars represent the polydispersity percentage ($n \geq 5$) or standard deviation (PCD = 0%, $n \geq 100$). Particles on right shown to scale from 50 nm to 12 μm diameters.

These particles retain the unique phase transition behavior of the component ELP chains, shrinking upon heating and reversibly swelling upon cooling. The particles reach thermodynamic equilibrium rapidly (i.e., on the order of seconds) and robustly over many cycles, providing an active mechanism for actuation and a dynamic response to the environment.

3.4.2 Future perspectives

Future work with this material system will allow further fine-tuning of gel network density at any given temperature. For example, changing the ELP sequence (i.e. guest residue, length) will modulate the functional dependence of monomer-excluded volume on temperature: more hydrophilic guest residues and longer ELP chains than those explored in our system will result in even less dense networks and more pronounced swelling and de-swelling behavior.⁶² Increasing the concentration of *pAzF* residues will also tune the swelling properties, with more photocrosslinking sites resulting in a more tightly enmeshed network. Changing the spacing and location of these residues – for example, by clustering them at one terminus or repositioning them within the hydrophilic block of PCD – will undoubtedly affect the porosity of the network and mechanical strength of the resulting particles in unique ways. Exploring additional block architectures such as triblocks and mixing a variety of *pAzF*-containing polymers will expectedly produce novel particle geometries, as well. These hydrogels can be extended beyond the microscale by eliminating the use of microfluidic droplets and employing instead a variety of templating agents to create macroscale hydrogels with the desired size and shape.

These crosslinked particles are ideally suited to be used in future work in a wide variety of fields, ranging from biomedical applications as drug delivery vehicles, actuators, biosensors, tissue scaffolds, artificial cells, and cell encapsulators, to colloidal

stabilizers and emulsifiers for food and personal care products. While both synthetic and natural polymer-based hydrogel particles have been leveraged for these applications, our genetically encoded biopolymers are innately biocompatible and have the capacity for further functionalization with bioactive domains.¹⁶³ Irrespective of the component material, hydrogels swell in order to reach thermodynamic equilibrium with their surrounding environment, resulting in a highly adaptive material that favorably integrates with biological systems.¹⁷⁶ As discussed, the size of these hydrogel particles is a critical parameter which dictates particle utility.

Nano-scale hydrogel particles are frequently employed as carriers for systemic delivery of small molecules, nucleotides, peptides, and proteins.¹⁴ Particles within this size regime are ideally suited for cellular uptake and tissue extravasation, with preferential accumulation in tumors.¹¹ These versatile particles can be administered intravenously, inhaled, ingested, or implanted for local delivery.¹⁷⁷ As we corroborated with our *in vivo* study, crosslinked particles have proven pharmacokinetic advantages over non-covalently assembled carriers.¹⁴³ While delivery via nanoscale carriers of any formulation extends the half-life of loaded cargo by increasing apparent molecular weight and thereby reducing renal clearance, this effect is amplified when the particles are stabilized against disassembly.¹⁷⁸ Our base diblock biopolymer can easily be modified to include residues for drug attachment in addition to targeting or adhesion ligands to further augment efficacy.

The mesoparticles we developed can be used as delivery agents, emulsifiers, and preservatives. Our strategy for mesoparticle synthesis – through solubilization of homopolymers with diblock copolymers – endows our particles with a uniquely hydrophilic surface. The surfactant-like amphiphile at the particle interface positions these particles to serve as effective colloidal suspensions for modeling and preserving biological systems.¹⁷⁹ In addition, the unique size of the mesoparticles, larger than the pores of epithelial vessel walls but smaller than blood cells, can be leveraged to strategically prevent particle uptake for exclusive cargo release in circulation.^{10, 180-181}

Micron-scale hydrogel particles are the most versatile and widely used; the base biopolymers in our system can be recombinantly modified to enhance their existing utility further. For example, these microparticles can be tailored for drug delivery by derivatization with protease recognition motifs for sustained release of physically entrapped cargo via controlled degradation.¹⁷⁷ Introducing a biosensor component to induce particle swelling and cargo release in response to external cues is another potential approach for delivery. For example, genetic fusion of glucose-metabolizing enzymes can detect blood glucose fluctuations or inclusion of charged amino acid groups can respond to increasing pH levels throughout the gastrointestinal tract.¹⁸²⁻¹⁸³

Another potential application for these microparticles is as emulsifying agents in personal care and food-grade products to modulate texture.¹⁸⁴⁻¹⁸⁵ Our entirely polypeptide-based particles are highly biocompatible, enabling topical application or

rapid digestion into amino acids, and the component polypeptides can be modified at the gene level to introduce desirable cosmetic properties or impart flavor.¹⁸⁶⁻¹⁸⁸

The genetically encoded nature of our system affords the flexibility and precision necessary to empower rationally-designed particles across multiple size scales. For example, crosslinked particles spanning the size regime enabled with our technology can be developed for the study and manipulation of protocells, membrane-less organelles, and artificial cells.¹⁸⁹⁻¹⁹⁰ Furthermore, previous work generating additional self-assemblies of ELPs (e.g. rod-like and cylindrical micelles), along with the wealth of information on the biophysical properties of ELPs will inform future studies to create unique particle architectures and geometries.^{5, 55-57, 191-194}

4. A bioorthogonal strategy for simultaneous drug loading and active targeting of nanoparticles

4.1 Introduction and motivation

As demonstrated in the previous chapter, we have developed the tools to engineer precisely defined thermoresponsive hydrogel particles using elastin-like polypeptides (ELPs). Polypeptides such as these are exceptional nanoscale drug carriers for chemotherapeutics: they have minimal toxicity, can be recombinantly synthesized with precise control of their sequence and molecular weight, and can be designed to self-assemble into colloidally stable nanoparticles that carry their chemotherapeutic payload in their core, enhancing the solubility, pharmacokinetics, and tumor accumulation of drugs. While passive targeting of nanoparticles promotes accumulation of these nanocarriers in solid tumors, active targeting provides an additional layer of tunable control and widens the therapeutic window by reducing off-target toxicity. Unfortunately, the fusion of most targeting protein domains to polypeptide carriers exposes the limitations of this approach, because the cysteine and lysine residues that are typically used to attach drugs to polypeptide carriers are also promiscuously distributed in solvent accessible — and hence highly reactive — locations on the protein surface.³⁴⁻³⁶

To solve this problem, we have genetically encoded an unnatural amino acid that provides a unique, bio-orthogonal reactive moiety in its side-chain for site specific attachment of small molecule drugs or imaging agents into a polypeptide. We

demonstrated the utility of this approach by recombinant synthesis of a nanobody-functionalized ELP nanoparticle with a *p*-acetylphenylalanine residues (*p*AcF), that provides a biorthogonal ketone residue to which we attached doxorubicin, the small-molecule drug of interest. We have shown that a nanobody-decorated, doxorubicin-loaded nanoparticle which targets the epidermal growth factor receptor (EGFR) exhibits significantly greater cytotoxicity compared to the non-targeted version of this nanoparticle in multiple cancer cell lines that overexpress EGFR. This approach provides a universal methodology for the site-specific attachment of extrinsic moieties to polypeptide drug delivery systems without cross-reactivity with a protein targeting domain that is fused to the carrier. The work presented in this chapter resulted in a publication in *Nano Letters*, adapted here with permission from the American Chemical Society (copyright 2019).⁷⁶

4.1.1 Nanoscale biopolymer drug carriers

While small molecule drugs are highly potent cytotoxic agents, their poor solubility, short half-life and insufficient bioavailability often require the use of delivery strategies, such as polymeric nanoscale drug carriers, to improve their delivery to solid tumors.¹⁹⁵⁻¹⁹⁸ Recent work has demonstrated the importance of three key elements for effective tumor treatment by nanoparticle drug carriers: (1) long circulation time;^{10, 199} (2) active targeting;²⁰⁰⁻²⁰⁴ and (3) site-specific attachment of cytotoxic drugs.²⁰⁵⁻²¹⁰ Extended circulation time is advantageous for regional accumulation in tumors via the

enhanced permeability and retention effect, also called “passive” targeting.^{22, 211} Active targeting of nanoparticles to tumors provides the second stage of tumor specific delivery as it enables tumor cell-selective uptake, complementary to the regional accumulation provided by passive targeting, thereby widening the therapeutic window of the drug.^{85, 161, 212-215} Finally, site-specific conjugation of small molecule drugs to these carriers ensures homogenous drug release.^{20, 22, 216}

Recombinant peptide polymers are attractive for the design of nanoparticle delivery systems because they can be produced recombinantly in high yield in *E. coli* as monodisperse macromolecules and their sequence and chain length are easily manipulated at the gene level.²¹⁷⁻²¹⁸ They are also non-toxic and biodegradable.²³ We have pioneered the development of elastin-like polypeptides (ELPs) for drug delivery, including ELPs that self-assemble into nanoparticles.^{65, 84-85, 161, 212, 215, 219-222}

Genetically encoded synthesis provides exquisite control over the design and tunability of ELP nanoparticles for drug delivery, as it enables the size and shape of the nanoparticle to be controlled, as well as the site and stoichiometry of small molecule drug conjugation, and allows introduction of targeting protein peptide domains.^{65, 84-85, 213, 215, 223-224} However, because of the limited chemical diversity available with the twenty naturally-occurring amino acids, we cannot simultaneously control all of these parameters in the same nanoparticle. This is because we typically use chemically reactive lysine and cysteine residues to site-specifically conjugate small molecule drugs

and imaging agents to ELPs; this approach works well with nanoparticles that consist solely of ELPs (or in some instances ELPs appended with short peptide tags that direct their self-assembly) as ELPs can be designed without either of these two residues while preserving their two major properties of interest — their thermally responsive phase behavior or their self-assembly into nanoparticles.^{31-33, 225-226} Unfortunately, the fusion of most targeting protein domains to an ELP or other polypeptides exposes the limitations of this approach, because cysteine and lysine residues are typically found in most targeting proteins and are often in solvent accessible — and hence highly reactive— locations.³⁴⁻³⁶ A bioorthogonal, site-specific attachment strategy is necessary to alleviate these natural residues for their essential role in bioactive domains.

4.1.2 Active targeting of drug delivery vehicles

Active targeting of nanoparticle carriers to tumors, in which a drug carrier presents a ligand that specifically recognizes and binds to a receptor over-expressed by tumor cells, resulting in receptor-mediated internalization of the carrier and its cargo. While passive targeting – local accumulation of nanocarriers due to the tissue-specific aberrancies of tumors – provides one layer of targeting, active targeting further reduces off-target effects and widens the therapeutic window.^{85, 161, 212-215} The method of uptake – receptor-mediated endocytosis – presents a unique pathway for carrier intracellular trafficking as compared to simple diffusion of the free drug across the cell membrane, or micropinocytosis of a naked drug carrier, allowing for more precisely specified timing of

acid-catalyzed drug release.²⁰⁰ There is a delicate balance for the affinity requirements of this targeting interaction: too weak and the carrier will non-specifically bind to healthy cells, but too strong and only the periphery of the solid tumor mass will receive drug.¹⁰ Researchers have previously determined that low nanomolar affinity (< 100 nM) of targeting groups for their receptors is ideal and both peptides and proteins have been used as targeting agents, with distinct advantages for each.²²⁷⁻²³¹ Active targeting is accomplished through the introduction of engineered peptides or affinity protein domains, such as antibodies and antibody fragments, fibronectin and other scaffold domains, affibodies, and nanobodies.

4.1.2.1 Criteria for targeting domain selection

We had several criteria for selection of the targeting domain, with the goal of developing a universal, proof-of-concept platform for active targeting and drug loading. The selected domains needed to be small, compact, and inert enough so as to not perturb the diblock self-assembly; this limited our search to cyclic peptides and small scaffold domains such as affibodies and nanobodies, which are both ≤ 15 kDa, and therefore less than approximately 20% of the total protein molecular weight. With the domain fused to the C-terminus of the ELP diblock, we looked for domains that do not require their N-terminus to be free for binding, and especially those that had previously been successfully recombinantly fused at their N-termini. To demonstrate the generalizability of this platform, we looked for proteins and peptides that contain disulfide bonds. For

ease of purification and maximization of yield, we focused on domains and peptides that have been successfully expressed solubly in bacteria. Lastly, we looked for domains with multiple literature sources that demonstrated targeting and internalization on commercially available cancer cell lines for ease of characterization. Additionally, we were interested in receptor antagonists, or those that do not engage the signaling axis upon receptor binding, to minimize background cytotoxicity of non-drug loaded carriers, and to prevent the development of extrinsic resistance to our treatment. We selected the EgA1 nanobody and RGD4C cyclic peptide as two candidates for our preliminary testing and characterization.

4.1.2.2 EgA1 nanobody

We chose the EgA1 nanobody — a small antibody fragment derived from camelid single-chain antibodies — as one of the targeting domain candidates for our system.²³² Nanobodies are small and compact, and are therefore unlikely to perturb self-assembly of the ELP into nanoparticles when appended on the corona, and unlike full-length antibodies, they can be expressed recombinantly in *E. coli* alone or as fusions.²³³⁻²³⁶ Importantly, they contain four lysine residues and a pair of cysteine residues, thereby representing a good candidate for validating the generality of our approach.^{232, 237} The EgA1 nanobody recognizes and binds to human epidermal growth factor receptor (EGFR) with an affinity of 276 nM.²³⁸⁻²³⁹ We chose EGFR as the target as it is highly

upregulated or aberrantly expressed in multiple cancer types including breast, ovarian, brain, lung, and as many as 30% of all carcinomas.²⁴⁰⁻²⁴³

4.1.2.3 RGD4C cyclic peptide

Peptides are compact and innocuous targeting moieties and can bind with high affinity after directed evolution for their intended target, particularly when cyclized with disulfide bonds. These cyclic peptides have higher affinities and are more stable than their linear counterparts.²⁴⁴ The second candidate we chose was the cyclic peptide RGD4C, which contains two disulfide bonds to stabilize the stalk of the peptide and promote presentation of the $\alpha v \beta_3$ integrin-binding amino acid sequence RGD. This peptide has been confirmed to recognize $\alpha v \beta_3$ with nanomolar affinity, 200-fold greater affinity than its linear counterpart.²⁴⁴

4.1.3 Small molecule drug selection and conjugation to nanoscale carriers

As the cytotoxic payload for our system, we chose a small molecule chemotherapeutic —doxorubicin (Dox). Dox stabilizes an intermediate covalent complex between topoisomerase II and genomic DNA, causing damaging double-stranded breaks and exit from the cell cycle.²⁴⁵ This drug is widely used for the treatment of hematopoietic malignancies, breast, lung, ovary, stomach, and thyroid carcinomas, and bone and soft tissue sarcomas.^{85, 213, 215, 220, 222, 246-247} However, Dox exhibits dose-limiting myelosuppression, mucositis, and cardiotoxicity, and a nanoparticle formulation of this drug can greatly improve its *in vivo* performance.²⁴⁸

Various strategies have been used to load small molecule drugs into nanoparticles. Attachment at cysteine or lysine residues is most commonly employed but both of these will require introduction of engineered residues or potential disruption to biological activity. Drug encapsulation is accomplished by modulation of the hydrophobicity of the component polymer domains but is not as effective as formation of a covalent bond between a drug and its carrier. The spatial and temporal control of release is limited and encapsulated drug is prone to leakage prior to uptake in a tumor cell.^{195, 210} Many researchers have taken advantage of the low pH environment of the endo-lysosomal compartments to enable drug release from an acid labile bond only after intracellular uptake.²⁴⁹⁻²⁵¹ A direct conjugation to the drug carrier is superior for stability, pharmacokinetic profile enhancement, and overall efficacy.

4.2 Materials and methods

4.2.1 Molecular biology and design of constructs

The design of the initial constructs for testing our targeting domain candidates, ELP_{BC}-EgA1 and ELP_{BC}-RGD4C, is shown in Figure 50. We designed and synthesized a gene that encodes a self-assembling diblock ELP fused to either of the targeting candidates at the C-terminus.

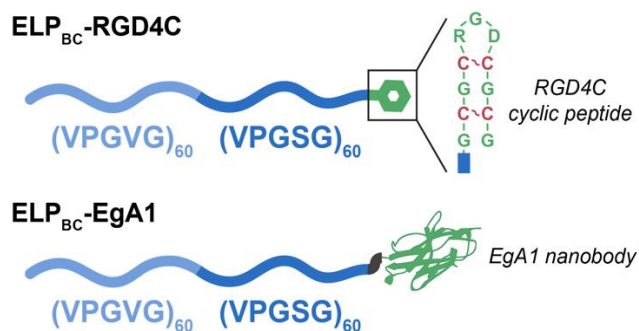


Figure 50: Design of targeted ELP_{BC} candidates displaying the RGD4C cyclic peptide or the EgA1 nanobody.

We designed and synthesized a gene that encodes a self-assembling diblock ELP fused to a peptide leader at the N-terminus of the hydrophobic block that incorporates the site of Dox attachment, *p*-acetylphenylalanine (*p*AcF, Figure 51), followed by a site for trypsin cleavage for analysis by mass spectrometry. As with our test constructs, we positioned the EgA1 nanobody at the C-terminus of the hydrophilic block (*p*AcF-ELP_{BC}-EgA1).

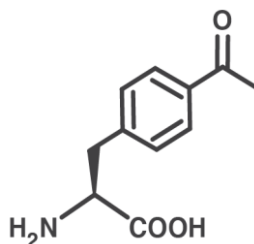


Figure 51: Structure of *p*-acetylphenylalanine (*p*AcF), the unnatural residue used for Dox conjugation.

We optimized the diblock ELP in this final construct so that it has a critical micellization temperature (CMT) that lies between room temperature and body temperature. Upon heating to a temperature above the CMT, the N-terminal

hydrophobic ELP block desolvates while the C-terminal hydrophilic ELP block remains solvated, creating an amphiphile that self-assembles into nanoscale micelles that are stable at physiological temperatures. The EgA1 nanobody is displayed on the corona of the micelle, while Dox is sequestered in the core of and is covalently attached to the ketone group of *pAcF* via a linker that creates a pH-sensitive oxime bond between the drug and the ELP,²⁵²⁻²⁵³ allowing for release of Dox in the acidic lysosomal compartments of cells after uptake by receptor-mediated endocytosis (Figure 52).

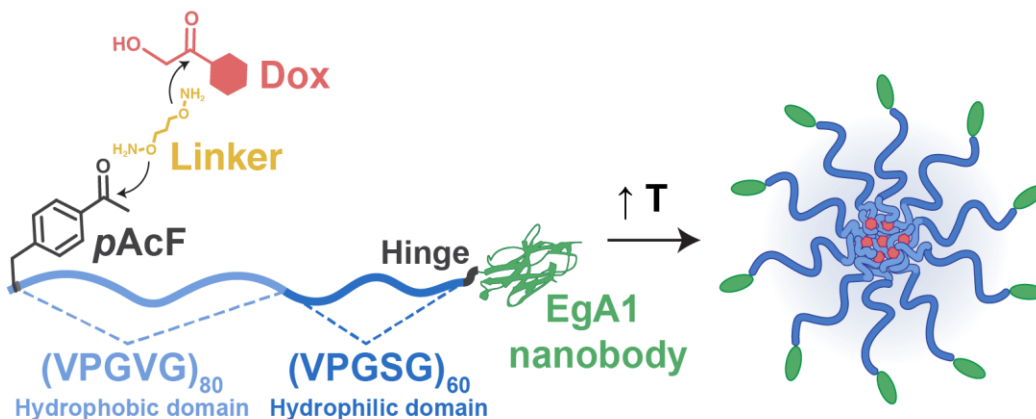


Figure 52: Design and assembly of Dox-*pAcF*-ELP_{BC}-EgA1 nanoparticles.

Genes encoding ELP_{BC} and *pAcF*-ELP_{BC} were synthesized using recursive directional ligation by plasmid reconstruction.¹³⁶ In brief, two populations of modified cloning vectors (m-pET-24+) containing two genes of interest were digested with either *AclI*/*BglII* or *BseRI*/*BglII* to create compatible plasmid fragments, which upon ligation, seamlessly encode the new gene product. In this case, the site of incorporation for *pAcF*, the amber stop codon, was introduced in the form of a peptide leader with sequence

GVGVPGpAcFGVPGVGR by first annealing together complementary ssDNA strands that encode for this sequence along with “sticky end” overhangs, digesting the m-pET-24+ plasmid with BseRI, and inserting this oligonucleotide. This vector was then digested with AcuI and BglI to create an “A” population and the ELP_{BC}-containing vector was digested with BseRI and BglI to create a “B” population. These two populations were then ligated to create a vector containing the gene encoding pAcF-ELP_{BC}. The gene encoding the EgA1 nanobody was ordered as a gBlock (IDT Technologies, Skokie, IL) and inserted into m-pET-24+ using Gibson assembly. This gene was then fused to the C-terminus of either ELP_{BC} or pAcF-ELP_{BC} by a similar plasmid reconstruction strategy as above. We then transferred the genes of interest to the expression vector, m-pTac (see Section 2.2.1.2), by digesting the pAcF-ELP_{BC} and pAcF-ELP_{BC}-EgA1-containing m-pET-24+ vectors with BseRI/BamHI, extracting the insert using agarose gel separation and purification, and ligating with a similarly digested m-pTac. The amino acid sequences of the constructs are shown in Appendix C, Table 18.

pET24+ vectors were purchased from Novagen (Madison, WI). Oligonucleotides and gBlocks encoding sequences of interest were purchased from Integrated DNA Technologies (Coralville, IA). Ligation enzymes, restriction enzymes, and calf intestinal alkaline phosphatase were purchased from New England Biolabs (Ipswich, MA). EB5 α and BL21(DE3) chemically competent *E. coli* cells were purchased from Bioline (Taunton, MA). SHuffle T7 Express competent *E. coli* cells were purchased from New England

Biolabs (Ipswich, MA). Genomically recoded *E. coli* cells (C321.ΔA) were generously provided by Prof. Farren Isaacs (Yale University). All *E. coli* cultures were grown in 2xYT media comprised of sodium chloride (5 g L⁻¹; Alfa Aesar, Ward Hill, MA), tryptone (16 g L⁻¹, Becton, Dickinson and Co., Franklin Lakes, NJ), and yeast extract (10 g L⁻¹, Becton, Dickinson and Co., Franklin Lakes, NJ). Kanamycin sulfate was purchased from EMD Millipore (Billerica, MA) and chloramphenicol was purchased from Sigma-Aldrich (St. Louis, MO). *p*-Acetylphenylalanine hydrochloride was purchased from Synchem, Inc. (Elk Grove Village, IL). Protein expression was induced with isopropyl β-d-1-thiogalactopyranoside (IPTG) from Gold Biotechnology (St. Louis, MO) and L-(+)-arabinose from Sigma-Aldrich (St. Louis, MO). 1× phosphate buffered saline (1xPBS) tablets (10 × 10⁻³ M phosphate buffer, 140 × 10⁻³ M NaCl, and 3 × 10⁻³ M KCl, pH 7.4 at 25°C) were purchased from EMD Millipore (Billerica, MA). A molecular organic fluorophore (AlexaFluor488-NHS ester) was purchased from Life Technologies (Grand Island, NY).

4.2.3 Selection of bacterial expression host

We expressed these constructs in one of three *E. coli* expression hosts; the base diblock ELP_{BC} was solubly expressed in the standard protein expression cell line, BL21(DE3). The introduction of the *pAcF* residue and EgA1 nanobody directed us to investigate the use of two different *E. coli* lines previously reported for expression of constructs containing these elements.^{113, 236} The constructs containing *pAcF* —*pAcF*-ELP_{BC}

and *pAcF-ELP_{BC}-EgA1* — were expressed in the genomically recoded C321.ΔA cell line with yields of 30 mg L⁻¹ and 15 mg L⁻¹, respectively. For constructs including the EgA1 nanobody — *ELP_{BC}-EgA1* and *pAcF-ELP_{BC}-EgA1* — which introduces a disulfide bond into the protein, we used the SHuffle T7 Express *E. coli*, as this line is optimized to enhance disulfide bond formation and protein solubility. We explored expression of our final product, *pAcF-ELP_{BC}-EgA1*, in both SHuffle and C321.ΔA *E. coli* as each provides a unique advantage for expression. The engineered SHuffle strain expresses heterologous chaperones to enhance the production of functional, soluble disulfide-bonded protein under the control of a T7 promoter. Conversely, the recoded C321.ΔA strain is ideally suited for unnatural amino acid incorporation with an unassigned stop codon that can be reassigned exclusively for an unnatural residue of interest, as well as the corresponding release factor deleted to eliminate any competition with a termination signal.

4.2.4 Protein expression and purification

The construct-bearing vectors described above were then co-transformed with a modified pEvol tRNA/aaRS vector that contained two copies of the *pAcFRS.1.t1* synthetase (generously provided by Prof. Farren Isaacs) into the C321.ΔA *E. coli* for expression with *pAcF* incorporation.

To express ELP_{BC}, liquid BL21DE3 *E. coli* cultures (50 mL) of strains harboring ELP plasmids (m-pET24+) were inoculated from frozen glycerol stocks and grown to

confluence overnight. Cultures were then inoculated at 1:20 dilution in 2xYT media (1 L) supplemented with kanamycin (45 $\mu\text{g ml}^{-1}$). Cells were grown at 37°C in a shaking incubator at 200 rpm for 6 h, at which time ELP expression was induced by the addition of IPTG (1 mM), and the cultures incubated at 37°C for an additional 18 h. Cell pellets were harvested by centrifugation at 3500xg and resuspended in 1xPBS (20 mL). Cells were lysed by sonication for a total of 3 min (Misonix; Farmingdale, NY) and DNA was precipitated by addition of polyethyleneimine (10%; MP Biomedicals, Santa Ana, CA). Precipitated DNA and cellular debris were removed by centrifugation at 20,000xg at 4 °C. Proteins were then purified using four rounds of inverse transition cycling, as described elsewhere.⁶⁹ Briefly, solutions of proteins were heated and salt (NaCl) was added to induce the phase transition of the ELP, centrifuged to collect all insoluble material at 35°C, 20,000xg (“hot spin”), and re-suspended in cold 1xPBS. Upon cooling, the ELP resolubilizes, while contaminants remain insoluble and can be removed by centrifugation at 4°C, 20,000xg (“cold spin”).

To express *pAcF-ELP_{BC}*, liquid C321. Δ A *E. coli* cultures (50 mL) of strains harboring *pEvol* and ELP plasmids (*m-pTac*) were inoculated from frozen glycerol stocks and grown to confluence overnight. Cultures were then inoculated at 1:20 dilution in 2xYT media (1 L) supplemented with kanamycin (45 $\mu\text{g ml}^{-1}$) and chloramphenicol (25 $\mu\text{g ml}^{-1}$). aaRS expression was simultaneously induced by the addition of arabinose (0.2%) and *pAcF* (1 mM). Cells were grown at 34°C in a shaking

incubator at 200 rpm for 6 h, at which time ELP expression was induced by the addition of IPTG (1 mM), and the cultures incubated at 34°C for an additional 18 h at which point cells were harvested and proteins purified as described above.

To express ELP_{BC}-EgA1 and ELP_{BC}-RGD4C, liquid SHuffle *E. coli* cultures (50 mL) of strains harboring the ELP plasmid (m-pET24+) were inoculated from frozen glycerol stocks and grown to confluence overnight. Cultures were then inoculated at 1:20 dilution in 2xYT media (1 L) supplemented with kanamycin (45 µg ml⁻¹). Cells were grown at 30°C in a shaking incubator at 200 rpm for 6 h, at which time ELP expression was induced by the addition of IPTG (1 mM), and the cultures incubated at 16°C for an additional 18 h. Cells were harvested, and proteins purified as described above.

To express pAcF-ELP_{BC}-EgA1, both C321.ΔA *E. coli* cultures harboring pEvol and the ELP plasmid (m-pTac) and SHuffle *E. coli* cultures harboring pEvol and the ELP plasmid (m-pET24+) were used as described above. Both expression hosts yielded proteins with pAcF incorporated (as determined by MALDI-TOF mass spectroscopy) and active EgA1 (as determined by flow cytometry), and pAcF-ELP_{BC}-EgA1 expressed from the C321.ΔA *E. coli* cultures were used for Dox conjugation studies.

Protein purity was characterized by 4–20% gradient Tris-HCl (Biorad, Hercules, CA) sodium dodecyl sulfate polyacrylamide gel electrophoresis (SDS-PAGE) and staining with copper chloride (0.5 M; Thermo Fisher Scientific, Hampton, NH). The expression yield of pAcF-ELP_{BC} was determined gravimetrically after dialysis into

Nanopure water and lyophilization. The expression yield of nanobody-containing proteins (ELP_{BC}-EgA1, *p*AcF-ELP_{BC}-EgA1) was determined by UV/Vis spectrophotometry (NanoDrop 1000, Thermo Fisher Scientific, Waltham, MA), using extinction coefficients of $\epsilon = 34505 \text{ cm}^{-1} \text{ M}^{-1}$ and $\epsilon = 37884.5 \text{ cm}^{-1} \text{ M}^{-1}$, respectively.

4.2.5 Doxorubicin conjugation to *p*AcF

The linkers explored for doxorubicin conjugation include 1) adipic acid dihydrazide, 2) O,O'-1,3-propanediylbis hydroxylamine dihydrochloride (both purchased from Sigma-Aldrich (St. Louis, MO)) and 3) (9H-fluoren-9-yl)methyl N-(3-aminopropoxy)carbamate, synthesized by Enamine (Kyiv, Ukraine), with linker 2 being selected for final conjugation studies. Doxorubicin hydrochloride was purchased from CarboSynth (San Diego, CA). Aniline and *p*-phenylenediamine catalysts were purchased from Sigma-Aldrich (St. Louis, MO).

Doxorubicin was conjugated to *p*AcF-containing proteins via a two-step reaction: first, the telechelic linker was attached to the *p*-acetylphenylalanine (*p*AcF) residue via ketone condensation, and second, doxorubicin was attached to the linker via the same mechanism. After each reaction step, excess, unreacted products were removed. First, *p*AcF-ELP_{BC} or *p*AcF-ELP_{BC}-EgA1 were buffer exchanged from PBS into labeling buffer (50 mM sodium acetate, pH 5.0, 150 mM sodium chloride) and concentrated by centrifugal ultrafiltration (Amicon Ultra-15, 10 kDa cut-off, Millipore Sigma, Burlington, MA) to 125 μM . The linker was resuspended in labeling buffer and twenty molar

equivalents were added, along with aniline at a final concentration of 10 mM, which raised the pH of the reaction to pH 6.2. The reaction was carried out with stirring at 30°C in a mineral oil bath for 24 h. The linker-*pAcF*-ELP was then dialyzed against 8 L of PBS to remove excess linker and buffer exchanged into labeling buffer and concentrated to 125 μM by centrifugal ultrafiltration (Amicon Ultra-15). For the second reaction step, doxorubicin HCl was resuspended in water and ten molar equivalents added. Aniline was added to a final concentration of 10 mM. The second reaction was carried out with stirring in a mineral oil bath at 30°C for 24 hours. Excess doxorubicin was removed first with a PD-10 column (GE Healthcare, Chicago, IL) and then by washing with 15% acetonitrile/PBS by centrifugal ultrafiltration (Amicon Ultra-15). *pAcF*-ELP_{BC}-EgA1 concentration and reaction efficiency was determined by UV/Vis spectrophotometry (NanoDrop) with extinction coefficients $\epsilon = 37,884.5 \text{ cm}^{-1} \text{ M}^{-1}$ for *pAcF*-ELP_{BC}-EgA1 and $\epsilon = 10,000 \text{ cm}^{-1} \text{ M}^{-1}$ for Doxorubicin. The following formula (Equation 1) was used to calculate the labeling of *pAcF*-ELP_{BC}-EgA1 with an A280 correction factor of 0.767:

Equation 1: Calculating Dox labeling efficiency

$$\% \text{ Labeling} = \frac{A_{490} / \epsilon_{\text{Dox}}}{[A_{280} - (0.767 \times A_{490})] / \epsilon_{\text{ELP}}}$$

The concentration of *pAcF*-ELP_{BC} was determined gravimetrically by weighing the lyophilized protein and resuspending in a known volume of PBS.

4.2.6 Size exclusion chromatography and pH release

For size exclusion chromatography analysis of the purity of Dox conjugates and fluorescently labeled proteins, a Shodex OHPak SB-804 column (New York, NY) was used with isocratic flow of 0.5 mL min⁻¹ of PBS: acetonitrile [70:30] on a Shimadzu high performance liquid chromatography system (Shimadzu Scientific Instruments, Columbia, MD). HPLC-grade solvents were purchased from VWR International (Radnor, PA).

To assay for the release of drug, samples of Dox-*p*AcF-ELP_{BC}-EgA1 (25 μM Dox equivalents) in PBS (pH 7.4) were buffer exchanged into either pH 4.5 (0.1 M sodium acetate) or pH 7.4 (PBS) buffers with centrifugal ultrafiltration (Amicon Ultra-0.5, 10 kDa MWCO). Samples were incubated at 37 °C for 0, 1, 3, 6, 24, or 48 h and quenched by dilution 1:1 [vol: vol] into PBS, pH 7.4, to stop hydrolysis prior to analysis by HPLC. 100 μL of each sample at a 25 μM Dox equivalent concentration was analyzed using a LC10 HPLC (Shimadzu Scientific Instruments; Columbia, MD) on a Shodex OHPak KB-804 column (New York, NY) with isocratic flow of 0.5 mL min⁻¹ of PBS: acetonitrile [70:30]. The integrated area under the curve (AUC) was quantified at an absorbance of 495 nm (A_{495}) corresponding to Dox. Two peaks eluted during the assay for Dox-*p*AcF-ELP_{BC}-EgA1 at 15.5 ± 0.5 min and for free Dox at 23.5 ± 0.5 min. The % Dox released was determined by normalizing the AUC₄₉₅ for the free Dox peak at each time point to the total AUC₄₉₅ of the initial sample.

4.2.7 Mass spectrometry analysis

pAcF-containing samples were designed such that the leader sequence contains a trypsin-cleavable arginine residue following the stop codon to allow for mass spectrometry analysis of *pAcF* incorporation. Lyophilized trypsin was reconstituted using 50 mM acetic acid to 1 mg mL⁻¹ as per the manufacturer's instructions. Samples of *pAcF*-ELP_{BC} and *pAcF*-ELP_{BC}-EgA1 at 100 μM were incubated with MS-grade trypsin protease (Pierce, Waltham, MA) at a ratio of 20:1 in 50 mM ammonium bicarbonate, pH 8. These reactions were incubated for 16 hours at 37°C and then analyzed with matrix-assisted laser desorption/ionization time-of-flight mass spectrometry (MALDI-TOF-MS) using a Bruker Autoflex Speed LRF MALDI-TOF System. Digested samples were mixed at a ratio of 1:1 with α-cyano-4-hydroxycinnamic acid (HCCA) matrix and 2 μL deposited onto a ground steel target plate and dried in air at room temperature. All spectra were calibrated against adrenocorticotrophic hormone fragment 18-39 (Sigma Aldrich, St. Louis, MO).

For ESI-LC/MS, tryptic digests were similarly prepared and analyzed with an Agilent 1100 Series LC/MSD Trap SL (Agilent Technologies, Santa Clara, CA). Samples were injected into a Phenomenex Luna C18 column (50 × 1 mm, 3 μm; 0.2% formic acid in water as buffer A, 0.2% formic acid in acetonitrile as buffer B) and then into the mass spectrometer using a fully automated system. Spectra were acquired in positive mode followed by analysis and deconvolution using LC/MSD Trap Data Analysis software

(Agilent Technologies, Santa Clara, CA). Mass spectra were acquired at the Mass Spectrometry Shared Facility at Duke University. Incorporation and reaction step efficiencies were calculated by taking the ratio of intensities for the peak of a specific product over the total peak intensities of all relevant peaks in the sample.

4.2.8 *In vitro* characterization of targeted constructs

4.2.8.1 Fluorescent protein labeling and flow cytometry

To fluorescently label proteins, 1 mg of AlexaFluor488-NHS ester was dissolved in 100 μ L DMSO. The N-terminal amine of ELP_{BC} and ELP_{BC}-EgA1 were labeled with AlexaFluor488-NHS ester by incubating 100 μ M protein with ten molar equivalents of dye, rotating for 24 h at 4°C in sodium phosphate buffer, pH 7.4. Excess unreacted dye was removed with a hot spin followed by washing with centrifugal ultrafiltration (Amicon Ultra-15, 10 kDa MWCO). Briefly, a hot spin consists of heating the solution of labeled protein above the T_i to initiate phase separation and centrifuging at high speeds to pellet the ELP, with free dye in the supernatant. After removal of the supernatant, the pellet is resuspended in cold PBS and the ELP resolubilizes. The purity of the labeled proteins was assessed by size exclusion chromatography. The following equations were used to calculate protein (Equation 2) and A488 concentration (Equation 3).

Equation 2: Calculating protein concentration

$$[\text{ELP}_{\text{BC}}\text{-EgA1}] = \frac{A_{280} - (A_{494} \times 0.11)}{34,505 \text{ cm}^{-1}\text{M}^{-1} \times 1 \text{ cm path length}}$$

Equation 3: Calculating fluorescent labeling efficiency

$$[\text{AlexaFluor488}] = \frac{A_{494}}{73,000 \text{ cm}^{-1}\text{M}^{-1} \times 1 \text{ cm path length}}$$

The concentration of ELP_{BC} and labeling efficiency were determined gravimetrically after dialysis into DI water, lyophilization, weighing, and resuspension in 1xPBS. The labeling efficiency of both proteins by Alexa488 was approximately 25%.

Overnight cultures of adherent cells were prepared for flow cytometry by first trypsinizing cells with 0.05% trypsin/EDTA and harvesting the cells by centrifugation for 3 min at 1,000xg. The cell pellet was resuspended in PBS/1% BSA, the cells were counted with a hemocytometer after 1:1 dilution into Trypan blue solution (0.4%, Thermo Fisher Scientific, Waltham, MA), and the cell density adjusted to 2×10^6 cells mL⁻¹. Cells were incubated with fluorescently labeled proteins by gently mixing 90 μ L of the cell suspension with 10 μ L of 100 μ M ELP (25 μ M Alexa488) followed by a 1 h incubation with rocking at 4°C to minimize uptake by the cells. Flow experiments with incubation at 37°C ensure micelle self-assembly showed equivalent or higher levels of cell binding as those performed at 4°C. After incubation, cells were collected and washed 3x with 0.5 mL PBS/1% BSA on ice, with a final cell concentration prior to flow analysis of 2×10^5 cells mL⁻¹. Live cells were analyzed for population fluorescence on a BD FACSCanto Analyzer (BD Biosciences, San Jose, CA) at the Duke Cancer Institute Flow Cytometry Shared Resource Facility to determine the geometric mean fluorescence intensity (gMFI) of samples.

4.2.8.2 Cell viability assays

The *in vitro* cytotoxicity of Dox conjugates was determined by a colorimetric assay, as follows. First, 0.5×10^3 A431 or SKOV-3 cells were seeded per 40 μL complete media on BD Falcon™ 384-well cell culture plates (BD, Franklin Lakes, NJ) and allowed to adhere for 16–18 h. After adherence, 10 μL of serial dilutions of Dox, Dox-*p*AcF-ELP_{BC}, or Dox-*p*AcF-ELP_{BC}-EgA1 were added to the wells and incubated at 37°C for 24 h. After the treatment period, 10 μL of CellTiter 96 AQueous™ MTS reagent (Promega, Madison, WI) were added to each well. Following incubation for 3 hours, the absorbance of the solution was measured twice at 490 nm and 650 nm with a Victor3 microplate reader (PerkinElmer, Waltham, MA). The background A₆₅₀ was subtracted from the A₄₉₀ readings to determine the cell viability (Equation 4) as compared to untreated controls. Wells containing media only with equivalent concentrations of Dox were also prepared to subtract background contribution from free Dox.

Equation 4: Calculating cell viability

$$\% \text{ Viability} = \frac{\text{Corr. } A_{490} - A_{490_{\text{Media}}}}{\text{Corr. } A_{490_{\text{Untreated}}} - A_{490_{\text{Media, Untreated}}}} \times 100\%$$

To calculate the IC₅₀, the data was fit to a sigmoidal curve and used in the following equation (Equation 5), where C_{Dox} is the effective Dox concentration in the well, the IC₅₀ measures the necessary dose to kill 50% of the cell population, and *p* represents the slope of the sigmoidal curve.

Equation 5: Calculating IC₅₀

$$\% \text{ Viability} = \frac{1}{1 + \left(\frac{C_{\text{Dox}}}{\text{IC}_{50}}\right)^p}$$

4.2.8.3 Intracellular imaging

For fluorescence visualization of ELP_{BC}-EgA1 and ELP_{BC}-RGD4C uptake, 4 × 10⁴ transfected fibroblast cells were seeded on Lab-Tek® II CC2™ chamber slides (Electron Microscopy Sciences, Hatfield, PA) and allowed to adhere for 18 h. Cell media was replaced with complete media containing either (1) 10 μM AlexaFluor488-ELP_{BC}-EgA1 or AlexaFluor488-ELP_{BC}-RGD4C, (2) 10 μM AlexaFluor488-ELP_{BC}, or (3) 10 μM AlexaFluor488-ELP_{BC}-EgA1 with 100 μM excess unlabeled ELP_{BC}-EgA1 (or with the RGD4C targeting moiety), and incubated for 24 h at 37°C. Following treatment, the media was removed, and cells were incubated for 10 min with 2 μM Hoechst 33342 (Life Technologies, Carlsbad, CA) to stain cell nuclei and 5 μg mL⁻¹ wheat germ agglutinin (WGA) AlexaFluor 594 (Thermo Fisher Scientific, Waltham, MA) to stain cell membranes. The cells were then washed twice with Hank's Balanced salt solution (HBSS, Thermo Fisher Scientific, Waltham, MA) at room temperature. The slide was mounted with ProLong Gold Antifade Mountant (Thermo Fisher Scientific, Waltham, MA) prior to visualization on a Nikon TE-2000U widefield fluorescence microscope with a 60× oil-immersion objective. Hoechst 33342 dye was detected with a standard UV-2E/C filter set, WGA was detected with a 540/25 nm excitation filter, 565 nm long pass dichromatic mirror, and 605-655 nm band pass emission filter set, and Alexa488 was

detected with a 450–490 nm excitation filter, 505 nm long pass dichromatic mirror, and 590–650 nm emission filter set.

For colocalization of Dox conjugates with lysosomal compartments, 2.75×10^4 A431 cells were seeded in 110 μL of complete media into each of the four chambers of a $\mu\text{-Dish}^{35 \text{ mm, high}}$, Culture-Insert 4 Well (1.5 coverslip, Ibidi, Madison, WI) and allowed to adhere for 18 h. Cell media was replaced with complete media containing either 25 μM Dox-*pAcF-ELP_{BC}-EgA1* or 25 μM Dox-*pAcF-ELP_{BC}* and incubated for either 4 or 24 h at 37°C. After treatment, the media was gently removed and replaced with complete media containing 1x CytoPainter LysoDeep Red Indicator Reagent (Abcam, Cambridge, MA) to stain lysosomal compartments and incubated for 30 min at 37°C. Following this incubation, the media was gently removed and replaced with complete media containing 2 μM Hoechst 33342 (Life Technologies, Carlsbad, CA) to stain cell nuclei for 10 min at 37°C. Cells were then washed twice with Hank's Balanced salt solution (HBSS, Thermo Fisher Scientific, Waltham, MA) at room temperature and maintained in fresh HBSS prior to imaging on an Andor Dragonfly Spinning Disk 500 series confocal on a LeicaDMi8 microscope stand (Oxford Instruments, Abingdon, UK) with a 63 \times water immersion objective and equipped with a Zyla 4.2 series camera. Hoechst 33342 dye was detected with a 400 nm excitation filter and 450/50 nm emission filter, Dox with a 488 nm excitation laser and 525/50 nm emission filter, and CytoPainter with a 637 nm excitation laser and 700/75 nm emission filter in CF40 imaging mode. Imaging processing and

colocalization analysis was performed using the Coloc2 plug-in available with FIJI (ImageJ, National Institutes of Health).

To confirm specificity of EgA1 nanobody for EGF, 1.5×10^4 transfected fibroblasts were seeded in 110 μL of complete media into each of the four chambers of a $\mu\text{-Dish}^{35\text{ mm}}$,^{high}, Culture-Insert 4 Well (1.5 coverslip, Ibidi, Madison, WI) and allowed to adhere for 18 h. Cell media was replaced with complete media containing either 2 $\mu\text{g mL}^{-1}$ pHrodo Green EGF (Invitrogen, Carlsbad, CA) or fresh media and incubated for 1 h at 37°C. pHrodo Green EGF is a weakly fluorescent, pH-sensitive dye that is brightly fluorescent only after endocytosis into cells via EGFR. Cells were then washed twice with Hank's Balanced salt solution (HBSS, Thermo Fisher Scientific, Waltham, MA) and complete cell media containing 10 μM Alexa647-ELP_{BC}-EgA1 was added to the wells and cells incubated for 1 h at 37°C. Following this incubation, the media was gently removed and replaced with complete media containing 2 μM Hoechst 33342 (Life Technologies, Carlsbad, CA) to stain cell nuclei for 10 min at 37°C. Cells were then washed twice with HBSS at room temperature and maintained in complete media prior to imaging on an Andor Dragonfly Spinning Disk 500 series confocal on a LeicaDMi8 microscope stand (Oxford Instruments, Abingdon, UK) with a 63 \times water immersion objective and equipped with a Zyla 4.2 series camera. Hoechst 33342 dye was detected with a 400 nm excitation filter and 450/50 nm emission filter, pHrodo Green EGF with a 488 nm

excitation laser and 525/50 nm emission filter, and Alexa647-ELP_{BC}-EgA1 with a 561 nm excitation laser and 600/50 nm emission filter in CF40 imaging mode.

4.3 Results and discussion

4.3.1 Characterization of purified proteins

We purified all constructs by inverse transition cycling (ITC), a non-chromatographic method for the purification of ELPs and their fusions that exploits the LCST phase behavior of ELPs and their fusions.^{69, 254}

4.3.1.1 Characterization of targeting domain candidates and selection of EgA1

After purifying both ELP_{BC}-EgA1 and ELP_{BC}-RGD4C, we tested these constructs for their ability to form nanoparticles and for intracellular uptake on candidate cell lines. We first analyzed the critical micellization temperature (CMT) of both via dynamic light scattering (DLS) to confirm assembly at physiologically relevant temperatures.

We observed a moderate (~ 5°C) increase in the CMT of ELP_{BC}-EgA1 as compared to ELP_{BC} due to the introduction of the nanobody on the corona (Figure 53A, blue). This is expected as the nanobody contains charged residues that augment the hydrophilicity of the hydrophilic block. We further tuned the CMT of the next generation of ELP_{BC}-EgA1 by increasing the length of the hydrophobic block, to ensure the CMT is within in a physiological range. The CMT of ELP_{BC}-RGD4C is approximately 33°C (Figure 53A, red), but required addition of 10 mM dithiothreitol (DTT) to disrupt undesirable intrachain disulfide bond formation.

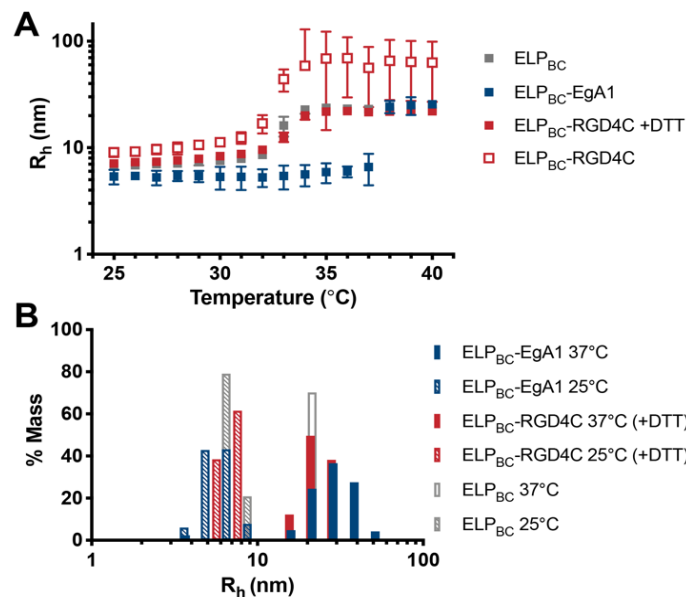


Figure 53: Characterization of ELP_{BC}-EgA1 and ELP_{BC}-RGD4C self-assembly via dynamic light scattering. (A) The CMT of ELP_{BC}-EgA1 is 37°C and the CMT of ELP_{BC}-RGD4C is 33°C. ELP_{BC}-RGD4C required addition of 10 mM DTT to disrupt intrachain disulfide bond formation. (B) ELP_{BC}, ELP_{BC}-EgA1, ELP_{BC}-RGD4C assemble into micelles ~ 60 nm in hydrodynamic diameter at 37°C

The CMTs of both of these constructs ensure these diblocks will self-assemble into nanoparticles *in vitro* and *in vivo*, a critical parameter for drug carriers. The ELP_{BC}-EgA1 particles have hydrodynamic diameters of approximately 60 nm (Figure 53B). As the ELP_{BC}-RGD4C construct exhibited transient intramolecular disulfide bond formation, these particles had ostensibly larger hydrodynamic radii when measured by DLS. We performed DLS of ELP_{BC}-RGD4C under reducing conditions (10 mM DTT) to confirm the size of these individual particles to be approximately 60 nm in hydrodynamic diameter in the absence of disulfide-driven particle aggregation (Figure 53B).

We then qualitatively assessed the uptake of these targeted constructs via fluorescence microscopy in receptor-overexpressing cell lines. We fluorescently labeled the N-termini of both constructs with Alexa488-NHS ester and purified via ITC to remove excess free dye. To assess the EGFR-specific uptake of ELP_{BC}-EgA1, we incubated the fluorescently labeled construct with NIH3T3 mouse fibroblast cells stably transfected to over-express human EGFR.²⁵⁵ To assess the $\alpha_v\beta_3$ -specific uptake of ELP_{BC}-RGD4C, we incubated this construct with the $\alpha_v\beta_3$ -over-expressing MDA-MB-231 human mammary carcinoma line.²⁵⁶ To confirm specificity of these constructs for their receptors, we also incubated these cells with 10-fold excess unlabeled construct to block receptor binding and prevent fluorescent particle uptake. We assayed the uptake of fluorescently labeled ELP_{BC} in these cells as a negative control. After an incubation period of 24 h, we washed the cells to remove excess free dye and fluorescently stained the nuclei and cell membranes. These preliminary results confirm enhanced internalization of both fluorescently labeled ELP_{BC}-EgA1 (Figure 54A) and ELP_{BC}-RGD4C (Figure 54D) as compared to the controls. The samples incubated with excess, unlabeled targeted ELP_{BC} prevent uptake of the fluorescently labeled constructs, demonstrating the specificity of each construct for the corresponding receptor (Figure 54B, E). There is expected non-specific uptake of fluorescently labeled non-targeted ELP_{BC} in each cell line due to phagocytosis, though these levels are nominal (Figure 54C, F).

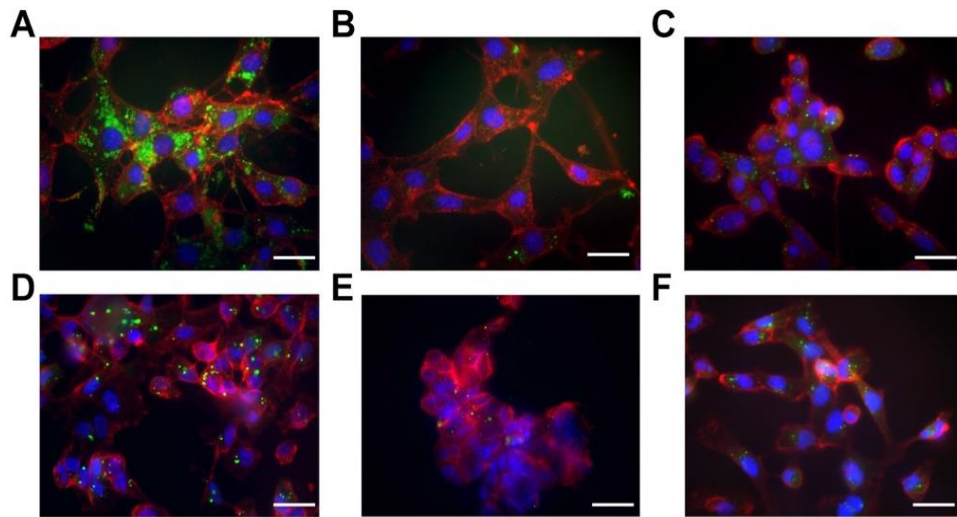


Figure 54: Fluorescence microscopy imaging of ELP_{BC}-RGD4C and ELP_{BC}-EgA1 nanoparticle uptake. EGFR-expressing fibroblasts incubated with A) 10 μ M Alexa488-ELP_{BC}-EgA1, B) 10 μ M Alexa488-ELP_{BC}-EgA1 + 100 μ M ELP_{BC}-EgA1, C) 10 μ M Alexa488-ELP_{BC}. $\alpha_v\beta_3$ -expressing MDA-MB-231 cells incubated with D) 10 μ M Alexa488-ELP_{BC}-RGD4C, E) 10 μ M Alexa488-ELP_{BC}-RGD4C + 100 μ M ELP_{BC}-RGD4C, F) 10 μ M Alexa488-ELP_{BC}. Green, Alexa488; blue, nuclei stained with Hoechst; red, cell membranes stained with wheat germ agglutinin. Scale bar: 25 μ m.

The extent of fluorescent particle internalization for both constructs indicates both the nanobody and cyclic peptide are presented with the correct orientation and retain specificity for their targets on the surface of the ELP_{BC} micelles. However, given the potential for aggregation of ELP_{BC}-RGD4C by aberrant intramolecular disulfide bonds and the lower levels of intracellular uptake with the candidate cell line, we chose to eliminate RGD4C as a targeting candidate and focus the remainder of our studies on the promising EgA1.

4.3.1.2 Qualitative characterization of EgA1-targeted constructs and *pAcF* incorporation with gel electrophoresis

Sodium dodecyl sulfate polyacrylamide gel electrophoresis (SDS-PAGE) of ITC-purified *pAcF*-ELP_{BC}-EgA1 from C321.ΔA and SHuffle T7 Express *E. coli* showed that four cycles of ITC provided proteins with > 95% purity (Figure 55, lanes 1 and 2). We obtained similar purity levels with the control constructs expressed as well (Figure 55, lanes 3, 4, 5).

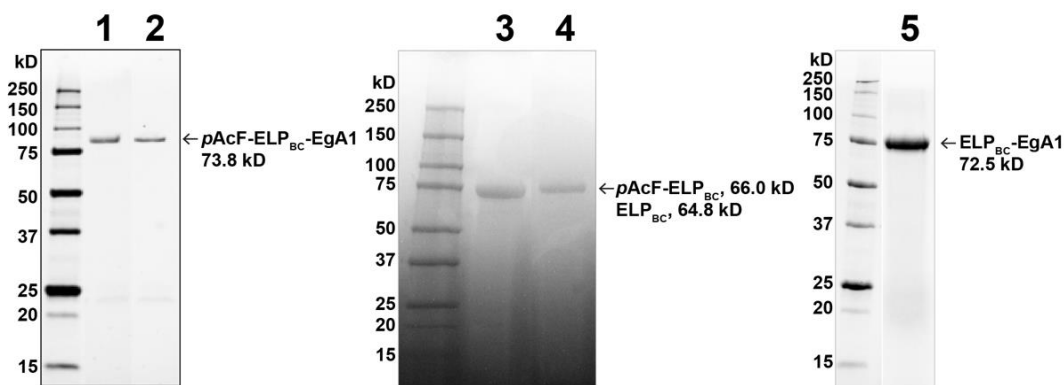


Figure 55: SDS-PAGE of purified constructs for targeted nanoparticle study. 1) *pAcF*-ELP_{BC}-EgA1 expressed in C321.Δ and 2) *pAcF*-ELP_{BC}-EgA1 expressed in SHuffle *E. coli*, both 73.8 kDa; 3) ELP_{BC}, 64.8 kDa; 4) *pAcF*-ELP_{BC}, 73.9 kDa; 5) ELP_{BC}-EgA1, 72.5 kDa.

We investigated the incorporation of *pAcF* with a labeling experiment wherein *pAcF*-ELP_{BC} and *pAcF*-ELP_{BC}-EgA1 were combined with ketone-reactive Alexa697-hydroxylamine dye (Figure 56). Fluorescence imaging of SDS-PAGE of the reaction product qualitatively confirms reactivity of the *pAcF*-ELP_{BC} (lane 1) and *pAcF*-ELP_{BC}-EgA1 (lane 2) with the ketone-reactive dye, and hence indicated the successful incorporation of *pAcF* in these constructs.

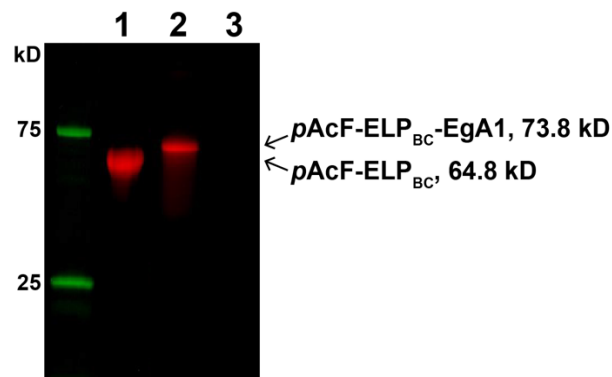


Figure 56: Confirming *pAcF* incorporation with fluorescent SDS-PAGE. The fluorescent hydroxylamine dye labels *pAcF*-ELP_{BC} (lane 1) and *pAcF*-ELP_{BC}-EgA1 (lane 2), but not the negative control ELP_{BC} without *pAcF* incorporated (lane 3).

4.3.1.3 Quantifying *pAcF* incorporation efficiency with MALDI-TOF-MS and ESI-LC/MS

We also confirmed the incorporation of *pAcF* in *pAcF*-ELP_{BC}-EgA1 expressed in the SHuffle and C321.ΔA cell lines by mass spectrometry. The leader peptide containing the *pAcF* residue was cleaved by trypsin and analyzed by matrix assisted laser desorption ionization time-of-flight mass spectrometry (MALDI-TOF-MS). The observed mass of the N-terminal peptide generated by trypsin cleavage of *pAcF*-ELP_{BC}-EgA1 is 1296.73 Da for protein expressed in C321.ΔA.2 and 1296.81 Da expressed in SHuffle *E. coli*, both of which are in excellent agreement with the theoretical mass of 1296.66 Da, confirming the successful incorporation of *pAcF* (Figure 57).

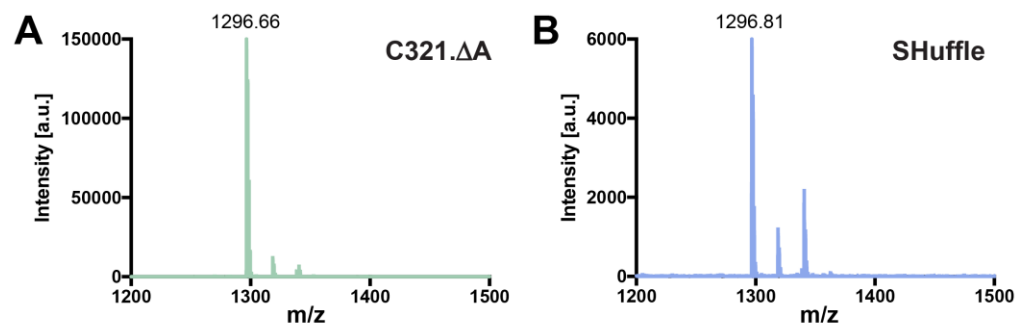


Figure 57: Tryptic digest of *pAcF*-ELP_{BC}-EgA1 followed by MALDI-TOF-MS mass spectrometry in both *E. coli* expression hosts. Both spectra contain a single peak (with sodium adducts) that is consistent with *pAcF* incorporation in *pAcF*-ELP_{BC}-EgA1 expressed in (A) C321.ΔA (1296.73 m/z) and (B) SHuffle *E. coli* (1296.81 m/z).

While we determined that either *E. coli* line would be a suitable expression host for simultaneously encoding *pAcF* and the structured EgA1 nanobody, we selected the C321.ΔA.2 line for *pAcF*-ELP_{BC}-EgA1 expression in all our subsequent experiments as this line provided a modestly greater yield compared to the SHuffle strain (Table 4).

Table 4: Summary of *E. coli* strains, growth conditions, and yield of constructs for drug-loaded, targeted nanoparticle platform.

Construct	<i>E. coli</i> line	Temperature	Yield (mg L ⁻¹)
ELP _{BC}	BL21(DE3)	37°C	160
<i>pAcF</i> -ELP _{BC}	C321.ΔA.2	34°C	30
ELP _{BC} -EgA1	SHuffle T7 Express	30°C / 16°C	50
<i>pAcF</i> -ELP _{BC} -EgA1	C321.ΔA.2	34°C	15
	SHuffle T7 Express	30°C / 16°C	12

We further quantified the incorporation efficiency of *pAcF* with ESI-LC/MS and found > 98% incorporation in both *pAcF*-ELP_{BC} and *pAcF*-ELP_{BC}-EgA1 (Figure 58).

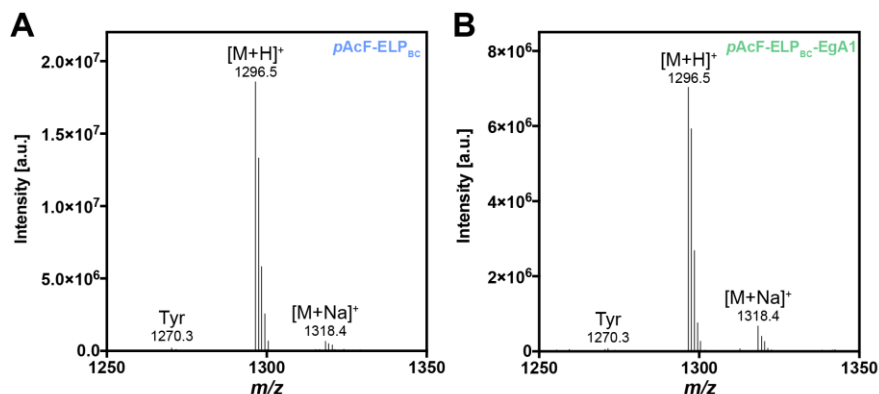


Figure 58: Confirming *pAcF* incorporation into *pAcF-ELP_{BC}* and *pAcF-ELP_{BC}-EgA1* with ESI-LC/MS. Tryptic digests of (A) *pAcF-ELP_{BC}* and (B) *pAcF-ELP_{BC}-EgA1* were analyzed to quantify extent of *pAcF* incorporation as well as identify any misincorporation products with natural residues. Expected molecular weight of *pAcF*-containing peptide is 1296.66 Da. Peptides with Tyr, Trp, and Phe were detected as minor populations, with Tyr representing the primary residue misincorporated in both samples.

While the C321.ΔA.2 line and tRNA/synthetase pair we employed for protein expression have been optimized for greatest incorporation fidelity of *pAcF*, there is a minor population of natural amino acids misincorporated at the *pAcF* site (< 2%, Table 5). The misincorporated residues we detected include the aromatic Tyr, Trp, and Phe, consistent with literature reports for this cell line.^{123, 257-259}

Table 5: Percent composition of *pAcF*-containing constructs by ESI-LC/MS

Construct	Component	% Composition
<i>pAcF-ELP_{BC}</i>	<i>pAcF</i>	98.72
	Tyr	1.17
	Trp	0.11
<i>pAcF-ELP_{BC}-EgA1</i>	<i>pAcF</i>	98.37
	Tyr	0.81

Phe	0.63
Trp	0.16

4.3.2 Quantifying EgA1 binding on a panel of cancer cell lines with flow cytometry

We next validated the specificity of ELP_{BC}-EgA1 for EGFR and confirmed cellular uptake to identify candidate cell lines for *in vitro* testing of our conjugates. We incubated fluorescently labeled ELP_{BC}-EgA1 and ELP_{BC} with a panel of eight cell lines with a range of EGFR expression levels and analyzed the cells for population fluorescence by flow cytometry. In a mouse NIH3T3 fibroblast line transfected with human EGFR (NIH3T3 EGFR+) which abundantly overexpresses EGFR (1.5×10^6 receptors per cell²⁵⁵), ELP_{BC}-EgA1 exhibited 18-fold higher uptake as compared to the non-targeted ELP_{BC} (Figure 59A, D). Two cell lines with a range of reported sensitivity to Dox also exhibited significantly higher uptake as compared to ELP_{BC}.²⁶⁰⁻²⁶¹ These are the squamous carcinoma line A431 (Figure 59B, D), that showed a 13-fold higher uptake as compared to the non-targeted ELP_{BC}, and the ovarian adenocarcinoma line SKOV-3 (Figure 59C, D) that exhibited a 5-fold higher uptake of ELP_{BC}-EgA1 than ELP_{BC}.

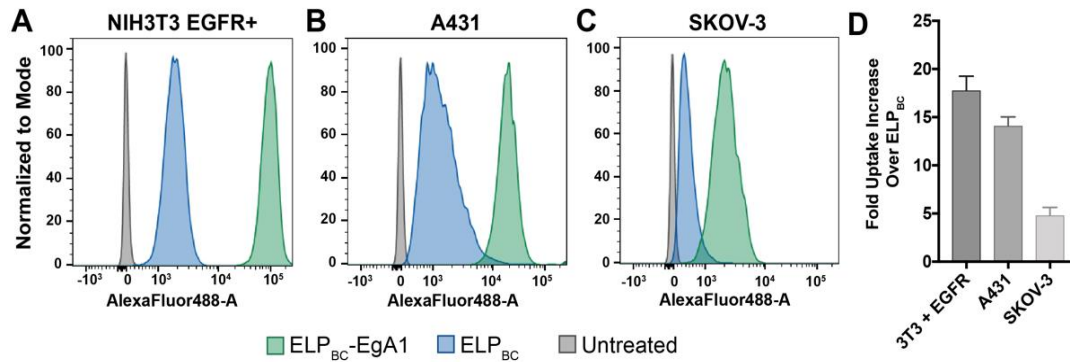


Figure 59: Analysis of fluorescently labeled ELP_{BC}-EgA1 or ELP_{BC} by flow cytometry in EGFR-expressing cell lines. (A) NIH3T3 murine fibroblasts transfected with human EGFR (NIH3T3 EGFR+); (B) A431 squamous carcinoma cells; and (C) SKOV-3 ovarian adenocarcinoma cells all indicate enhanced uptake of the ELP_{BC}-EgA1 as compared to ELP_{BC}. (D) The geometric mean fluorescent intensities (gMFI) of the cell populations were used to quantify the fold uptake of ELP_{BC}-EgA1 over ELP_{BC} and shows the range of nanobody-mediated targeting of EGFR across the cell lines.

Cell lines with a wide range of EGFR expression levels were also assayed (Figure 60A-D,F). Flow cytometry experiments with an untransfected fibroblast cell line (NIH3T3 EGFR-) showed no significant difference between uptake of the targeted and non-targeted constructs, confirming the specificity of the EgA1 nanobody for EGFR (Figure 60E,F).

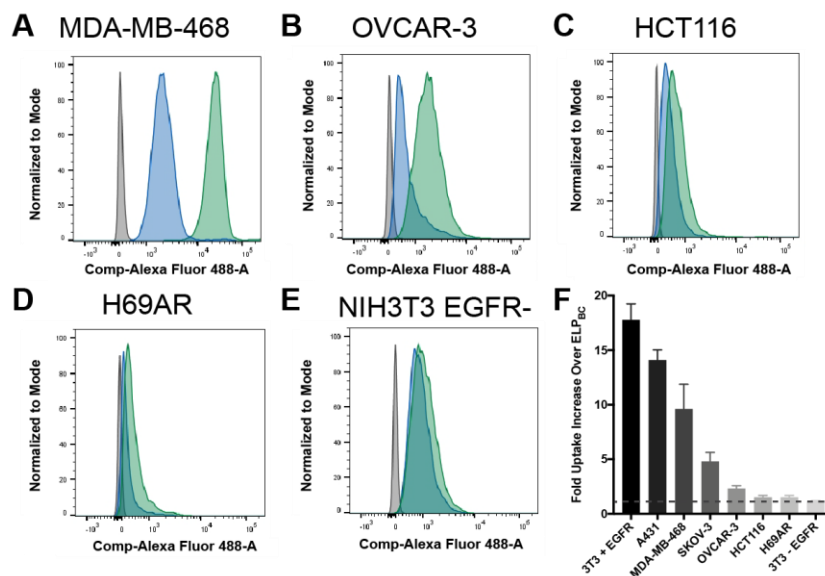


Figure 60: Flow cytometry of fluorescently labeled ELP_{BC}-EgA1 and ELP_{BC} in additional cell lines with diverse EGFR expression levels. (A) MDA-MB-468 mammary carcinoma; (B) OVCAR-3 ovarian carcinoma; (C) HCT116 colorectal carcinoma; (D) H69AR small cell lung cancer; and (E) untransfected murine fibroblasts that do not express human EGFR. (F) Quantified fold uptake increases of ELP_{BC}-EgA1 over ELP_{BC} demonstrate the range of EGFR expression across the panel of cell lines tested as well as lack of non-specific ELP_{BC}-EgA1 uptake in the untransfected fibroblasts. Dotted line indicates equivalent uptake as ELP_{BC} (fold uptake = 1).

Together, the flow cytometry and fluorescence imaging demonstrate that the EgA1 nanobody: (1) maintains specificity for EGFR when fused to ELP_{BC}, (2) enhances intracellular uptake of an ELP_{BC} fusion by cells that overexpress EGFR, and (3) can be used for targeting the ELP_{BC} to a panel of EGFR-overexpressing human cancer cell lines.

4.3.3 Confirming and quantifying extent of Doxorubicin conjugation

We next used the bioorthogonal ketone group on the *p*AcF residue as the site of conjugation for our drug payload, Dox. To conjugate Dox to *p*AcF, we explored three

different potential linkers with the centralized goal of introducing an acid-labile bond between the Dox molecule and linker (structures shown in Figure 61). Linker 1 will result in a pH-sensitive hydrazone bond between Dox and the linker, while linkers 2 and 3 will result in a pH-sensitive oxime bond between Dox and these two moieties. We were interested in evaluating the labeling efficiency of these two chemistries as oxime bonds are reported to be more hydrolytically stable than hydrazone bonds, but with a lower reaction rate for their formation.²⁵³

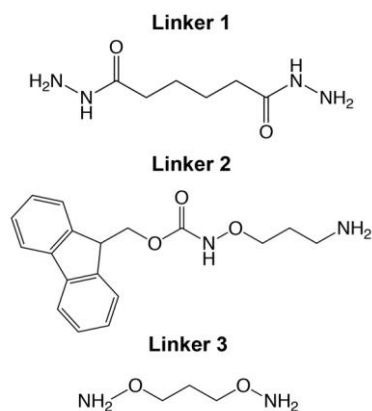


Figure 61: Linker candidates explored for Dox conjugation reactions.

In pilot optimization reactions, we varied length of reaction time (6, 12, 24, 48 h) and temperature of reaction (25, 30, and 37°C) to identify starting conditions for the later comprehensive optimization reactions, which we performed in triplicate (Table 6). From these initial experiments, we determined 24 h is a suitable length of time for reaction and a temperature of 30°C provides enough heat to be kinetically favorable for the reaction to proceed, while ensuring the diblock chains do not self-assemble. In addition to varying the linker type and chemistry, we modified the molar equivalents of linker and

reaction buffer pH to maximize labeling efficiency. While the reaction with *p*AcF-ELP_{BC} proceeds at pH 4.0 with high efficiency, we found the same reaction conditions caused degradation of *p*AcF-ELP_{BC}-EgA1. We found that the presence of a nucleophilic catalyst allowed the reaction to proceed nearly to completion at pH 6.2, a pH that is more optimal for the stability of *p*AcF-ELP_{BC}-EgA1. We evaluated either an aniline²⁶² or *p*-phenylenediamine (*p*-PDE)²⁶³ catalyst, and found 10 mM aniline catalyst provided the highest reaction efficiency for both *p*AcF-ELP_{BC} and *p*AcF-ELP_{BC}-EgA1.

Table 6: Reaction conditions and labeling efficiency of Dox reactions.

Construct	Linker type (Figure 61)	Mol. equiv. linker	pH	Catalyst	% Dox Labeling ^[a]
<i>p</i> AcF-ELP _{BC}	1	10	4.0	--	12.5 ± 0.8
<i>p</i> AcF-ELP _{BC}	2	10	4.0	--	3.2 ± 1.1
<i>p</i> AcF-ELP _{BC}	3	5	4.0	--	40.1 ± 1.7
<i>p</i> AcF-ELP _{BC}	3	10	4.0	--	74.5 ± 1.5
<i>p</i> AcF-ELP _{BC}	3	10	6.2	10 mM <i>p</i> -PDE	62.5 ± 2.5
<i>p</i>AcF-ELP_{BC}	3	10	6.2	10 mM aniline	90.9 ± 5.6
<i>p</i> AcF-ELP _{BC} -EgA1	3	10	4.0	--	Degradation
<i>p</i> AcF-ELP _{BC} -EgA1	3	10	5.2	10 mM aniline	51.6 ± 4.4
<i>p</i>AcF-ELP_{BC}-EgA1	3	10	6.2	10 mM aniline	80.7 ± 6.1
<i>p</i> AcF-ELP _{BC} -EgA1	3	10	7.2	10 mM aniline	18.5 ± 6.6

[a] n ≥ 3; variability reported as standard error of the mean.

Our final optimized reaction, which resulted in > 90% labeling efficiency of *p*AcF-ELP_{BC}, involves a simple two-step reaction scheme (Figure 62). First, we activated *p*AcF in **1** with an excess of the telechelic linker **2**. We removed unreacted linker by centrifugal ultrafiltration and then reacted the intermediate construct **3** with an excess of Dox **4** in the presence of aniline, and subsequently purified the final product **5**.

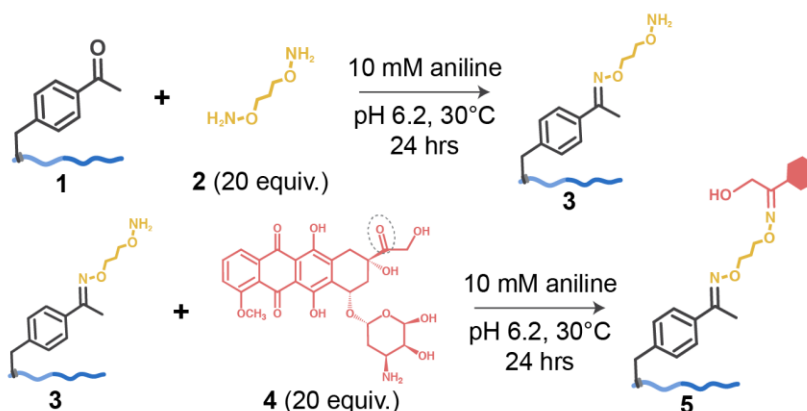


Figure 62: Schematic of the two-step Dox conjugation to *pAcF*. First, *pAcF*-ELP_{BC} 1 is reacted with the hydroxylamine linker 2 in the presence of 10 mM aniline catalyst to form the intermediate 3. This product is purified and reacted with excess doxorubicin 4 under the same conditions to form the final conjugate 5.

4.3.3.1 Confirming successful reaction with size exclusion chromatography

We confirmed the successful reaction and purity of our final reaction product, Dox-*pAcF*-ELP_{BC}-EgA1 using size exclusion chromatography (SEC) and the characteristic absorbance of Dox at 488 nm (Figure 63). The retention time of the peaks in these traces corresponds to that of *pAcF*-ELP_{BC}-EgA1, while the peak has both absorbance at 220 nm, characteristic of peptide bonds, and 488 nm, characteristic of Dox.

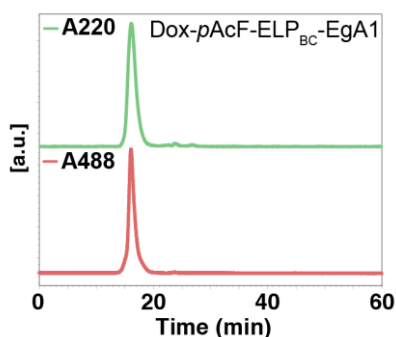


Figure 63: Attachment of Dox to *pAcF*-ELP_{BC}-EgA1 and confirmation of purity of the final conjugate using size exclusion chromatography (SEC). The spectrum trace

at both A220 nm (green) shows the elution time of the conjugate while the trace at A488nm, the characteristic absorbance of Dox, confirms attachment and purity.

We also confirmed the successful reaction and purity of our control reaction product, Dox-*p*AcF-ELP_{BC}, with SEC (Figure 64).

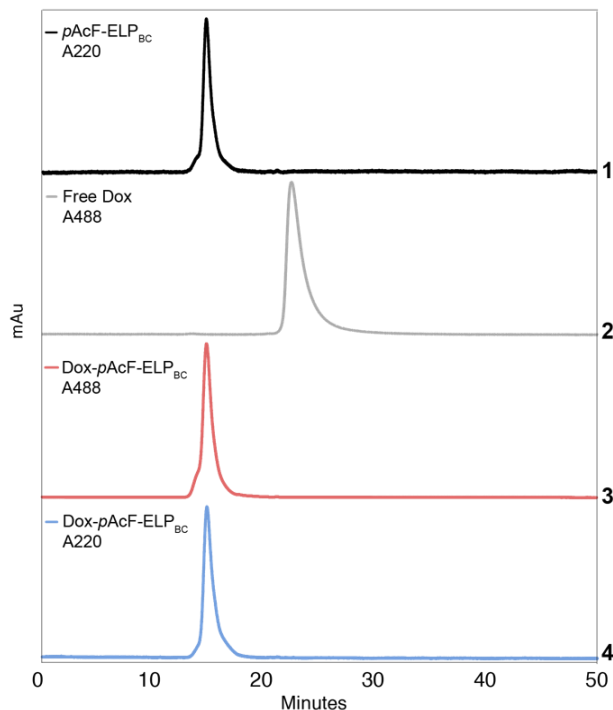


Figure 64: Confirmation of Dox conjugation to Dox-*p*AcF-ELP_{BC} using size exclusion chromatography (SEC). *p*AcF-ELP_{BC} elution at 15.5 min (trace 1, black) is detected by its absorbance at 220 nm. Free Dox is detected by its absorbance at 488 nm and elutes at 23.5 m.

4.3.3.2 Quantifying labeling efficiency with mass spectrometry

We confirmed each individual reaction step by digesting the products 1, 3, and 5 with trypsin and analyzing the digests with MALDI-TOF-MS (Figure 65).

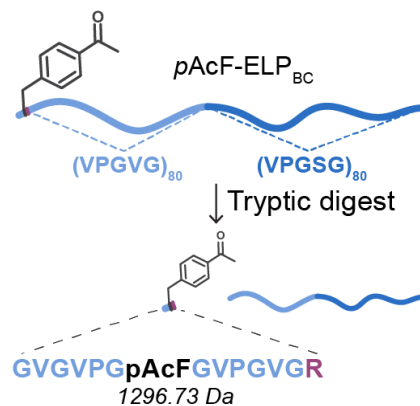


Figure 65: Schematic of tryptic digest of $pAcF-ELP_{BC}$.

The spectra of the liberated peptides showed one major peak for each product which increased in molecular weight by the expected amount after each reaction step (Figure 66).

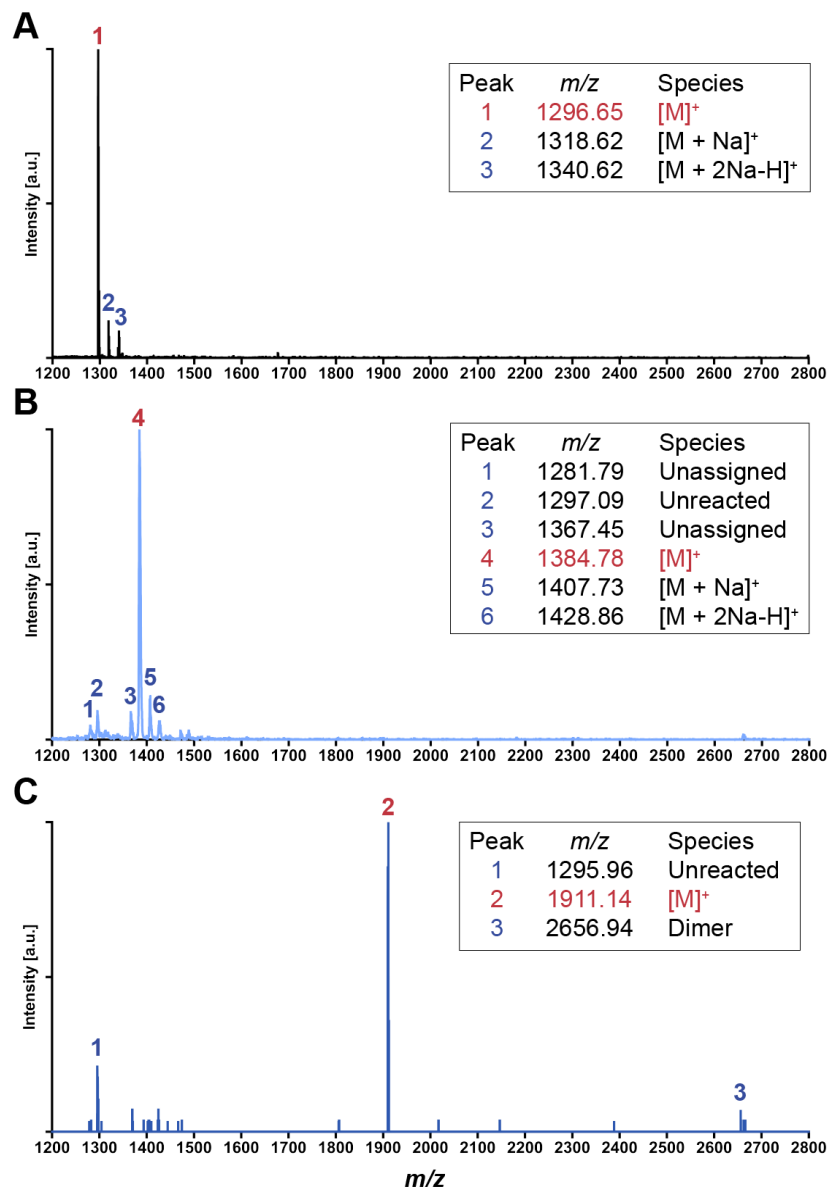


Figure 66: MALDI-TOF-MS spectra of Dox reaction steps following tryptic digest. (A) Starting material, *pAcF-ELP_{BC}*. (B) Intermediate reaction step after addition of linker shows a minor population of unreacted starting material. (C) Final reaction product Dox-*pAcF-ELP_{BC}* shows minor populations of unreacted starting material and dimer between *pAcF*-containing peptides.

We further validated linker and Dox attachment after each reaction step with ESI/LC-MS and analyzed the composition of the reaction products (Figure 67).

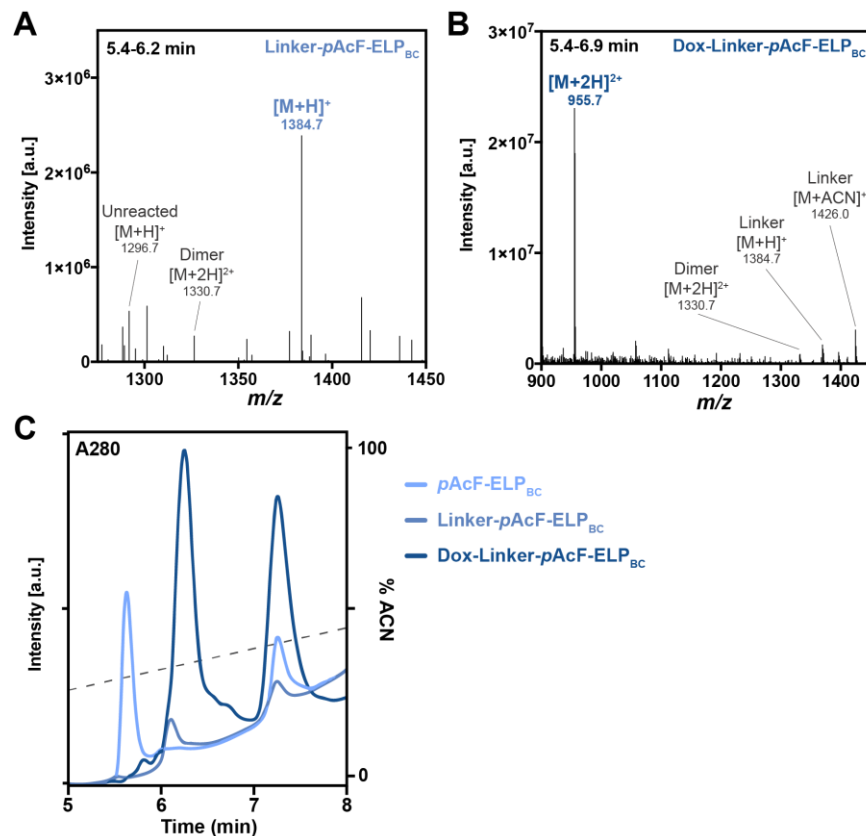


Figure 67: Evaluating efficiency of Dox reaction steps with ESI-LC/MS. Tryptic digests of (A) linker-*pAcF-ELP*_{BC} and (B) Dox-linker-*pAcF-ELP*_{BC} were analyzed to quantify reaction efficiency and identify the composition of the reaction mixture after each reaction step. (C) A280 UV chromatogram of starting material and samples from each reaction step show two peaks: the first peak (elution time 5 - 7 min) corresponds to the digested peptide with retention time increasing with reaction progress. The second peak (elution time 7 - 8 min) corresponds to the remainder of the protein resulting from tryptic digest.

We found each reaction step had > 85% of the desired product and minor populations of starting material and dimer reaction products (Table 7).

Table 7: Percent composition of Dox reaction products.

Construct, reaction step	Component	% Composition
Linker- <i>pAcF</i> -ELP _{BC} Reaction step 1	Linker- <i>pAcF</i> -ELP _{BC}	85.10
	<i>pAcF</i> -ELP _{BC}	5.03
	ELP _{BC} - <i>pAcF</i> -linker- <i>pAcF</i> -ELP _{BC} dimer	9.87
Dox-Linker- <i>pAcF</i> -ELP _{BC} Reaction step 2	Dox-linker- <i>pAcF</i> -ELP _{BC}	93.45
	Linker- <i>pAcF</i> -ELP _{BC}	1.33
	<i>pAcF</i> -ELP _{BC}	0.83
	ELP _{BC} - <i>pAcF</i> -linker- <i>pAcF</i> -ELP _{BC} dimer	4.37

4.3.3.3 pH-mediated release of Doxorubicin from ELP nanoparticles

We validated the mechanism of Dox release — acid-catalyzed oxime hydrolysis— by incubating solutions of Dox-*pAcF*-ELP_{BC}-EgA1 conjugates in either pH 4.0 or pH 7.4 buffer and quantifying the amount of Dox released at various time points with SEC by taking the area-under-the-curve (AUC) of the free Dox peaks (Figure 68). We observed steady-state release of $58.2 \pm 1.4\%$ after incubation for 48 h in pH 4.0 buffer and negligible release at pH 7.4, indicating these micelles will release drug only after receptor-mediated endocytosis into acidic lysosomal compartments.

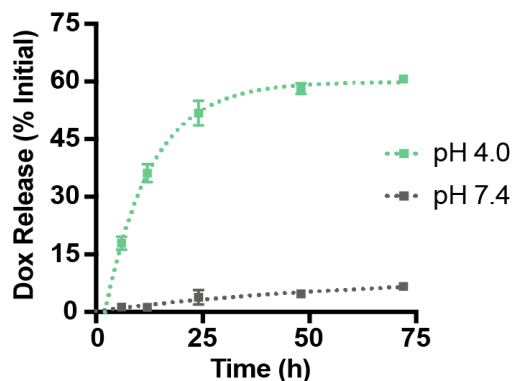


Figure 68: pH-mediated release of Dox from Dox-*pAcF*-ELP_{BC}-EgA1. Solutions of Dox-*pAcF*-ELP_{BC}-EgA1 were incubated at either pH 4.0 (green) or pH 7.4 (grey) and the amount of Dox released assessed at various time points by size exclusion chromatography.

4.3.4 Biophysical characterization of Doxorubicin conjugates

4.3.4.1 Dynamic light scattering of Doxorubicin conjugates

We used dynamic light scattering (DLS), performed in dilute solution as a function of temperature, to identify the critical micellization temperature (CMT) of both *pAcF*-ELP_{BC}-EgA1 and *pAcF*-ELP_{BC}. We found the CMT for both constructs to be approximately 32°C and unchanged upon conjugation of Dox (Figure 69A). The Dox-*pAcF*-ELP_{BC}-EgA1 construct assembles into monodisperse nanoparticles with a hydrodynamic radius (R_h) of 44.7 ± 4.4 nm while the Dox-*pAcF*-ELP_{BC} construct forms smaller particles with a R_h of 23.7 ± 0.9 nm (Figure 69B).

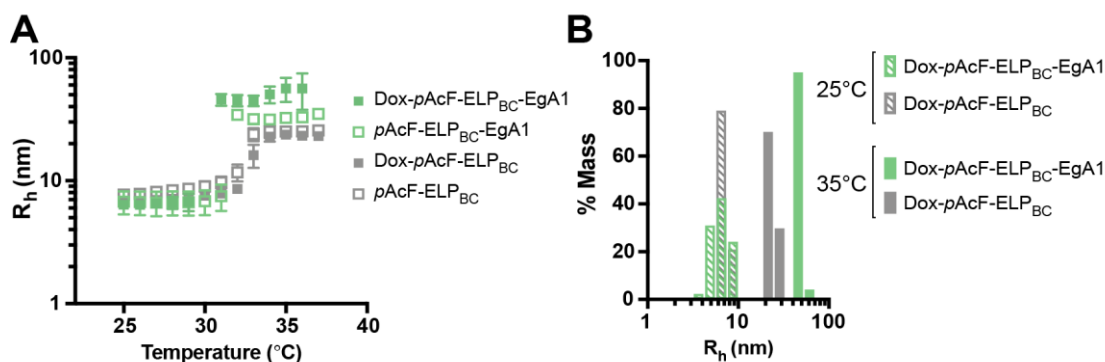


Figure 69: Characterization of Dox-*pAcF-ELP*_{BC}-EgA1 self-assembly by dynamic light scattering. (A) The hydrodynamic radius (R_h) as a function of temperature for *pAcF-ELP*_{BC}-EgA1 (green) and *pAcF-ELP*_{BC} (grey) before and after Dox conjugation. (B) The polydispersity of the samples by % mass at temperatures below (25°C, unimers) and above (35°C, micelles) the critical micellization temperature (CMT).

A dilution series of Dox-*pAcF-ELP*_{BC}-EgA1 analyzed by DLS revealed the critical micellization concentration (CMC) to be between 1 and 5 μM , consistent with findings for other *ELP*_{BC} nanoparticles (Figure 70).²²⁴

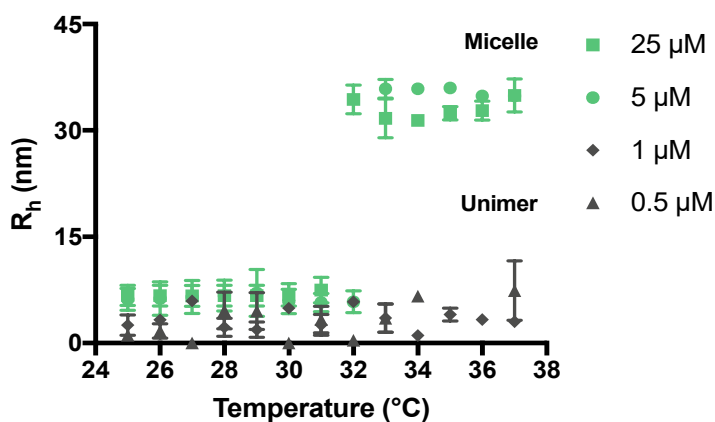


Figure 70: Approximating critical micellization concentration (CMC) of Dox-*pAcF-ELP*_{BC}-EgA1 by analyzing dilution series with dynamic light scattering. Two samples with concentrations above the CMC (green; 25 μM and 5 μM) self-assemble into micelles above the critical micellization temperature (CMT), approximately 32°C.

In contrast, the samples with concentrations below the CMC (grey; 1 μ M and 0.5 μ M) remain as unimers throughout the temperature ramp.

4.3.4.2 Static light scattering of Doxorubicin conjugates

Static light scattering (SLS) performed above the CMT of both of the Dox conjugates, at 35°C revealed the Dox-*p*AcF-ELP_{BC}-EgA1 particles to contain approximately 22 chains per particle while the Dox-*p*AcF-ELP_{BC} particles contain approximately 28 chains per particle (Table 8, Figure 71). The positively charged EgA1 nanobody (pI 9.08) likely increases Dox-*p*AcF-ELP_{BC}-EgA1 particle size while reducing the N_{agg} by charge repulsion as compared to Dox-*p*AcF-ELP_{BC}. The SLS data collection and analysis was performed by my co-worker, Michael Dzuricky. Together with the Dox conjugation efficiency, these data indicate each EgA1-targeted nanoparticle is loaded with 17-18 Dox molecules.

Table 8: Static light scattering of Dox conjugates.

	$R_g^{[a]}$ (nm)	$R_h^{[b]}$ (nm)	$\rho^{[c]}$	$MW_{micelle}$ (g mol ⁻¹)	$N_{agg}^{[d]}$
Dox- <i>p</i> AcF-ELP _{BC}	20.3	18.4	1.1	1.85×10^6	27.8
Dox- <i>p</i> AcF-ELP _{BC} -EgA1	37.2	41.8	0.9	1.63×10^6	21.8

[a] R_g , radius of gyration; [b] R_h , hydrodynamic radius; [c] ρ , form factor; [d] N_{agg} , number of chains per micelle

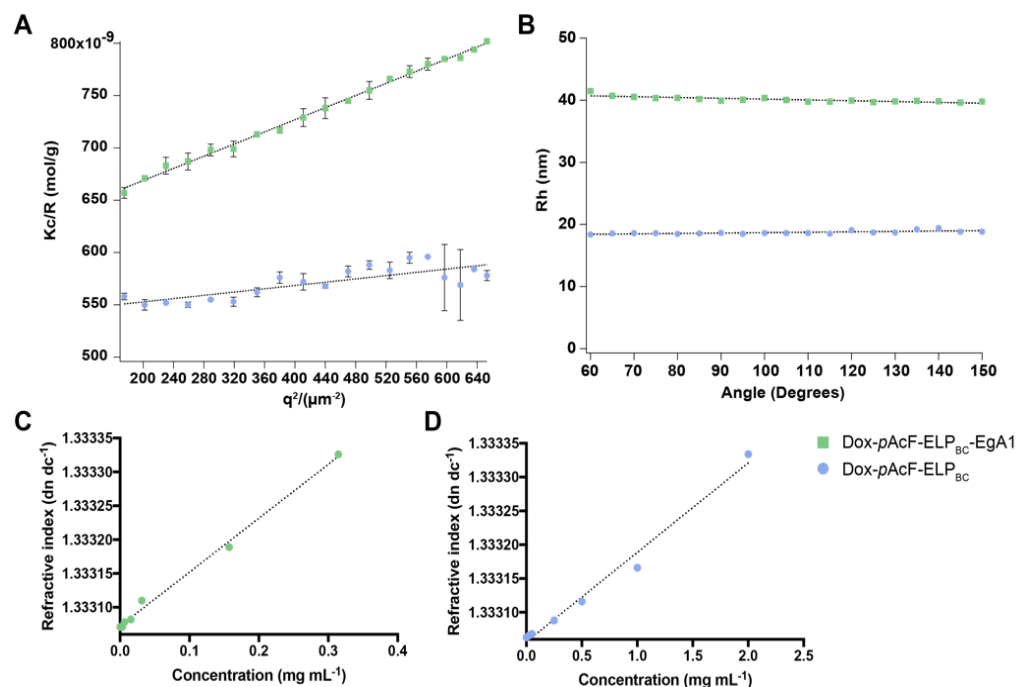


Figure 71: Static light scattering characterization of Dox conjugates. (A) Partial Zimm plot of Dox-pAcF-ELP_{BC}-EgA1 (green) and Dox-pAcF-ELP_{BC} (blue) with dashed lines showing best linear fit and error bars represent the standard deviation (n = 5 measurements). (B) Dynamic light scattering analysis of hydrodynamic radius as a function of scattering angle of Dox-pAcF-ELP_{BC}-EgA1 (green) and Dox-pAcF-ELP_{BC} (blue). Refractive index of (C) Dox-pAcF-ELP_{BC}-EgA1 and (D) Dox-pAcF-ELP_{BC} as a function of concentration. All data was collected at 35°C.

4.3.4.3 Cryo-transmission electron microscopy imaging of Doxorubicin conjugates

We visualized both particles with cryo-TEM to further confirm their spherical shape and size; this imaging and analysis was performed by my co-worker, Michael Dzuricky (Figure 72).

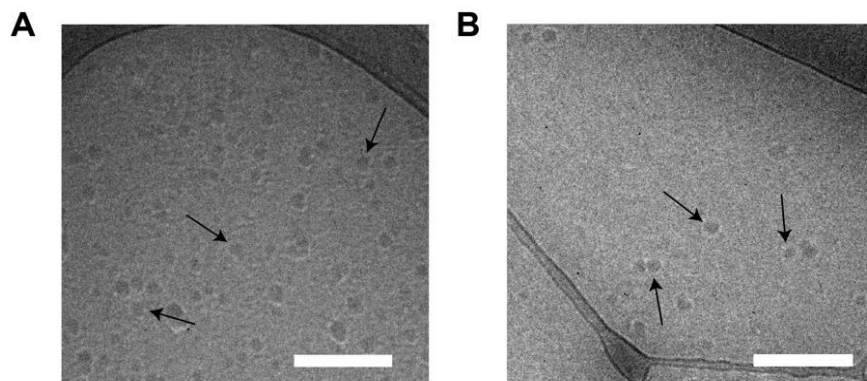


Figure 72: Visualization of Dox-*pAcF*-ELP_{BC}-EgA1 and Dox-*pAcF*-ELP_{BC} micelles by cryogenic transmission electron microscopy (cryo-TEM). (A) Dox-*pAcF*-ELP_{BC}-EgA1 and (B) Dox-*pAcF*-ELP_{BC}. Scale bars, 200 nm.

Core-sizing analysis of these particles indicated roughly equivalent core diameters of 24.7 ± 4.4 nm for the Dox-*pAcF*-ELP_{BC} particles and 29.4 ± 6.2 nm for the Dox-*pAcF*-ELP_{BC}-EgA1 nanoparticles. This further indicates the increased size of the Dox-*pAcF*-ELP_{BC}-EgA1 particles is due to size differences in the corona, where the EgA1 nanobody is presented. These studies confirm that the Dox-loaded particles are spherical, stable above their CMT at physiological temperature (37°C), and in the ideal sub-100 nm size range for tumor penetration, making them suitable for the delivery of drugs to solid tumors.¹¹

4.3.5 *In vitro* characterization of Doxorubicin conjugate cytotoxicity

We next evaluated the cytotoxicity of the Dox-*pAcF*-ELP_{BC}-EgA1 and Dox-*pAcF*-ELP_{BC} particles in two EGFR positive cell lines, A431 and SKOV-3.²⁶⁴⁻²⁶⁵ We chose these two tumor lines as they express different level of the EGFR, with A431 expressing higher levels of EGFR than SKOV-3. Examining the response of tumor cells that have different

levels of receptor expression is critical to demonstrate the clinical utility of our platform, as EGFR expression level varies widely between cancer types,²⁶⁶ within individual tumors,²⁶⁷ and at different time points of treatment.²⁶⁸ These two cell lines also differ in their relative sensitivity to Dox, with the A431 line being more sensitive than SKOV-3. After treatment with increasing concentrations of free drug and assessing cell viability, we determined the IC₅₀ of Dox in A431 cells is 1.38 μM while that of SKOV-3 cells is 31.8 μM (Figure 73A, B). While A431 represents the ideal tumor for targeted drug treatment as it is a highly receptor-positive, drug-sensitive line, SKOV-3 represents a more clinically relevant subset of tumor cells — those with intermediate receptor expression and a lower sensitivity to Dox.²⁶¹

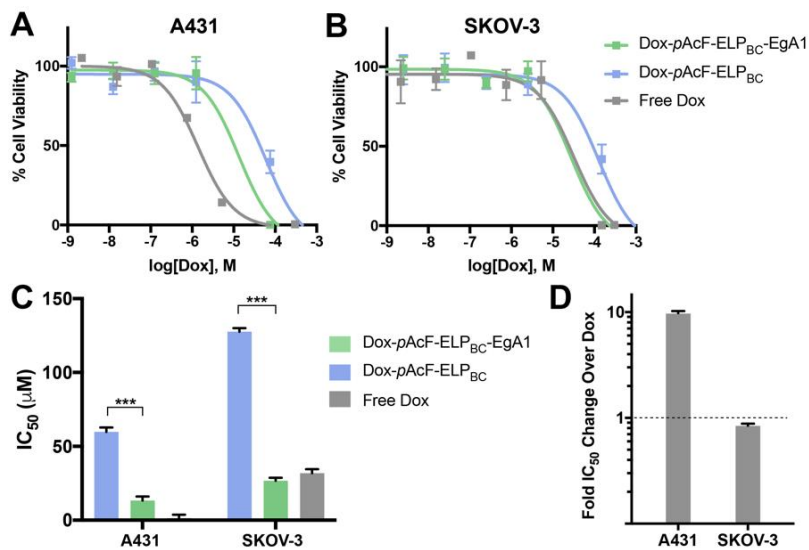


Figure 73: EgA1-targeted Dox-pAcF-ELP_{BC}-EgA1 is significantly more potent in cancer cells. Cytotoxicity of Dox-pAcF-ELP_{BC}-EgA1 (green), Dox-pAcF-ELP_{BC} (blue), and free Dox (grey) in (A) A431 and (B) SKOV-3 cells. (C) The IC₅₀ values of these cell viability assays confirms the targeted Dox-pAcF-ELP_{BC}-EgA1 is more cytotoxic than the non-targeted control, Dox-pAcF-ELP_{BC}. p < 0.001. (D) Normalized IC₅₀ of Dox-

***p*AcF-ELP_{BC}-EgA1 to IC₅₀ of free Dox indicates the effect of active targeting on the cytotoxicity of Dox.**

We treated the two cell lines with increasing concentrations of the targeted and non-targeted Dox conjugates and measured cell viability after treatment. In both cell lines, the Dox-*p*AcF-ELP_{BC}-EgA1 particles have significantly lower IC₅₀ values than the non-targeted control Dox-*p*AcF-ELP_{BC} particles, confirming the therapeutic utility of the targeting domain in an *in vitro* setting (Figure 73C). We further analyzed the data by normalizing the IC₅₀ values of the targeted Dox-*p*AcF-ELP_{BC}-EgA1 to that of free Dox, as it illustrates the effect of targeting on treatment efficacy (Figure 73D). Importantly, in the SKOV-3 line with lower Dox sensitivity, the presence of the targeting domain drives the IC₅₀ to be better than that of free drug (normalized value 0.84), strongly highlighting the ability of this targeting domain to enhance the cytotoxicity of Dox. Because the A431 line is already highly sensitive to free drug, it is therefore difficult to affect the cytotoxic threshold, and we observe a modest increase in IC₅₀ of the targeted therapy as compared to free Dox. Nevertheless, in both cell lines, the decrease in IC₅₀ over an order of magnitude with the targeted as compared to non-targeted control indicates a significant widening of the therapeutic window. This attribute of the targeted construct, along with the potential benefits of delivering a drug in a nanoparticle formulation *in vivo* — improved pharmacokinetics and tumor accumulation — is likely to far outweigh the observed higher *in vitro* cytotoxicity of free drug.¹⁰ The fusions without attached Dox

exhibited no cytotoxicity, indicating that neither EgA1 nor the ELP contributed to cytotoxicity observed for the Dox-conjugated constructs (Figure 74).

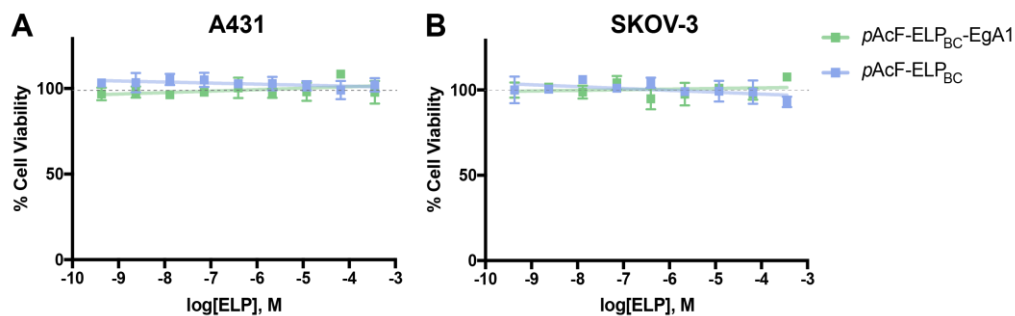


Figure 74: Control cell viability assays for Dox conjugates. *pAcF-ELP_{BC}* (blue) and *pAcF-ELP_{BC}-EgA1* (green) are not cytotoxic in (A) A431 and (B) SKOV-3 cells. The concentrations of ELP assayed correspond to the concentrations of these constructs in the Dox conjugates tested.

4.3.6 Intracellular localization of EgA1-targeted constructs

4.3.6.1 Confirming EgA1 specificity for EGFR by EGF competition

We confirmed the specificity of EgA1 for EGFR by pre-incubating cells with excess, fluorescently-labeled EGF – the ligand for EGFR – followed by Alexa647-ELP_{BC}-EgA1. We observed simultaneously high levels of intracellular EGF and little Alexa647-ELP_{BC}-EgA1, whereas uptake of Alexa647-ELP_{BC}-EgA1 was significant in a control experiment in which cells were not preincubated with EGF (Figure 75). These data indicate the method of uptake for EgA1-targeted nanoparticles is by EGFR-mediated endocytosis, positioning these carriers to traffic through the endolysosomal pathway upon cellular entry.

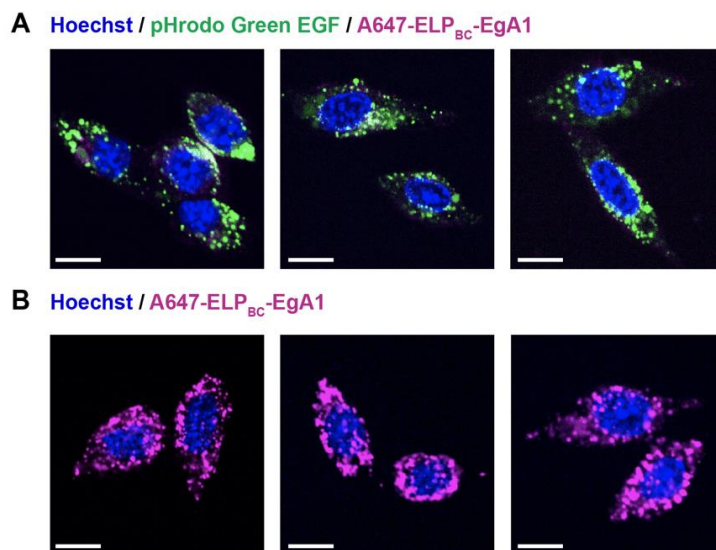


Figure 75: Confirming EGFR specificity of EgA1 nanobody by EGF competitive uptake assay. NIH 3T3 murine fibroblasts transfected with human EGFR were (A) pre-incubated with excess fluorescently labeled pHrodo Green EGF, followed by AlexaFluor647-ELP_{BC}-EgA1 or (B) treated with AlexaFluor647-ELP_{BC}-EgA1 alone. Hoechst stains cell nuclei in both panels. Scale bars 20 μm .

4.3.6.2 Colocalization of Doxorubicin conjugates and endolysosomes

To investigate the subcellular trafficking of these particles after uptake, we imaged the Dox-loaded particles using spinning-disk confocal microscopy in the A431 cell line. We incubated adherent A431 cells with Dox-*pAcF*-ELP_{BC}-EgA1 and Dox-*pAcF*-ELP_{BC} for 4 h (Figure 76A) and 24 h (Figure 76B). We then imaged colocalization of Dox with endolysosomes by staining cells with a lysosomal tracking dye — CytoPainter LysoDeep Red — that selectively accumulates and fluoresces in the acidic late endosomal and lysosomal compartments (pH 4.5-4.8). In these cells, we found significantly greater intracellular accumulation of Dox delivered by Dox-*pAcF*-ELP_{BC}-EgA1 compared to

Dox-*p*AcF-ELP_{BC}. We also found significant colocalization of Dox and Cytopainter at both 4 h and 24 h of incubation when Dox was delivered via EgA1 targeting.

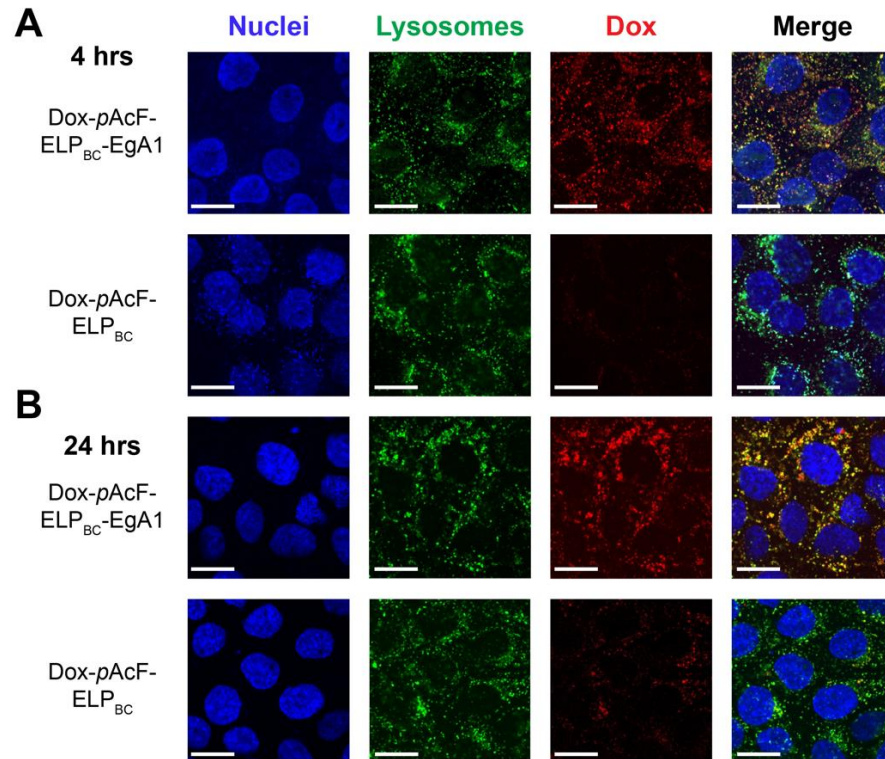


Figure 76: Spinning disk confocal imaging of A431 cells incubated with Dox-*p*AcF-ELP_{BC}-EgA1 or Dox-*p*AcF-ELP_{BC}. Samples were incubated for (A) 4 hours or (B) 24 hours. Hoechst (blue) staining shows nuclei, CytoPainter (green) indicates low pH endolysosomal compartments, and Dox (red) shows subcellular localization of Dox conjugates. Merged images show colocalization (yellow) between lysosomes and Dox. Scale bars 20 μ m.

We evaluated the degree of colocalization with Pearson's R coefficient. This metric is a measure of the linear correlation between two variables — herein the fluorescence intensities for Dox and Cytopainter at each pixel location in the confocal images. R = 1.0 indicates a perfect linear relationship and hence exact colocalization of the drug with endolysosomes, and R = -1.0 indicates a negative linear correlation between

the two variables, and in this context indicates a complete lack of colocalization of Dox with endolysosomes (Figure 77A).²⁶⁹⁻²⁷⁰ The Dox-*p*AcF-ELP_{BC}-EgA1 samples increased in endolysosomal colocalization from R = 0.66 to R = 0.76 from 4 h to 24 h incubation. Conversely, the non-targeted control Dox-*p*AcF-ELP_{BC} had R < 0.5 at both time points, indicating little colocalization and suggesting a longer time required for uptake of these particles, which results in the lower efficacy observed in the *in vitro* cytotoxicity studies. We also confirmed the intensity of lysosomal dye was similar between all four regions of interest analyzed to ensure that the observed differences in colocalization were not due to a different number of, or intensity of, lysosomes analyzed in the different images (Figure 77B).

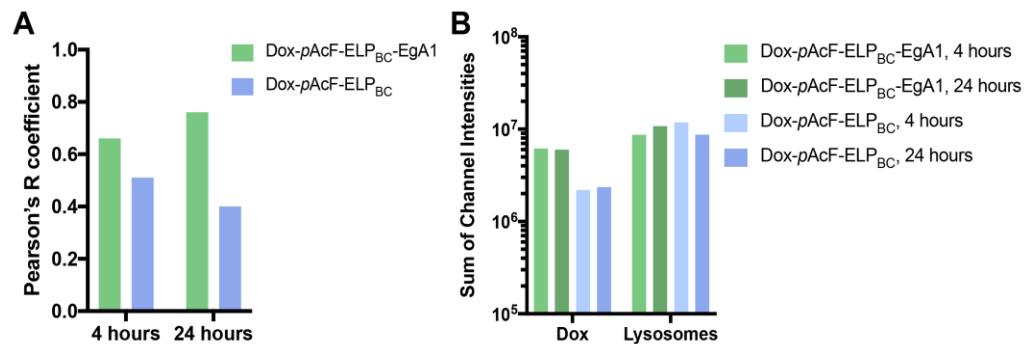


Figure 77: Quantifying colocalization of Dox conjugates and endolysosomal compartments. (A) Pearson's R coefficient for colocalization of areas analyzed in Figure 76 show higher levels of colocalization between Dox and lysosomes for Dox-*p*AcF-ELP_{BC}-EgA1 at both 4 and 24 h times points as compared to Dox-*p*AcF-ELP_{BC}. (B) Sum of channel intensities for Dox and lysosomes for images analyzed for colocalization to ensure lysosomal channel intensity is similar between images analyzed and does not account for the differences in colocalization observed.

These colocalization analyses revealed both 1) greater levels of and 2) a time-dependent increase in endolysosomal colocalization with Dox-*p*AcF-ELP_{BC}-EgA1 as compared to the non-targeted Dox-*p*AcF-ELP_{BC}. This demonstrates that the receptor-mediated endocytosis of the EgA1-containing construct concurrently promotes both more rapid entry into the cell and pH-mediated drug release. Taken together, these *in vitro* experiments validate that the active targeting of Dox-*p*AcF-ELP_{BC}-EgA1 directly translates into the exceptional tumor cytotoxicity of this construct.

4.4 Conclusions and future directions

4.4.1 Summary and significance

The platform we have developed combines a bioorthogonal reactive group with high-affinity targeting in a single protein-based particle and has three distinct advantages over existing approaches: (1) our biopolymer vehicles are monodisperse, non-toxic nanoparticles, synthesized with starting materials that are easily produced recombinantly by overexpression in *E. coli* and purified at high yield via its LCST phase behavior; (2) the location of drug-loading is precisely specified, and the orthogonal UAA-mediated drug conjugation chemistry permits the inclusion of the cysteine-containing targeting domain into the construct; (3) the EgA1 nanobody delivers the targeted drug-loaded nanoparticles to EGFR-positive cancer cells via receptor-mediated endocytosis.²⁷¹⁻²⁷² While previous approaches to cancer nanotherapeutics have directed targeting of nanoparticles with scaffold proteins,^{230, 273} utilized UAAs for biorthogonal

drug attachment,²⁷⁴⁻²⁷⁶ and formulated biopolymer nanoparticles as small molecule drug carriers,²⁷⁷⁻²⁷⁸ ours is the first to combine these three elements into one powerful therapeutic platform (Figure 78).

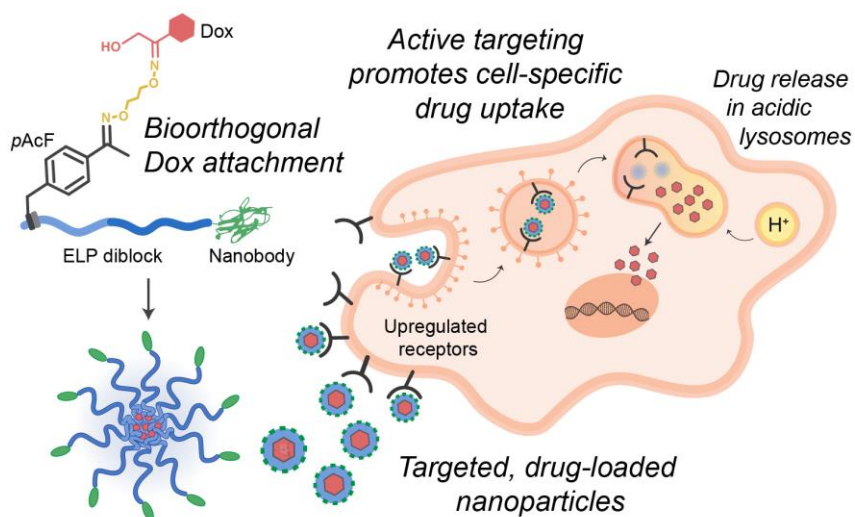


Figure 78: Universal platform for orthogonal drug loading and active targeting of ELP nanoparticles.

Our platform maintains site-specificity of drug attachment against the complex chemical background of proteins that have a distribution of reactive amino acids. The use of an unnatural amino acid as the site of drug attachment allows for the incorporation of a nanobody as the targeting element, which requires a disulfide bond for its stability. The platform described herein reveals a promising strategy for simultaneously genetically encoding both a drug conjugation site and structured bioactive domain into a biopolymer-based nanoparticle, an approach previously inaccessible with existing techniques.

The work described in this chapter directly contributes to the overall goal of this thesis work to identify and solidify novel strategies for bioorthogonal modification of ELP-based platforms. The specific chemistries we optimized can be extended for use in other applications, and importantly, we established a precedent for integrating bioorthogonal chemistries into a functional therapeutic system. This study is the first example of using molecular engineering to deftly decouple drug reactivity from any polypeptide or protein of interest.

4.4.2 Future perspectives

As researchers across disciplines develop novel drugs, advanced targeting moieties, and next-generation polypeptide and protein vehicles, we will increasingly rely on adaptable, universal carrier platforms in order to facilitate drug delivery. We anticipate future work will validate the efficacy of these carriers in a range of tumor models *in vivo* to elucidate the full therapeutic potential of our multifunctional targeted, drug-loaded biopolymer nanoparticles. The strategy we have described herein lays the foundation for this exciting future work. In addition, our highly tunable system can be modified and expanded upon to incorporate a variety of cytotoxic drugs or active targeting domains.

There are a wide variety of targeting proteins and domains available to substitute with the EgA1 nanobody, many of which we identified after applying our design criteria to the available literature. EgA1 may be easily substituted with an

alternative nanobody; there are dozens of these scaffold domains reported for applications in oncology, imaging, diagnostics, infection, and autoimmune diseases, and several of these currently in clinical trials.²⁷⁹ Other targeting and bioactive moieties that could feasibly be substituted into this platform include fibronectin domains,²⁸⁰ knottin-derived peptides,²⁸¹ cytokines,²⁸² and antibody fragments.²⁸³

The conjugated cargo in our system, a cytotoxic chemotherapeutic, may also be easily substituted for other small molecules, including drugs and imaging probes. Drugs with an available ketone will be most easily substituted, such as unoprostone, nabumetone, or aminoxy-modified auristatins. Additional payloads may be explored through the introduction of alternative linker chemistries.

While the linkers we explored resulted in a pH-sensitive bond between our nanoparticles and cargo, introducing a non-cleavable linker can expand the utility of this system further. Similarly, heterobifunctional linkers with an aminoxy group for attachment to *pAcF* and a unique R-group bioorthogonal to both the ketone and natural residues (such as those depicted in Figure 79) can be used to attach cargo with an even greater degree of orthogonality. Beyond cargo loading, the reactive ketone in *pAcF* could also be used for pH-responsive core-crosslinking of targeted or otherwise cytotoxic ELP nanoparticles containing multiple *pAcF* residues.

While the ketone in *pAcF* is a highly versatile reactive group, our genetically encoded system provides the ease of substituting the UAA residue incorporated while

5. Developing a novel immunotoxin formulation for treatment of brain tumors

5.1 Introduction and motivation

We have invested our effort thus far in the development of ELP particles for direct application in therapeutic systems or to provide the framework for future biomaterials studies. ELPs are exquisitely versatile biopolymers that can be easily prepared in different formulations, ranging from particles to macroscale coacervates with programmable release kinetics. The sequence-behavior relationship of ELPs has been extensively studied, empowering us to rationally engineer ELP-based platforms *de novo* for yet unexplored applications, such as glioblastoma multiforme (GBM).

GBM is the most advanced, aggressive, and commonly diagnosed form of brain cancer with a poor survival prognosis of less than a year.²⁸⁵⁻²⁸⁶ GBM tumors are unique from other solid tumors in that the site of recurrence is typically within 2 cm of the initial lesion; metastasis outside of the brain is rare.²⁸⁷ This distinctively confined disease state, while nonetheless complex and challenging to treat, motivated the design and development of our intratumoral, sustained-release therapeutic platform for GBM. A critical barrier to progress in this field has been the inability to deliver and maintain a high, local concentration of powerful drugs, especially biologics.²⁸⁸⁻²⁹³ Biologics are orders of magnitude more potent than small molecule drugs and can be tailored for tumor-specific markers, sparing healthy tissue.²⁹⁴ ELPs provide the ideal biopolymer for

building this delivery platform as they can be recombinantly fused to these protein drugs, such as immunotoxins.

There are two current solutions for local, extended drug administration in the brain. A catheter pump can be inserted into the tumor, with drug infusion taking place over hours to days for convection enhanced delivery.²⁹⁵ This method is burdensome for patients and can result in inconsistent administration or catheter leakage.²⁹⁶ An alternative approach is the implantable Gliadel® wafer, a small disc of copolymer matrix which slowly dissolves and continuously releases the embedded small molecule drug into the resection cavity over time.²⁹⁷ This therapy is restricted to carmustine, a drug with limited effectiveness that is not curative as a single agent and has been associated with adverse events such as seizures, infection, and cerebral edema.²⁹⁸⁻³⁰¹ Furthermore, these wafers are comprised of a synthetic polymer, which limits the potential for incorporation of targeted biologic drugs such as immunotoxins. Thus, there is an urgent clinical demand for treatments that can maintain high local concentrations of powerful drugs, such as immunotoxins.

5.1.1 Immunotoxins

Immunotoxins are protein drugs comprised of a targeting domain linked to a bacterial toxin. The targeting domain, which can range from a full-length monoclonal antibody to an antibody fragment to a scaffold domain, directs the toxic payload for

endocytic uptake into cancer cells. The toxin can be derived from bacterial, insect, or plant toxins, which comprise the most lethal class of molecules known. (Figure 80)

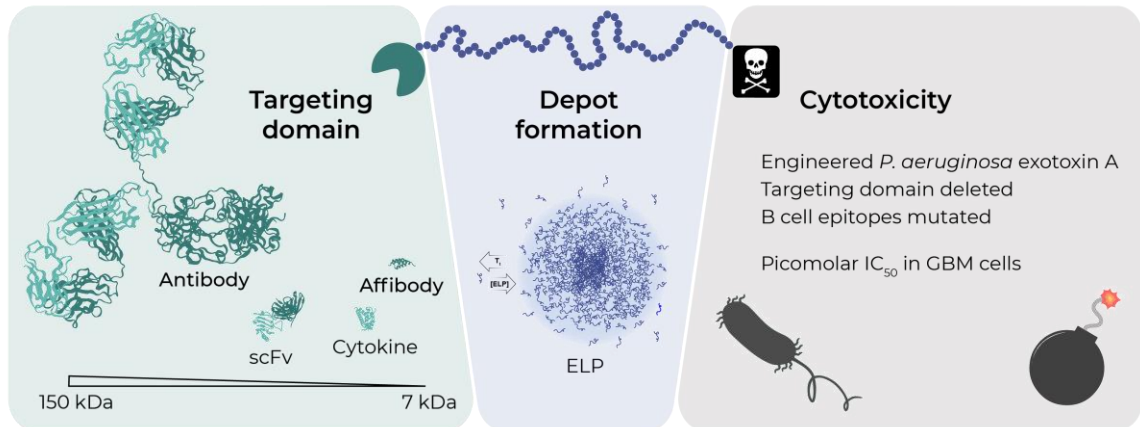


Figure 80: Components of an immunotoxin-ELP fusion.

We have investigated two possible targeting ligands for our immunotoxin: a monoclonal antibody and an affibody domain. Both of these are specific for two receptors upregulated in GBM. Epidermal growth factor receptor (EGFR) is found in undetectable levels in healthy brain and is overexpressed in GBM.³⁰²⁻³⁰³ EGFR is the most frequently amplified gene in GBM, the extent to which defines this cancer's subtype.³⁰⁴ The second target is a constitutively active variant of EGFR, EGFRvIII, which is also overexpressed in GBM.³⁰⁵ EGFRvIII is a deletion mutant with a distinct epitope from EGFR expressed in approximately 70% of GBM tumors with concurrent EGFR amplification.³⁰⁶ Critical for the success of immunotoxin therapy, both of the targeting domains selected have been previously confirmed to be internalized following receptor binding.³⁰⁷⁻³⁰⁸

The toxin we have selected is derived from the bacterial *P. aeruginosa* exotoxin A. Bacterial toxins kill cells at picomolar concentrations, regardless of cell cycle status, in a manner orthogonal to small molecule chemotherapeutics by inhibiting protein translation.²⁹⁴ This specific toxin potently inhibits protein translation by ADP-ribosylating and inactivating elongation factor-2; a single molecule is enough to kill an entire target cell.^{290, 309-311} One of the classic hallmarks of cancer cells is their ability to resist pro-apoptotic, genotoxic signals by aberrantly modulating anti-apoptotic pathways, which immunotoxins effectively circumvent by directly disrupting protein translation.³¹²⁻³¹⁴ The variant we employ in our system has been engineered to remove its natural targeting domain as well as B- and T-cell epitopes for both mice and humans.³¹⁵⁻³¹⁶ Truncated toxins are non-toxic without the addition of an exogenous targeting domain, which allows us to tailor the specificity of these lethal proteins through fusion to a targeting ligand.

Combining an immunotoxin with an ELP has not been previously explored and necessitated thorough optimization and strategy adaptation. We designed a variety of schemes to produce an immunotoxin-ELP fusion through both protein conjugation and genetic fusion and these are described in detail in Sections 5.1.3 and 5.3.1. The ultimate goal of this work, irrespective of synthesis strategy, is to endow an immunotoxin with the unique phase transition behavior of ELPs to enable sustained-release delivery.

5.1.2 Sustained-release formulations with ELPs

A notable feature of ELPs is their phase behavior, which enables them to transition from a soluble state to an aqueous immiscible coacervate following an increase in temperature.³¹⁷ The thermal responsiveness of an ELP is retained when fused to a peptide or protein, making these non-toxic peptide polymers an attractive platform for drug delivery applications.^{254, 318} By manipulating the transition temperature (T_t) at which they coacervate, an ELP-drug fusion can be designed such that body heat alone triggers the phase transition, thereby creating an injectable depot from which soluble fusion molecules are released into circulation at a steady rate (Figure 81A).^{73, 88}

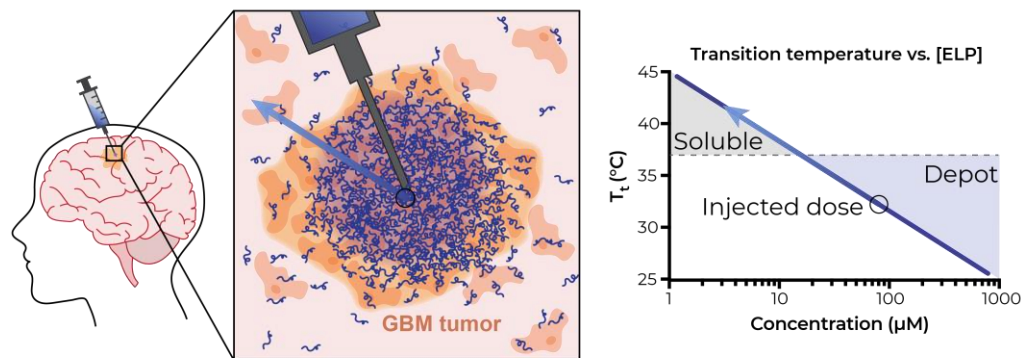


Figure 81: Sustained-release immunotoxin platform for treatment of GBM. (A) Intratumoral injection of soluble ELP-immunotoxin will result in formation of a gel-like drug depot that will slowly release drug unimers over time. (B) Principle of diffusion-driven ELP depot release, illustrated with the inverse-log relationship between ELP concentration and transition temperature, T_t .

The sustained release is a product of the inverse-log relationship between the T_t and concentration.⁸⁷ As the perimeter of the depot is diluted by interstitial flow, the ELP fusion concentration in this region decreases, causing the T_t to increase above body

temperature. Unimers residing at the depot margins thereby resolubilize and diffuse into the surrounding tissue (Figure 81B). In previous work, we created an injectable ELP depot that released soluble fusion molecules for up to 10 days in mice with zero-order kinetics, and up to 20 days in non-human primates.⁸⁸

5.1.3 Strategies for immunotoxin-ELP synthesis

We explored three strategies for synthesis of our immunotoxin-ELP fusion drug, described in detail below. Our initial studies involved conjugation of a monoclonal antibody with an ELP-toxin fusion; as complex mammalian and cytotoxic bacterial proteins cannot be recombinantly expressed in the same system, we investigated both chemical ligation and enzymatic attachment to combine these proteins post-purification. The benefits of using a monoclonal antibody were ultimately outweighed by the low yield of these approaches, and we found success with an alternative strategy: a recombinant immunotoxin-ELP fusion we designed to be expressed entirely in *E. coli*. In addition to the ELP and toxin, this linear fusion protein features an affibody targeting element, which also provides the benefit of increased valency. Through the many stages of this project, we have gained valuable insights in antibody purification, conjugation chemistry, enzymatic processing, and protein engineering. We share these to illustrate the trajectory of this work, from its origins in genetic code expansion to the current recombinant strategy, guided by the challenges and successes we encountered.

5.1.3.1 Click chemistry attachment enabled by genetic code expansion

Antibodies are tetrameric glycoproteins exquisitely evolved by mammalian immune systems to recognize and neutralize a diverse range of foreign invaders.²⁸³ The potential to recognize ligands with high affinity has spurred substantial investment in developing monoclonal antibodies specific for useful targets, such as cancer cell-specific receptors.³¹⁹ When loaded with cargo, monoclonal antibodies provide the means to precisely target highly potent drugs to specific cells as antibody-drug conjugates (ADCs). A major drawback to clinical use of ADCs is their heterogeneous attachment of drug by the currently available attachment methods, most frequently at lysine residues. With an average of eighty lysine residues per antibody, there are over one million possible configurations of drug attachment via this method.³²⁰ A heterogeneous ADC population has a low therapeutic index as each conjugate can have distinct pharmacokinetic, efficacy, and safety profiles.³²¹ We were therefore interested in generating a chemically reactive monoclonal antibody that can be site-specifically combined with a clickable ELP-toxin protein reaction partner.

The monoclonal antibody (mAb) selected for our system has a high affinity on the order of 100 pM for both EGFR and EGFRvIII.³⁰⁷ After expression in mammalian cells, we enzymatically modified the mAb post-purification to attach a click chemistry handle, dibenzylcyclooctyne (DBCO). Sortase A is a bacterial enzyme which cleaves between a threonine and glycine residue in its recognition motif (LPETG) in one

substrate, forming a thioester intermediate with the threonine residue. This intermediate is resolved by nucleophilic attack of the α -amine of an N-terminal triglycine motif (Gly₃) in the target substrate to regenerate an amide bond.¹⁶⁵ We chemically conjugated the DBCO moiety to a Gly₃ peptide and genetically introduced the LPETG motif into the C-terminus of the antibody to facilitate Sortase A attachment (Figure 82).

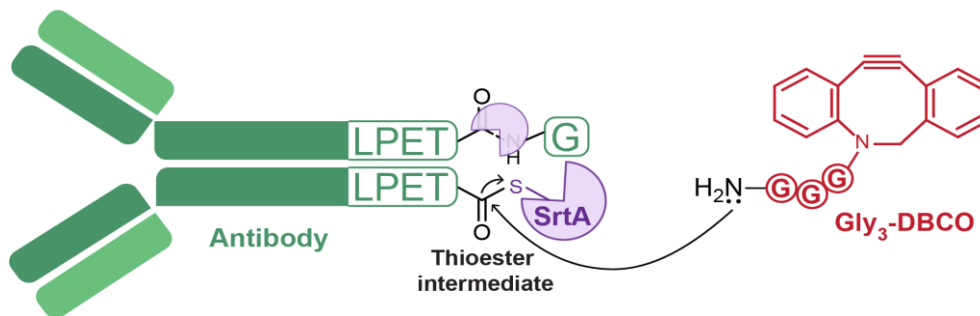


Figure 82: Sortase A-mediated attachment of clickable DBCO handle to antibody.

The click reaction partner for DBCO, an azide, was co-translationally incorporated as *p*-azidophenylalanine (*p*AzF) into the ELP-toxin protein, expressed as a fusion in bacteria. The purified and appropriately modified proteins were then combined using a strain-promoted alkyne-azide cycloaddition (SPAAC) reaction (Figure 83). This bioorthogonal reaction proceeds spontaneously to relieve the high level of strain present in the cycloalkyne group without the need for cytotoxic copper catalysts,⁹¹ and results in a stable covalent bond between the two groups in the final immunotoxin conjugate, which we termed “AbETox”.



Figure 83: Spontaneous strain-promoted alkyne-azide cycloaddition (SPAAC) between the modified antibody-DBCO and *pAzF*-ELP-toxin for AbETox synthesis.

5.1.3.2 Enzymatic protein-protein ligation with Sortase A

Our second approach for constructing AbETox employed Sortase A as well, but instead explored direct protein-protein enzymatic fusion. With the Sortase A recognition motif installed in the C-terminus of the antibody, we genetically introduced the Gly₃ sequence into the N-terminus of the ELP-toxin fusion. We were initially uncertain of the success of enzymatic fusion of two large substrates and had therefore designed the small-molecule based strategy described in Section 5.1.3.1; however, upon evaluation we discovered this is also a viable approach to synthesize AbETox (Figure 84).

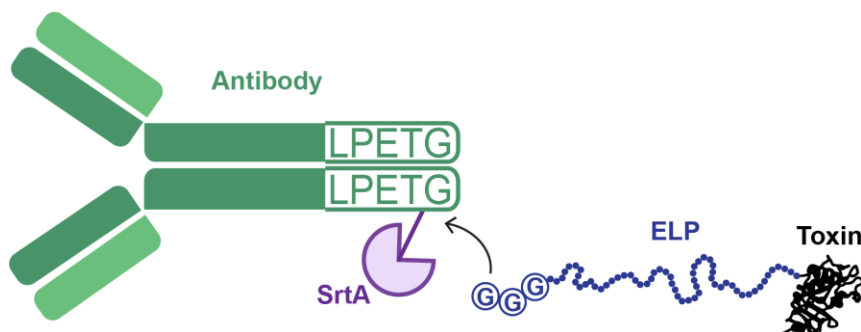


Figure 84: Direct Sortase A-mediated ligation for AbETox synthesis.

5.1.3.3 Recombinant fusion

While AbETox has the advantage of incorporating a stable and versatile mAb, producing this multi-component drug required expression of the mAb and toxin elements in separate expression hosts, followed by conjugation and multiple purification steps. The complexity of these schemes resulted in significant challenges in optimizing yield and motivated us to explore alternative strategies.

To circumvent the need to produce multiple distinct components for AbETox, we designed a recombinant immunotoxin-ELP fusion to be expressed entirely in *E. coli*. We genetically fused three different proteins into one molecular agent to provide the three desired elements: 1) multivalent, active targeting, 2) potent cytotoxicity, and 3) sustained-release properties as an injectable formulation for intratumoral treatment of GBM. The targeting component in this construct is an affibody domain; affibody proteins are helical, small (~7 kDa) scaffold proteins derived from the IgG-binding (Z) domain of *S. aureus* that have been engineered to bind unique targets with high affinity, comparable to that of monoclonal antibodies but with the greater ease of genetic manipulation and production possible with a bacterial expression system.³²² These proteins are highly stable without disulfide bonds, expressed in high yield, and amenable to head-to-tail genetic fusions and combination for multiplexed targeting.³²³ The affibody selected for our system, ZEGFR₁₉₀₇, has established nanomolar affinity for EGFR; we discovered through this work that this affibody also recognizes EGFRvIII.²³¹

³⁰⁸ Given the benefit of increasing affinity – and hence potency – through multivalency, we have developed a library of fusions with one, two, or four affibody domains fused to the ELP-toxin, which we termed AffETox (Figure 85). We also explored ELPs with a variety of guest residues and molecular weights to provide AffETox with a range of phase transition behavior.

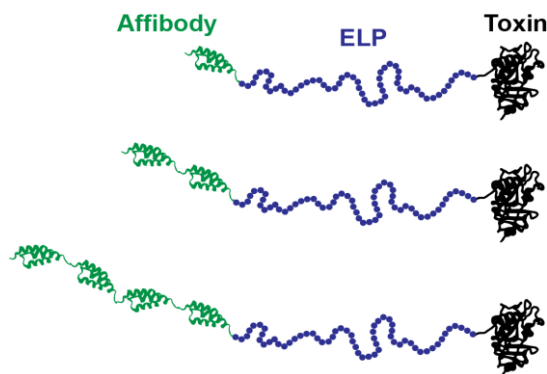


Figure 85: AffETox recombinant fusion proteins with one, two, or four Affibody domains.

5.2 Materials and methods

5.2.1 Construct design and synthesis

5.2.1.1 Monoclonal antibody

The genes encoding the anti-EGFR/EGFRvIII antibody (mAb) were constructed by introducing the variable heavy and light chain sequences from a published scFv (D2C7)³²⁴ into the heavy and light chain genes of a humanized kappa isotype IgG1 (provided by Joseph Bellucci, Duke University). Both genes contain an N-terminal signal peptide to ensure proper secretion of the translated proteins, which is cleaved after protein processing.³²⁵ We investigated two signal peptides – IL-2 and azurocidin – for

5.2.1.3 *pAzF*-ELP-toxin for click chemistry attachment

We designed the *pAzF*-ELP-toxin fusion protein with the *pAzF*-ELP gene fused at its C-terminus to an engineered *P. aeruginosa* exotoxin A.³¹⁵ We selected this orientation as the C-terminus of this toxin is required to be free for activity; the terminal RDELK sequence promotes efficient retrograde traffic to the endoplasmic reticulum to inhibit translation.³²⁷ The site of incorporation for the clickable unnatural amino acid, *p*-azidophenylalanine, was positioned at the N-terminus to minimize steric hindrance of the click reaction. We selected an ELP with the sequence (VPGVG)₆₀ – ELP_{D1} – for our initial experiments as we predicted this ELP would be sufficiently hydrophobic to drive depot formation at physiological temperatures.¹⁹⁴ The ELP sequences and nomenclature used for our immunotoxin fusions are summarized in Table 9.

The gene encoding the ELP_{D1}-toxin was synthesized using recursive directional ligation by plasmid reconstruction.¹³⁶ The gene for the toxin was purchased as a gBlock (IDT Technologies, Skokie, IL) and inserted into a modified cloning vector (m-pET-24+) using Gibson assembly. The m-pET-24+ vector containing the ELP_{D1} gene was then digested with *AcuI* and *BglII* to create an “A” population, and the toxin-containing vector was digested with *BseRI* and *BglII* to create a “B” population. These compatible plasmid fragments were then ligated to create a vector containing the fusion gene, ELP_{D1}-toxin. The site of incorporation for *pAzF*, the amber stop codon (DNA sequence: TAG), was introduced in the form of a peptide leader with sequence *GpAcFG*.

Oligonucleotides encoding this sequence along with “sticky end” overhangs were purchased as ssDNA (IDT Technologies, Skokie, IL) and then annealed together. The ELP_{D1}-toxin vector was digested with BseRI and the annealed fragment inserted via its complementary overhangs to make the final product encoding *pAzF-ELP_{D1}-toxin*.

5.2.1.4 Gly₃-ELP-toxin for Sortase A-mediated attachment

The Gly₃-ELP-toxin gene has the Sortase A substrate sequence, Gly₃, positioned at the N-terminus for conjugation to the mAb. The N-terminal amine of this motif is the nucleophile which resolves the Sortase A-catalyzed intermediate and, therefore, must be positioned directly at the N-terminus.¹⁰¹

The ELP_{D1}-toxin gene was synthesized as described in Section 5.2.1.1. In place of the *pAzF* leader, we ordered oligonucleotides encoding the sequence GGG along with “sticky” overhangs as ssDNA (IDT Technologies, Skokie, IL), annealed these, and inserted at the N-terminus of the ELP_{D1}-toxin after digestion with BseRI to synthesize the final gene product, Gly₃-ELP_{D1}-toxin. The ELP sequences and nomenclature used for our immunotoxin fusions are summarized in Table 9.

5.2.1.5 Affibody-ELP-toxin (AffETox)

The AffETox recombinant fusion protein library was constructed by genetic fusion of one, two, or four Affibody genes (ZEGFR) at the N-terminus of an ELP gene, followed by fusion of the toxin gene at the C-terminus of the ELP. Comparing AffETox constructs with different ZEGFR copy numbers allowed us to study the importance of

avidity for optimal targeting and potency, as EGFR dimerizes and oligomerizes prior to internalization.³²⁸ The ELP genes selected have the same number of repeat units (60-mers) to maintain molecular weight but differ in their guest residue composition to provide a range of depot-forming or non-depot-forming behavior *in vivo* (Table 9).

Table 9: ELP nomenclature used for immunotoxin fusion proteins.

Nomenclature	Amino acid sequence	Predicted T_i (°C) at 100 μM ¹⁹⁴ ; behavior at 37°C
ELP _{D1}	(VPGVG) ₆₀	31.5; ideal depot
ELP _{D1-80}	(VPGVG) ₈₀	27.8; strong depot
ELP _{D1-120}	(VPGVG) ₁₂₀	24.1; strong depot
ELP _{D2}	(VPGA ₁ V ₄ G) ₆₀	37.8; weak depot
ELP _S	(VPGAG) ₆₀	76.4; soluble/no depot

A more hydrophobic valine guest residue promotes a lower T_i and will therefore create a more stable depot *in vivo*; conversely, a more hydrophilic alanine guest residue will result in a T_i above that of physiological temperature and this construct will remain soluble after injection *in vivo*. A ratio of these two guest residues will result in an intermediate behavior, with moderately stable depot formation *in vivo* but more rapid release than the more hydrophobic ELP construct containing valine alone.

The genes for the ELP-toxin fusions were constructed as described in Section 5.2.1.3. The genes encoding ZEGFR and (ZEGFR)₂ (provided by Mandana Manzari, Duke University) were inserted into a modified cloning vector (m-pET-24+) using Gibson assembly. The m-pET-24+ vector containing the ZEGFR or (ZEGFR)₂ gene was then digested with *AcuI* and *BglII* to create an “A” population, and the ELP-toxin-

containing vector was digested with BseRI and BglII to create a “B” population. These compatible plasmid fragments were then ligated to create a vector containing the fusion genes, ZEGFR-ELP-toxin or (ZEGFR)₂-ELP-toxin. To synthesize the (ZEGFR)₄-ELP-toxin gene, the vector containing the (ZEGFR)₂ gene was digested to create an “A” population, and the vector containing the (ZEGFR)₂-ELP-toxin gene was digested to create a “B” population. These were ligated to create the final gene product, (ZEGFR)₄-ELP-toxin. Genes encoding control constructs – ZEGFR_n-ELP and ELP-toxin – were also similarly synthesized to assess the cytotoxic effects of either the Affibody or the toxin alone.

5.2.2 Protein expression and purification

5.2.2.1 HEK293 transient expression of monoclonal antibodies

The pCDNA plasmids encoding the mAb-LPETG heavy chain and mAb light chain were purified from bacterial cultures using a QIAGEN® Plasmid Midi or Maxi Purification Kit (QIAGEN, Hilden, Germany) to obtain transfection quality DNA at sufficiently high concentrations ($\geq 1000 \text{ ng } \mu\text{L}^{-1}$).³²⁹ We transiently transfected these plasmids into a commercially-available expression system using human embryonic kidney cells (HEK293T) according to the manufacturer’s protocol (Life Technologies, Carlsbad, CA). Briefly, we diluted 30 μg of DNA (12 μg light chain, 18 μg heavy chain) in a total volume of 1.5 mL Opti-MEM reduced serum medium. In a separate tube, we diluted 81 μL of ExpiFectamine 293 reagent in a total volume of 1.5 mL of Opti-MEM reduced serum medium, and incubated for 5 min. At the end of this incubation, the two

dilutions were mixed and incubated for an additional 20 min at room temperature to allow for the formation of lipid-DNA complexes. At the end of this incubation, we added the 3 mL of complex to 25.5 mL Expi293 cells with cell density adjusted to 2.9×10^6 cells mL⁻¹. After incubating the cells for 20 h at 37°C, 8% CO₂ atmosphere, we added the ExpiFectamine 293 Transfection Enhancers 1 and 2 and incubated for an additional 5 days.

This system secretes high titers of stable, recombinant antibody into the culture medium that we recovered with Protein G affinity chromatography. Protein G binds specifically to the interface between the CH2 and CH3 domains of the Fc domain of antibodies; the addition of the Sortase A recognition sequence to the C-terminus of the heavy chain is not anticipated to affect mAb binding and recovery with this method.³³⁰⁻³³¹ After Protein G column chromatography and we concentrated solutions of mAb-LPETG using by centrifugal ultrafiltration (Amicon Ultra-15, 10 kDa cut-off, Millipore Sigma, Burlington, MA) to concentrations of 5-10 mg mL⁻¹ (approximately 50 μM) and buffer exchanged into 20 mM Tris, pH 6.9 for long-term storage at 4°C. Typical yields from these expressions were 6-8 mg of pure mAb-LPETG.

5.2.2.2 Bacterial expression of Sortase A and toxin fusion proteins

We explored two versions of the Sortase A enzyme for our reactions, both expressed under the control of the T7 promoter in the soluble fraction of BL21(DE3) *E. coli*. We expressed an ELP-SrtA fusion protein (provided by Joseph Bellucci, Duke

University) and purified this using inverse transition cycling in 50 mM Tris, pH 7.5, 1 mM DTT buffer. This variant has the 59 N-terminal amino acids deleted from the wild-type sequence to enhance activity.³³² We also expressed an evolved Sortase A mutant, mSrtA, and purified this using His-tag affinity chromatography. This high activity mutant (provided by Parisa Yousefpour, Duke University) has four point mutations at rationally selected locations which result in a more catalytically active variant.³³³ These proteins were concentrated to approximately 300 μM and frozen at -20°C for long-term storage. These expressions yielded approximately 50 mg L^{-1} of pure protein.

All toxin-containing fusion proteins (*pAzF-ELP-toxin*, *Gly₃-ELP-toxin*, *ZEGFR_n-ELP-toxin*, *ELP-toxin*) were expressed under the control of the T7 promoter in *E. coli* BL21(DE3) and required solubilization and refolding from inclusion bodies. Of note, there was consistently a minor population of protein expressed in the soluble fraction, though we determined this protein was unstable and not suitable for future use. The *pAzF-ELP-toxin* construct was expressed in bacteria co-transformed with the evolved *pEvol tRNA/aaRS* vector and *pAzF* incorporation protocol performed as described in Section 3.2.2.

To express these proteins, starter cultures (50 mL, 2xYT media) of transformed or co-transformed *E. coli* BL21DE3 strains were inoculated from frozen glycerol stocks and grown for 18 h. The starter cultures were then inoculated at 1:20 dilution in 2xYT media (1 L) supplemented with kanamycin (45 $\mu\text{g ml}^{-1}$). The cultures were grown at 37°C in a

shaking incubator at 200 r.p.m. until the OD₆₀₀ reached 1.0 as assessed by UV/Vis spectrophotometry (NanoDrop 1000, Thermo Fisher Scientific, Waltham, MA), at which time protein expression was induced by the addition of 1 mM isopropyl β-D-1 thiogalactopyranoside (IPTG). The cultures were then grown for an additional 3 h at 37°C. Cell pellets were harvested by centrifugation at 3,500xg and resuspended in 20 mL of 50 mM Tris, pH 8.0, 750 mM sucrose buffer. Cells were lysed by sonication for a total of 3 min (Misonix; Farmingdale, NY) and incubated for 15 min at room temperature with 10 μg mL⁻¹ DNase I and RNase I, 10 mM MgCl₂. The lysate was centrifuged at 22,000xg for 40 min at 4°C and the supernatant discarded. The insoluble pellet was resuspended in sufficient 50 mM Tris, pH 8.0, 150 mM NaCl, 2 mM EDTA, 0.5 mM benzamidine, 0.5% TritonX-100 buffer to homogenize the inclusion body, followed by centrifugation at 22,000xg for 30 min. This wash step was repeated four additional times, without the inclusion of TritonX-100 in the wash buffer. The increasing purity of the inclusion body was evident by a color change from grey to white and a decrease in size of the insoluble pellet after each successive wash step. After the final wash, the pellet was dissolved in 6 M guanidine-HCl, pH 1.5 and dialyzed against 8 L 50 mM Tris, pH 8.0, 150 mM NaCl, 2 mM EDTA, 0.5 mM benzamidine at 4°C in 12-14 MWCO dialysis tubing. The dialysate was then centrifuged at 22,000xg for 30 min and the solubilized protein found in the resulting supernatant; the insoluble pellet after this final

centrifugation step was discarded. This refolding protocol was adapted from published procedures.³³⁴⁻³³⁵

The proteins were then dialyzed into 1xPBS and kept at -80°C for long-term storage; we observed degradation and aggregation with proteins stored at -20°C or 4°C for longer than 24-48 h. We further refined the purity with size exclusion chromatography (SEC) on an ÄKTA automated system (GE Healthcare, Chicago, IL) equipped with a photodiode detector and a HiLoad Superdex 26/60 200 PG column operated at 4°C using 1xPBS as the mobile phase and a flow rate of 3 mL min⁻¹. Typical yields of toxin-containing proteins were approximately 10 mg L⁻¹ culture. The control ZEGFR_n-ELP protein was expressed in the soluble fraction of *E. coli* and purified using inverse transition cycling, as described in Section 1.2.2.1; these proteins had higher yielding expressions of approximately 80 mg L⁻¹ culture. The final yields of the purified proteins from these bacterial expressions are summarized in Table 10.

Table 10: Expression yields of immunotoxin proteins and controls.

Construct	Yield (mg L ⁻¹)	Construct	Yield (mg L ⁻¹)
<i>pAzF</i> -ELP _{D1} -toxin	16.9	ZEGFR-ELP _S -toxin	9.1
Gly ₃ -ELP _{D1} -toxin	23.6	(ZEGFR) ₂ -ELP _S -toxin	4.1
ZEGFR-ELP _{D1} -toxin	6.3	(ZEGFR) ₄ -ELP _S -toxin	3.3
(ZEGFR) ₂ -ELP _{D1} -toxin	3.2	(ZEGFR) ₂ -ELP _{D1}	83.8
(ZEGFR) ₄ -ELP _{D1} -toxin	3.6	(ZEGFR) ₄ -ELP _{D1}	71.0
(ZEGFR) ₂ -ELP _{D1-80} -toxin	17.9	ELP _{D1} -toxin	10.5
(ZEGFR) ₂ -ELP _{D1-120} -toxin	14.9	ELP _S -toxin	25.9
(ZEGFR) ₂ -ELP _{D2} -toxin	13.2		

5.2.2.3 Endotoxin purification

Endotoxins, a contaminant of proteins recombinantly expressed in Gram-negative bacteria, are complex aggregates of lipopolysaccharides from bacterial cell walls.³³⁶ Endotoxins are highly immunogenic and pyrogenic even at low quantities in therapeutic formulations and must be removed with an additional purification step.³³⁷ There are several established approaches for endotoxin removal including ion exchange and affinity chromatography, which both rely on the net negative charge of this contaminant (pI ~ 2.5).³³⁸ We compared two affinity-based endotoxin removal protocols for maximum protein yield and extent of endotoxin removal.

First, we explored an affinity resin purification protocol with gravity flow by packing columns with Detoxi-Gel resin (Thermo Fisher Scientific, Pittsburgh, PA). This resin uses immobilized polymyxin B, which binds to the lipid A domains of endotoxin.³³⁹ We regenerated the resin using three column volumes of 1% sodium deoxycholate in endotoxin-free water, followed by three column volumes of endotoxin-free water and three column volumes of endotoxin-free 1xPBS. We then incubated our protein sample (5 μ M in 10 mM sodium phosphate, 0.1 M NaCl buffer, pH 7.0) with the resin, rotating in the capped column at 4°C for 1 h. After this incubation, we collected the flow-through containing the protein. We repeated the incubation step with the same sample of protein for a total of four rounds, and then concentrated and buffer exchanged into endotoxin-free 1xPBS by centrifugal ultrafiltration (Amicon Ultra-15, 10 kDa cut-off, Millipore

Sigma, Burlington, MA). Purification with this method reduced endotoxin levels to ≤ 0.25 EU mL⁻¹, an acceptable level for our *in vivo* studies, but concurrently resulted in loss of > 98% of total protein. The immunotoxin fusion constructs have an isoelectric point of 4.8, and like endotoxin, are therefore negatively charged at neutral pH and indiscriminately bind to the affinity resin.

To address this significant loss of protein, we also investigated the use of Pierce™ High Capacity Endotoxin Removal Spin columns (ThermoFisher Scientific, Pittsburgh, PA). This resin contains immobilized poly(ϵ -lysine) as the affinity ligand, which has a higher binding capacity than polymixin B and is more selective for binding to endotoxin, improving protein recovery. For purification with these columns, we adjusted the endotoxin concentration of the protein sample to be purified, rather than the protein concentration. The starting concentration of endotoxin in these immunotoxin fusion proteins ranged from 50,000 to 890,000 EU mL⁻¹, with a corresponding protein concentration of approximately 50 μ M. We diluted the protein sample to 10,000 EU mL⁻¹ in endotoxin-free buffer prior to the spin column purification protocol. We first regenerated the column with 0.2 N NaOH/95% EtOH for 1 h at room temperature followed by 2 M NaCl washing. We equilibrated the spin columns with 10 mM sodium phosphate, 0.1 M NaCl buffer, pH 7.0, followed by incubation with the protein sample at 4°C for 1 h, rotating. We collected the sample and repeated this process for a total of three times and after the final round of purification, concentrated and buffer exchanged

the sample into endotoxin-free 1xPBS by centrifugal ultrafiltration (Amicon Ultra-15, 10 kDa cut-off, Millipore Sigma, Burlington, MA). Purification with this method reduced endotoxin levels to ≤ 0.25 EU mL⁻¹ with higher protein recovery (approximately 15% as compared to < 2% with the first method).

The level of endotoxin in the protein samples was assessed with two methods: both a gel-clot and a chromogenic limulus amoebocyte lysate (LAL) assay. LAL reacts strongly to and coagulates in the presence of endotoxin and is the FDA-approved method for detecting and quantifying endotoxin levels.³³⁶ For the gel-clot assay, samples were diluted to the concentrations to be used *in vivo* and tested for formation of a gel clot after incubation at 37° C for 1 h with an endotoxin detection limit of 0.25 EU mL⁻¹ (ToxinSensor™ Gel Clot Endotoxin Assay Kit, GenScript, Piscataway, NJ). For the chromogenic assay, we diluted samples and analyzed with the EndoSafe® cartridge reader with a cartridge sensitivity of 0.1 EU mL⁻¹.

5.2.2.4 AbETox conjugation and purification strategies

As discussed in Section 5.1.3, we designed and evaluated two strategies for synthesizing AbETox. The first of these involved Sortase A modification of the mAb-LPETG followed by a click chemistry conjugation reaction. The purified mAb-LPETG was modified with Sortase A to attach the “clickable” substrate we synthesized, Gly₃-DBCO, to the C-terminus of the heavy chains. To do this, the mAb-LPETG, Gly₃-DBCO, and ELP-SrtA or His₈-mSrtA were combined in molar ratios of 1: 300: 4 (i.e. 15 μ M mAb-

LPETG, 4500 μM Gly₃-DBCO, 60 μM ELP-SrtA) in Sortase A reaction buffer (0.5 M Tris, pH 7.5, 1.5 M NaCl, 0.1 M CaCl₂). The reaction was incubated at 25°C for 18 h, at which point the Sortase A was removed to stop the reaction, either by inverse transition cycling or His-tag purification. Excess unreacted components were removed by ultrafiltration prior to click reaction. The success of Sortase A labeling was assessed by monitoring the increase in absorbance at 310 nm, the characteristic absorbance of DBCO.

After obtaining and purifying mAb-DBCO, we combined this with *pAzF*-ELP_{D1}-toxin to synthesize the final immunotoxin product. For this click reaction, we tested an array of reaction conditions. We varied the molar ratio of DBCO: azide, ranging from 2:1 to 1:1 to 1:2, but kept the individual concentrations of both of these components above 100 μM to drive the reaction to completion. We also varied the incubation time, ranging from 24 to 72 h, with all reactions performed at 25°C. To purify the final reaction product, we used both azide- and DBCO-conjugated magnetic beads (Jena Bioscience, Jena, Germany) to remove unreacted starting material.

We also explored an alternative AbETox synthetic route. For this, we used Sortase A for direct protein-protein ligation of the two components, mAb-LPETG and Gly₃-ELP-toxin. We explored a variety of reaction conditions to optimize this conjugation, in particular modulating the ratio of Gly₃-ELP-toxin to mAb-LPETG and testing two Sortase A variants. A typical labeling reaction was comprised of mAb-

LPETG, Gly₃-ELP-toxin, and Sortase A in 1: 25: 3 molar ratios (i.e. 20 μM mAb-LPETG, 500 μM Gly₃-DBCO, 60 μM ELP-SrtA).

We devised a two-step purification scheme to address the challenges we faced with purifying the resulting complex reaction mixture (Figure 87).

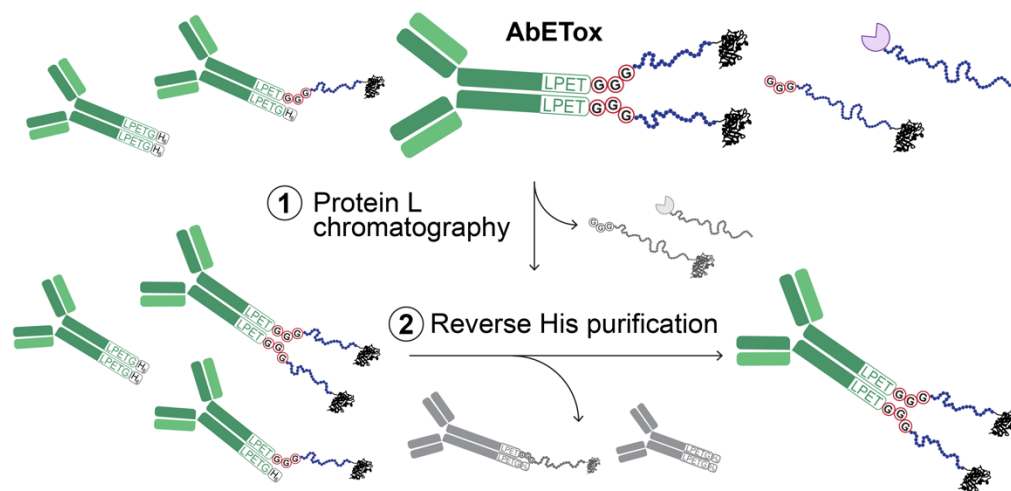


Figure 87: AbETox two-step purification scheme #1.

In the first step, we used Protein L chromatography to collect mAb-containing components, as this protein selectively binds to kappa light chains without Fc interference.³⁴⁰ This eliminated ELP-SrtA and unconsumed Gly₃-ELP-toxin, with the potential components remaining after this purification step including unmodified mAb-LPETG, singly labeled mAb-ELP-toxin, and the desired AbETox product, mAb-(ELP-toxin)₂. The second reaction step relied on the His₆ tag we installed immediately following the LPETG sequence on mAb; any intact, unlabeled heavy chains will have this affinity tag present, which we used to “reverse” His purify and pull these components out of the reaction mixture. This initial purification scheme assumed we

would obtain successful labeling of both heavy chains in sufficient yield.

Experimentally, we determined the proportion of singly-labeled and unlabeled mAb both dwarfed that of the doubly-labeled species. We accordingly modified our purification protocol to instead separate these two components in the second purification step by inverse transition cycling, rather than reverse His purification (Figure 88). We monitored the purity and success of the reaction by observing the molecular weight increase of the heavy chain with SDS-PAGE and MALDI-TOF-MS.

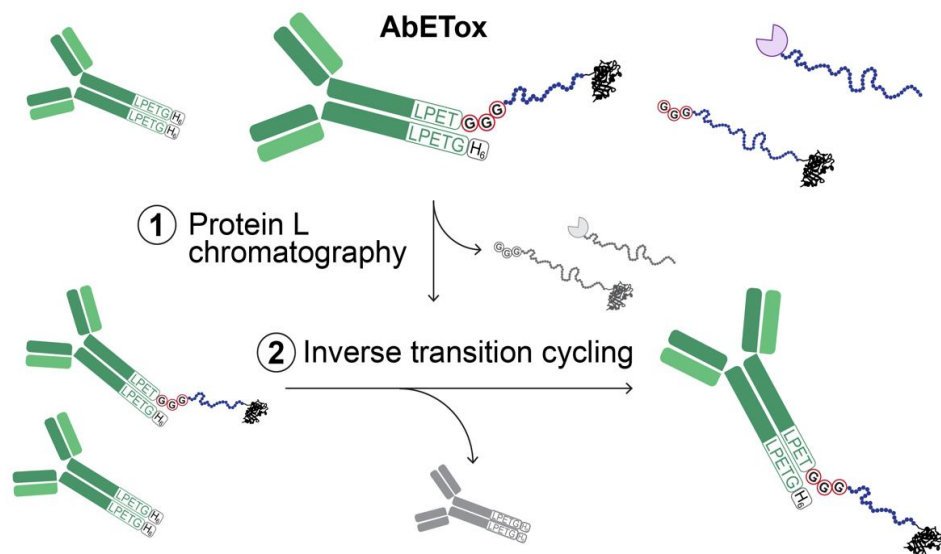


Figure 88: AbETox two-step purification scheme #2.

We empirically determined a certain degree of non-specific Sortase A labeling in negative control reactions which resulted in undesirable intra-mAb heavy chain dimers, and which we hypothesized were caused by the prevalent solvent-exposed lysine residues in the mAb HC. The resulting low Sortase A reaction efficiency made it difficult to recover the AbETox using inverse transition cycling. We subsequently modified this

purification scheme further to reposition the His tag between the Gly₃ leader and ELP-toxin, to instead His purify the final AbETox product (Figure 89).

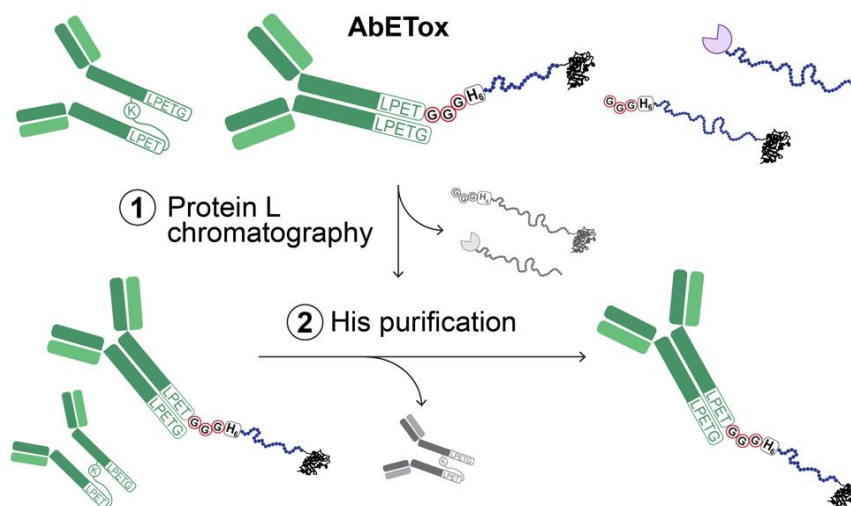


Figure 89: AbETox two-step purification scheme #3.

5.2.3 Immunotoxin characterization

5.2.3.1 Mass spectrometry

To confirm the attachment of Gly₃-ELP-toxin to mAb, we performed a tryptic digest and analyzed this digest with matrix-assisted laser desorption/ionization time-of-flight mass spectrometry (MALDI-TOF-MS). Lyophilized trypsin was reconstituted using 50 mM acetic acid to 1 mg mL⁻¹ as per the manufacturer's instructions. Samples of *pAcF-ELP_{BC}* and *pAcF-ELP_{BC}-EgA1* at 100 μM were incubated with MS-grade trypsin protease (Pierce, Waltham, MA) at a ratio of 20:1 in 50 mM ammonium bicarbonate, pH 8. These reactions were incubated at 37°C for 16 h and then analyzed with a Bruker Autoflex Speed LRF MALDI-TOF System. Digested samples were mixed at a ratio of 1:1

with sinapinic acid (SA) matrix and 2 μ L was deposited onto a ground steel target plate and dried in air at room temperature. All spectra were calibrated against apomyoglobin (Sigma Aldrich, St. Louis, MO).

The products of Gly₃-DBCO synthesis were analyzed by electron spray ionization liquid chromatography/mass spectroscopy analysis with an Agilent 1100 Series LC/MSD Trap SL (Agilent Technologies, Santa Clara, CA). Samples were injected into a Phenomenex Luna C18 column (50 \times 1 mm, 3 μ m; 0.2% formic acid in water as buffer A, 0.2% formic acid in acetonitrile as buffer B) and then into the mass spectrometer using a fully automated system. Spectra were acquired in positive mode followed by analysis using LC/MSD Trap Data Analysis software (Agilent Technologies, Santa Clara, CA). Mass spectra were acquired at the Mass Spectrometry Shared Facility at Duke University.

5.2.3.2 Phase transition behavior

The transition temperatures (T_t) of the immunotoxin-ELP fusion proteins were determined by temperature-controlled spectrophotometry using a Cary 300 (Agilent Technologies, Santa Clara, CA). Samples containing various concentrations of these proteins in 1xPBS were heated at 1°C min⁻¹ and the optical turbidity at 350 nm was recorded every 0.1°C. The T_t was determined for each sample as the maximum of the first derivative of the turbidity as a function of temperature.

5.2.3.3 Cell-free protein translation inhibition assay

We confirmed the mechanism of action of the toxin using a modified cell-free protein translation inhibition assay.³⁴¹ We selected a cell-free kit with the eukaryotic cellular components required for transcription and translation of a reporter gene, *R. reniformis* luciferase (T7 TnT® Quick Coupled Transcription/Translation System, Promega, Madison, WI). In this assay, the negative control reaction expresses luciferase and produces luminescence after addition of the luciferin reagent (Figure 90A). Addition of a translation inhibitor, such as ELP-toxin, prevents translation of luciferase and eliminates the luminescent signal, providing a quantifiable measure of protein translation or its lack thereof (Figure 90B).

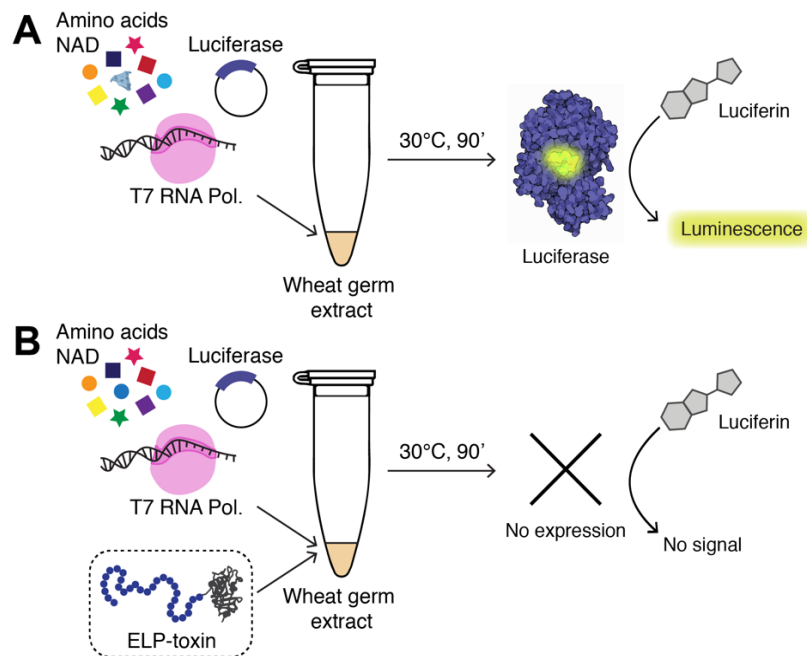


Figure 90: Cell-free protein translation inhibition assay. (A) A luciferase reporter gene under the control of a T7 promoter provides a luminescent signal after incubation of the necessary cell-free components. (B) Addition of a *P. aeruginosa*

exotoxin A-containing protein inhibits protein translation, preventing translation of luciferase and eliminating the luminescent signal.

These reactions were prepared according to the manufacturer's instructions, with the kit components (WGA extract, T7 RNA polymers, TnT reaction buffer, amino acid mix, RNase inhibitor, T7 luciferase DNA at 500 ng μL^{-1}) mixed immediately before addition of the toxin (at 1 $\mu\text{g mL}^{-1}$) and necessary co-factor, nicotinamide adenine dinucleotide (NAD, 100 $\mu\text{g mL}^{-1}$) in a total reaction volume of 50 μL . These reactions were then incubated at 30°C for 90 min. At the end of the incubation period, 30 μL of each reaction was transferred to a black-walled 96-well microplate and 50 μL of luciferin (24 mg mL^{-1}) added to each well simultaneously with a multichannel pipette. Following incubation for 5 min, the luminescent signal of the solution was measured with a 1 s counting time using a Victor3 microplate reader (PerkinElmer, Waltham, MA). These reactions were prepared and analyzed in triplicate to provide an *n* of 3 for each experimental condition.

5.2.3.4 Cell viability assays and flow cytometry

We assessed the potency of the AffETox proteins in a panel of relevant cell lines including murine 3T3 fibroblasts stably transfected to express either human EGFR, human EGFRvIII, or null (negative control), A431 patient-derived squamous carcinoma, A172 patient-derived GBM, D270MG patient-derived GBM, D270MG xenograft GBM, CT-2A murine GBM (chemically induced tumors), and SMA560 murine GBM

(spontaneously developed tumors). The transfected fibroblasts, D270MG, CT-2A, and SMA560 lines were generously provided by Darrell Bigner, Duke University.

The *in vitro* cytotoxicity of AffETox was determined by a colorimetric assay, as follows. First, 2.5×10^3 cells were seeded per 90 μL complete media on BD Falcon™ 96-well cell culture plates (BD; Franklin Lakes, NJ) and allowed to adhere for 16-18 h. After adherence, 10 μL of serial dilutions of AffETox and relevant controls were added to the wells and incubated at 37°C for 72 h. After the treatment period, 10 μL of CellTiter 96 AQueous™ 3-(4,5,-dimethyl-2-yl)-5-(3-carboxymethoxyphenyl)-2-(4-sulfophenyl)-2H-tetrazolium (MTS) reagent (Promega; Madison, WI) was added to each well. Following incubation for 2 h, the absorbance of the solution was measured twice at 490 nm and 650 nm with a Victor3 microplate reader (Perkin Elmer; Waltham, MA). The background A650 was subtracted from the A490 readings to determine the cell viability as compared to untreated controls according to Equation 6:

Equation 6: Calculating cell viability

$$\% \text{ Viability} = \frac{\text{Corr. A490} - \text{A490}_{\text{Media}}}{\text{Corr. A490}_{\text{Untreated}} - \text{A490}_{\text{Media, Untreated}}} \times 100\%$$

To calculate the IC₅₀, the data was fit to a sigmoidal curve and fit to Equation 7, where C_{protein} is the effective protein concentration in the well, the IC₅₀ measures the necessary dose to kill 50% of the cell population, and *p* represents the slope of the sigmoidal curve.

Equation 7: Calculating IC₅₀

$$\% \text{ Viability} = \frac{1}{1 + \left(\frac{C_{\text{protein}}}{IC_{50}}\right)^p}$$

To fluorescently label proteins, 1 mg of AlexaFluor488-NHS ester was dissolved in 100 μ L DMSO. The N-terminal amine of (ZEGFR)₂-ELP_{D1} was labeled with AlexaFluor488-NHS ester by incubating these proteins (100 μ M) with ten molar equivalents of dye, rotating at 4°C for 24 h in sodium phosphate buffer, pH 7.4. Excess unreacted dye was removed with a hot spin followed by washing with centrifugal ultrafiltration (Amicon Ultra-15, 10 kDa cut-off limit). Briefly, a hot spin consists of heating the solution of labeled protein above the T_i to initiate phase separation and centrifuging at high speeds to pellet the ELP, with free dye in the supernatant. The supernatant is removed, and the pellet is resuspended in cold PBS, whereupon the ELP resolubilizes. The following equations were used to calculate protein concentration (Equation 8) and A488 concentration (Equation 9). The typical dye labeling efficiency was approximately 25%.

Equation 8: Calculating protein concentration

$$[(\text{ZEGFR})_2\text{-ELP}_{D1}] = \frac{A_{280} - (A_{494} \times 0.11)}{33,000 \text{ cm}^{-1}\text{M}^{-1} \times 1 \text{ cm path length}}$$

Equation 9: Calculating fluorescent labeling efficiency

$$[\text{AlexaFluor488}] = \frac{A_{494}}{73,000 \text{ cm}^{-1}\text{M}^{-1} \times 1 \text{ cm path length}}$$

Overnight cultures of adherent cells (3T3+EGFR) were prepared for flow cytometry by first trypsinizing cells with 0.05% trypsin/EDTA and harvesting the cells by centrifugation for 3 min at 1,000xg. The D270MG xenograft cells were prepared in a single cell suspension by first treating tumor homogenate with 100 µg collagenase (Worthington Biochemical Corporation, Lakewood, NJ) at 37°C for 15 min at which point the reaction was stopped by dilution 1:1 with 5% human serum albumin (Sigma Aldrich, St. Louis, MO) in cell culture grade 1xPBS. The dissociated cells were then passed through a 70 µm cell strainer and centrifuged for 5 min at 300xg. The cell pellet was resuspended in 5 mL Red Blood Cell Lysing Buffer HybriMax (Sigma Aldrich, St. Louis, MO) and incubated at room temperature for 1 min. The solution was centrifuged for 7 min at 300xg and the supernatant decanted; this red blood cell lysis procedure was repeated until the cell pellet was no longer visibly red.

The final cell pellets collected were resuspended in PBS/1% BSA, the cells were counted with a hemocytometer after 1:1 dilution into Trypan blue solution (0.4%, Thermo Fisher Scientific, Waltham, MA), and the cell density adjusted to 2×10^6 cells mL⁻¹. Cells were incubated with fluorescently labeled proteins by gently mixing 90 µL of the cell suspension with 10 µL of 100 µM (ZEGFR)₂-ELP_{D1} (25 µM Alexa488) followed by a 1 h incubation with rocking at 4°C to minimize protein uptake by the cells. After incubation, cells were collected and washed three times with 0.5 mL PBS/1% BSA on ice, with final cell concentration adjusted to 2×10^5 cells mL⁻¹ prior to flow analysis. Live cells

were analyzed for population fluorescence on a BD Accuri Analyzer (BD Biosciences, San Jose, CA).

5.2.4 *In vivo* studies

We tested the *in vivo* efficacy of AffETox constructs in immunocompetent, eight-week-old C57BL/6 female mice (Jackson Laboratories, Bar Harbor, ME) with a syngeneic GBM tumor model, CT-2A-dmEGFRvIII-Luc (provided by Darell Bigner, Duke University). To establish orthotopic tumors, the mice were anesthetized with a continuous isoflurane vaporizer (2.5% isoflurane in 2 L min⁻¹) and then secured in a Stoelting stereotactic frame. The anterior cranial region was shaved and after disinfecting the area with Betadine, a 1 cm midline incision was made in the skin over the skull. The bregma was located and used to determine the coordinates for injection (0.5 mm anterior; 2 mm lateral). A sterile pencil was used to mark the coordinates and a Dremel 105 engraving cutter was used to gently break through the animal's skull. A mounting holder/stereotaxic injector on the frame held a Hamilton syringe containing the cell suspension in a PBS solution containing 3% methylcellulose (Sigma Aldrich, St. Louis, MO). A sterile 27G needle attached to the syringe was introduced through the skull and into the brain at a depth of 3.3 mm from the dura mater. We then injected 2×10^5 CT-2A cells in a volume of 5 μ L at a rate of 3.33 μ L min⁻¹. After injection and a 1 min delay, the syringe was removed, and a small amount of bone wax placed to occlude the

hole. The mouse was removed from the frame and the skin was closed using Vetbond tissue adhesive (Santa Cruz Animal Health, Dallas, TX).

After five days, the mice were randomized into groups by tumor size. The tumors were visualized by luminescence and the total flux quantified using an IVIS Lumina Series III imager (PerkinElmer, Waltham, MA). These values were correlated to tumor size and the groups accordingly stratified; after five days with this model, the tumors reach an approximate spherical volume of 0.5 mm³. The next day, six days after tumor inoculation, groups were then locally treated with AffETox, controls, or vehicle (1xPBS) directly injected into the established tumors. The mice were oriented in the stereotactic frame as before and the incision site located according to the original coordinates. The endotoxin-purified AffETox or control solutions were then injected intratumorally in a volume of 10 µl at a rate of 3 µl min⁻¹. After treatment, the mice were weighed and monitored daily for signs of distress until humane endpoints were reached or the termination of the study, on day 60. Overall survival and body weight changes were recorded for each of the treatment groups. Cumulative survival curves were compared using Kaplan–Meier analysis followed by the Mantel-Cox log rank test.

5.3 Results and discussion

5.3.1 Adapting strategies for immunotoxin-ELP synthesis

5.3.1.1 Click chemistry attachment for synthesis of antibody-ELP-toxin (AbETox)

Our first approach for synthesizing an immunotoxin-ELP conjugate involved conjugation of a monoclonal antibody (mAb) to a recombinantly expressed ELP-toxin fusion protein. The distinct cellular origin of these two components necessitates their conjugation after protein expression, purification, and, in the case of the mAb, functionalization. We designed two synthetic routes which would allow us to site-specifically conjugate the ELP-toxin on the C-terminus of the heavy chains of the mAb, maintaining specificity for EGFR and EGFRvIII. Our first strategy was to use Sortase A to functionalize the mAb heavy chains with a clickable DBCO handle, and then conjugate to *pAzF*-ELP-toxin via the azide-containing unnatural amino acid.

We expressed mAb with transiently transfected HEK293 cells and purified using Protein G affinity chromatography in high yield (60 mg L⁻¹). We confirmed >95% purity using SDS-PAGE (Figure 91).

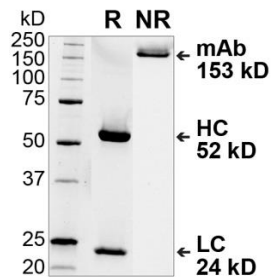


Figure 91: SDS-PAGE of purified mAb. Heavy and light chains are separated by addition of a reducing agent, β -mercaptoethanol (reduced, R), and the full-length visualized in the absence of this reducing agent (non-reduced, NR).

To functionalize the mAb with DBCO, we needed two additional components: purified, active Sortase A and its substrate, Gly₃-DBCO. We expressed Sortase A in *E. coli* and evaluated two variants – ELP-SrtA and His₈-mSrtA – for reaction efficiency, with the latter variant having a higher reported reaction efficiency, but which was not published until a year into this work.³³³ We expressed these and purified using either inverse transition cycling or His affinity purification in high yield (50 mg L⁻¹). We confirmed >95% purity of both constructs with SDS-PAGE (Figure 92).

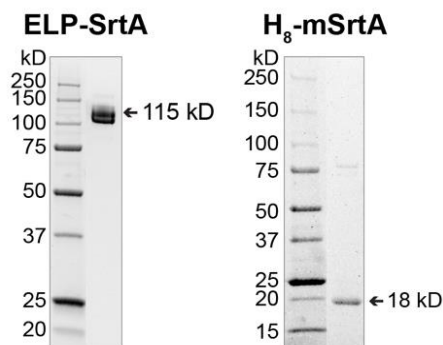


Figure 92: SDS-PAGE of purified Sortase A variants.

To synthesize the Gly₃-DBCO small molecule, we performed an amide condensation between a commercially available protected triglycine peptide and amine-functionalized DBCO (dibenzylcyclooctyne). We first confirmed successful ligation of these two components with electron spray ionization mass spectroscopy (ESI-LC/MS) prior to deprotection (Figure 93A). We then performed mass spectroscopy analysis after protecting group removal to confirm the molecular weight of our final reaction product,

Gly₃-DBCO (Figure 93B). Furthermore, we found no evidence of the protected starting material, allowing us to conclude the deprotection step was > 99% efficient.

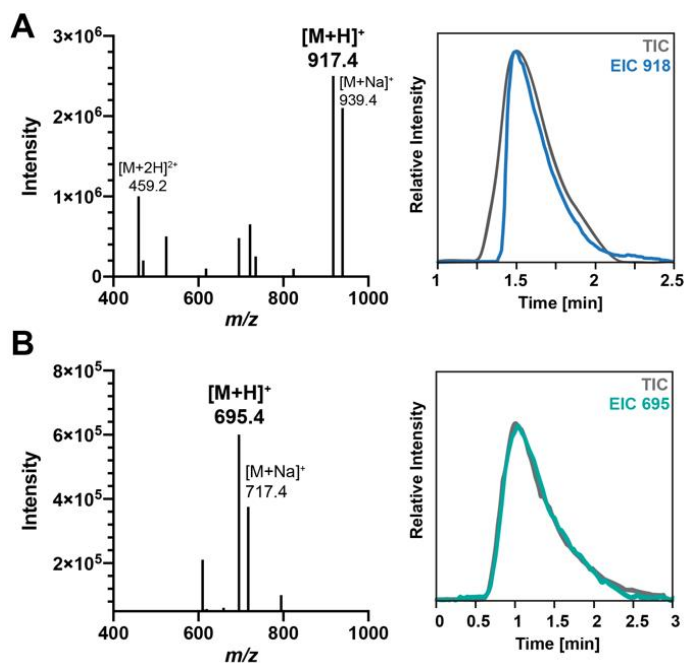


Figure 93: ESI-LC/MS analysis of Gly₃-DBCO synthesis. A) Mass spectrum and corresponding ion chromatograms of Fmoc-Gly₃-DBCO indicate successful product formation, with expected molecular weight 918.4 Da. B) Mass spectrum of final reaction product Gly₃-DBCO, with expected molecular weight 695.4 Da. TIC, total ion chromatogram; EIC, extracted ion chromatogram.

After securing the three necessary components – mAb, Sortase A, and Gly₃-DBCO – we proceeded with the enzymatic functionalization of mAb. We purified the reaction first with inverse transition cycling to remove ELP-SrtA, then with either magnetic beads or size exclusion chromatography to remove excess Gly₃-DBCO. We qualitatively confirmed success of the reaction and the reactivity of the mAb-DBCO heavy chains with fluorescent SDS-PAGE. We reacted the modified mAb-DBCO with a clickable, fluorescent dye, N₃-Cy5 and confirmed click reactivity of the heavy chain

(Figure 94). We quantified the extent of Gly₃-DBCO functionalization by monitoring the increase in absorbance at 310 nm, normalized to the absorbance at 280 nm. This characterization revealed a labeling efficiency of $31.2 \pm 9.4\%$, which indicates approximately one third of total mAb is reactive and able to participate in the final click reaction with *pAzF*-ELP-toxin. As we later determined with mass spectroscopy, which revealed extensive DBCO degradation after even short-term storage, this percentage is more reflective of the instability of DBCO rather than enzymatic efficiency.

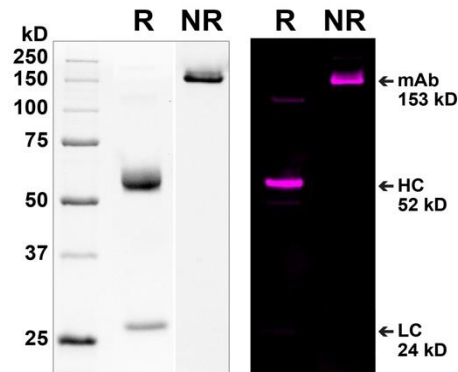


Figure 94: Confirming DBCO functionalization of mAb with fluorescent SDS-PAGE. mAb-DBCO was reacted with azide-Cy5 and visualized for fluorescence. Reduced sample confirms successful modification of the heavy chain. Corresponding stain-free gel (left) shows mAb is unaffected by DBCO labeling.

Prior to click conjugation with *pAzF*-ELP-toxin, we first validated mAb-DBCO specificity for the mAb targets, EGFR and EGFRvIII. We incubated fluorescently labeled mAb-DBCO by click attachment of N₃-Cy5 and incubated this fluorescently-labeled antibody with stably transfected murine fibroblast cells which overexpress human EGFR or EGFRvIII. The prominent increase in population fluorescence as compared to unlabeled mAb controls for both cell lines confirms the successful recognition of these

two receptors and, importantly, indicates the Sortase A functionalization has not impaired target recognition. We further confirmed specificity of mAb binding with a negative control, untransfected murine fibroblast line (Figure 95).

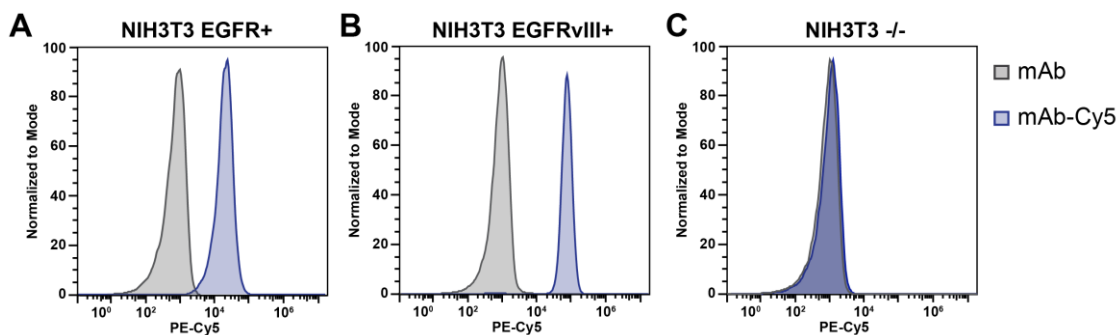


Figure 95: Confirming specificity of mAb for EGFR and EGFRvIII using flow cytometry. mAb-DBCO was reacted with fluorescent N₃-Cy5 and incubated with murine NIH3T3 fibroblasts that are (A) stably transfected with EGFR, (B) with EGFRvIII, or (C) untransfected controls.

We expressed *pAzF*-ELP-toxin in BL21(DE3) *E. coli* under the control of the T7 promoter with *pAzF* added directly to the culture media. This recombinant protein accumulated in inclusion bodies and required refolding for solubilization; one important outcome of this component of this work was unnatural amino acid incorporation in an insolubly expressed protein. We confirmed successful expression and assessed purity with SDS-PAGE. We further qualitatively assessed successful *pAzF* incorporation by fluorescently labeling the *pAzF* residue with a clickable, fluorescent DBCO-Cy5 dye and visualizing with SDS-PAGE (Figure 96). We quantified the dye labeling efficiency as an indirect measure of *pAzF* incorporation efficiency and calculated $12.0 \pm 1.3\%$ labeling after DBCO-Cy5 purification. Based on our previous studies with this expression

system, we expect the *pAzF* incorporation efficiency to be $\geq 98\%$. We therefore attributed the incongruous labeling efficiency again to the instability of DBCO, which contributes to our challenges with click synthesis of AbETox via this moiety.

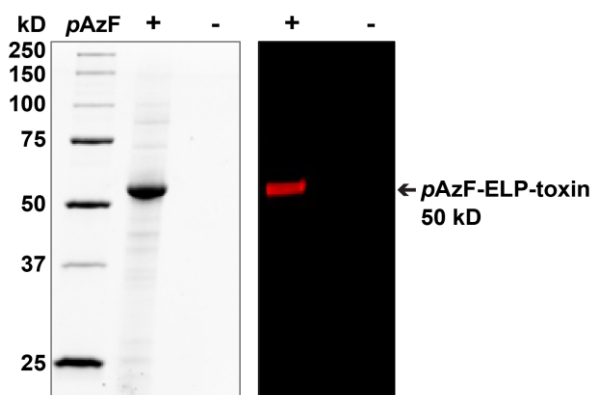


Figure 96: Confirming *pAzF* incorporation in *pAzF*-ELP-toxin with fluorescent SDS-PAGE. *pAzF*-ELP-toxin was reacted with DBCO-Cy5 and visualized for fluorescence. There was no appreciable protein produced in the absence of *pAzF* added to the growth media.

We proceeded with our initial attempts to perform click conjugation of mAb-DBCO and *pAzF*-ELP-toxin. We assessed successful conjugation by SDS-PAGE; the appearance of a new band in the reduced sample lane at a higher molecular weight than the heavy chain would indicate successful attachment of *pAzF*-ELP-toxin. We first evaluated our click conditions with a *pAzF*-ELP control protein. While we did observe the appearance of a new band at the expected molecular weight of a heavy chain conjugated to this ELP, the conversion efficiency is not appreciable as judged by the relative size of the bands in this lane (Figure 97).

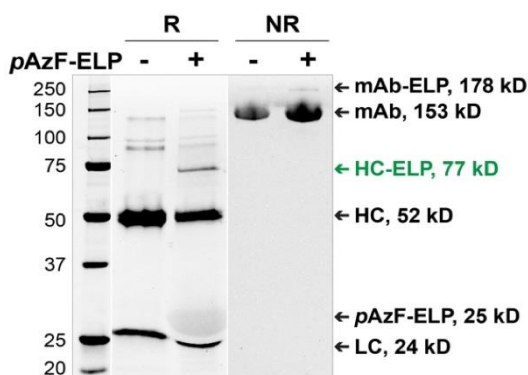


Figure 97: SDS-PAGE demonstrating click attachment of mAb-DBCO and *pAzF*-ELP. The appearance of the new product, HC-ELP (green), in the reduced sample lane with addition of *pAzF*-ELP, demonstrates click attachment of the heavy chain and ELP. R, reduced; NR, non-reduced.

We achieved similarly low conversion with the attachment of *pAzF*-ELP-toxin, which proved too insignificant to attempt to quantify (Figure 98).

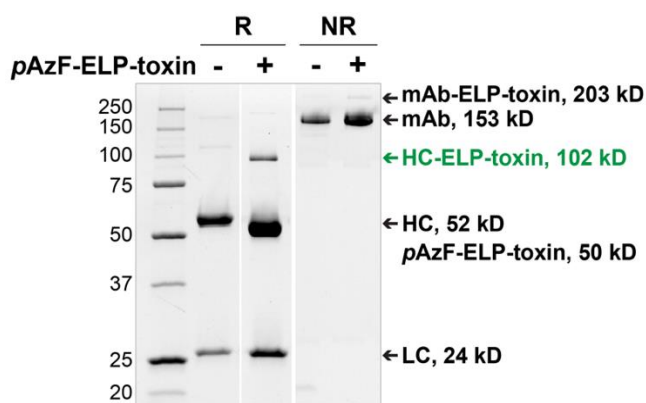


Figure 98: SDS-PAGE demonstrating click attachment of mAb-DBCO and *pAzF*-ELP-toxin. The appearance of the new product, HC-ELP-toxin (green), in the reduced sample lane with addition of *pAzF*-ELP-toxin, demonstrates click attachment of the heavy chain and the ELP-toxin fusion. R, reduced; NR, non-reduced.

Given the low yield of desired AbETox product, we adapted our strategies to eliminate our dependence on DBCO, the small molecule required for these reactions, the instability of which severely limited the click reaction efficiency.

5.3.1.2 Sortase A-mediated fusion for synthesis of antibody-ELP-toxin (AbETox)

We adapted our Sortase A-based strategy to directly enzymatically fuse the mAb and ELP-toxin. Given that we had already produced and characterized the mAb with the Sortase A recognition motif, LPETG, in the C-terminus of the heavy chain, we merely needed to genetically modify the ELP-toxin gene to incorporate the Sortase A substrate, Gly₃, at the N-terminus. This updated strategy streamlines the conjugation process, eliminating the additional small molecule substrate and click reaction step.

We successfully cloned the necessary Gly₃-ELP-toxin gene and expressed this recombinant fusion protein in BL21(DE3) *E. coli* as before. We confirmed successful Gly₃-ELP-toxin expression, refolding, and purification with SDS-PAGE (Figure 99).

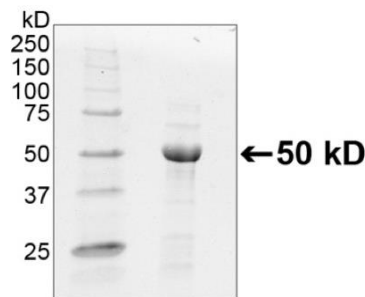


Figure 99: SDS-PAGE of purified Gly₃-ELP-toxin.

Having the three components required for our new synthetic strategy for AbETox in hand – mAb, Gly₃-ELP-toxin, and Sortase A – we proceeded with optimizing the enzymatic attachment and purification. Through these experiments, we identified a non-specific Sortase A intra-mAb dimerization of the heavy chains, as evidenced by the appearance of a band at double the molecular weight of one heavy chain in a negative

control Sortase A reaction (Figure 100A). Given that the molecular weight of one heavy chain is approximately equivalent to the molecular weight of Gly₃-ELP-toxin, we expressed Gly₃-toxin and performed the same Sortase A labeling to evaluate the ratio of desired product to the HC-HC dimer. As we determined from the SDS-PAGE, the HC-HC dimer is the major product being formed as judged by the relative weight of these bands (Figure 100B). This side-reaction persisted, albeit to a lesser extent, with the use of the higher efficiency Sortase A mutant we tested, H₈-mSrtA.

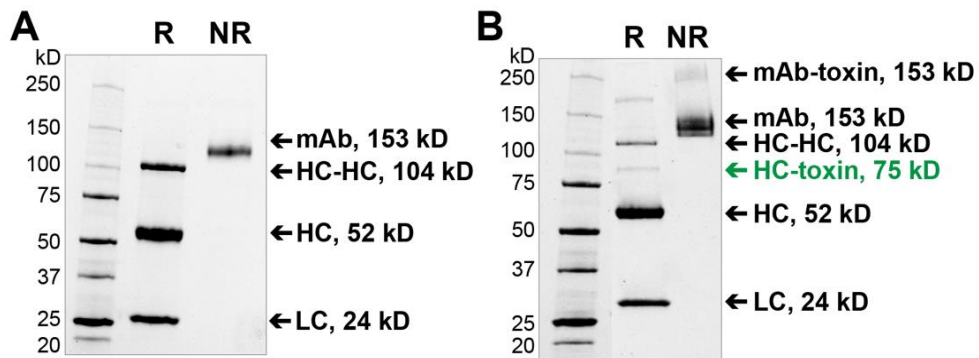


Figure 100: SDS-PAGE of Sortase A reaction products and non-specific activity. (A) Negative control reaction with mAb, free Gly₃ peptide, and Sortase A illustrates formation of intramolecular HC-HC dimer. (B) Sortase A reaction with mAb, Gly₃-toxin, and Sortase A illustrates ratio of HC-HC to HC-toxin formation.

The non-specific Sortase A labeling reduced the overall reaction efficiency and made our original purification strategies – either reverse His purification of doubly-labeled AbETox (Figure 87) or inverse transition cycling of singly-labeled AbETox (Figure 88) – largely ineffectual. We modified our proteins to include the His₆ tag instead on the ELP-toxin component, rather than the heavy chain of the mAb, to enable His-tag purification of the AbETox conjugate after Protein L purification (Figure 89, Figure 101).

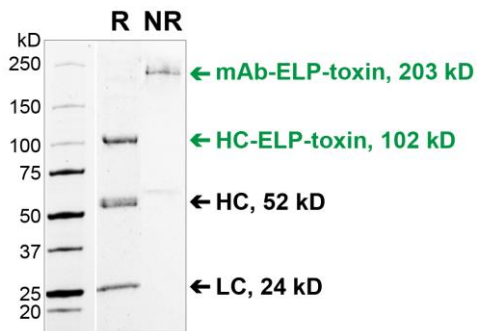


Figure 101: SDS-PAGE of purified AbETox.

It is important to note, however, that given the characterization methods employed and molecular weight of the components involved, we are unable to ascertain whether our AbETox product also bears an intramolecular HC-HC dimer in addition to the appended Gly₃-H₆-ELP-toxin. We confirmed successful Gly₃-H₆-ELP-toxin addition with MALDI characterization after tryptic digest, though, we are unable to account for the level of HC-HC dimers using this method (Figure 102).

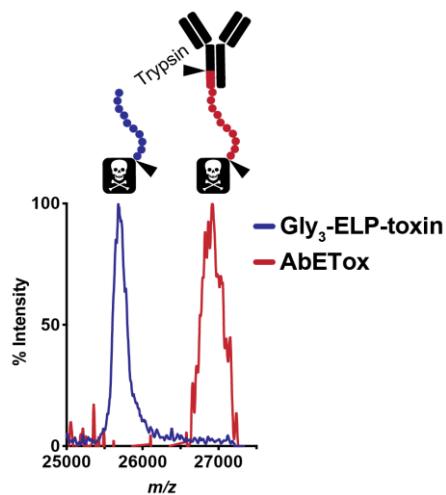


Figure 102: MALDI-TOF/MS analysis of AbETox to confirm ELP-toxin attachment. MALDI spectrum of ELP-toxin (blue) and AbETox (red) tryptic digests

shows expected molecular increase in digest fragment after Sortase A modification (expected Δ : 1298.2 Da, observed Δ : 1287.8 Da).

Given the uncertainty about the exact composition of AbETox, and because the yield of this purified material was too low for the additional *in vitro* and *in vivo* characterization necessary, we adapted our immunotoxin synthesis strategy further to eliminate the need to express and conjugate proteins of distinct cellular origin.

5.3.1.3 Recombinant fusion of affibody-ELP-toxin (AffETox)

Given the low yields for the purified AbETox conjugates, we turned our attention to developing a recombinant fusion protein that could be expressed exclusively in *E. coli*. While we already had experience with expression of the ELP and toxin components in *E. coli*, we needed to identify a targeting domain that could be expressed in bacteria in high yield as an N-terminal fusion protein, would be stable enough to withstand the refolding process, and with an affinity for EGFR comparable to that of the monoclonal antibody. We identified an affibody domain, ZEGFR, that fulfilled each of these criteria. Affibodies are highly stable, even in the absence of any disulfide bonds, and have one of the highest protein folding rate constants ever measured; affibodies spontaneously fold approximately 200,000 times faster than superfolder GFP.³²² The ZEGFR affibody has nanomolar affinity for EGFR and superior affinity as a head-to-tail dimer than a monomer.³⁰⁸ We successfully cloned and expressed the AffETox library, as described in Sections 5.2.1.5 and 5.2.2.2, and assessed purity and molecular weight using SDS-PAGE (Figure 103).

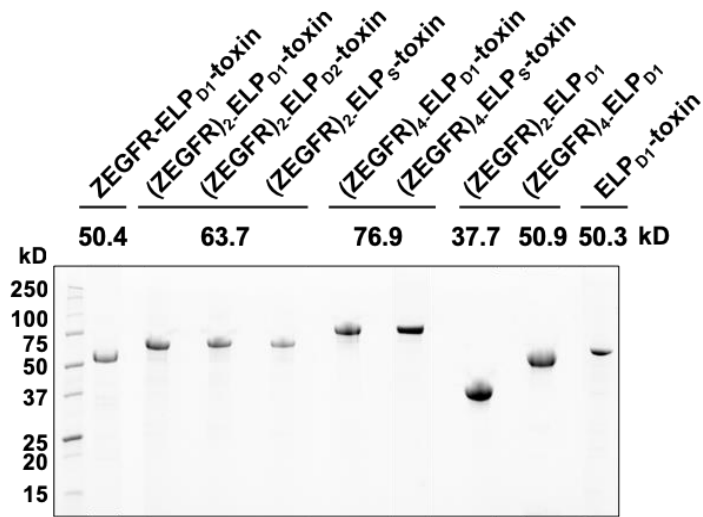


Figure 103: SDS-PAGE of AffETox library and control proteins.

5.3.2 Characterization of AffETox library

5.3.2.1 Thermal responsivity of AffETox

To evaluate the ability of the AffETox constructs to form a coacervate depot *in vivo*, we assessed the phase transition behavior of our AffETox library. We first evaluated the transition temperatures (T_t) by UV/Vis spectroscopy as a function of solution temperature, as the thermally-triggered coacervation results in a visual change in turbidity (Figure 104). The depot-forming AffETox proteins undergo a rapid soluble-to-insoluble transition when heated above their T_t ; we therefore anticipate immediate depot formation upon injection of these constructs into the brain.

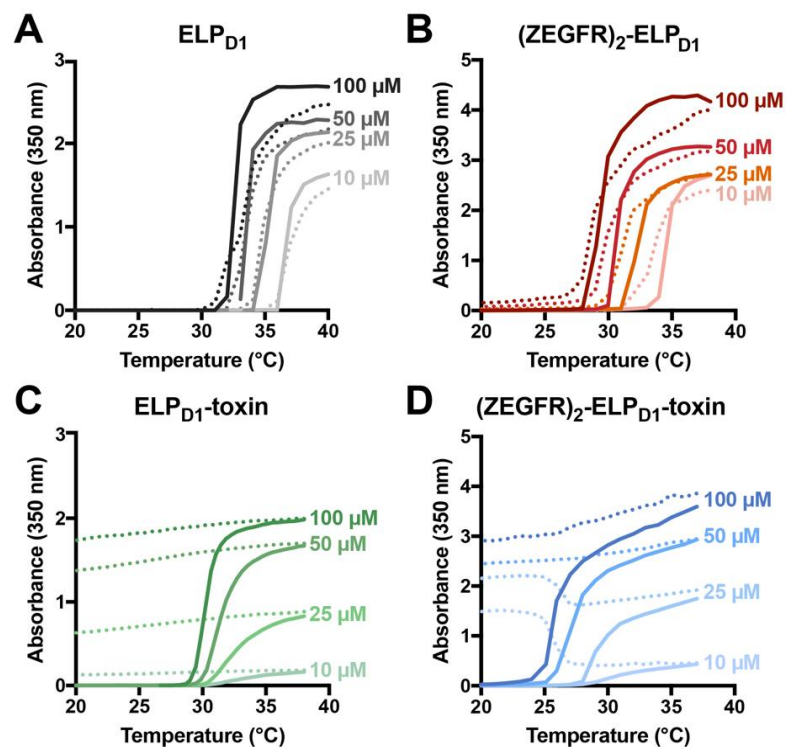


Figure 104: Phase transition behavior of AffETox and control proteins as assessed by thermal ramp UV/Vis spectroscopy. The rapid increase in turbidity of the solutions of (A) ELP_{D1}, (B) (ZEGFR)₂-ELP_{D1}, (C) ELP_{D1}-toxin, and (D) (ZEGFR)₂-ELP_{D1}-toxin indicate the unimer-to-aggregate transition or T_t . The solid lines correspond to the optical density upon heating; the dotted lines represent the optical density upon cooling.

We used this data to construct semi-log plots of T_t versus concentration for each construct to provide a calibration of the relationship between injection concentration and construct solubility (Figure 105). The insoluble-to-soluble transition and therefore depot release will occur at the concentration at which these lines intersect with body temperature (dotted horizontal line), with the rate of dissolution proportional to the slope of these lines. This log-linear relationship therefore also provides an estimate of the degree of dilution needed to reverse the transition.

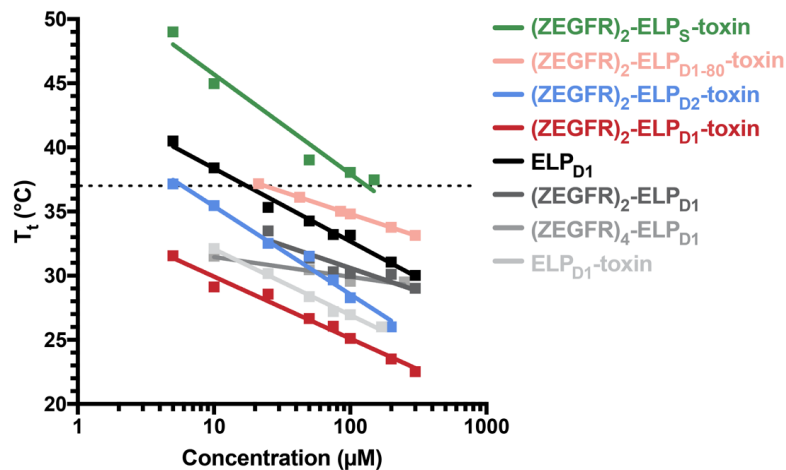


Figure 105: Relationship between T_t and concentration for AffETox library. Dotted line indicates body temperature, 37°C.

We identified two candidates (blue and red curves) whose T_t versus concentration behavior indicates they that will both form depots but demonstrate different rates of release. The range of possible injection concentrations with viable T_t 's for depot formation affords us the flexibility to further tune depot release. In contrast, the soluble construct (green curve) has a T_t above body temperature across the range of relevant concentrations and will remain soluble upon injection into the brain. Surprisingly, despite having a longer ELP block than the $(ZEGFR)_2$ - ELP_{D1} -toxin construct, the $(ZEGFR)_2$ - ELP_{D1-80} -toxin construct exhibits a higher T_t at each concentration (pink curve). This behavior is not what would be expected: canonically, increasing the length of an ELP lowers its T_t .¹⁹⁴ The presence of the fusion protein partners (ZEGFR, toxin) demonstrably affects the phase transition behavior in unique ways, a phenomenon which merits future exploration.

5.3.2.2 Protein translation inhibition by toxin

To validate the activity of the toxin when fused to the ELP, and confirm the mechanism of action through irreversible ADP-ribosylation and inactivation of elongation factor-2 (EF-2), which effectively blocks all protein translation, we modified a published cell-free translation inhibition assay.³⁴¹ As described in Section 5.2.3.3, this assay quantifies luminescence output from a luciferase reporter as a direct measure of protein synthesis. The benefit of this approach is the lack of dependence on intact, live cells associated with standard cell viability assays, allowing us to confirm activity of the toxin without an exogenous targeting domain attached. This aspect was particularly critical during synthesis of the AbETox construct to confirm activity of the ELP-toxin protein prior to attachment of the monoclonal antibody (Figure 106).

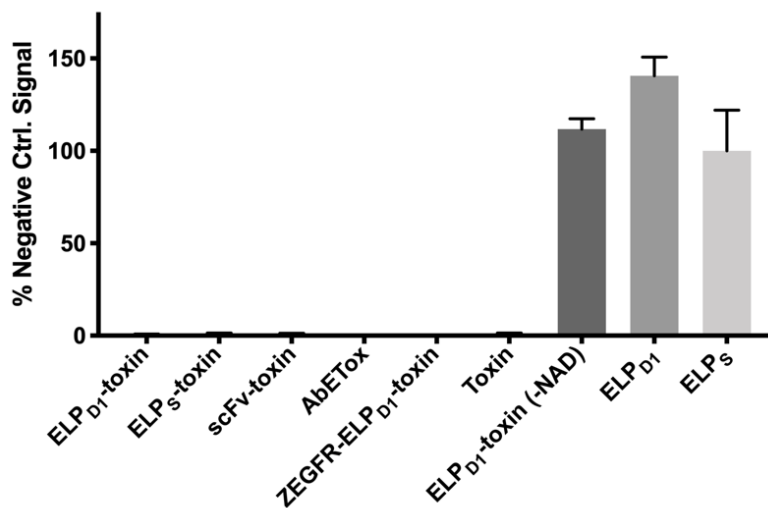


Figure 106: Cell-free translation inhibition of luciferase expression by immunotoxins and control proteins. The resulting luminescent signal from each of the experimental conditions was normalized to a negative control reaction with no inhibitory components added.

The negative control, without any additional components added, provided a baseline level of luciferase expression and therefore luminescent output with which to normalize our experimental conditions. Upon addition of the ELP-toxin fusion proteins (both ELP_{D1}-toxin and ELP_S-toxin), the luminescent signal is $\leq 1\%$ of the positive control, and therefore indicates inhibition of $\geq 99\%$ of protein translation with the toxin and is comparable to the activity of an scFv-toxin control (provided by Darell Bigner, Duke University). We found a similar level of absolute translation inhibition with both the AbETox ($0.2 \pm 0.06\%$) and ZEGFR-ELP_{D1}-toxin ($0.5 \pm 0.06\%$) constructs, as well as a toxin-only control ($1.0 \pm 0.2\%$). A reaction in which we withheld NAD⁺, the necessary cofactor for *P. aeruginosa* exotoxin A, had comparable levels of luminescence as the negative control reaction. We also tested the impact of adding ELP_{D1} or ELP_S on protein translation, a necessary control reaction given the phase transition behavior of ELP and the incubation temperature for the assay at 30°C. As anticipated, neither of these ELPs negatively affected protein translation, allowing us to confirm that the potent inhibition of protein translation can be attributed to the active toxin.

5.3.2.3 *In vitro* characterization of AffETox

The complete inhibition of protein translation by our immunotoxin rapidly instigates apoptosis of target-bearing cells. We tested our immunotoxin first in stably transfected murine fibroblasts which overexpress either human EGFR or EGFRvIII to confirm specificity for these receptors and assess potency of the drug in relevant cell

lines. We evaluated the potency of AffETox constructs bearing one, two, or four affibody domains by treating adherent fibroblasts with serial dilutions of these proteins and quantifying the percentage of viable cells after 72 h of treatment as compared to untreated controls (Figure 107).

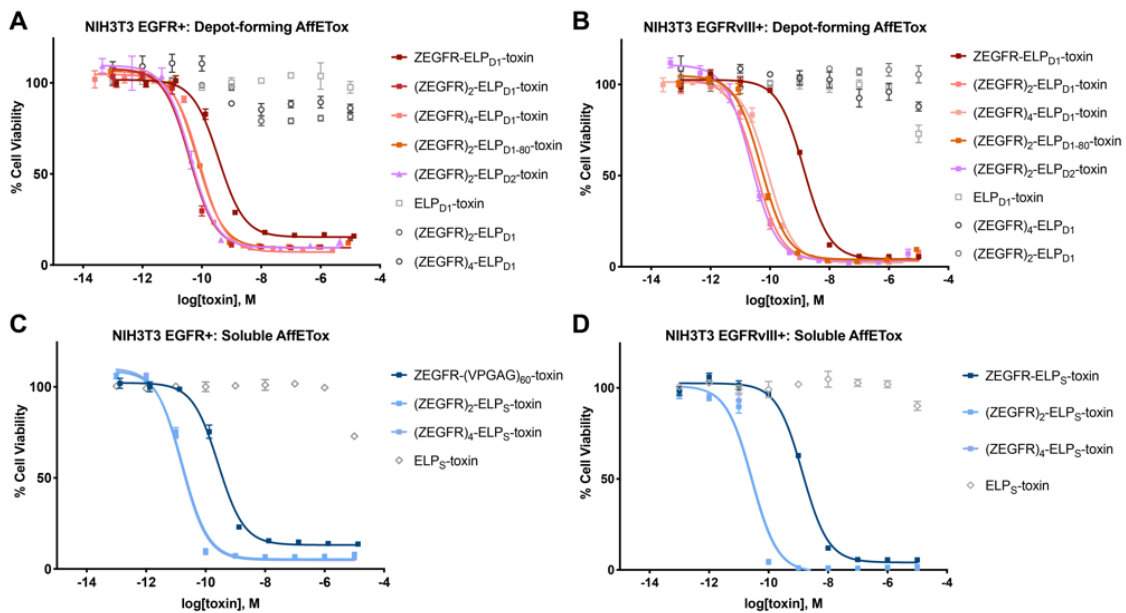


Figure 107: Cytotoxicity of AffETox constructs in transfected murine fibroblasts expressing human EGFR or EGFRvIII. (A), (B) AffETox with depot-forming ELPs. (C), (D) AffETox with soluble ELPs.

We found that both (ZEGFR)₂-ELP-toxin and (ZEGFR)₄-ELP-toxin were more potent than (ZEGFR)-ELP-toxin, regardless of the ELP sequence. This effect was true for both the EGFR+ and EGFRvIII+ fibroblast lines, and which revealed the previously unknown specificity of this affibody domain for EGFRvIII. The negative control proteins, (ZEGFR)_N-ELP or ELP-toxin, showed no significant potency in these cell lines, indicating both the ZEGFR affibody and toxin are required on the same molecule for

cytotoxic effect. AffETox is highly potent in these cell lines, with IC₅₀ values in the low picomolar range, comparable to that reported for similar *P. aeruginosa*-bearing immunotoxins.³²⁴ The ELP_s-bearing AffETox constructs were slightly more potent than those with a depot-forming ELP, likely due to the phase transition of the latter during treatment and therefore slightly lower available material in the wells for cytotoxic effect (Figure 108).

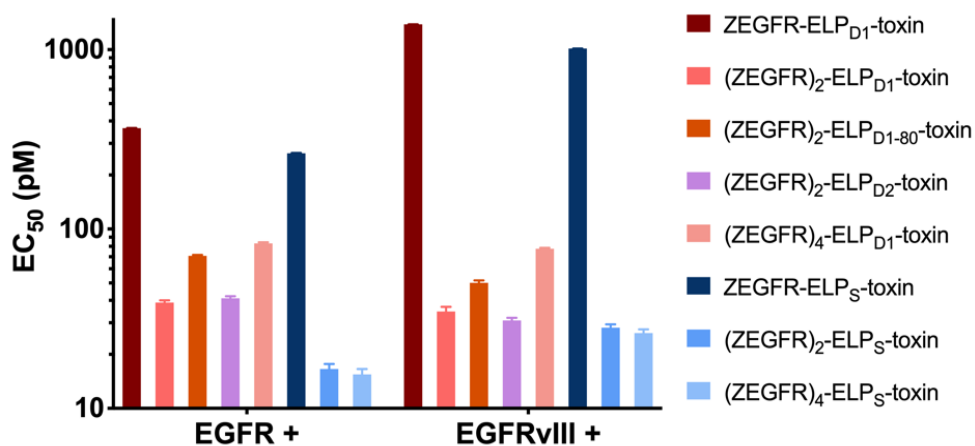


Figure 108: Summary of IC₅₀ values for AffETox library in murine fibroblasts expressing EGFR or EGFRvIII.

We further confirmed specificity of the affibody domain for these two receptors in untransfected murine fibroblasts, which exhibited no cell death after treatment, and bolsters our confidence in an expected lack of nonspecific toxicity *in vivo* (Figure 109).

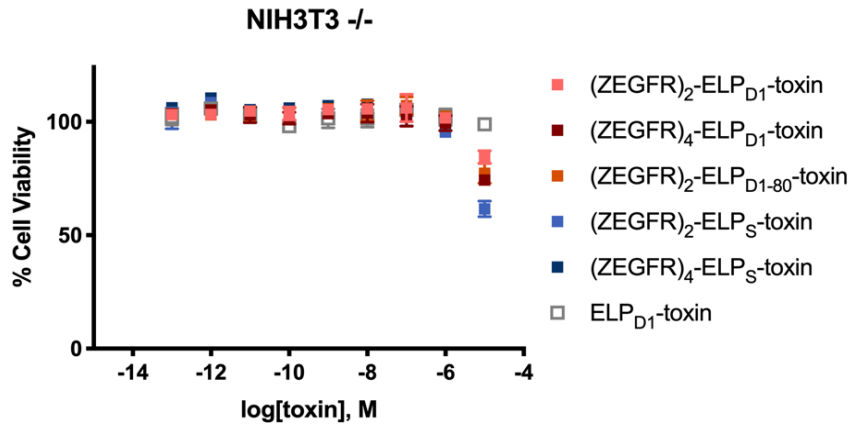


Figure 109: Untransfected murine fibroblasts which do not express EGFR or EGFRvIII are not sensitive to treatment with AffETox.

We further confirmed picomolar efficacy of our AffETox constructs in an EGFR-overexpressing patient-derived squamous cell carcinoma line, A431.²⁶⁵ We observed a similar increase in potency with the dimeric and tetrameric AffETox constructs as compared with the monomeric constructs, though this effect is less pronounced than with the NIH3T3 lines (Figure 110).

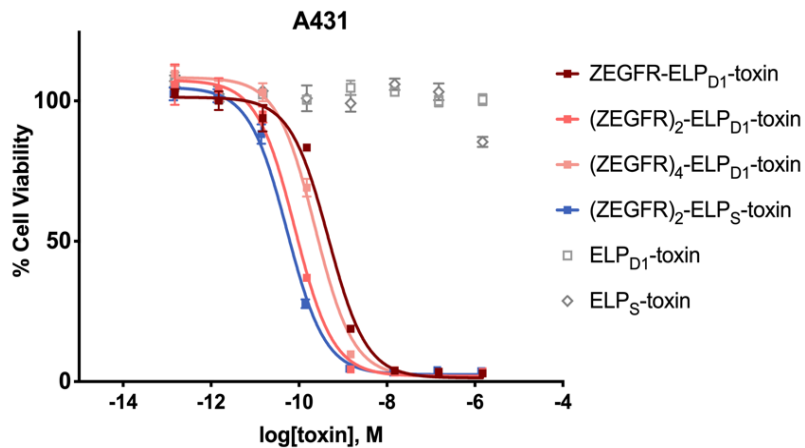


Figure 110: AffETox constructs demonstrate picomolar efficacy in A431 squamous cell carcinoma lines.

We next assessed AffETox efficacy in both human and mouse GBM lines to identify the best cell line for our *in vivo* studies. We first evaluated potency in two patient-derived tumor lines (Figure 111). It is important to note that patient-derived GBM lines lose EGFR amplification and overexpression with establishment in culture and continued passage.³⁴² The EGFR genomic amplification is most frequently carried in GBM cells as double minute extra-chromosomes, which must be maintained in high copy number through repeated selection during replication; these fragments are routinely lost under tissue culture conditions in complete media.³⁴³⁻³⁴⁴

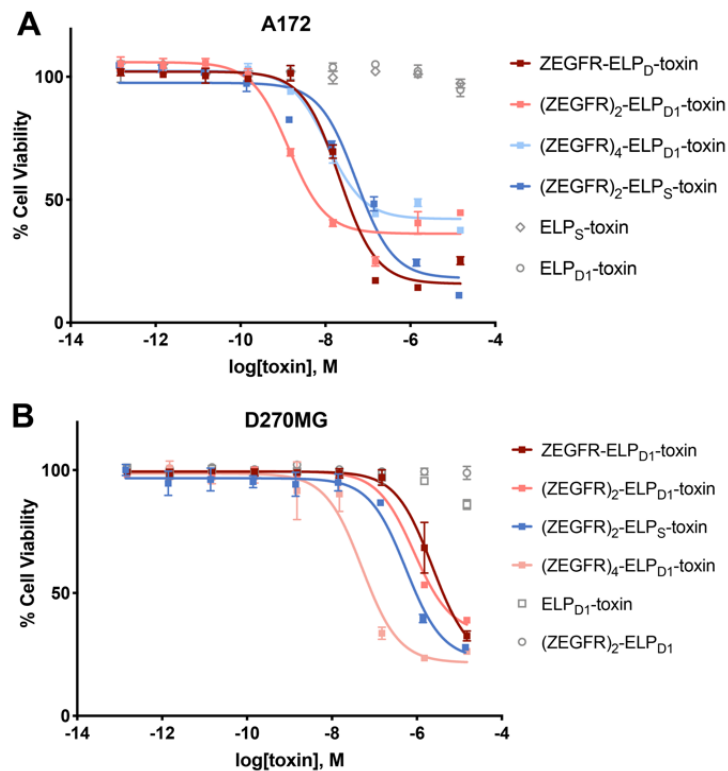


Figure 111: Efficacy of AffETox in two patient-derived GBM lines. AffETox exhibits nanomolar potency in (A) A172 and (B) D270MG established tumor cell lines.

While our AffETox constructs were modestly potent in these two lines, A172 and D270MG, the order of magnitude increase in IC₅₀ can be directly attributed to the lower levels of surface EGFR and is constituent with previous findings.³⁴⁵ The levels of EGFR mRNA are as many as twenty times lower in established lines than the corresponding xenograft tumor cells, indicating that this loss of potency is not anticipated to be recapitulated *in vivo*.³⁴²

To maximize our options for *in vivo* tumor models, and confirm specificity of AffETox for murine EGFR, we also assessed cytotoxicity in two mouse GBM lines, developed and generously provided by Darell Bigner in the Duke University Preston Robert Tisch Brain Tumor Center. SMA560-mEGFRvIII-D2C7-FFLuc-sort3 was established from a spontaneous brain tumor developed in VM/Dk mice.³⁴⁶ CT-2A-mEGFRvIII-D2C7-FFLuc-Inf1-sort1 was established from a chemical carcinogen-induced brain tumor in C57BL/6 mice.³⁴⁷ Both of these lines express endogenous mouse WT EGFR and have been stably transfected to express a mouse EGFRvIII with seven point mutations which preserve the human EGFRvIII epitope. These lines also both express luciferase for imaging purposes *in vivo*. We found the AffETox constructs we tested were potent in both lines, with IC₅₀ values in the picomolar range (Figure 112). However, the constructs were more potent in the CT-2A line, and we therefore selected this line for future *in vivo* studies. For example, the IC₅₀ of (ZEGFR)₂-ELP_{D1}-toxin in CT-2A was 64.5 pM and that of the same construct in the SMA560 was 196 pM.

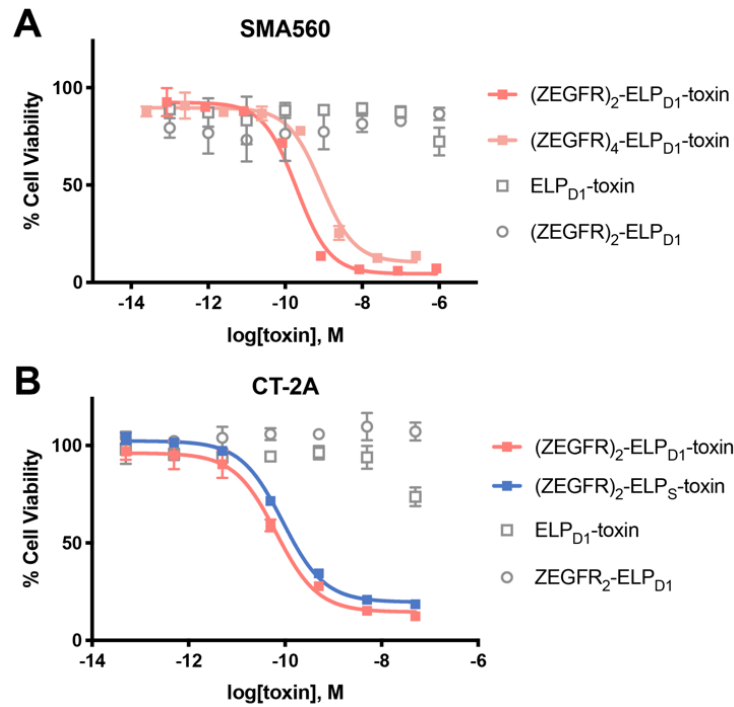


Figure 112: Potency of AffETox in two murine GBM lines. AffETox exhibits picomolar efficacy in (A) SMA560 and (B) CT-2A tumor lines.

We further confirmed the specificity and utility of AffETox using flow cytometry performed on both the murine NIH3T3 fibroblasts transfected with EGFR and on explanted D270MG xenograft cells. D270MG xenograft cells were used to establish subcutaneous tumors in nude BALB/C mice, which were then removed by dissection, homogenized, and processed into a single-cell suspension. (ZEGFR)₂-ELP_{D1} was fluorescently labeled at its N-terminus and incubated with either cell line, followed by washing and analysis with flow cytometry for population fluorescence. (ZEGFR)₂-ELP_{D1} binds to both cell populations, with expectedly higher population fluorescence in the model transfected NIH3T3 EGFR+ line (Figure 113). This indicates the specificity of these

constructs will be well-maintained in the orthotopic model cell line, ensuring the success of any future *in vivo* studies with the D270MG xenograft cell line.

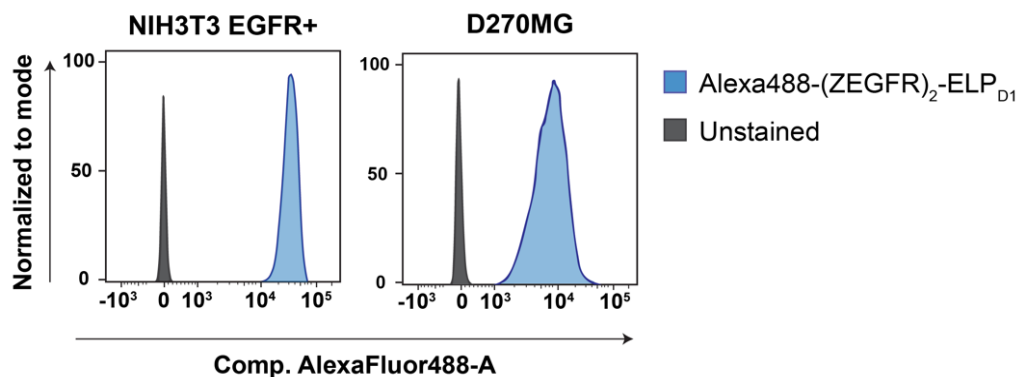


Figure 113: Flow cytometry confirms binding of ZEGFR affibody to EGFR-expressing fibroblasts and xenograft GBM line.

5.3.3 *In vivo* efficacy of AffETox

We evaluated the *in vivo* efficacy of AffETox in an orthotopic, syngeneic GBM model. These studies were designed with the assistance of Vidya Chandramohan and all animal work performed by Charlotte McDowall and Scott Parker. CT-2A tumors were established orthotopically in immunocompetent C57BL/6 mice at precise intracranial coordinates, enabled by the use of a stereotaxic frame.³⁴⁸ After five days of growth, the established, luminescent tumors were imaged and the resulting signal correlated to tumor volume, allowing us to randomize the mice into treatment groups. The following day, six days after tumor inoculation, we treated the mice intratumorally with AffETox, using the same coordinates as tumor implantation to ensure local delivery. We monitored the mice daily for any symptoms of neurological distress as well as body

weight changes below the acceptable threshold, until the humane endpoint or termination of the study sixty days after tumor inoculation (Figure 114).

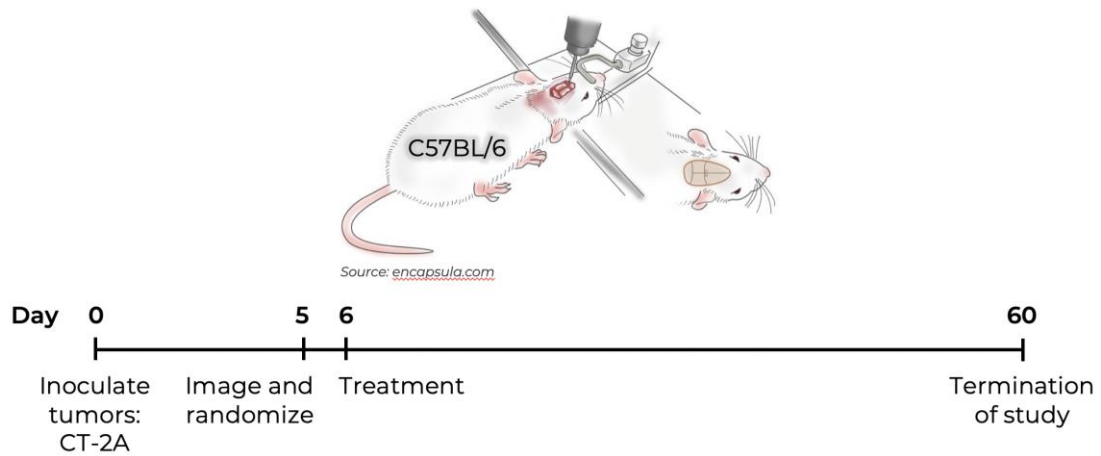


Figure 114: Study design for AffETox efficacy in an orthotopic, syngeneic mouse GBM tumor model. The mouse is positioned with a stereotaxic frame to ensure local delivery of the AffETox to the intracranially implanted tumors.³⁴⁸

We first needed to identify the maximum tolerated dose (MTD) of AffETox with this tumor model to develop an understanding of the therapeutic window for this drug. We selected the initial doses by dose-matching with previous work by the Bigner group with immunotoxins and this tumor model.^{324, 349} Our treatment groups for this pilot study included one depot-forming and one soluble dimeric AffETox ((ZEGFR)₂-ELP-toxin), each with three increasing doses (Table 11).

Table 11: Treatment groups for GBM maximum tolerated dose study #1

Treatment	<i>n</i>	Dose (μ M)	Dose (μ g)
Vehicle	5	--	--
(ZEGFR) ₂ -ELP _{D1} -toxin	5	0.5	0.3
	6	1.5	1
	6	5	3
(ZEGFR) ₂ -ELP _S -toxin	5	0.5	0.3
	6	1.5	1
	6	5	3

If there is drug-induced toxicity, this will present in the mice within 72 h after treatment as neurological distress (hunching, ataxia, lethargy), rapid weight loss, or sudden death. These symptoms will intensify over the course of the three days post-treatment and require humane euthanasia. In this study, none of the treatment groups exhibited drug-related toxicity and all deaths at later time points can be attributed to tumor-related toxicity. While we were unable to assess the MTD from these doses, we did observe significant improvement to median and overall survival in several of the treatment groups (Figure 115). Remarkably, two of the soluble AffETox treatment groups had the greatest improvement to survival over the vehicle control. Given that several mice from each group survived until the termination of the study, these mice presumably had complete tumor regression.

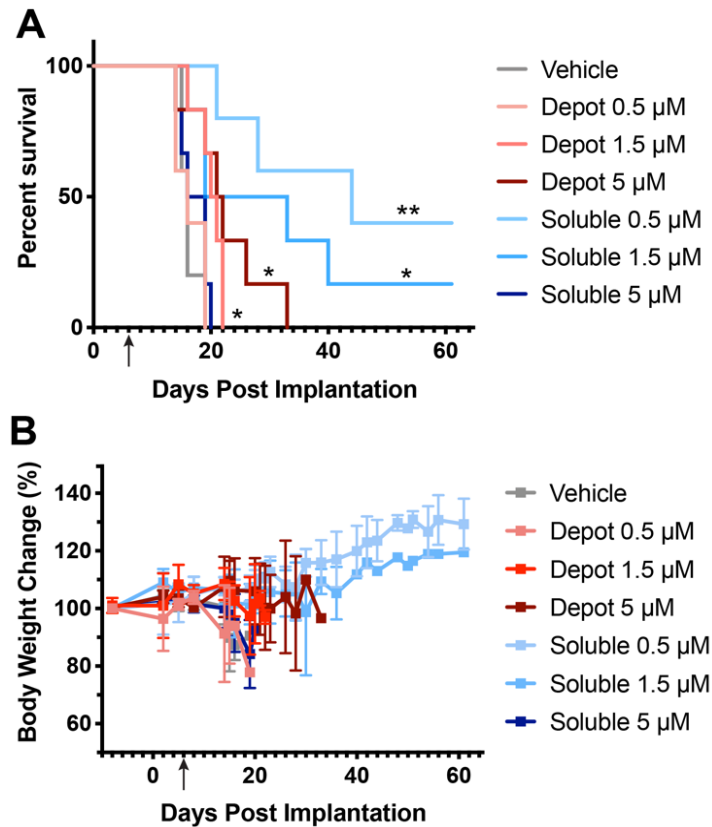


Figure 115: AffETox efficacy in CT-2A orthotopic model (MTD study #1). (A) Cumulative survival of mice reveals four treatment groups with significantly improved survival as compared to vehicle control, with () indicating $p < .01$ and (*) indicating $p < .05$ (Mantel-Cox log rank test). (B) Body weight change as a percentage of starting body weight. Arrow indicates day of AffETox treatment.**

This exceptional response to soluble AffETox, with the 0.5 μM dose extending the median survival to 44 days post-tumor inoculation, is a result that has not previously been achieved with a single injection of any immunotoxin formulation in this tumor type (Table 12). These results bolstered our confidence in the effectiveness of AffETox and suggested that additional fine-tuning of the depot release kinetics was needed to

achieve sustained-release, with the expectation of improving survival even beyond that observed with the soluble formulation. This hypothesis, coupled with the lack of identification of the MTD from these doses, provided the motivation for a follow-up *in vivo* study with dose escalation and additional depot-forming AffETox.

Table 12: Median survival of treatment groups in AffETox MTD study #1

Treatment	Dose (μM)	Median survival (days)
Vehicle	--	16
(ZEGFR) ₂ -ELP _{D1} -toxin	0.5	16
	1.5	20
	5	21.5
(ZEGFR) ₂ -ELP _S -toxin	0.5	44
	1.5	26
	5	17.5

In the second animal study, we had several goals: 1) assess the replicability of the best-performing soluble AffETox construct; 2) identify the MTD; 3) compare our treatment to an existing immunotoxin currently in clinical trials, D2C7; and 4) identify the best-performing depot formulation. For the latter, we introduced our second depot-forming dimeric AffETox candidate ((ZEGFR)₂-ELP_{D2}-toxin) as this construct exhibited a less hydrophobic profile than ELP_{D1} and also expectedly has a different rate of release. The inverse log-linear relationship between T₁ and concentration, and therefore dilution profile, of ELP_{D2} has a more negative slope than ELP_{D1}, suggesting a weaker depot and

more rapid release. We also increased the number of mice per group to $n = 8$ for all groups to improve confidence in our findings (Table 13).

Table 13: Treatment groups for GBM maximum tolerated dose study #2

Treatment	Dose (μM)	Dose (μg)
Vehicle	--	--
(ZEGFR) ₂ -ELP _{D1} -toxin	15	10
	45	30
(ZEGFR) ₂ -ELP _{D2} -toxin	7.5	5
	15	10
	45	30
(ZEGFR) ₂ -ELP _S -toxin	0.5	0.3
D2C7	0.5	0.3

We were able to achieve some of the goals outlined for this study, but these findings also revealed several areas which warrant further exploration and will require additional *in vitro* and *in vivo* studies. In terms of the achievements from this study, we were able to identify a toxicity-inducing dose at the maximum AffETox dose tested in this study. Both the (ZEGFR)₂-ELP_{D1}-toxin and (ZEGFR)₂-ELP_{D2}-toxin constructs at a dose of 45 μM resulted in rapid, significant body weight loss and co-incident morbidity within the first 72 h following treatment (Figure 116). Whether this dose is also the MTD will require further investigation, but this dose importantly provides an upper-bound for the therapeutic window.

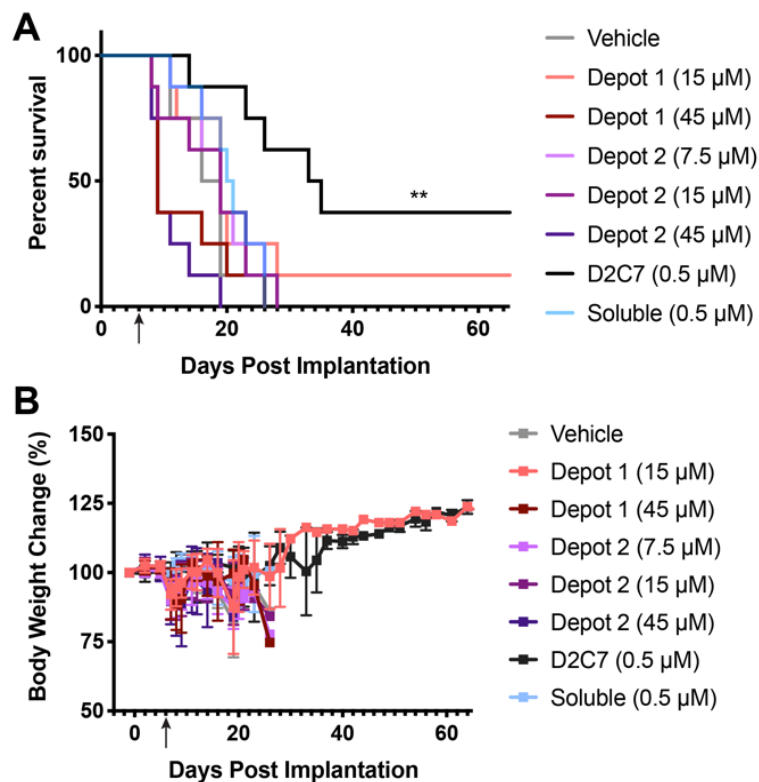


Figure 116: AffETox efficacy in CT-2A orthotopic model (MTD study #2). (A) Cumulative survival of mice reveals one treatment group with significantly improved survival as compared to vehicle control, with () indicating $p < .01$ (Mantel-Cox log rank test). (B) Body weight change as a percentage of starting body weight. Arrow indicates day of treatment.**

We were also able to evaluate all of our *in vivo* data, from both this study and the first, in the context of a clinically used immunotoxin, D2C7. This immunotoxin was developed and generously provided by Darell Bigner, Duke University, and is comprised of a single chain variable fragment (scFv) specific for EGFR/EGFRvIII linked to a previous generation of *P. aeruginosa* exotoxin A with immunogenic epitopes still intact. In both clinical trials and pre-clinical testing, D2C7 is administered orthotopically through use of an osmotic pump implanted in the brain for 24 h to seven days.³²⁴ Bigner

and co-workers had not previously explored the efficacy of D2C7 administered as a bolus injection, as we have done with AffETox. We included a D2C7 group in this study to provide a useful metric for evaluating the efficacy of AffETox and found a significant improvement to survival in this treatment group as compared to the vehicle control. However, in considering the results from both studies, the 0.5 μM soluble AffETox treatment group from the first MTD study remains unsurpassed with respect to median survival.

Despite these fruitful conclusions, there are some additional questions raised in view of the finding that none of the AffETox groups significantly increased survival in this study (Table 14).

Table 14: Median survival of treatment groups in AffETox MTD study #2

Treatment	Dose (μM)	Median survival (days)
Vehicle	--	17.5
(ZEGFR) ₂ -ELP _{D1} -toxin	15	19
	45	9
(ZEGFR) ₂ -ELP _{D2} -toxin	7.5	19
	15	19
	45	9
(ZEGFR) ₂ -ELP _S -toxin	0.5	20.5
D2C7	0.5	34

In addition, there is an apparent lack of reproducibility of the 0.5 μM soluble AffETox treatment between this and the previous MTD study. To address the latter, we

re-examined the preparation of the AffETox constructs for this study. In an effort to enhance reproducibility, we had used the same batch of soluble AffETox for both sets of *in vivo* studies, with the second taking place six months after the first. Without having performed long-term stability testing of AffETox and given the similar performance of the soluble AffETox to the vehicle control, we hypothesize the lack of efficacy seen in this study is due to degradation of this protein over the time period between the two studies. This certainly warrants further, rigorous testing to ensure we can reliably recapitulate the exceptional response we observed in our first study.

Considering the results from the two depot-forming AffETox constructs investigated in both of these MTD studies, the best performing group was that of (ZEGFR)₂-ELP_{D1}-toxin, at a dose of 5 μ M. This treatment group significantly improved overall survival with a median survival of 21.5 days. Given that the most effective dose is an intermediate concentration of the five doses we have tested for this construct (0.5, 1.5, 5, 15, and 45 μ M), we may need to reduce the dose of (ZEGFR)₂-ELP_{D2}-toxin further to see comparable therapeutic efficacy.

More broadly, these findings persuade us to re-consider the essentiality of sustained release in this system and, at the very least, demand a more thorough delineation of the factors required to achieve depot release in the context of the complex intracranial space. The seemingly paradoxical relationship between decreasing dose and increasing survival with the soluble AffETox, and to a certain extent the (ZEGFR)₂-

ELP_{D1}-toxin construct, indicates there are additional factors influencing the phase transition behavior and bioactivity of these constructs which we have not yet uncovered through our *in vitro* characterizations. The previously studied and modeled ELP depots which provided the guidance for selecting these depot formulations were administered in the subcutaneous space or intratumorally in other solid tumor types. The dynamics of depot release in the brain are likely uniquely and considerably influenced by the inimitable characteristics of both the cerebral cortex and this heterogenous, diffuse tumor type.

5.4 Conclusions and future directions

5.4.1 Summary and significance

The two distinct phases of this project – first, synthesis of AbETox, and second, production of AffETox – each have their own scientific merit, challenges, and opportunities for future work. The former was inspired by the overarching theme of this thesis work to address the challenges of bioorthogonal conjugation of two complex proteins. The latter evolved out of necessity but allowed us to achieve the original goal of this project by assessing a sustained-release immunotoxin *in vivo*. Retrospectively, it is the entirety of this work alone which illustrates the thrill of engaging in scientific research – the directions in which our findings guide us often lead to the most unexpected yet rewarding destinations, which we could not have predicted at the project's inception. It is through a comprehensive view of this project, with the many

trials and ultimate successes, that this work provided the most richly fulfilling graduate training. While the scope of technical skills and understanding required was wide-ranging, this project provided the most invaluable insight into a critical requirement of a scientific investigator: learning to be adaptable yet purposeful in experimental approach, by rigorously evaluating results and accordingly amending strategies.

Beyond the personal and professional significance of this work, we have deepened our scientific understanding of conjugation chemistry, enzymatic modification, protein engineering and purification, cancer biology, and the biophysical properties of ELP-based fusion proteins. Notably, the challenges we faced in these subject areas resulted in some of the most valuable conclusions. With respect to AbETox synthesis, this work brought to light yet unpublished issues with cycloalkyne instability and non-specific Sortase A activity in the modification of monoclonal antibodies, which both merit deeper investigation than our efforts here. The three iterations of purification strategies we devised for AbETox also produced several observations of note. When separating ELP-containing components from free ELPs, despite differences in transition temperatures, we found that inverse transition cycling did not provide discrete separation of these species due to the nature of ELP phase separation and entanglement of the chains. This effect carries through with chromatography-based purification as well; it was difficult to eliminate all traces of ELP-containing starting material from our AbETox conjugates with His-tag and Protein L affinity chromatography. Although not

discussed, we also attempted anion exchange and size exclusion chromatography to purify the reaction mixtures with little success. The many rounds of purification required directly contributed to the untenably low yield of pure AbETox conjugate.

Despite these challenges and the ultimate change of project direction, we did profit from the development of AbETox in certain regards. First, we successfully genetically grafted the variable domains of a published scFv onto an IgG scaffold and confirmed the specificity of our mAb was maintained for EGFR and EGFRvIII. Second, being confronted with the insoluble expression of the ELP-toxin fusion required us to carefully optimize our refolding protocol to produce active protein. Third, because we could not test this ELP-toxin fusion for activity without a targeting domain, we investigated and optimized a published cell-free protein translation inhibition assay for this purpose. Consequently, we were able to more directly confirm the mechanism of action of the toxin than a cell viability assay can alone. These efforts also confirmed that the bioactivity of the toxin is maintained when fused to an ELP. These latter two endeavors streamlined the AffETox phase of this project and enabled us to get from gene synthesis to preparing for *in vivo* experiments in merely six months' time.

Our primary accomplishment in this work was in confirming the efficacy of a novel, highly potent immunotoxin-biopolymer fusion (AffETox) *in vivo* in GBM-tumor bearing mice. The response we observed with our soluble AffETox constructs in the first *in vivo* study are unlike those obtained in any previous study, even with continuous

infusion of an immunotoxin. These highly promising results bolster our expectations for superior responses after continued optimization. More broadly, AffETox is a first-in-class sustained-release biologic, with a precisely specified modular design. The toxin payload, high-affinity targeting domain, and extensively tunable ELP components can be tailored to introduce the possibility of sustained-release biologic drugs for a wide range of other solid tumor types.

5.4.2 Future perspectives

Future work with this platform will necessarily focus on evaluating the factors controlling depot dissolution in the brain, with the ultimate goal of either affirming or disproving the hypothesis that sustained-release will promote superior AffETox efficacy. There are three critical areas of consideration for the next phase of this project: 1) how the intracranial milieu affects AffETox phase transition, and determining a strategy to recapitulate this environment with *in vitro* characterization; 2) the extent of extracellular fluid movement in the brain, and how this compares to the other locations in which we have previously demonstrated sustained release from ELP depots, such as the subcutaneous space; and 3) whether the apparent irreversibility of AffETox phase transition as measured *in vitro* translates to lower efficacy *in vivo*.

Future endeavors will benefit from more accurately predicting AffETox phase transition *in vivo* using the available *in vitro* characterization techniques. Thus far, we have only measured AffETox phase transition behavior in aqueous buffer (1xPBS).

Previous work has demonstrated that assessing ELP phase transition in 1xPBS is not necessarily predictive of the behavior in a more physiologically relevant solution, such as mock serum. For example, the phase transition behavior of a diblock ELP measured in 90% fetal bovine serum wholly abolished the self-assembly observed in 1xPBS.³⁵⁰ We require a more nuanced understanding of how AffETox transitions in cerebral spinal fluid (CSF), the principal fluid in the extracellular space of the brain. Furthermore, we will need to compare predictions for AffETox phase transition in CSF to the expected behavior in plasma and interstitial fluid (ISF), as previously studied ELP depots have relied on the unique properties of these physiological fluids to establish efficacy and model depot performance.^{88, 351}

A comparison of reported electrolyte levels and rates of fluid movement between CSF, plasma, and ISF reveals distinct characteristics of each. While sodium ion levels are similar, the level of chloride ions in the CSF are incongruent from those in in plasma, ISF, as well as the 1xPBS solutions in which we have assessed AffETox phase transition (approximately 119 mM versus 100 mM, 105 mM, and 143 mM, respectively).³⁵² This level of dissimilarity will expectedly influence phase transition behavior as chloride is a kosmotropic anion which depresses the LCST of an ELP by approximately 1°C with each 100 mM increase in concentration.⁶⁸ Given that the phase transition of ELP is very sharp, occurring within 1°C of reaching its transition temperature, even small deviations in chloride concentration can skew AffETox characterization. In addition, the protein

content of CSF is over 200 times lower than plasma and approximately 75 times lower than ISF.³⁵² The concentration of albumin, immunoglobulins, and other globular proteins dictates the osmotic pressure and viscosity of these fluids, which impacts the movement of other macromolecules. While it is impossible to exactly recapitulate physiological conditions with cuvette-based spectrophotometry, we can better approximate these fluids based on the reported characteristics and evaluate the influence on phase transition behavior.

Beyond composition, the flow rate of these physiological fluids differs widely. Given that the predicted method of depot dissolution is via diffusion-driven dilution, a higher rate of physiologic fluid movement will expectedly expedite this process. The flow rate of CSF is approximately 0.32 mL min^{-1} while cardiac output is on the order of liters per minute and interstitial fluid movement is approximately 55 mL min^{-1} .³⁵³⁻³⁵⁴ These values are generalized averages as there are several parameters influencing fluid flow and particle diffusion in the circulation and subcutaneous space, including location of sampling, vessel diameter, particle size, organism size, and many others.³⁵⁵⁻³⁵⁶ Nonetheless, the major discrepancies between fluid flow must be taken into account when predicting AffETox dissolution in the context of established ELP depots. The reduced fluid movement in the brain may singularly account for the ineffectiveness of depot-forming AffETox through lack of flow-promoted dissolution.

Another important factor to consider in future work is the apparent irreversibility of phase transition with AffETox (see Figure 104). Upon heating, these proteins undergo the characteristic, rapid liquid-liquid phase separation of ELPs. However, neither ELP_D-toxin nor (ZEGFR)₂-ELP_D-toxin resolubilize upon cooling, with the latter exhibiting an unusual kinetically arrested response, particularly at lower concentrations. This response is only observed with constructs containing toxin; the control proteins, ELP_D and (ZEGFR)₂-ELP_D, do resolubilize upon cooling after heating past 37°C. This may indicate a certain level of toxin-driven aggregation upon injection *in vivo*, the extent of which will impact the bioavailable drug and may be responsible for the lower efficacy of the depot-forming constructs we observed. The soluble AffETox construct may have exhibited superior efficacy due to the solvation of the ELP chains which prevents aggregation, a concept which has been previously employed in combining polyethylene glycol and aggregation-prone biologics.³⁵⁷⁻³⁵⁸ In addition, the liquid-liquid phase separation itself may drive protein aggregation due to the high concentration of densely-packed AffETox in the protein-rich phase.³⁵⁹⁻³⁶⁰

The level of AffETox efficacy *in vivo* is undoubtedly collectively governed by these various factors, which merits deeper investigation than afforded here. Building a comprehensive view of the precise influence of each of these parameters on the biophysical behavior of AffETox will expectedly clarify our previous findings and provide an informed foundation for future work.

6. Conclusions

6.1 Summary of technologies developed

This thesis work has produced three distinct elastin-like polypeptide platforms, all with an overarching focus on refining and defining the *de novo* material properties, and a footing in both genetic code expansion and complex recombinant protein design.

We invested our initial efforts in optimizing genetic code expansion systems for unnatural amino acid incorporation into elastin-like polypeptides (ELPs). These efforts, described in Chapter 2, allowed us to maximize outputs both in terms of yield and incorporation efficiency, and enable the platform development in subsequent chapters.

The first platform, described in Chapter 3, defines an orthogonal strategy for crosslinking and stabilizing ELP assemblies and architectures. This we accomplished through the introduction of a unique photocrosslinkable unnatural residue, *p*-azidophenylalanine. This residue provides never-before-achieved temporal and spatial control over crosslinking ELP assemblies, allowing us to immobilize desired architectures precisely as we designed them. We used two simple ELP chains as the starting materials and required only heat and ultraviolet (UV) light to stabilize crosslinked hydrogel particles ranging from 100 nm to 25 μm in length, spanning four orders of magnitude in size. These studies establish the framework for synthesizing stable, monodisperse ELP particles of precise size with potential utility as therapeutic drug carriers, actuators, biosensors, and in consumer care products.

The second platform developed introduces a new strategy for simultaneous drug loading and active targeting of ELP-based nanoparticles via bioorthogonal chemistry. As described in Chapter 4, we utilized the unnatural amino acid *p*-acetylphenylalanine to introduce an orthogonal ketone residue, allowing us to conjugate a small molecule drug with new chemistries while affording all twenty natural residues their role as essential components of a targeting ligand sequence. We demonstrated the utility of this system in a panel of relevant cancer cell lines, and demonstrated with flow cytometry, cytotoxicity assays, and imaging studies that the targeted, drug-loaded system is superior to non-targeted controls. Our targeted system consistently outperforms the controls in terms of potency and specificity, with the latter representing the current gold standard for drug-loaded biopolymer nanoparticles synthesized using existing methods. These studies provide the proof-of-principle studies necessary for future evaluation of this drug delivery system *in vivo*, while our modular system encourages the exploration of alternative targeting domains and payloads.

The third platform describes another novel therapeutic ELP formulation and follows a unique trajectory from genetic code expansion to glioblastoma multiforme. As described in Chapter 5, we have devised a new strategy to deliver a biologic drug in a tissue and tumor model previously unexplored using ELP-based therapeutics: brain tumors. What started as a deep-dive into the conjugation of two complex proteins via unnatural amino acid-mediated click chemistry evolved into a study in recombinant

protein engineering to make a potent immunotoxin equipped to target glioblastoma-specific markers. We tested these constructs –termed AffETox – in a panel of relevant cell lines to confirm specificity and potency, which provided the impetus to test efficacy *in vivo* in an orthotopic, syngeneic GBM mouse tumor model. From those studies, we identified potent candidates which resulted in significant improvements to survival. This platform has substantial potential for continued pre-clinical and clinical success, with room for future studies to further fine-tune the pharmacokinetic properties of AffETox to improve efficacy even further.

With this work, we have combined and reimagined the utility of existing technologies to push the boundaries of biotechnology with three primary areas of focus within each platform (Figure 117).

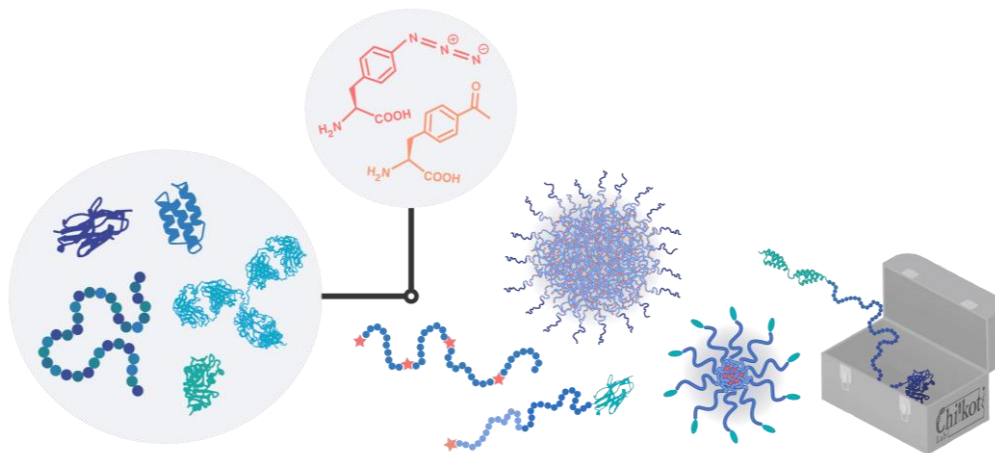


Figure 117: Bioorthogonality unlocks new potential for ELPs.

Our orthogonally crosslinked ELP particle platform represents a fundamental advance in the generation of novel biomaterials, especially in the form of crosslinked,

soft matter colloids. Our second area of expansion resulted in a novel formulation strategy for targeted drug delivery vehicles, pushing the boundaries of nanoparticle functionalization. Finally, our third venture into biologic development for treatment of brain tumors has expanded the scope of ELP-based therapeutics to a target organ previously unexplored with this class of therapeutics, the brain. The trajectory of scientific research begins with systematic exploration of hypotheses to answer fundamental questions; this process inevitably reveals new unknowns, which richly furnish the avenues of future discovery.

6.2 Combining platforms in future work

The proposed future directions of each of the individual platforms have been discussed in the corresponding sections (see Sections 3.4, 4.4, and 5.4). Taking a more comprehensive view of this work, we can envision the ways in which combining our technologies would produce radically innovative and useful materials.

First, we can combine our crosslinking technology with our drug-loaded, targeted nanoparticle platform to generate powerful drug delivery vehicles. Recent work has demonstrated the importance of combining three key factors for effective tumor treatment via nanoparticle drug carriers, which we have yet to explore in one particle: 1) active targeting, 2) attachment of cytotoxic drugs, and 3) stabilization via crosslinking.^{200-210, 361-362} As discussed, active targeting of nanoparticles to tumors *in vivo* reduces off-target effects and widens the therapeutic window, while conjugation of

small molecule drugs to these carriers increases effective drug half-life via the enhanced permeability and retention (EPR) effect.^{22, 85, 161, 212, 216} However, while our amphiphilic ELP polymers drive spontaneous self-assembly of unimers into stable nano-scale micelles upon heating in solution, these micelles can disassemble in the complex physiological milieu of the circulation, as the unimer-to-micelle equilibrium is in constant dynamic flux.¹⁴¹⁻¹⁴² Crosslinked nanoparticles confirmed to be stable in buffer have been shown to disassemble in serum and multi-component media.¹⁴² Stabilization of these polymeric nanoscale micelles by crosslinking has been proven to enhance their systemic exposure and reduce renal clearance.¹⁴³⁻¹⁴⁴

To generate crosslinked, drug-loaded, targeted nanoparticles we can incorporate both crosslinking and Dox-attachment sites using the two unnatural residues *p*-azidophenylalanine (*pAzF*) and *p*-acetylphenylalanine (*pAcF*), respectively, into the amphiphilic ELP diblocks described in Chapters 3 and 4. Given that both *pAzF* and *pAcF* are encoded by the same amber stop codon, the constructs containing these residues will be expressed, purified, and processed separately. The drug-loaded, targeted diblock can then be simply mixed in solution with the photocrosslinkable diblock, heated to promote self-assembly into micelles, and crosslinked. The genetic tunability of ELPs at the sequence level provides the means to ensure these diblocks have the same critical micellization temperature to ensure adequate mixing prior to crosslinking. These particles can then be assessed in tumor-bearing mice *in vivo* to prove the hypothesis that

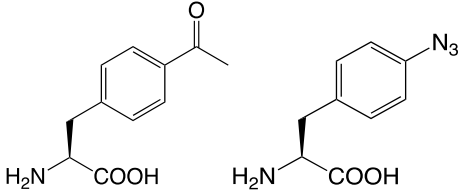
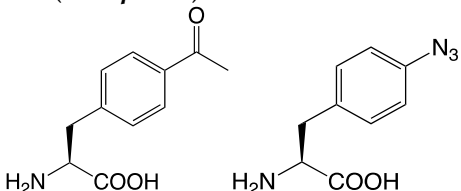
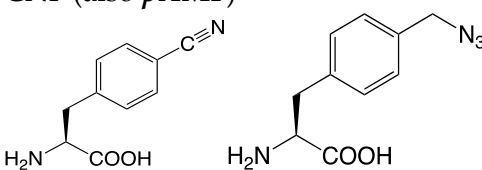
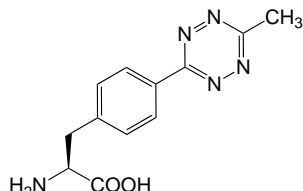
all three elements – crosslinking, covalent drug loading, and active targeting – produce the most efficacious drug delivery vehicle.

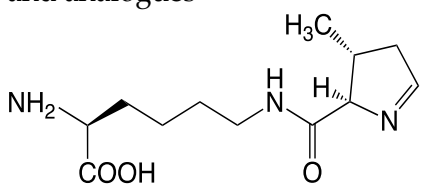
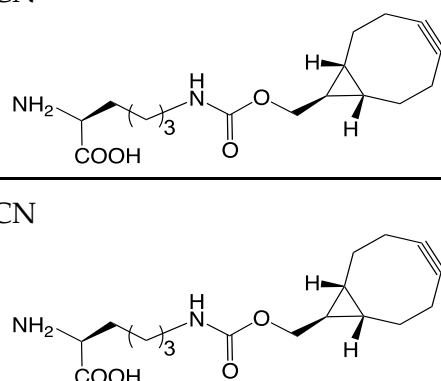
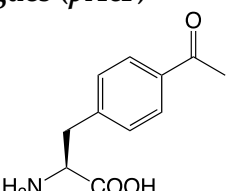
Considering our two drug delivery platforms, with a new strategy for drug loading as well as a sustained-release biologic, we can identify the pronounced opportunity for combining these technologies. The standard of care for glioblastoma multiforme (GBM) is currently surgical resection followed by treatment with temozolomide (TMZ), a small molecule alkylating agent, concomitant with radiotherapy.³⁶³ This drug is typically administered intravenously, and while it does not have difficulty crossing the blood-brain barrier, systemic side effects can result in dose-limiting toxicity.³⁶⁴ Accordingly, intracranial administration of TMZ via convection-enhanced delivery had fewer side effects than repeated intravenous dosing.³⁶⁵ Conjugating TMZ to our sustained-release immunotoxin via *p*AcF would allow for dual-pronged treatment of GBM with a single injection. While TMZ is not amenable to conjugation to *p*AcF on its own, several groups have investigated conjugates of this drug which would provide chemical handles for attachment.³⁶⁶⁻³⁶⁷ The benefit of combining TMZ with our sustained-release immunotoxin ensures the diffusion limits encountered by the more potent biologic can be compensated for by this small molecule drug. This strategy could then be adapted for a variety of drugs and targeted biologics to design a highly tailored GBM treatment platform.

A common thread unifies this work and the proposed future directions: while recombinant engineering, a powerful mainstay of biotechnology and medicine alike, enables the precise *de novo* design of proteins, genetic code expansion provides the tools necessary to drive these purely biological species into the realm of bioorthogonality. Here, we can customize these products to our exact specifications. As new biologically-inspired materials are adapted for recombinant synthesis, and novel unnatural residues are explored, the future is bright for innovative protein engineering with applications in medicine to materials science and beyond.

Appendix A

Table 15: Library of orthogonal translation systems explored.

Vector	Parent aaRS/tRNA	Unnatural amino acid(s)	Vector source
pEvol	MjTyr	<p><i>pAcF</i> (also <i>pAzF</i>)</p> 	Eric Brustad, University of North Carolina at Chapel Hill
pAcFRS.1.t1	MjTyr	<p><i>pAcF</i> (also <i>pAzF</i>)</p> 	Farren Isaacs, Yale University
pDule1	MjTyr	<p>BiBaF</p> 	Ryan Mehl, Oregon State University
pDule 2	MjTyr	<p><i>pCNF</i> (also <i>pAMF</i>)</p>  <p>Tet-v2.0</p> 	Ryan Mehl, Oregon State University

		Pyl and analogues	
pUltra	MmPylIWT		Eric Brustad, University of North Carolina at Chapel Hill
	MmPyl	BCN	
pBK	MbPyl		Eric Brustad, University of North Carolina at Chapel Hill
		BCN	
pQE	<i>E. coli</i> PheRS**	Phe analogues (pAcF) 	David Tirrell, California Institute of Technology

Residues in **bold** text have been successfully recombinantly incorporated with our system.

Abbreviations:

MjTyr; *M. janaschii* tyrosine aminoacyl synthetase and tRNA

pAcF, *p*-acetylphenylalanine

pAzF, *p*-azidophenylalanine

BiBaF, 4-(2-bromoisobutyramido)-phenylalanine

pCNF, *p*-cyanophenylalanine

pAMF, *p*-azidomethylphenylalanine

Tet-v2.0, tetrazine-containing residue¹²⁸

MmPyl, *M. marzei* WT pyrrolysine aminoacyl synthetase

MbPyl, *M. barkeri* pyrrolysine amino acyl synthetase

Pyl, pyrrolysine

BCN, bicyclononyne-containing residue

Table 16: Growth media composition for recombinant unnatural amino acid incorporation.

Media	Component	Amount per L
Minimal media (M9)	M9 Salts (6X, see below)	167 mL
	MgSO ₄ (100 mM), CaCl ₂ (10 mM)	10 mL
	Vitamins (100X, see below)	10 mL
	Trace metals (500X, see below)	2 mL
	Thiamine (5 mg mL ⁻¹)	1 mL
	FeCl ₃ (1 mM)	1 mL
	ZnSO ₄	250 µL
	Glycerol (40% v/v)	10 mL
	NH ₄ Cl (0.2 g mL ⁻¹)	5 mL
M9 Salts (6X) <i>500 mL total volume</i>	NaH ₂ PO ₄	18 g
	KH ₂ PO ₄	9 g
	NaCl	1.5 g
Vitamin stock for M9 (500X) <i>500 mL total volume</i>	Biotin	50 mg
	Choline Chloride salt	50 mg
	Folic Acid	50 mg
	Niacinamide	50 mg
	Calcium D-pantothenate	50 mg
	Pyridoxal	50 mg
	Riboflavin	5 mg
Trace metal stock for M9 (500X) <i>100 mL total volume</i>	Na ₂ EDTA	2.5 g
	ZnCl ₂	0.52 g
	H ₃ BO ₃	0.57 g
	MnCl ₂ ·4·H ₂ O	0.25 g
	FeCl ₃ ·6·H ₂ O	0.24 g
	CoCl ₂ ·6·H ₂ O	0.15 g
	CuSO ₄ ·5·H ₂ O	0.125 g
	(NH ₄) ₆ Mo ₇ O ₂₄ ·4·H ₂ O	0.055 g
Auto-induction media (AIM)	Aspartate (5% w/v)	50 mL
	Glycerol (10% v/v)	50 mL
	18 amino acid mix (5 g L ⁻¹ each AA)	40 mL
	25X M salts (1.25 M NaCl, 1.25 M KH ₂ PO ₄ , 2.5 M NH ₄ Cl, 0.25 M Na ₂ SO ₄)	40 mL
	Glucose (40% w/v)	12.5 mL

	Leucine (4 mg mL ⁻¹)	10 mL
	Arabinose (20% w/v)	10 mL
	Lactose (10% w/v)	2 mL
	MgSO ₄ (1 M)	2 mL
	D-biotin (0.8 mg mL ⁻¹)	0.5 μL
	Trace metals (5000X, see below)	200 μL
	CaCl ₂ (4 μM)	500 μL
	MnCl ₂ (2 μM)	500 μL
	ZnSO ₄ (2 μM)	500 μL
Trace metal stock for AIM (5000X) <i>30 mL total volume</i>	CoCl ₂ (0.4 μM)	500 μL
	CuCl ₂ (0.4 μM)	500 μL
	NiCl ₂ (0.4 μM)	500 μL
	Na ₂ SeO ₃ (0.4 μM)	500 μL
	Na ₂ MoO ₄ (0.4 μM)	500 μL
	H ₃ BO ₃ (0.4 μM)	500 μL
	FeCl ₃ (10 μM)	25 mL
Luria-Bertani broth (LB)	Tryptone	10 g
	Yeast extract	5 g
	Sodium chloride	10 g
2xYT	Tryptone	16 g
	Yeast extract	10 g
	Sodium chloride	5 g

GVGVPGVGVPGVGVPGVGVPGVGVPGVGVPGVGV
PGVGVPGVGVPGVGVPGVGVPGVGVPGVGVPGVGV
VPGVGVPGVGVPGVGVPGVGVPGVGVPGVGVPGV
GVPGVGVPGSGVPGSGVPGSGVPGSGVPGSGVPGSG
VPGSGVPGSGVPGSGVPGSGVPGSGVPGSGVPGSGV
PGSGVPGSGVPGSGVPGSGVPGSGVPGSGVPGSGV
GSGVPGSGVPGSGVPGSGVPGSGVPGSGVPGSGV
SGVPGSGVPGSGVPGSGVPGSGVPGSGVPGSGV
GVPGSGVPGSGVPGSGVPGSGVPGSGVPGSGV
VPGSGVPGSGVPGSGVPGSGVPGSGVPGSGV
PGSGVPGSGVPGSGVPGSGVPGSGVPGSGV
GSGVPGSGVPGSGVPGSGVPGSGVPGSGVPGSGV
SGVPGSGVPGSGVPGSGVPGSGVPGSGVPGSGV
GVPGSGVPGSGVPGSGVPGSGVPGSGVPGSGV
VPGSGVPGSGVPGY

ELP_{BC}-EgA1
Hinge
EgA1

GVGVPGVGVPGVGVPGVGVPGVGVPGVGVPGVGV
PGVGVPGVGVPGVGVPGVGVPGVGVPGVGVPGVGV
VPGVGVPGVGVPGVGVPGVGVPGVGVPGVGVPGV
GVPGVGVPGVGVPGVGVPGVGVPGVGVPGVGVPGV
VGVPGVGVPGVGVPGVGVPGVGVPGVGVPGVGV
GVGVPGVGVPGVGVPGVGVPGVGVPGVGVPGVGV
PGVGVPGVGVPGVGVPGVGVPGVGVPGVGVPGV
VPGVGVPGVGVPGVGVPGVGVPGVGVPGVGVPGV
GVPGVGVPGVGVPGVGVPGVGVPGVGVPGVGVPGV
VGVPGVGVPGVGVPGVGVPGVGVPGVGVPGVGV
GVGVPGVGVPGVGVPGVGVPGVGVPGVGVPGVGV
PGVGVPGVGVPGVGVPGVGVPGVGVPGSGVPGSGV
PGSGVPGSGVPGSGVPGSGVPGSGVPGSGVPGSGV
GSGVPGSGVPGSGVPGSGVPGSGVPGSGVPGSGV
SGVPGSGVPGSGVPGSGVPGSGVPGSGVPGSGV
GVPGSGVPGSGVPGSGVPGSGVPGSGVPGSGV
VPGSGVPGSGVPGSGVPGSGVPGSGVPGSGV
PGSGVPGSGVPGSGVPGSGVPGSGVPGSGV
GSGVPGSGVPGSGVPGSGVPGSGVPGSGVPGSGV
SGVPGSGVPGSGVPGSGVPGSGVPGSGVPGSGV
GVPG**EPKTPKQP****AAAQVQLQESGGGLVQPGGSLR**
LSCAASGRTFSSYAMGWFRQAPGKQREFVAAIRWS
GGYTYTDSVKGRFTISRDNAKTTVYLQMNSLKPED
TAVYYCAATYLSSDYSRYALPQRPLDYDYWGQGTQ

72582.54

VTVSSLE

pAcF-ELP_{BC}-EgA1 GVGVPGpAcFGVPGVGRGVGVPGVPGVGVPGVGV 73879.02
pAcF leader VPGVGVPGVGVPGVGVPGVGVPGVGVPGVGVPGVGVPGV
Hinge GVPGVGVPGVGVPGVGVPGVGVPGVGVPGVGVPGVGVPGV
EgA1 VGVPGVGVPGVGVPGVGVPGVGVPGVGVPGVGVPGVGVPGV
GVGVPGVGVPGVGVPGVGVPGVGVPGVGVPGVGVPGVGVPGV
PGVGVPGVGVPGVGVPGVGVPGVGVPGVGVPGVGVPGVGVPGV
VPGVGVPGVGVPGVGVPGVGVPGVGVPGVGVPGVGVPGVGVPGV
GVPGVGVPGVGVPGVGVPGVGVPGVGVPGVGVPGVGVPGVGVPGV
VGVPGVGVPGVGVPGVGVPGVGVPGVGVPGVGVPGVGVPGVGVPGV
GVGVPGVGVPGVGVPGVGVPGVGVPGVGVPGVGVPGVGVPGVGVPGV
PGVGVPGVGVPGVGVPGVGVPGVGVPGVGVPGVGVPGVGVPGVGVPGV
VPGVGVPGVGVPGVGVPGVGVPGVGVPGVGVPGVGVPGVGVPGV
GVPGVGVPGSGVPGSGVPGSGVPGSGVPGSGVPGSGVPGSGVPGSGV
VPGSGVPGSGVPGSGVPGSGVPGSGVPGSGVPGSGVPGSGVPGSGV
PGSGVPGSGVPGSGVPGSGVPGSGVPGSGVPGSGVPGSGVPGSGVPG
GSGVPGSGVPGSGVPGSGVPGSGVPGSGVPGSGVPGSGVPGSGVPGSGV
SGVPGSGVPGSGVPGSGVPGSGVPGSGVPGSGVPGSGVPGSGVPGSGV
GVPGSGVPGSGVPGSGVPGSGVPGSGVPGSGVPGSGVPGSGVPGSGV
VPGSGVPGSGVPGSGVPGSGVPGSGVPGSGVPGSGVPGSGVPGSGV
PGSGVPGSGVPGSGVPGSGVPGSGVPGSGVPGSGVPGSGVPGSGVPG
GSGVPGSGVPGSGVPGSGVPGSGVPGSGVPGSGVPGSGVPGSGVPGSGV
LQESGGGLVQPGGSLRLSCAASGRTFSSYAMGWFRQ
APGKQREFVAAIRWSGGYTYTDSVKGRFTISRDNA
KTTVYLQMNSLKPEDTAVYYCAATYLSSDYSRYALP
QRPLDYDYWGQGTQVTVSSLE

Appendix D

Table 19: Amino acid sequences of constructs used in sustained-release immunotoxin platform.

Construct	Sequence	MW(Da)
mAb heavy chain <i>V_H</i> <i>C_H</i> SrtA motif His tag	(Signal peptide)EVHLQQSGPELEKPGASVKISCKASG YSFTGYNMNWWVKQSNKCLEWIGNIDPYYGDTDYD QKFKGKATLTADKSSNTVYMQQLQSLTSEDSAVYYCA RGAHRDYYAMDYWGQGTSVTVSSASTKGPSVFPLAP SSKSTSGGTAALGCLVKDYFPEPVTVSWNSGALTSGV HTFPAVLQSSGLYSLSSVTVPSSSLGTQTYICNVNHK PSNTKVDKKEPKSCDKTHTCPPCPAPELLGGPSVFL FPPKPKDTLMISRTPEVTCVVDVSHEDPEVKFNWYV DGVEVHNAKTKPREEQYNSTYRVVSVLTVLHQDWL NGKEYKCKVSNKALPAPIEKTISKAKGQPREPQVYTL PPSRDELTKNQVSLTCLVKGFYPSDIAVEWESNGQPE NNYKTTTPVLDSDGSFFLYSKLTVDKSRWQQGNVFC SVMHEALHNHYTQKSLSLSPGKGGGSGGGSLPETGG RAGGGSHHHHHHSSG	52069.3
mAb light chain <i>V_L</i> <i>C_L</i>	(Signal peptide)DIQMTQSPASLSASVGETVTITCRTSE NIYYLAWYQQKQKSPQLLVYNAKTLAEGVPSRFSG SGGTQFSLKINGLQPEDFGGYCQQHYGTPYTFGCG TKLEKKKRTVAAPSVFIFPPSDEQLKSGTASVVCLLNN FYPREAKVQWKVDNALQSGNSQESVTEQDSKDESTYS LSSTLTLSKADYEEKHKVYACEVTHQGLSSPVTKSFNR GEC	23622.4
	Signal peptides	
	IL-2: MYRMQLLSCIALSLALVTNS	--
	Azurocidin: MRTLTVLALLAGLLASSRA	--

	GRLETILGWPLAERTVVIPSAIPTDPRNVGGDLDPSIP DKEQAISALPDYASQPGKPPREDLK	
(ZEGFR)₄-ELP_{D1}- toxin	GVDNKFNKEMWAAWEEIRNLPNLNGWQMTAFIAS LVDDPSQSANLLAEAKKLNDQAQAPKGVDNKFNKEM WAAWEEIRNLPNLNGWQMTAFIASLVDDPSQSANL LAEAKKLNDQAQAPKGVDNKFNKEMWAAWEEIRNLP NLNGWQMTAFIASLVDDPSQSANLLAEAKKLNDQA QAPKGVDNKFNKEMWAAWEEIRNLPNLNGWQMT AFIASLVDDPSQSANLLAEAKKLNDQAQAPKGVGVP VGVPGVGVPGVGVPGVGVPGVGVPGVGVPGVGVP VGVPGVGVPGVGVPGVGVPGVGVPGVGVPGVGVP VGVPGVGVPGVGVPGVGVPGVGVPGVGVPGVGVP VGVPGVGVPGVGVPGVGVPGVGVPGVGVPGVGVP VGVPGVGVPGVGVPGVGVPGVGVPGVGVPGVGVP VGVPGVGVPGVGVPGVGVPGVGVPGVGVPGVGVP VGVPGVGVPGVGVPGVGVPGVGVPGVGVPGVGVP VGVPGVGVPGGGGSGGGSGGGSKASGGRHRQPRGW EQLGGSPTGAEFLGDGGDVSFSTRGTQNWTVRLLQ AHAQLEERGYVFGYHGTFLAAQSIVFGGVAARSQ DLAAIWAGFYIAGDPALAYGYAQDQEPDAAGRIRN GALLRVYVPASSLPGFYRTSLTLAAPEAAGEVERLIGH PLPLALDAITGPEEEGGRLLETILGWPLAERTVVIPSAIP TDPRNVGGDLDPSIPDKEQAISALPDYASQPGKPPRE DLK	76581.22
ELP_{D2}	GVGVPGVGVPGAGVPGVPGVPGVPGVPGVPGVPGV GAGVPGVPGVPGVPGVPGVPGVPGVPGVPGVPGV GVGVPGVGVPGVGVPGAGVPGVPGVPGVPGVPGV GVGVPGAGVPGVPGVPGVPGVPGVPGVPGVPGV GVGVPGVGVPGVGVPGVGVPGAGVPGVPGVPGV GVGVPGVGVPGAGVPGVPGVPGVPGVPGVPGVPGV GAGVPGVPGVPGVPGVPGVPGVPGVPGVPGVPGV GVGVPGVGVPGVGVPGAGVPGVPGVPGVPGVPGV GAGVPGVPGVPGVPGVPGVPGVPGVPGVPGVPGV GAGVPGVPGVPGVPGVPGVPGVPGVPGVPGVPGV GAGVPGVPGVPGVPGVPGVPGVPGVPGVPGVPGV	24307.56
ELP_S	GAGVPGAGVPGAGVPGAGVPGAGVPGAGVPGAGV PGAGVPGAGVPGAGVPGAGVPGAGVPGAGVPGAG VPGAGVPGAGVPGAGVPGAGVPGAGVPGAGVPGA GVPGAGVPGAGVPGAGVPGAGVPGAGVPGAGVPG AGVPGAGVPGAGVPGAGVPGAGVPGAGVPGAGVPG	22579.6

GAGVPGAGVPGAGVPGAGVPGAGVPGAGVPGAGV
PGAGVPGAGVPGAGVPGAGVPGAGVPGAGVPGAGVPGAG
VPGAGVPGAGVPGAGVPGAGVPGAGVPGAGVPGAGVPGA
GVPGAGVPGAGVPGAGVPGAGVPG

References

- 1 Walton AG, Blackwell J (1973). *Biopolymers*.
- 2 Silva SS, Oliveira JM, Sá-Lima H, Sousa RA, Mano JF, Reis RL, in *Comprehensive biomaterials*, **2011**, pp. 187-205.
- 3 Brett WG, Tong C, Santaneel G, Zhibing H, Arup N (2009). "Refractive index change due to volume-phase transition in polyacrylamide gel nanospheres for optoelectronics and bio-photonics." *Applied Physics Express* 2(5): 057001.
- 4 Debord JD, Lyon LA (2000). "Thermoresponsive photonic crystals." *The Journal of Physical Chemistry B* 104(27): 6327-6331.
- 5 McDaniel JR, Weitzhandler I, Prevost S, Vargo KB, Appavou MS, Hammer DA, Gradzielski M, Chilkoti A (2014). "Noncanonical self-assembly of highly asymmetric genetically encoded polypeptide amphiphiles into cylindrical micelles." *Nano Lett* 14(11): 6590-6598.
- 6 Oh JK, Drumright R, Siegwart DJ, Matyjaszewski K (2008). "The development of microgels/nanogels for drug delivery applications." *Prog Polym Sci* 33(4): 448-477.
- 7 Fan X, Zhu L, Wang K, Wang B, Wu Y, Xie W, Huang C, Chan BP, Du Y (2017). "Stiffness-controlled thermoresponsive hydrogels for cell harvesting with sustained mechanical memory." *Advanced Healthcare Materials*: 1601152-n/a.
- 8 Jang Y, Champion JA (2016). "Self-assembled materials made from functional recombinant proteins." *Acc. Chem. Res.* 49(10): 2188-2198.
- 9 Gelperina S, Kisich K, Iseman MD, Heifets L (2005). "The potential advantages of nanoparticle drug delivery systems in chemotherapy of tuberculosis." *Am. J. Respir. Crit. Care Med.* 172(12): 1487-1490.

- 10 Blanco E, Shen H, Ferrari M (2015). "Principles of nanoparticle design for overcoming biological barriers to drug delivery." *Nat. Biotechnol.* 33(9): 941-951.
- 11 Wittrup KD, Thurber GM, Schmidt MM, Rhoden JJ (2012). "Practical theoretic guidance for the design of tumor-targeting agents." *Methods Enzymol.* 503: 255-268.
- 12 Fernandez-Nieves A, Wyss HM, Mattsson J, Weitz DA (2011). *Microgel suspensions.*
- 13 Toma M, Jonas U, Mateescu A, Knoll W, Dostalek J (2013). "Active control of spr by thermoresponsive hydrogels for biosensor applications." *J. Phys. Chem. C Nanomater. Interfaces* 117(22): 11705-11712.
- 14 Hamidi M, Azadi A, Rafiei P (2008). "Hydrogel nanoparticles in drug delivery." *Adv Drug Deliv Rev* 60(15): 1638-1649.
- 15 Sharma N, Petri C, Jonas U, Dostalek J (2016). "Reversibly tunable plasmonic bandgap by responsive hydrogel grating." *Opt. Express* 24(3): 2457-2465.
- 16 Liang L, Feng XD, Martin PFC, Peurrung LM (2000). "Temperature-sensitive switch from composite poly(n-isopropylacrylamide) sponge gels." *Journal of Applied Polymer Science* 75(14): 1735-1739.
- 17 Hoffmann J, Plötner M, Kuckling D, Fischer W-J (1999). "Photopatterning of thermally sensitive hydrogels useful for microactuators." *Sensors and Actuators A: Physical* 77(2): 139-144.
- 18 van den Brom CR, Anac I, Roskamp RF, Retsch M, Jonas U, Menges B, Preece JA (2010). "The swelling behaviour of thermoresponsive hydrogel/silica nanoparticle composites." *J. Mater. Chem.* 20(23): 4827.
- 19 Gan DJ, Lyon LA (2001). "Tunable swelling kinetics in core-shell hydrogel nanoparticles." *J. Am. Chem. Soc.* 123(31): 7511-7517.

- 20 Torchilin VP, Lukyanov AN (2003). "Peptide and protein drug delivery to and into tumors: Challenges and solutions." *Drug Discovery Today* 8(6): 259-266.
- 21 Joy MS (2012). "Impact of glomerular kidney diseases on the clearance of drugs." *J. Clin. Pharmacol.* 52(1 Suppl): 23S-34S.
- 22 Matsumura Y, Maeda H (1986). "A new concept for macromolecular therapeutics in cancer chemotherapy: Mechanism of tumoritropic accumulation of proteins and the antitumor agent smancs." *Cancer Res.* 46(12 Part 1): 6387-6392.
- 23 Nettles DL, Chilkoti A, Setton LA (2010). "Applications of elastin-like polypeptides in tissue engineering." *Adv Drug Deliv Rev* 62(15): 1479-1485.
- 24 Yadav P, Yadav H, Shah VG, Shah G, Dhaka G (2015). "Biomedical biopolymers, their origin and evolution in biomedical sciences: A systematic review." *J Clin Diagn Res* 9(9): ZE21-25.
- 25 Garay RP, El-Gewely R, Armstrong JK, Garratty G, Richette P (2012). "Antibodies against polyethylene glycol in healthy subjects and in patients treated with peg-conjugated agents." *Expert Opin Drug Deliv* 9(11): 1319-1323.
- 26 Wang C, Cheng X, Sui Y, Luo X, Jiang G, Wang Y, Huang Z, She Z, Deng Y (2013). "A noticeable phenomenon: Thiol terminal peg enhances the immunogenicity of pegylated emulsions injected intravenously or subcutaneously into rats." *Eur. J. Pharm. Biopharm.* 85(3 Pt A): 744-751.
- 27 Armstrong JK, in *Pegylated protein drugs: Basic science and clinical applications* (Ed.: F. M. Veronese), Birkhäuser Basel, Basel, 2009, pp. 147-168.
- 28 Wang X, Ishida T, Kiwada H (2007). "Anti-peg igm elicited by injection of liposomes is involved in the enhanced blood clearance of a subsequent dose of pegylated liposomes." *J. Control. Release* 119(2): 236-244.

- 29 Banskota S, Yousefpour P, Kirmani N, Li X, Chilkoti A (2019). "Long circulating genetically encoded intrinsically disordered zwitterionic polypeptides for drug delivery." *Biomaterials* 192: 475-485.
- 30 Ozer I, Chilkoti A (2017). "Site-specific and stoichiometric stealth polymer conjugates of therapeutic peptides and proteins." *Bioconjug. Chem.* 28(3): 713-723.
- 31 Chung C, Lampe KJ, Heilshorn SC (2012). "Tetrakis(hydroxymethyl) phosphonium chloride as a covalent cross-linking agent for cell encapsulation within protein-based hydrogels." *Biomacromolecules* 13(12): 3912-3916.
- 32 Raphael J, Parisi-Amon A, Heilshorn S (2012). "Photoreactive elastin-like proteins for use as versatile bioactive materials and surface coatings." *J. Mater. Chem.* 22(37): 19429-19437.
- 33 Lim DW, Nettles DL, Setton LA, Chilkoti A (2007). "Rapid cross-linking of elastin-like polypeptides with (hydroxymethyl)phosphines in aqueous solution." *Biomacromolecules* 8(5): 1463-1470.
- 34 Boohaker RJ, Lee MW, Vishnubhotla P, Perez JM, Khaled AR (2012). "The use of therapeutic peptides to target and to kill cancer cells." *Curr. Med. Chem.* 19(22): 3794-3804.
- 35 Shehu A, Kavraki LE, Clementi C (2008). "Unfolding the fold of cyclic cysteine-rich peptides." *Protein Sci.* 17(3): 482-493.
- 36 Thapa P, Espiritu MJ, Cabalteja C, Bingham J-P (2014). "The emergence of cyclic peptides: The potential of bioengineered peptide drugs." *Int. J. Pept. Res. Ther.* 20(4): 545-551.
- 37 Fuxreiter M, Tompa P (2012). Fuzziness: Structural disorder in protein complexes.

- 38 Vrhovski B, Weiss A (1998). "Biochemistry of tropoelastin." *European Journal of Biochemistry* 258(1): 1-18.
- 39 Muiznieks LD, Weiss AS, Keeley FW (2010). "Structural disorder and dynamics of elastin." *Biochem Cell Biol* 88(2): 239-250.
- 40 Gibbons C, Shadwick R (1991). "Circulatory mechanics in the toad *bufo marinus* i. Structure and mechanical design of the aorta." *Journal of Experimental Biology*(158): 275-289.
- 41 Shadwick RE (1999). "Mechanical design in arteries." *J Exp Biol* 202(Pt 23): 3305-3313.
- 42 Gosline J, Lillie M, Carrington E, Guerette P, Ortlepp C, Savage K (2002). "Elastic proteins: Biological roles and mechanical properties." *Philos Trans R Soc Lond B Biol Sci* 357(1418): 121-132.
- 43 Fung YC, 2 ed., Springer-Verlag, New York, **1993**.
- 44 Aaron BB, Gosline JM (1981). "Elastin as a random-network elastomer - a mechanical and optical analysis of single elastin fibers." *Biopolymers* 20(6): 1247-1260.
- 45 Lillie MA, Gosline JM (2002). "The viscoelastic basis for the tensile strength of elastin." *Int J Biol Macromol* 30(2): 119-127.
- 46 Rosenbloom J, Abrams W, Mecham R (1993). "Extracellular matrix 4: The elastic fiber." *The FASEB Journal* 7(13): 1208-1218.
- 47 Urry D (1988). "Entropic elastic processes in protein mechanisms. I. Elastic structure due to an inverse temperature transition and elasticity due to internal chain dynamics." *Journal of protein chemistry* 7(1): 1-34.

- 48 Antonicelli F, Bellon G, Debelle L, Hornebeck W (2007). "Elastin-elastases and inflamm-aging." *Curr Top Dev Biol* 79: 99-155.
- 49 Li DY, Brooke B, Davis EC, Mecham RP, Sorensen LK, Boak BB, Eichwald E, Keating MT (1998). "Elastin is an essential determinant of arterial morphogenesis." *Nature* 393(6682): 276-280.
- 50 Cox BA, Starcher BC, DW U (1974). "Coacervation of tropoelastin results in fiber formation." *Journal of Biological Chemistry* 249: 997-998.
- 51 Foster JA, Bruenger E, Gray WR, Sandberg LB (1973). "Isolation and amino acid sequences of tropoelastin peptides." *J Biol Chem* 248(8): 2876-2879.
- 52 Sandberg LB, Gray WR, Bruenger E (1972). "Structural studies of alanine- and lysine-rich regions of porcine aortic tropoelastin." *Biochim Biophys Acta* 285(2): 453-458.
- 53 Sandberg LB, Soskel NT, Leslie JG (1981). "Elastin structure, biosynthesis, and relation to disease states." *N Engl J Med* 304(10): 566-579.
- 54 Indik Z, Yeh H, Ornstein-Goldstein N, Sheppard P, Anderson N, Rosenbloom JC, Peltonen L, Rosenbloom J (1987). "Alternative splicing of human elastin mrna indicated by sequence analysis of cloned genomic and complementary DNA." *Proc Natl Acad Sci U S A* 84(16): 5680-5684.
- 55 Urry DW, Hugel T, Seitz M, Gaub HE, Sheiba L, Dea J, Xu J, Parker T (2002). "Elastin: A representative ideal protein elastomer." *Philos. Trans. R. Soc. Lond. B Biol. Sci.* 357(1418): 169-184.
- 56 Urry DW, Long MM, Cox BA, Ohnishi T, Mitchell LW, Jacobs M (1974). "The synthetic polypentapeptide of elastin coacervates and forms filamentous aggregates." *Biochim. Biophys. Acta* 371(2): 597-602.

- 57 Urry DW, Gowda DC, Parker TM, Luan CH, Reid MC, Harris CM, Pattanaik A, Harris RD (1992). "Hydrophobicity scale for proteins based on inverse temperature transitions." *Biopolymers* 32(9): 1243-1250.
- 58 White MJ, Fristensky BW, Thompson WF (1991). "Concatemer chain reaction: A taq DNA polymerase-mediated mechanism for generating long tandemly repetitive DNA sequences." *Anal. Biochem.* 199(2): 184-190.
- 59 Amiram M, Quiroz FG, Callahan DJ, Chilkoti A (2011). "A highly parallel method for synthesizing DNA repeats enables the discovery of 'smart' protein polymers." *Nat Mater* 10(2): 141-148.
- 60 Meyer DE, Chilkoti A (2002). "Genetically encoded synthesis of protein-based polymers with precisely specified molecular weight and sequence by recursive directional ligation: Examples from the elastin-like polypeptide system." *Biomacromolecules* 3(2): 357-367.
- 61 McDaniel JR, Mackay JA, Quiroz FG, Chilkoti A (2010). "Recursive directional ligation by plasmid reconstruction allows rapid and seamless cloning of oligomeric genes." *Biomacromolecules* 11(4): 944-952.
- 62 Rubinstein M, Colby RH (2003). *Polymer physics*, Oxford University Press.
- 63 Roberts S, Costa S, Schaal J, Simon JR, Dzuricky M, Quiroz FG, Chilkoti A, in *Comprehensive biomaterials ii*, 2017, pp. 90-108.
- 64 Meyer D, Chilkoti A (2004). "Quantification of the effects of chain length and concentration on the thermal behavior of elastin-like polypeptides." *Biomacromolecules* 5(3): 846-851.
- 65 MacEwan SR, Weitzhandler I, Hoffmann I, Genzer J, Gradzielski M, Chilkoti A (2017). "Phase behavior and self-assembly of perfectly sequence-defined and monodisperse multiblock copolypeptides." *Biomacromolecules* 18(2): 599-609.

- 66 McPherson D, Xu J, Urry D (1996). "Product purification by reversible phase transition following escherichia coli expression of genes encoding up to 251 repeats of the elastomeric pentapeptide gvgvp." *Protein Expression and Purification* 7(1): 51-57.
- 67 Meyer D, Chilkoti A (1999). "Purification of recombinant proteins by fusion with thermally-responsive polypeptides." *Nature biotechnology* 17(11): 1112-1115.
- 68 Cho Y, Zhang Y, Christensen T, Sagle LB, Chilkoti A, Cremer PS (2008). "Effects of Hofmeister anions on the phase transition temperature of elastin-like polypeptides." *J. Phys. Chem. B* 112(44): 13765-13771.
- 69 Meyer DE, Chilkoti A, in *Protein-protein interactions: A molecular cloning manual*, Cold Spring Harbor Laboratory Press, 2002, pp. 329-343.
- 70 Trabbic-Carlson K, Liu L, Kim B, Chilkoti A (2004). "Expression and purification of recombinant proteins from escherichia coli: Comparison of an elastin-like polypeptide fusion with an oligohistidine fusion." *Protein Sci.* 13(12): 3274-3284.
- 71 Christensen T, Hassouneh W, Trabbic-Carlson K, Chilkoti A (2013). "Predicting transition temperatures of elastin-like polypeptide fusion proteins." *Biomacromolecules* 14(5): 1514-1519.
- 72 Trabbic-Carlson K, Meyer DE, Liu L, Piervincenzi R, Nath N, LaBean T, Chilkoti A (2004). "Effect of protein fusion on the transition temperature of an environmentally responsive elastin-like polypeptide: A role for surface hydrophobicity?" *Protein Eng. Des. Sel.* 17(1): 57-66.
- 73 Amiram M, Luginbuhl KM, Li X, Feinglos MN, Chilkoti A (2013). "A depot-forming glucagon-like peptide-1 fusion protein reduces blood glucose for five days with a single injection." *Journal of Controlled Release* 172(1): 144-151.
- 74 Hassouneh W, Fischer K, MacEwan SR, Branscheid R, Fu CL, Liu R, Schmidt M, Chilkoti A (2012). "Unexpected multivalent display of proteins by temperature

triggered self-assembly of elastin-like polypeptide block copolymers." *Biomacromolecules* 13(5): 1598-1605.

- 75 Conrad U, Plagmann I, Malchow S, Sack M, Floss DM, Kruglov AA, Nedospasov SA, Rose-John S, Scheller J (2011). "Elpylated anti-human tnf therapeutic single-domain antibodies for prevention of lethal septic shock." *Plant Biotechnol J* 9(1): 22-31.
- 76 Costa S, Mozhdghi D, Dzuricky M, Isaacs FJ, Brustad E, Chilkoti A (2018). "Active targeting of cancer cells by nanobody decorated polypeptide micelle with bioorthogonally conjugated drug." *Nano Lett.*
- 77 Huang K, Duan N, Zhang C, Mo R, Hua Z (2017). "Improved antitumor activity of trail fusion protein via formation of self-assembling nanoparticle." *Sci. Rep.* 7: 41904.
- 78 Lin M, Rose-John S, Grötzinger J, Conrad U, Scheller J (2006). "Functional expression of a biologically active fragment of soluble gp130 as an elp-fusion protein in transgenic plants: Purification via inverse transition cycling." *Biochem. J.* 398(3): 577.
- 79 Trabbic-Carlson K, Meyer DE, Liu L, Piervincenzi R, Nath N, LaBean T, Chilkoti A (2004). "Effect of protein fusion on the transition temperature of an environmentally responsive elastin-like polypeptide: A role for surface hydrophobicity?" *Protein Engineering, Design and Selection* 17(1): 57-66.
- 80 Trabbic-Carlson K, Liu L, Kim B, Chilkoti A (2004). "Expression and purification of recombinant proteins from escherichia coli: Comparison of an elastin-like polypeptide fusion with an oligohistidine fusion." *Protein Sci.* 13(12): 3274-3284.
- 81 MacEwan SR, Chilkoti A (2010). "Elastin-like polypeptides: Biomedical applications of tunable biopolymers." *Biopolymers* 94(1): 60-77.
- 82 Lipinski CA, Lombardo F, Dominy BW, Feeney PJ (2001). "Experimental and computational approaches to estimate solubility and permeability in drug

- discovery and development settings." *Advanced Drug Delivery Reviews* 46(1-3): 3-26.
- 83 McDaniel JR, Bhattacharyya J, Vargo KB, Hassouneh W, Hammer DA, Chilkoti A (2013). "Self-assembly of thermally responsive nanoparticles of a genetically encoded peptide polymer by drug conjugation." *Angew. Chem. Int. Ed. Engl.* 52(6): 1683-1687.
- 84 Bhattacharyya J, Bellucci JJ, Weitzhandler I, McDaniel JR, Spasojevic I, Li X, Lin CC, Chi JT, Chilkoti A (2015). "A paclitaxel-loaded recombinant polypeptide nanoparticle outperforms abraxane in multiple murine cancer models." *Nat Commun* 6: 7939.
- 85 Mastria EM, Chen M, McDaniel JR, Li X, Hyun J, Dewhirst MW, Chilkoti A (2015). "Doxorubicin-conjugated polypeptide nanoparticles inhibit metastasis in two murine models of carcinoma." *J. Control. Release* 208: 52-58.
- 86 Bhattacharyya J, Weitzhandler I, Ho SB, McDaniel JR, Li X, Tang L, Liu J, Dewhirst M, Chilkoti A (2017). "Encapsulating a hydrophilic chemotherapeutic into rod-like nanoparticles of a genetically encoded asymmetric triblock polypeptide improves its efficacy." *Adv Funct Mater* 27(12).
- 87 Meyer DE, Kong GA, Dewhirst MW, Zalutsky MR, Chilkoti A (2001). "Targeting a genetically engineered elastin-like polypeptide to solid tumors by local hyperthermia." *Cancer Res.* 61(4): 1548.
- 88 Luginbuhl KM, Schaal JL, Umstead B, Mastria EM, Li X, Banskota S, Arnold S, Feinglos M, D'Alessio D, Chilkoti A (2017). "One-week glucose control via zero-order release kinetics from an injectable depot of glucagon-like peptide-1 fused to a thermosensitive biopolymer." *Nature Biomedical Engineering* 1: 0078.
- 89 Gilroy CA, Roberts S, Chilkoti A (2018). "Fusion of fibroblast growth factor 21 to a thermally responsive biopolymer forms an injectable depot with sustained anti-diabetic action." *J. Controlled Release* 277: 154-164.

- 90 Hang HC, Yu C, Kato DL, Bertozzi CR (2003). "A metabolic labeling approach toward proteomic analysis of mucin-type o-linked glycosylation." *Proc. Natl. Acad. Sci. U. S. A.* 100(25): 14846-14851.
- 91 Sletten EM, Bertozzi CR (2011). "From mechanism to mouse: A tale of two bioorthogonal reactions." *Acc. Chem. Res.* 44(9): 666-676.
- 92 Lang K, Chin JW (2014). "Cellular incorporation of unnatural amino acids and bioorthogonal labeling of proteins." *Chem. Rev.* 114(9): 4764-4806.
- 93 Devaraj NK (2018). "The future of bioorthogonal chemistry." *ACS Cent Sci* 4(8): 952-959.
- 94 Nanda JS, Lorsch JR (2014). "Labeling a protein with fluorophores using nhs ester derivitization." *Methods Enzymol.* 536: 87-94.
- 95 Banks PR, Paquette DM (2002). "Comparison of three common amine reactive fluorescent probes used for conjugation to biomolecules by capillary zone electrophoresis." *Bioconjug. Chem.* 6(4): 447-458.
- 96 Boutureira O, Bernardes GJ (2015). "Advances in chemical protein modification." *Chem. Rev.* 115(5): 2174-2195.
- 97 Nanda JS, Lorsch JR (2014). "Labeling of a protein with fluorophores using maleimide derivitization." *Methods Enzymol.* 536: 79-86.
- 98 Dawson PE, Muir TW, Clark-Lewis I, Kent SB (1994). "Synthesis of proteins by native chemical ligation." *Science* 266(5186): 776-779.
- 99 Muir TW (2003). "Semisynthesis of proteins by expressed protein ligation." *Annu. Rev. Biochem.* 72: 249-289.

- 100 Muir TW, Sondhi D, Cole PA (1998). "Expressed protein ligation: A general method for protein engineering." *Proceedings of the National Academy of Sciences* 95(12): 6705-6710.
- 101 Mao H, Hart SA, Schink A, Pollok BA (2004). "Sortase-mediated protein ligation: A new method for protein engineering." *J. Am. Chem. Soc.* 126(9): 2670-2671.
- 102 Zhang WB, Sun F, Tirrell DA, Arnold FH (2013). "Controlling macromolecular topology with genetically encoded spyttag-spycatcher chemistry." *J. Am. Chem. Soc.* 135(37): 13988-13997.
- 103 Rabuka D, Rush JS, deHart GW, Wu P, Bertozzi CR (2012). "Site-specific chemical protein conjugation using genetically encoded aldehyde tags." *Nat. Protoc.* 7(6): 1052-1067.
- 104 Noren CJ, Anthonycahill SJ, Griffith MC, Schultz PG (1989). "A general-method for site-specific incorporation of unnatural amino-acids into proteins." *Science* 244(4901): 182-188.
- 105 Wang L, Brock A, Herberich B, Schultz PG (2001). "Expanding the genetic code of escherichia coli." *Science* 292(5516): 498-500.
- 106 Bult CJ, White O, Olsen GJ, Zhou L, Fleischmann RD, Sutton GG, Blake JA, FitzGerald LM, Clayton RA, Gocayne JD, Kerlavage AR, Dougherty BA, Tomb JF, Adams MD, Reich CI, Overbeek R, Kirkness EF, Weinstock KG, Merrick JM, Glodek A, Scott JL, Geoghagen NSM, Weidman JF, Fuhrmann JL, Nguyen D, Utterback TR, Kelley JM, Peterson JD, Sadow PW, Hanna MC, Cotton MD, Roberts KM, Hurst MA, Kaine BP, Borodovsky M, Klenk HP, Fraser CM, Smith HO, Woese CR, Venter JC (1996). "Complete genome sequence of the methanogenic archaeon, *methanococcus jannaschii*." *Science* 273(5278): 1058-1073.
- 107 Han S, Yang A, Lee S, Lee HW, Park CB, Park HS (2017). "Expanding the genetic code of *mus musculus*." *Nat Commun* 8: 14568.

- 108 Hancock SM, Uprety R, Deiters A, Chin JW (2010). "Expanding the genetic code of yeast for incorporation of diverse unnatural amino acids via a pyrrolysyl-trna synthetase/trna pair." *J. Am. Chem. Soc.* 132(42): 14819-14824.
- 109 Bianco A, Townsley FM, Greiss S, Lang K, Chin JW (2012). "Expanding the genetic code of drosophila melanogaster." *Nat. Chem. Biol.* 8(9): 748-750.
- 110 Chatterjee A, Xiao H, Bollong M, Ai HW, Schultz PG (2013). "Efficient viral delivery system for unnatural amino acid mutagenesis in mammalian cells." *Proc. Natl. Acad. Sci. U. S. A.* 110(29): 11803-11808.
- 111 Liu W, Brock A, Chen S, Chen S, Schultz PG (2007). "Genetic incorporation of unnatural amino acids into proteins in mammalian cells." *Nat Methods* 4(3): 239-244.
- 112 Lang K, Davis L, Wallace S, Mahesh M, Cox DJ, Blackman ML, Fox JM, Chin JW (2012). "Genetic encoding of bicyclononynes and trans-cyclooctenes for site-specific protein labeling in vitro and in live mammalian cells via rapid fluorogenic diels-alder reactions." *J. Am. Chem. Soc.* 134(25): 10317-10320.
- 113 Amiram M, Haimovich AD, Fan C, Wang Y-S, Aerni H-R, Ntai I, Moonan DW, Ma NJ, Rovner AJ, Hong SH, Kelleher NL, Goodman AL, Jewett MC, Soll D, Rinehart J, Isaacs FJ (2015). "Evolution of translation machinery in recoded bacteria enables multi-site incorporation of nonstandard amino acids." *Nat Biotech* 33(12): 1272-1279.
- 114 Wang L, Magliery TJ, Liu D, Schultz P (2000). "A new functional suppressor trna/ aminoacyl-trna synthetase pair for the in vivo incorporation of unnatural amino acids into proteins." *JACS* 122: 5010-5011.
- 115 Wang L, Schultz PG (2001). "A general approach for the generation of orthogonal trnas." *Chem. Biol.* 8(9): 883-890.
- 116 Liu CC, Schultz PG (2010). "Adding new chemistries to the genetic code." *Annu. Rev. Biochem.* 79: 413-444.

- 117 Amiram M, Haimovich AD, Fan C, Wang YS, Aerni HR, Ntai I, Moonan DW, Ma NJ, Rovner AJ, Hong SH, Kelleher NL, Goodman AL, Jewett MC, Soll D, Rinehart J, Isaacs FJ (2015). "Evolution of translation machinery in recoded bacteria enables multi-site incorporation of nonstandard amino acids." *Nat. Biotechnol.* 33(12): 1272-1279.
- 118 Wang K, Neumann H, Peak-Chew SY, Chin JW (2007). "Evolved orthogonal ribosomes enhance the efficiency of synthetic genetic code expansion." *Nat. Biotechnol.* 25(7): 770-777.
- 119 Lee BS, Kim S, Ko BJ, Yoo TH (2017). "An efficient system for incorporation of unnatural amino acids in response to the four-base codon agga in *escherichia coli*." *Biochim Biophys Acta Gen Subj* 1861(11 Pt B): 3016-3023.
- 120 Chatterjee A, Sun SB, Furman JL, Xiao H, Schultz PG (2013). "A versatile platform for single- and multiple-unnatural amino acid mutagenesis in *escherichia coli*." *Biochemistry* 52(10): 1828-1837.
- 121 Kim S, Jeong H, Kim EY, Kim JF, Lee SY, Yoon SH (2017). "Genomic and transcriptomic landscape of *escherichia coli* bl21(de3)." *Nucleic Acids Res.* 45(9): 5285-5293.
- 122 Isaacs FJ, Carr PA, Wang HH, Lajoie MJ, Sterling B, Kraal L, Tolonen AC, Gianoulis TA, Goodman DB, Reppas NB, Emig CJ, Bang D, Hwang SJ, Jewett MC, Jacobson JM, Church GM (2011). "Precise manipulation of chromosomes in vivo enables genome-wide codon replacement." *Science* 333(6040): 348-353.
- 123 Lajoie MJ, Rovner AJ, Goodman DB, Aerni HR, Haimovich AD, Kuznetsov G, Mercer JA, Wang HH, Carr PA, Mosberg JA, Rohland N, Schultz PG, Jacobson JM, Rinehart J, Church GM, Isaacs FJ (2013). "Genomically recoded organisms expand biological functions." *Science* 342(6156): 357-360.
- 124 Wang HH, Isaacs FJ, Carr PA, Sun ZZ, Xu G, Forest CR, Church GM (2009). "Programming cells by multiplex genome engineering and accelerated evolution." *Nature* 460(7257): 894-898.

- 125 Sohn Y, Kang C (2005). "Sequential multiple functions of the conserved sequence in sequence-specific termination by t7 rna polymerase." *Proc. Natl. Acad. Sci. U. S. A.* 102(1): 75-80.
- 126 Datta D, Wang P, Carrico IS, Mayo SL, Tirrell DA (2002). "A designed phenylalanyl-trna synthetase variant allows efficient in vivo incorporation of aryl ketone functionality into proteins." *J. Am. Chem. Soc.* 124(20): 5652-5653.
- 127 Young TS, Ahmad I, Yin JA, Schultz PG (2010). "An enhanced system for unnatural amino acid mutagenesis in e. Coli." *J. Mol. Biol.* 395(2): 361-374.
- 128 Blizzard RJ, Backus DR, Brown W, Bazewicz CG, Li Y, Mehl RA (2015). "Ideal bioorthogonal reactions using a site-specifically encoded tetrazine amino acid." *J. Am. Chem. Soc.* 137(32): 10044-10047.
- 129 Bryson DI, Fan C, Guo LT, Miller C, Soll D, Liu DR (2017). "Continuous directed evolution of aminoacyl-trna synthetases." *Nat. Chem. Biol.* 13(12): 1253-1260.
- 130 Zhang M, Lin S, Song X, Liu J, Fu Y, Ge X, Fu X, Chang Z, Chen PR (2011). "A genetically incorporated crosslinker reveals chaperone cooperation in acid resistance." *Nat. Chem. Biol.* 7(10): 671-677.
- 131 Studier FW (2005). "Protein production by auto-induction in high-density shaking cultures." *Protein Expr. Purif.* 41(1): 207-234.
- 132 Yanofsky C (1981). "Attenuation in the control of expression of bacterial operons." *Nature* 289(5800): 751-758.
- 133 Lewis M (2005). "The lac repressor." *C R Biol* 328(6): 521-548.
- 134 de Boer HA, Comstock LJ, Vasser M (1983). "The tac promoter: A functional hybrid derived from the trp and lac promoters." *Proc. Natl. Acad. Sci. U. S. A.* 80(1): 21-25.

- 135 Orosz A, Boros I, Venetianer P (1991). "Analysis of the complex transcription termination region of the escherichia coli rrnB gene." *Eur. J. Biochem.* 201(3): 653-659.
- 136 McDaniel JR, MacKay JA, Quiroz FGa, Chilkoti A (2010). "Recursive directional ligation by plasmid reconstruction allows rapid and seamless cloning of oligomeric genes." *Biomacromolecules* 11(4): 944-952.
- 137 Jeong H, Barbe V, Lee CH, Vallenet D, Yu DS, Choi SH, Couloux A, Lee SW, Yoon SH, Cattolico L, Hur CG, Park HS, Segurens B, Kim SC, Oh TK, Lenski RE, Studier FW, Daegelen P, Kim JF (2009). "Genome sequences of escherichia coli b strains rel606 and bl21(de3)." *J. Mol. Biol.* 394(4): 644-652.
- 138 Buskirk AR, Green R (2017). "Ribosome pausing, arrest and rescue in bacteria and eukaryotes." *Philos. Trans. R. Soc. Lond. B Biol. Sci.* 372(1716).
- 139 Meyer DE, Chilkoti A (2004). "Quantification of the effects of chain length and concentration on the thermal behavior of elastin-like polypeptides." *Biomacromolecules* 5(3): 846-851.
- 140 McPherson DT, Xu J, Urry DW (1996). "Product purification by reversible phase transition following escherichia coli expression of genes encoding up to 251 repeats of the elastomeric pentapeptide gvgvp." *Protein Expr. Purif.* 7(1): 51-57.
- 141 Lu J, Owen SC, Shoichet MS (2011). "Stability of self-assembled polymeric micelles in serum." *Macromolecules* 44(15): 6002-6008.
- 142 Owen SC, Chan DPY, Shoichet MS (2012). "Polymeric micelle stability." *Nano Today* 7(1): 53-65.
- 143 Kim Y, Pourgholami MH, Morris DL, Stenzel MH (2012). "Effect of cross-linking on the performance of micelles as drug delivery carriers: A cell uptake study." *Biomacromolecules* 13(3): 814-825.

- 144 Lin W, Ma G, Kampf N, Yuan Z, Chen S (2016). "Development of long-circulating zwitterionic cross-linked micelles for active-targeted drug delivery." *Biomacromolecules* 17(6): 2010-2018.
- 145 Gritsan N, Platz M, in *Organic azides*, John Wiley & Sons, Ltd, 2009, pp. 311-372.
- 146 Gritsan NP, Platz MS (2006). "Kinetics, spectroscopy, and computational chemistry of aryl nitrenes." *Chem. Rev.* 106(9): 3844-3867.
- 147 Costa SA, Simon JR, Amiram M, Tang L, Zauscher S, Brustad EM, Isaacs FJ, Chilkoti A (2018). "Photo-crosslinkable unnatural amino acids enable facile synthesis of thermoresponsive nano- to microgels of intrinsically disordered polypeptides." *Adv Mater* 30(5).
- 148 Wang WX, Liang H, Al Ghanami RC, Hamilton L, Fraylich M, Shakesheff KM, Saunders B, Alexander C (2009). "Biodegradable thermoresponsive microparticle dispersions for injectable cell delivery prepared using a single-step process." *Advanced Materials* 21(18): 1809-+.
- 149 Ding T, Rüttiger C, Zheng X, Benz F, Ohadi H, Vandenbosch GAE, Moshchalkov VV, Gallei M, Baumberg JJ (2016). "Fast dynamic color switching in temperature-responsive plasmonic films." *Advanced Optical Materials* 4(6): 877-882.
- 150 Asai D, Xu D, Liu W, Garcia Quiroz F, Callahan DJ, Zalutsky MR, Craig SL, Chilkoti A (2012). "Protein polymer hydrogels by in situ, rapid and reversible self-gelation." *Biomaterials* 33(21): 5451-5458.
- 151 Chu LY, Kim JW, Shah RK, Weitz DA (2007). "Monodisperse thermoresponsive microgels with tunable volume-phase transition kinetics." *Advanced Functional Materials* 17(17): 3499-3504.
- 152 Coughlan DC, Quilty FP, Corrigan OI (2004). "Effect of drug physicochemical properties on swelling/deswelling kinetics and pulsatile drug release from thermoresponsive poly(n-isopropylacrylamide) hydrogels." *J. Control. Release* 98(1): 97-114.

- 153 DeForest CA, Tirrell DA (2015). "A photoreversible protein-patterning approach for guiding stem cell fate in three-dimensional gels." *Nat Mater* 14(5): 523-531.
- 154 Hoffmann J, Plotner M, Kuckling D, Fischer WJ (1999). "Photopatterning of thermally sensitive hydrogels useful for microactuators." *Sensors and Actuators a-Physical* 77(2): 139-144.
- 155 Li W, Zhang L, Ge X, Xu B, Zhang W, Qu L, Choi CH, Xu J, Zhang A, Lee H, Weitz DA (2018). "Microfluidic fabrication of microparticles for biomedical applications." *Chem. Soc. Rev.* 47(15): 5646-5683.
- 156 Wang Y, Angelatos AS, Caruso F (2008). "Template synthesis of nanostructured materials via layer-by-layer assembly." *Chem. Mater.* 20(3): 848-858.
- 157 Hartgerink JD, Beniash E, Stupp SI (2002). "Peptide-amphiphile nanofibers: A versatile scaffold for the preparation of self-assembling materials." *Proceedings of the National Academy of Sciences* 99(8): 5133-5138.
- 158 Utada AS, Lenceau E, Link DR, Kaplan PD, Stone HA, Weitz DA (2005). "Monodisperse double emulsions generated from a microcapillary device." *Science* 308(5721): 537-541.
- 159 Chu L-Y, Utada AS, Shah RK, Kim J-W, Weitz DA (2007). "Controllable monodisperse multiple emulsions." *Angewandte Chemie International Edition* 46(47): 8970-8974.
- 160 Nie Z, Li W, Seo M, Xu S, Kumacheva E (2006). "Janus and ternary particles generated by microfluidic synthesis: Design, synthesis, and self-assembly." *J. Am. Chem. Soc.* 128(29): 9408-9412.
- 161 Dreher MR, Simnick AJ, Fischer K, Smith RJ, Patel A, Schmidt M, Chilkoti A (2007). "Temperature triggered self-assembly of polypeptides into multivalent spherical micelles." *J. Am. Chem. Soc.* 130(2): 687-694.

- 162 Shah RK, Kim J-W, Agresti JJ, Weitz DA, Chu L-Y (2008). "Fabrication of monodisperse thermosensitive microgels and gel capsules in microfluidic devices." *Soft Matter* 4(12): 2303-2309.
- 163 Oh JK, Drumright R, Siegwart DJ, Matyjaszewski K (2008). "The development of microgels/nanogels for drug delivery applications." *Progress in Polymer Science* 33(4): 448-477.
- 164 Schaal JL, Li X, Mastria E, Bhattacharyya J, Zalutsky MR, Chilkoti A, Liu W (2016). "Injectable polypeptide micelles that form radiation crosslinked hydrogels in situ for intratumoral radiotherapy." *J. Control. Release* 228: 58-66.
- 165 Levary DA, Parthasarathy R, Boder ET, Ackerman ME (2011). "Protein-protein fusion catalyzed by sortase a." *PLoS One* 6(4): e18342.
- 166 McHale MK, Setton LA, Chilkoti A (2005). "Synthesis and in vitro evaluation of enzymatically cross-linked elastin-like polypeptide gels for cartilaginous tissue repair." *Tissue Eng.* 11(11-12): 1768-1779.
- 167 Petka WA, Harden JL, McGrath KP, Wirtz D, Tirrell DA (1998). "Reversible hydrogels from self-assembling artificial proteins." *Science* 281(5375): 389-392.
- 168 Leitner A, Walzthoeni T, Kahraman A, Herzog F, Rinner O, Beck M, Aebersold R (2010). "Probing native protein structures by chemical cross-linking, mass spectrometry, and bioinformatics." *Mol. Cell. Proteomics* 9(8): 1634-1649.
- 169 Preston GW, Wilson AJ (2013). "Photo-induced covalent cross-linking for the analysis of biomolecular interactions." *Chem. Soc. Rev.* 42(8): 3289-3301.
- 170 Sinz A (2006). "Chemical cross-linking and mass spectrometry to map three-dimensional protein structures and protein-protein interactions." *Mass Spectrom. Rev.* 25(4): 663-682.
- 171 Izzo D, Marques CM (2005). "Solubilization of homopolymers in a solution of diblock copolymers." *J. Phys. Chem. B* 109(13): 6140-6145.

- 172 Larson K, Raghuraman B, Wiencek J (1994). "Electrical and chemical demulsification techniques for microemulsion liquid membranes." *Journal of Membrane Science* 91: 231-248.
- 173 Dreher MR, Simnick AJ, Fischer K, Smith RJ, Patel A, Schmidt M, Chilkoti A (2008). "Temperature triggered self-assembly of polypeptides into multivalent spherical micelles." *J. Am. Chem. Soc.* 130(2): 687-694.
- 174 Gritsan N, Platz M, in *Organic azides*, John Wiley & Sons, Ltd, **2010**, pp. 311-372.
- 175 Simon JR, Carroll NJ, Rubinstein M, Chilkoti A, Lopez GP (2017). "Programming molecular self-assembly of intrinsically disordered proteins containing sequences of low complexity." *Nat. Chem.* 9(6): 509-515.
- 176 Kopecek J (2002). "Polymer chemistry: Swell gels." *Nature* 417(6887): 388-389, 391.
- 177 Li J, Mooney DJ (2016). "Designing hydrogels for controlled drug delivery." *Nat Rev Mater* 1(12).
- 178 Talelli M, Barz M, Rijcken CJ, Kiessling F, Hennink WE, Lammers T (2015). "Core-crosslinked polymeric micelles: Principles, preparation, biomedical applications and clinical translation." *Nano Today* 10(1): 93-117.
- 179 Chen D, Amstad E, Zhao CX, Cai L, Fan J, Chen Q, Hai M, Koehler S, Zhang H, Liang F, Yang Z, Weitz DA (2017). "Biocompatible amphiphilic hydrogel-solid dimer particles as colloidal surfactants." *ACS Nano* 11(12): 11978-11985.
- 180 Gentile F, Curcio A, Indolfi C, Ferrari M, Decuzzi P (2008). "The margination propensity of spherical particles for vascular targeting in the microcirculation." *J Nanobiotechnology* 6: 9.
- 181 Charoenphol P, Mocherla S, Bouis D, Namdee K, Pinsky DJ, Eniola-Adefeso O (2011). "Targeting therapeutics to the vascular wall in atherosclerosis--carrier size matters." *Atherosclerosis* 217(2): 364-370.

- 182 Podual K, Doyle FJ, Peppas NA (2000). "Glucose-sensitivity of glucose oxidase-containing cationic copolymer hydrogels having poly(ethylene glycol) grafts." *J. Control. Release* 67(1): 9-17.
- 183 Battista E, Causa F, Netti P (2017). "Bioengineering microgels and hydrogel microparticles for sensing biomolecular targets." *Gels* 3(2).
- 184 Zeeb B, Saberi AH, Weiss J, McClements DJ (2015). "Retention and release of oil-in-water emulsions from filled hydrogel beads composed of calcium alginate: Impact of emulsifier type and ph." *Soft Matter* 11(11): 2228-2236.
- 185 McClements DJ, Decker EA, Weiss J (2007). "Emulsion-based delivery systems for lipophilic bioactive components." *J. Food Sci.* 72(8): R109-124.
- 186 Song S, Zhang X, Hayat K, Huang M, Liu P, Karangwa E, Gu F, Jia C, Xia S, Xiao Z, Niu Y (2010). "Contribution of beef base to aroma characteristics of beeflike process flavour assessed by descriptive sensory analysis and gas chromatography olfactometry and partial least squares regression." *J. Chromatogr. A* 1217(49): 7788-7799.
- 187 Rahnamaeian M, Vilcinskas A (2015). "Short antimicrobial peptides as cosmetic ingredients to deter dermatological pathogens." *Appl. Microbiol. Biotechnol.* 99(21): 8847-8855.
- 188 Husein El Hadmed H, Castillo RF (2016). "Cosmeceuticals: Peptides, proteins, and growth factors." *J. Cosmet. Dermatol.* 15(4): 514-519.
- 189 Simon JR, Carroll NJ, Rubinstein M, Chilkoti A, López GP (2017). "Programming molecular self-assembly of intrinsically disordered proteins containing sequences of low complexity." *Nat. Chem.* advance online publication.
- 190 Xu C, Hu S, Chen X (2016). "Artificial cells: From basic science to applications." *Mater Today (Kidlington)* 19(9): 516-532.

- 191 Urry DW, Haynes B, Harris RD (1986). "Temperature dependence of length of elastin and its polypentapeptide." *Biochem. Biophys. Res. Commun.* 141(2): 749-755.
- 192 Urry DW, Luan CH, Parker TM, Gowda DC, Prasad KU, Reid MC, Safavy A (1991). "Temperature of polypeptide inverse temperature transition depends on mean residue hydrophobicity." *J. Am. Chem. Soc.* 113(11): 4346-4348.
- 193 Urry DW, Trapane TL, Prasad KU (1985). "Phase-structure transitions of the elastin polypentapeptide water-system within the framework of composition temperature studies." *Biopolymers* 24(12): 2345-2356.
- 194 McDaniel JR, Radford DC, Chilkoti A (2013). "A unified model for de novo design of elastin-like polypeptides with tunable inverse transition temperatures." *Biomacromolecules* 14(8): 2866-2872.
- 195 Cho K, Wang X, Nie S, Chen ZG, Shin DM (2008). "Therapeutic nanoparticles for drug delivery in cancer." *Clin. Cancer Res.* 14(5): 1310-1316.
- 196 Dawidczyk CM, Kim C, Park JH, Russell LM, Lee KH, Pomper MG, Searson PC (2014). "State-of-the-art in design rules for drug delivery platforms: Lessons learned from fda-approved nanomedicines." *J. Control. Release* 187: 133-144.
- 197 Huang Y, Cole SP, Cai T, Cai YU (2016). "Applications of nanoparticle drug delivery systems for the reversal of multidrug resistance in cancer." *Oncol. Lett.* 12(1): 11-15.
- 198 Xue X, Liang XJ (2012). "Overcoming drug efflux-based multidrug resistance in cancer with nanotechnology." *Chin. J. Cancer* 31(2): 100-109.
- 199 Yoo J-W, Chambers E, Mitragotri S (2010). "Factors that control the circulation time of nanoparticles in blood: Challenges, solutions and future prospects." *Curr. Pharm. Des.* 16(21): 2298-2307.

- 200 Bazak R, Hourri M, El Achy S, Kamel S, Refaat T (2015). "Cancer active targeting by nanoparticles: A comprehensive review of literature." *J. Cancer Res. Clin. Oncol.* 141(5): 769-784.
- 201 Zhong Y, Meng F, Deng C, Zhong Z (2014). "Ligand-directed active tumor-targeting polymeric nanoparticles for cancer chemotherapy." *Biomacromolecules* 15(6): 1955-1969.
- 202 Bertrand N, Wu J, Xu X, Kamaly N, Farokhzad OC (2014). "Cancer nanotechnology: The impact of passive and active targeting in the era of modern cancer biology." *Adv Drug Deliv Rev* 66: 2-25.
- 203 Basile L, Pignatello R, Passirani C (2012). "Active targeting strategies for anticancer drug nanocarriers." *Curr Drug Deliv* 9(3): 255-268.
- 204 Gary-Bobo M, Vaillant O, Maynadier M, Basile I, Gallud A, El Cheikh K, Bouffard E, Morere A, Rebillard X, Puche P, Nirde P, Garcia M (2013). "Targeting multiplicity: The key factor for anti-cancer nanoparticles." *Curr. Med. Chem.* 20(15): 1946-1955.
- 205 Hao Y, Zheng C, Wang L, Hu Y, Guo H, Song Q, Zhang H, Zhang Z, Zhang Y (2017). "Covalent self-assembled nanoparticles with ph-dependent enhanced tumor retention and drug release for improving tumor therapeutic efficiency." *J. Mater. Chem. B* 5(11): 2133-2144.
- 206 Moustafa A, Abd Rabo Moustafa MM, Zilinskas GJ, Gillies ER (2015). "Covalent drug immobilization in poly(ester amide) nanoparticles for controlled release." *The Canadian Journal of Chemical Engineering* 93(12): 2098-2106.
- 207 Morachis JM, Mahmoud EA, Almutairi A (2012). "Physical and chemical strategies for therapeutic delivery by using polymeric nanoparticles." *Pharmacol. Rev.* 64(3): 505-519.

- 208 Vigderman L, Zubarev ER (2013). "Therapeutic platforms based on gold nanoparticles and their covalent conjugates with drug molecules." *Adv Drug Deliv Rev* 65(5): 663-676.
- 209 Koo OM, Rubinstein I, Onyuksel H (2005). "Role of nanotechnology in targeted drug delivery and imaging: A concise review." *Nanomedicine* 1(3): 193-212.
- 210 Werengowska-Ciećwierz K, Wiśniewski M, Terzyk AP, Furmaniak S (2015). "The chemistry of bioconjugation in nanoparticles-based drug delivery system." *Advances in Condensed Matter Physics* 2015: 1-27.
- 211 Upponi JR, Torchilin VP, in *Nano-oncologicals*, **2014**, pp. 3-45.
- 212 Callahan DJ, Liu W, Li X, Dreher MR, Hassouneh W, Kim M, Marszalek P, Chilkoti A (2012). "Triple stimulus-responsive polypeptide nanoparticles that enhance intratumoral spatial distribution." *Nano Lett* 12(4): 2165-2170.
- 213 MacKay JA, Chen M, McDaniel JR, Liu W, Simnick AJ, Chilkoti A (2009). "Self-assembling chimeric polypeptide-doxorubicin conjugate nanoparticles that abolish tumours after a single injection." *Nat Mater* 8(12): 993-999.
- 214 McDaniel JR, Dewhirst MW, Chilkoti A (2013). "Actively targeting solid tumours with thermoresponsive drug delivery systems that respond to mild hyperthermia." *Int. J. Hyperthermia* 29(6): 501-510.
- 215 McDaniel JR, Macewan SR, Dewhirst M, Chilkoti A (2012). "Doxorubicin-conjugated chimeric polypeptide nanoparticles that respond to mild hyperthermia." *J. Control. Release* 159(3): 362-367.
- 216 Torchilin V (2011). "Tumor delivery of macromolecular drugs based on the epr effect." *Adv Drug Deliv Rev* 63(3): 131-135.
- 217 Meyer DE, Chilkoti A (2002). "Genetically encoded synthesis of protein-based polymers with precisely specified molecular weight and sequence by recursive

- directional ligation: Examples from the elastin-like polypeptide system." *Biomacromolecules* 3(2): 357-367.
- 218 Navon Y, Bitton R (2016). "Elastin-like peptides (elpeps) - building blocks for stimuli-responsive self-assembled materials." *Isr. J. Chem.* 56(8): 581-589.
- 219 Betre H, Liu W, Zalutsky MR, Chilkoti A, Kraus VB, Setton LA (2006). "A thermally responsive biopolymer for intra-articular drug delivery." *J. Control. Release* 115(2): 175-182.
- 220 Chilkoti A, Dreher MR, Meyer DE, Raucher D (2002). "Targeted drug delivery by thermally responsive polymers." *Adv Drug Deliv Rev* 54(5): 613-630.
- 221 Liu W, Dreher MR, Furgeson DY, Peixoto KV, Yuan H, Zalutsky MR, Chilkoti A (2006). "Tumor accumulation, degradation and pharmacokinetics of elastin-like polypeptides in nude mice." *J. Control. Release* 116(2): 170-178.
- 222 Hassouneh W, Fischer K, MacEwan SR, Branscheid R, Fu CL, Liu R, Schmidt M, Chilkoti A (2012). "Unexpected multivalent display of proteins by temperature triggered self-assembly of elastin-like polypeptide block copolymers." *Biomacromolecules* 13(5): 1598-1605.
- 223 Weitzhandler I, Dzuricky M, Hoffmann I, Garcia Quiroz F, Gradzielski M, Chilkoti A (2017). "Micellar self-assembly of recombinant resilin-/elastin-like block copolypeptides." *Biomacromolecules* 18(8): 2419-2426.
- 224 Wang J, Dzuricky M, Chilkoti A (2017). "The weak link: Optimization of the ligand-nanoparticle interface to enhance cancer cell targeting by polymer micelles." *Nano Lett* 17(10): 5995-6005.
- 225 Aluri S, Pastuszka MK, Moses AS, MacKay JA (2012). "Elastin-like peptide amphiphiles form nanofibers with tunable length." *Biomacromolecules* 13(9): 2645-2654.

- 226 Mozhdghi D, Luginbuhl KM, Simon JR, Dzuricky M, Berger R, Varol HS, Huang FC, Buehne KL, Mayne NR, Weitzhandler I, Bonn M, Parekh SH, Chilkoti A (2018). "Genetically encoded lipid–polypeptide hybrid biomaterials that exhibit temperature-triggered hierarchical self-assembly." *Nat. Chem.* 10(5): 496-505.
- 227 Gao H, Zhang Q, Yang Y, Jiang X, He Q (2015). "Tumor homing cell penetrating peptide decorated nanoparticles used for enhancing tumor targeting delivery and therapy." *Int. J. Pharm.* 478(1): 240-250.
- 228 Field LD, Delehanty JB, Chen Y, Medintz IL (2015). "Peptides for specifically targeting nanoparticles to cellular organelles: Quo vadis?" *Acc. Chem. Res.* 48(5): 1380-1390.
- 229 Fay F, Scott CJ (2011). "Antibody-targeted nanoparticles for cancer therapy." *Immunotherapy* 3(3): 381-394.
- 230 Friedman A, Claypool S, Liu R (2013). "The smart targeting of nanoparticles." *Curr. Pharm. Des.* 19(35): 6315-6329.
- 231 Friedman M, Orlova A, Johansson E, Eriksson TL, Hoiden-Guthenberg I, Tolmachev V, Nilsson FY, Stahl S (2008). "Directed evolution to low nanomolar affinity of a tumor-targeting epidermal growth factor receptor-binding affibody molecule." *J. Mol. Biol.* 376(5): 1388-1402.
- 232 Muyldermans S (2013). "Nanobodies: Natural single-domain antibodies." *Annu. Rev. Biochem.* 82: 775-797.
- 233 Tijink BM, Laeremans T, Budde M, Stigter-van Walsum M, Dreier T, de Haard HJ, Leemans CR, van Dongen GA (2008). "Improved tumor targeting of anti-epidermal growth factor receptor nanobodies through albumin binding: Taking advantage of modular nanobody technology." *Mol. Cancer Ther.* 7(8): 2288-2297.
- 234 Roovers RC, Laeremans T, Huang L, De Taeye S, Verkleij AJ, Revets H, de Haard HJ, van Bergen en Henegouwen PMP (2006). "Efficient inhibition of egfr

- signalling and of tumour growth by antagonistic anti-egfr nanobodies." *Cancer Immunol. Immunother.* 56(3): 303-317.
- 235 Hu Y, Liu C, Muyldermans S (2017). "Nanobody-based delivery systems for diagnosis and targeted tumor therapy." *Front. Immunol.* 8: 1442.
- 236 Zarschler K, Witecy S, Kapplusch F, Foerster C, Stephan H (2013). "High-yield production of functional soluble single-domain antibodies in the cytoplasm of escherichia coli." *Microb Cell Fact* 12: 97.
- 237 Els Conrath K, Lauwereys M, Wyns L, Muyldermans S (2001). "Camel single-domain antibodies as modular building units in bispecific and bivalent antibody constructs." *J. Biol. Chem.* 276(10): 7346-7350.
- 238 Hofman EG, Ruonala MO, Bader AN, van den Heuvel D, Voortman J, Roovers RC, Verkleij AJ, Gerritsen HC, van Bergen en Henegouwen PMP (2008). "Egf induces coalescence of different lipid rafts." *J. Cell Sci.* 121(15): 2519-2528.
- 239 van der Meel R, Oliveira S, Altintas I, Haselberg R, van der Veecken J, Roovers RC, van Bergen en Henegouwen PM, Storm G, Hennink WE, Schiffelers RM, Kok RJ (2012). "Tumor-targeted nanobullets: Anti-egfr nanobody-liposomes loaded with anti-igf-1r kinase inhibitor for cancer treatment." *J. Control. Release* 159(2): 281-289.
- 240 Yewale C, Baradia D, Vhora I, Patil S, Misra A (2013). "Epidermal growth factor receptor targeting in cancer: A review of trends and strategies." *Biomaterials* 34(34): 8690-8707.
- 241 Sasaki T, Hiroki K, Yamashita Y (2013). "The role of epidermal growth factor receptor in cancer metastasis and microenvironment." *Biomed Res Int* 2013: 546318.
- 242 Cerami E, Gao J, Dogrusoz U, Gross BE, Sumer SO, Aksoy BA, Jacobsen A, Byrne CJ, Heuer ML, Larsson E, Antipin Y, Reva B, Goldberg AP, Sander C, Schultz N

- (2012). "The cBio Cancer Genomics Portal: An open platform for exploring multidimensional cancer genomics data." *Cancer Discov.* 2(5): 401-404.
- 243 Gao J, Aksoy BA, Dogrusoz U, Dresdner G, Gross B, Sumer SO, Sun Y, Jacobsen A, Sinha R, Larsson E, Cerami E, Sander C, Schultz N (2013). "Integrative analysis of complex cancer genomics and clinical profiles using the cBioPortal." *Sci Signal* 6(269): p11.
- 244 Koivunen E, Wang B, Ruoslahti E (1995). "Phage libraries displaying cyclic peptides with different ring sizes: Ligand specificities of the RGD-directed integrins." *Nat. Biotechnol.* 13(3): 265-270.
- 245 Rivankar S (2014). "An overview of doxorubicin formulations in cancer therapy." *J. Cancer Res. Ther.* 10(4): 853-858.
- 246 Dreher MR, Raucher D, Balu N, Michael Colvin O, Ludeman SM, Chilkoti A (2003). "Evaluation of an elastin-like polypeptide-doxorubicin conjugate for cancer therapy." *J. Control. Release* 91(1-2): 31-43.
- 247 Furgeson DY, Dreher MR, Chilkoti A (2006). "Structural optimization of a "smart" doxorubicin-polypeptide conjugate for thermally targeted delivery to solid tumors." *J. Control. Release* 110(2): 362-369.
- 248 Tacar O, Sriamornsak P, Dass CR (2013). "Doxorubicin: An update on anticancer molecular action, toxicity and novel drug delivery systems." *J. Pharm. Pharmacol.* 65(2): 157-170.
- 249 Zhu YJ, Chen F (2015). "pH-responsive drug-delivery systems." *Chem. Asian J.* 10(2): 284-305.
- 250 Yoshida T, Lai TC, Kwon GS, Sako K (2013). "pH- and ion-sensitive polymers for drug delivery." *Expert Opin Drug Deliv* 10(11): 1497-1513.
- 251 He X, Li J, An S, Jiang C (2013). "pH-sensitive drug-delivery systems for tumor targeting." *Ther. Deliv.* 4(12): 1499-1510.

- 252 Jin Y, Song L, Su Y, Zhu L, Pang Y, Qiu F, Tong G, Yan D, Zhu B, Zhu X (2011). "Oxime linkage: A robust tool for the design of pH-sensitive polymeric drug carriers." *Biomacromolecules* 12(10): 3460-3468.
- 253 Kalia J, Raines RT (2008). "Hydrolytic stability of hydrazones and oximes." *Angew. Chem. Int. Ed. Engl.* 47(39): 7523-7526.
- 254 Meyer DE, Chilkoti A (1999). "Purification of recombinant proteins by fusion with thermally-responsive polypeptides." *Nat. Biotechnol.* 17(11): 1112-1115.
- 255 Pedersen MW, Tkach V, Pedersen N, Berezin V, Poulsen HS (2004). "Expression of a naturally occurring constitutively active variant of the epidermal growth factor receptor in mouse fibroblasts increases motility." *Int. J. Cancer* 108: 643-653.
- 256 Vellon L, Menendez JA, Lupu R (2005). "Avb3 integrin regulates heregulin (hrg)-induced cell proliferation and survival in breast cancer." *Oncogene* 24: 3579-3773.
- 257 Pirman NL, Barber KW, Aerni HR, Ma NJ, Haimovich AD, Rogulina S, Isaacs FJ, Rinehart J (2015). "A flexible codon in genomically recoded *Escherichia coli* permits programmable protein phosphorylation." *Nat Commun* 6: 8130.
- 258 O'Donoghue P, Prat L, Heinemann IU, Ling J, Odoi K, Liu WR, Soll D (2012). "Near-cognate suppression of amber, opal and quadruplet codons competes with aminoacyl-tRNA^l for genetic code expansion." *FEBS Lett.* 586(21): 3931-3937.
- 259 Aerni HR, Shifman MA, Rogulina S, O'Donoghue P, Rinehart J (2015). "Revealing the amino acid composition of proteins within an expanded genetic code." *Nucleic Acids Res.* 43(2): e8.
- 260 Kibria G, Hatakeyama H, Akiyama K, Hida K, Harashima H (2014). "Comparative study of the sensitivities of cancer cells to doxorubicin, and relationships between the effect of the drug-efflux pump p-gp." *Biol. Pharm. Bull.* 37(12).

- 261 Yang W, Soares J, Greninger P, Edelman EJ, Lightfoot H, Forbes S, Bindal N, Beare D, Smith JA, Thompson IR, Ramaswamy S, Futreal PA, Haber DA, Stratton MR, Benes C, McDermott U, Garnett MJ (2013). "Genomics of drug sensitivity in cancer (gdsc): A resource for therapeutic biomarker discovery in cancer cells." *Nucleic Acids Res.* 41(Database issue): D955-961.
- 262 Dirksen A, Hackeng TM, Dawson PE (2006). "Nucleophilic catalysis of oxime ligation." *Angew. Chem. Int. Ed. Engl.* 45(45): 7581-7584.
- 263 Wendeler M, Grinberg L, Wang X, Dawson PE, Baca M (2014). "Enhanced catalysis of oxime-based bioconjugations by substituted anilines." *Bioconjug. Chem.* 25(1): 93-101.
- 264 Wang K, Li D, Sun L (2016). "High levels of egfr expression in tumor stroma are associated with aggressive clinical features in epithelial ovarian cancer." *Onco Targets Ther.* 9: 377-386.
- 265 Zhang F, Wang S, Yin L, Yang Y, Guan Y, Wang W, Xu H, Tao N (2015). "Quantification of epidermal growth factor receptor expression level and binding kinetics on cell surfaces by surface plasmon resonance imaging." *Anal. Chem.* 87(19): 9960-9965.
- 266 Ponten F, Jirstrom K, Uhlen M (2008). "The human protein atlas--a tool for pathology." *J. Pathol.* 216(4): 387-393.
- 267 Algars A, Avoranta T, Osterlund P, Lintunen M, Sundstrom J, Jokilehto T, Ristimaki A, Ristamaki R, Carpen O (2014). "Heterogeneous egfr gene copy number increase is common in colorectal cancer and defines response to anti-egfr therapy." *PLoS One* 9(6): e99590.
- 268 Bozic I, Reiter JG, Allen B, Antal T, Chatterjee K, Shah P, Moon YS, Yaquobie A, Kelly N, Le DT, Lipson EJ, Chapman PB, Diaz LA, Jr., Vogelstein B, Nowak MA (2013). "Evolutionary dynamics of cancer in response to targeted combination therapy." *Elife* 2: e00747.

- 269 Adler J, Parmryd I (2010). "Quantifying colocalization by correlation: The pearson correlation coefficient is superior to the mander's overlap coefficient." *Cytometry A* 77(8): 733-742.
- 270 Bolte S, Cordelieres FP (2006). "A guided tour into subcellular colocalization analysis in light microscopy." *J. Microsc.* 224(Pt 3): 213-232.
- 271 Oliveira S, Schiffelers RM, van der Veeken J, van der Meel R, Vongpromek R, van Bergen En Henegouwen PM, Storm G, Roovers RC (2010). "Downregulation of egfr by a novel multivalent nanobody-liposome platform." *J. Control. Release* 145(2): 165-175.
- 272 Bareford L, Swaan P (2007). "Endocytic mechanisms for targeted drug delivery☆." *Advanced Drug Delivery Reviews* 59(8): 748-758.
- 273 Wang M, Thanou M (2010). "Targeting nanoparticles to cancer." *Pharmacol. Res.* 62(2): 90-99.
- 274 Kularatne SA, Deshmukh V, Ma J, Tardif V, Lim RK, Pugh HM, Sun Y, Manibusan A, Sellers AJ, Barnett RS, Srinagesh S, Forsyth JS, Hassenpflug W, Tian F, Javahishvili T, Felding-Habermann B, Lawson BR, Kazane SA, Schultz PG (2014). "A cxcr4-targeted site-specific antibody-drug conjugate." *Angew. Chem. Int. Ed. Engl.* 53(44): 11863-11867.
- 275 Hutchins BM, Kazane SA, Staflin K, Forsyth JS, Felding-Habermann B, Schultz PG, Smider VV (2011). "Site-specific coupling and sterically controlled formation of multimeric antibody fab fragments with unnatural amino acids." *J. Mol. Biol.* 406(4): 595-603.
- 276 Oller-Salvia B, Kym G, Chin JW (2018). "Rapid and efficient generation of stable antibody-drug conjugates via an encoded cyclopropene and an inverse-electron-demand diels-alder reaction." *Angew. Chem. Int. Ed. Engl.* 57(11): 2831-2834.
- 277 Nitta S, Numata K (2013). "Biopolymer-based nanoparticles for drug/gene delivery and tissue engineering." *Int. J. Mol. Sci.* 14(1): 1629-1654.

- 278 Hudson D, Margaritis A (2013). "Biopolymer nanoparticle production for controlled release of biopharmaceuticals." *Crit. Rev. Biotechnol.* 34(2): 161-179.
- 279 Siontorou CG (2013). "Nanobodies as novel agents for disease diagnosis and therapy." *Int J Nanomedicine* 8: 4215-4227.
- 280 Kumra H, Reinhardt DP (2016). "Fibronectin-targeted drug delivery in cancer." *Adv Drug Deliv Rev* 97: 101-110.
- 281 Kintzing JR, Cochran JR (2016). "Engineered knottin peptides as diagnostics, therapeutics, and drug delivery vehicles." *Curr. Opin. Chem. Biol.* 34: 143-150.
- 282 List T, Casi G, Neri D (2014). "A chemically defined trifunctional antibody-cytokine-drug conjugate with potent antitumor activity." *Mol. Cancer Ther.* 13(11): 2641-2652.
- 283 Demarest SJ, Glaser SM (2008). "Antibody therapeutics, antibody engineering, and the merits of protein stability." *Curr Opin Drug Discov Devel* 11(5): 675-687.
- 284 Wagner JA, Mercadante D, Nikic I, Lemke EA, Grater F (2015). "Origin of orthogonality of strain-promoted click reactions." *Chemistry (Easton)* 21(35): 12431-12435.
- 285 Holland EC (2000). "Glioblastoma multiforme: The terminator." *Proc. Natl. Acad. Sci. U. S. A.* 97(12): 6242-6244.
- 286 Krex D, Klink B, Hartmann C, von Deimling A, Pietsch T, Simon M, Sabel M, Steinbach JP, Heese O, Reifenberger G, Weller M, Schackert G, German Glioma N (2007). "Long-term survival with glioblastoma multiforme." *Brain* 130(Pt 10): 2596-2606.
- 287 Markert J (2005). *Glioblastoma multiforme*. Sudbury, MA, Jones and Bartlett Publishers.

- 288 Ochiai H, Archer GE, Herndon JE, Kuan CT, Mitchell DA, Bigner DD, Pastan IH, Sampson JH (2008). "Egfrviii-targeted immunotoxin induces antitumor immunity that is inhibited in the absence of cd4+ and cd8+ t cells." *Cancer Immunology Immunotherapy* 57(1): 115-121.
- 289 Kuan CT, Wakiya K, Keir ST, Li J, Herndon JE, 2nd, Pastan I, Bigner DD (2011). "Affinity-matured anti-glycoprotein nmb recombinant immunotoxins targeting malignant gliomas and melanomas." *Int. J. Cancer* 129(1): 111-121.
- 290 Chandramohan V, Sampson JH, Pastan I, Bigner DD (2012). "Toxin-based targeted therapy for malignant brain tumors." *Clin. Dev. Immunol.* 2012: 480429.
- 291 Tang L, Persky AM, Hochhaus G, Meibohm B (2004). "Pharmacokinetic aspects of biotechnology products." *J. Pharm. Sci.* 93(9): 2184-2204.
- 292 Alfarouk KO, Stock CM, Taylor S, Walsh M, Muddathir AK, Verduzco D, Bashir AH, Mohammed OY, Elhassan GO, Harguindey S, Reshkin SJ, Ibrahim ME, Rauch C (2015). "Resistance to cancer chemotherapy: Failure in drug response from adme to p-gp." *Cancer Cell Int.* 15: 71.
- 293 Guo R, Guo W, Cao L, Liu H, Liu J, Xu H, Huang W, Wang F, Hong Z (2016). "Fusion of an albumin-binding domain extends the half-life of immunotoxins." *Int. J. Pharm.* 511(1): 538-549.
- 294 Pastan I, Willingham MC, FitzGerald DJ (1986). "Immunotoxins." *Cell* 47(5): 641-648.
- 295 Yun J, Rothrock RJ, Canoll P, Bruce JN (2013). "Convection-enhanced delivery for targeted delivery of anti-glioma agents: The translational experience." *J Drug Deliv* 2013: 107573.
- 296 Debinski W, Tatter SB (2009). "Convection-enhanced delivery for the treatment of brain tumors." *Expert Rev. Neurother.* 9(10): 1519-1527.

- 297 Brem H, Gabikian P (2001). "Biodegradable polymer implants to treat brain tumors." *J. Control. Release* 74(1-3): 63-67.
- 298 Murai S, Ichikawa T, Kurozumi K, Shimazu Y, Oka T, Otani Y, Shimizu T, Date I (2016). "Quantitative analysis of brain edema in patients with malignant glioma treated with bcnu wafers." *J. Clin. Neurosci.* 33: 148-153.
- 299 Bregy A, Shah AH, Diaz MV, Pierce HE, Ames PL, Diaz D, Komotar RJ (2013). "The role of gliadel wafers in the treatment of high-grade gliomas." *Expert Rev. Anticancer Ther.* 13(12): 1453-1461.
- 300 Kuramitsu S, Motomura K, Natsume A, Wakabayashi T (2015). "Double-edged sword in the placement of carmustine (bcnu) wafers along the eloquent area: A case report." *NMC Case Rep J* 2(1): 40-45.
- 301 Chowdhary SA, Ryken T, Newton HB (2015). "Survival outcomes and safety of carmustine wafers in the treatment of high-grade gliomas: A meta-analysis." *J. Neurooncol.* 122(2): 367-382.
- 302 Frederick L, Wang X-Y, Eley G, James CD (2000). "Diversity and frequency of epidermal growth factor receptor mutations in human glioblastomas." *Cancer Research* 60(5): 1383-1387.
- 303 Estrada C, Villalobo A, in *The cell cycle in the central nervous system* (Ed.: D. Janigro), Humana Press, Totowa, NJ, 2006, pp. 265-277.
- 304 Shinojima N, Tada K, Shiraishi S, Kamiryo T, Kochi M, Nakamura H, Makino K, Saya H, Hirano H, Kuratsu J, Oka K, Ishimaru Y, Ushio Y (2003). "Prognostic value of epidermal growth factor receptor in patients with glioblastoma multiforme." *Cancer Res.* 63(20): 6962-6970.
- 305 Frederick L, Wang XY, Eley G, James CD (2000). "Diversity and frequency of epidermal growth factor receptor mutations in human glioblastomas." *Cancer Res.* 60(5): 1383-1387.

- 306 Choi BD, Kuan CT, Cai M, Archer GE, Mitchell DA, Gedeon PC, Sanchez-Perez L, Pastan I, Bigner DD, Sampson JH (2013). "Systemic administration of a bispecific antibody targeting egfrviii successfully treats intracerebral glioma." *Proc. Natl. Acad. Sci. U. S. A.* 110(1): 270-275.
- 307 Zalutsky MR, Boskovitz A, Kuan CT, Pegram CN, Ayriss J, Wikstrand CJ, Buckley AF, Lipp ES, Herndon JE, McLendon RE, Bigner DD (2012). "Radioimmunotargeting of malignant glioma by monoclonal antibody d2c7 reactive against both wild-type and variant iii mutant epidermal growth factor receptors." *Nucl. Med. Biol.* 39(1): 23-34.
- 308 Haggblad Sahlberg S, Spiegelberg D, Lennartsson J, Nygren P, Glimelius B, Stenerlow B (2012). "The effect of a dimeric affibody molecule (zegfr:1907)2 targeting egfr in combination with radiation in colon cancer cell lines." *Int. J. Oncol.* 40(1): 176-184.
- 309 Simon NC, Aktories K, Barbieri JT (2014). "Novel bacterial adp-ribosylating toxins: Structure and function." *Nat. Rev. Microbiol.* 12(9): 599-611.
- 310 Yamaizumi M, Mekada E, Uchida T, Okada Y (1978). "One molecule of diphtheria toxin fragment a introduced into a cell can kill the cell." *Cell* 15(1): 245-250.
- 311 Michalska M, Wolf P (2015). "Pseudomonas exotoxin a: Optimized by evolution for effective killing." *Front. Microbiol.* 6: 963.
- 312 Helmy K, Halliday J, Fomchenko E, Setty M, Pitter K, Hafemeister C, Holland EC (2012). "Identification of global alteration of translational regulation in glioma in vivo." *PLoS One* 7(10): e46965.
- 313 Fan Q, Aksoy O, Wong RA, Ilkhanizadeh S, Novotny CJ, Gustafson WC, Truong AY, Cayanan G, Simonds EF, Haas-Kogan D, Phillips JJ, Nicolaides T, Okaniwa M, Shokat KM, Weiss WA (2017). "A kinase inhibitor targeted to mtorc1 drives regression in glioblastoma." *Cancer Cell* 31(3): 424-435.

- 314 Hanahan D, Weinberg RA (2011). "Hallmarks of cancer: The next generation." *Cell* 144(5): 646-674.
- 315 Liu W, Onda M, Lee B, Kreitman RJ, Hassan R, Xiang L, Pastan I (2012). "Recombinant immunotoxin engineered for low immunogenicity and antigenicity by identifying and silencing human b-cell epitopes." *Proc. Natl. Acad. Sci. U. S. A.* 109(29): 11782-11787.
- 316 Onda M, Beers R, Xiang L, Lee B, Weldon JE, Kreitman RJ, Pastan I (2011). "Recombinant immunotoxin against b-cell malignancies with no immunogenicity in mice by removal of b-cell epitopes." *Proc. Natl. Acad. Sci. U. S. A.* 108(14): 5742-5747.
- 317 Urry DW (1997). "Physical chemistry of biological free energy transduction as demonstrated by elastic protein-based polymers." *Journal of Physical Chemistry B* 101(51): 11007-11028.
- 318 Chilkoti A, Christensen T, MacKay JA (2006). "Stimulus responsive elastin biopolymers: Applications in medicine and biotechnology." *Curr. Opin. Chem. Biol.* 10(6): 652-657.
- 319 Buss NA, Henderson SJ, McFarlane M, Shenton JM, de Haan L (2012). "Monoclonal antibody therapeutics: History and future." *Curr. Opin. Pharmacol.* 12(5): 615-622.
- 320 Hallam TJ, Wold E, Wahl A, Smider VV (2015). "Antibody conjugates with unnatural amino acids." *Mol. Pharm.* 12(6): 1848-1862.
- 321 Diamantis N, Banerji U (2016). "Antibody-drug conjugates--an emerging class of cancer treatment." *Br. J. Cancer* 114(4): 362-367.
- 322 Lofblom J, Feldwisch J, Tolmachev V, Carlsson J, Stahl S, Frejd FY (2010). "Affibody molecules: Engineered proteins for therapeutic, diagnostic and biotechnological applications." *FEBS Lett.* 584(12): 2670-2680.

- 323 Stahl S, Graslund T, Eriksson Karlstrom A, Frejd FY, Nygren PA, Lofblom J (2017). "Affibody molecules in biotechnological and medical applications." *Trends Biotechnol.* 35(8): 691-712.
- 324 Chandramohan V, Bao X, Keir ST, Pegram CN, Szafranski SE, Piao H, Wikstrand CJ, McLendon RE, Kuan CT, Pastan IH, Bigner DD (2013). "Construction of an immunotoxin, d2c7-(scdsfv)-pe38kdel, targeting egfrwt and egfrviii for brain tumor therapy." *Clin. Cancer Res.* 19(17): 4717-4727.
- 325 Rapoport TA (2007). "Protein translocation across the eukaryotic endoplasmic reticulum and bacterial plasma membranes." *Nature* 450(7170): 663-669.
- 326 Kober L, Zehe C, Bode J (2013). "Optimized signal peptides for the development of high expressing cho cell lines." *Biotechnol. Bioeng.* 110(4): 1164-1173.
- 327 Simon N, FitzGerald D (2016). "Immunotoxin therapies for the treatment of epidermal growth factor receptor-dependent cancers." *Toxins (Basel)* 8(5).
- 328 Needham SR, Roberts SK, Arkhipov A, Mysore VP, Tynan CJ, Zanetti-Domingues LC, Kim ET, Losasso V, Korovesis D, Hirsch M, Rolfe DJ, Clarke DT, Winn MD, Lajevardipour A, Clayton AH, Pike LJ, Perani M, Parker PJ, Shan Y, Shaw DE, Martin-Fernandez ML (2016). "Egfr oligomerization organizes kinase-active dimers into competent signalling platforms." *Nat Commun* 7: 13307.
- 329 Liu CY, Liu J, Yan W, Williston K, Irvin K, Chou H, Zmuda J, Thermo Fisher Scientific, **2018**.
- 330 Akerstrom B, Bjorck L (1986). "A physicochemical study of protein g, a molecule with unique immunoglobulin g-binding properties." *J. Biol. Chem.* 261(22): 10240-10247.
- 331 Kato K, Lian L-Y, Barsukov IL, Derrick JP, Kim H, Tanaka R, Yoshino A, Shiraishi M, Shimada I, Arata Y, Roberts GCK (1995). "Model for the complex between protein g and an antibody fc fragment in solution." *Structure* 3(1): 79-85.

- 332 Ilangovan U, Ton-That H, Iwahara J, Schneewind O, Clubb RT (2001). "Structure of sortase, the transpeptidase that anchors proteins to the cell wall of staphylococcus aureus." *Proc. Natl. Acad. Sci. U. S. A.* 98(11): 6056-6061.
- 333 Chen L, Cohen J, Song X, Zhao A, Ye Z, Feulner CJ, Doonan P, Somers W, Lin L, Chen PR (2016). "Improved variants of *srtA* for site-specific conjugation on antibodies and proteins with high efficiency." *Sci. Rep.* 6: 31899.
- 334 Chilkoti A, Tan PH, Stayton PS (1995). "Site-directed mutagenesis studies of the high-affinity streptavidin-biotin complex: Contributions of tryptophan residues 79, 108, and 120." *Proceedings of the National Academy of Sciences* 92(5): 1754-1758.
- 335 Sano T, Cantor CR (1990). "Expression of a cloned streptavidin gene in *escherichia-coli*." *Proc. Natl. Acad. Sci. U. S. A.* 87(1): 142-146.
- 336 Malyala P, Singh M (2008). "Endotoxin limits in formulations for preclinical research." *J. Pharm. Sci.* 97(6): 2041-2044.
- 337 Gorbet MB, Sefton MV (2005). "Endotoxin: The uninvited guest." *Biomaterials* 26(34): 6811-6817.
- 338 Ribeiro MM, Xu X, Klein D, Kenyon NS, Ricordi C, Felipe MS, Pastori RL (2010). "Endotoxin deactivation by transient acidification." *Cell Transplant.* 19(8): 1047-1054.
- 339 Cao X, Zhu B, Zhang X, Dong H (2016). "Polymyxin b immobilized on cross-linked cellulose microspheres for endotoxin adsorption." *Carbohydr Polym* 136: 12-18.
- 340 Darcy E, Leonard P, Fitzgerald J, Danaher M, Ma H, O'Kennedy R (2017). "Purification of antibodies using affinity chromatography." *Methods Mol. Biol.* 1485: 305-318.

- 341 Pastrana DV, FitzGerald DJ (2006). "A nonradioactive, cell-free method for measuring protein synthesis inhibition by pseudomonas exotoxin." *Anal. Biochem.* 353(2): 266-271.
- 342 Humphrey PA, Wong AJ, Vogelstein B, Friedman HS, Werner MH, Bigner DD, Bigner SH (1988). "Amplification and expression of the epidermal growth factor receptor gene in human glioma xenografts." *Cancer Res.* 48(8): 2231-2238.
- 343 Schulte A, Gunther HS, Martens T, Zapf S, Riethdorf S, Wulfing C, Stoupien M, Westphal M, Lamszus K (2012). "Glioblastoma stem-like cell lines with either maintenance or loss of high-level egfr amplification, generated via modulation of ligand concentration." *Clin. Cancer Res.* 18(7): 1901-1913.
- 344 Sanborn JZ, Salama SR, Grifford M, Brennan CW, Mikkelsen T, Jhanwar S, Katzman S, Chin L, Haussler D (2013). "Double minute chromosomes in glioblastoma multiforme are revealed by precise reconstruction of oncogenic amplicons." *Cancer Res.* 73(19): 6036-6045.
- 345 William D, Mokri P, Lamp N, Linnebacher M, Classen CF, Erbersdobler A, Schneider B (2017). "Amplification of the egfr gene can be maintained and modulated by variation of egf concentrations in in vitro models of glioblastoma multiforme." *PLoS One* 12(9): e0185208.
- 346 Serano RD, Pegram CN, Bigner DD (1980). "Tumorigenic cell culture lines from a spontaneous vm/dk murine astrocytoma (sma)." *Acta Neuropathol.* 51(1): 53-64.
- 347 Wainwright DA, Horbinski CM, Hashizume R, James CD (2017). "Therapeutic hypothesis testing with rodent brain tumor models." *Neurotherapeutics* 14(2): 385-392.
- 348 *Encapsula, Vol. 2019* (Ed.: E. NanoSciences), **2019**.
- 349 Bao X, Chandramohan V, Reynolds RP, Norton JN, Wetsel WC, Rodriguiz RM, Aryal DK, McLendon RE, Levin ED, Petry NA, Zalutsky MR, Burnett BK, Kuan CT, Pastan IH, Bigner DD (2016). "Preclinical toxicity evaluation of a novel

immunotoxin, d2c7-(scdsfv)-pe38kdel, administered via intracerebral convection-enhanced delivery in rats." *Invest. New Drugs* 34(2): 149-158.

- 350 MacEwan SR, Duke University (Durham, NC, USA), **2014**.
- 351 Amiram M, Luginbuhl KM, Li X, Feinglos MN, Chilkoti A (2013). "Injectable protease-operated depots of glucagon-like peptide-1 provide extended and tunable glucose control." *Proc. Natl. Acad. Sci. U. S. A.* 110(8): 2792-2797.
- 352 Segal MB (1993). "Extracellular and cerebrospinal fluids." *J. Inherit. Metab. Dis.* 16(4): 617-638.
- 353 Brinker T, Stopa E, Morrison J, Klinge P (2014). "A new look at cerebrospinal fluid circulation." *Fluids Barriers CNS* 11: 10.
- 354 Richter WF, Jacobsen B (2014). "Subcutaneous absorption of biotherapeutics: Knowns and unknowns." *Drug Metab. Dispos.* 42(11): 1881-1889.
- 355 Reddy ST, Berk DA, Jain RK, Swartz MA (2006). "A sensitive in vivo model for quantifying interstitial convective transport of injected macromolecules and nanoparticles." *J Appl Physiol* (1985) 101(4): 1162-1169.
- 356 Caccialanza R, Constans T, Cotogni P, Zaloga GP, Pontes-Arruda A (2016). "Subcutaneous infusion of fluids for hydration or nutrition." *Journal of Parenteral and Enteral Nutrition*.
- 357 Rajan RS, Li T, Aras M, Sloey C, Sutherland W, Arai H, Briddell R, Kinstler O, Lueras AM, Zhang Y, Yeghnazar H, Treuheit M, Brems DN (2006). "Modulation of protein aggregation by polyethylene glycol conjugation: Gcsf as a case study." *Protein Sci.* 15(5): 1063-1075.
- 358 Annunziata O, Asherie N, Lomakin A, Pande J, Ogun O, Benedek GB (2002). "Effect of polyethylene glycol on the liquid-liquid phase transition in aqueous protein solutions." *Proc. Natl. Acad. Sci. U. S. A.* 99(22): 14165-14170.

- 359 Raut AS, Kalonia DS (2016). "Effect of excipients on liquid-liquid phase separation and aggregation in dual variable domain immunoglobulin protein solutions." *Mol. Pharm.* 13(3): 774-783.
- 360 Vekilov PG (2010). "Phase transitions of folded proteins." *Soft Matter* 6(21).
- 361 Kim S, Shi Y, Kim JY, Park K, Cheng JX (2010). "Overcoming the barriers in micellar drug delivery: Loading efficiency, in vivo stability, and micelle-cell interaction." *Expert Opin Drug Deliv* 7(1): 49-62.
- 362 Miller T, Rachel R, Besheer A, Uezguen S, Weigandt M, Goepferich A (2012). "Comparative investigations on in vitro serum stability of polymeric micelle formulations." *Pharm. Res.* 29(2): 448-459.
- 363 De Vleeschouwer S (2017). *Glioblastoma*. Brisbane, Australia, Codon Publications.
- 364 Armstrong TS, Cao Y, Scheurer ME, Vera-Bolanos E, Manning R, Okcu MF, Bondy M, Zhou R, Gilbert MR (2009). "Risk analysis of severe myelotoxicity with temozolomide: The effects of clinical and genetic factors." *Neuro Oncol.* 11(6): 825-832.
- 365 Nordling-David MM, Yaffe R, Guez D, Meirov H, Last D, Grad E, Salomon S, Sharabi S, Levi-Kalishman Y, Golomb G, Mardor Y (2017). "Liposomal temozolomide drug delivery using convection enhanced delivery." *J. Control. Release* 261: 138-146.
- 366 Park M, Song C, Yoon H, Choi KH (2016). "Double blockade of glioma cell proliferation and migration by temozolomide conjugated with nppb, a chloride channel blocker." *ACS Chem. Neurosci.* 7(3): 275-285.
- 367 Jhaveri N, Agasse F, Armstrong D, Peng L, Commins D, Wang W, Rosenstein-Sisson R, Vaikari VP, Santiago SV, Santos T, Chen L, Schonthal AH, Chen TC, Hofman FM (2016). "A novel drug conjugate, neo212, targeting proneural and

mesenchymal subtypes of patient-derived glioma cancer stem cells." *Cancer Lett.* 371(2): 240-250.

Biography

Simone Costa received her Bachelor of Science in Biology, with a minor in Biomedical Engineering, from Carnegie Mellon University in May 2012. In August 2013, Simone began her doctoral work in Biomedical Engineering at Duke University. While in graduate school, Simone was recognized with a National Science Foundation Graduate Research Fellowship (2013-2016) and a National Science Foundation Triangle Materials Research Science and Engineering Fellowship (2016-2017). Her work in the research group of Professor Ashutosh Chilkoti secured the funding of a National Institutes of Health R21 award from the National Cancer Institute. Along with her colleagues in the Chilkoti group, she authored and contributed to the following publications, reviews, and patents:

Costa SA, Mozhdehi DM, Dzuricky MJ, Isaacs FJ, Brustad EM, Chilkoti A. "Active targeting of cancer cells by nanobody decorated polypeptide micelle with bioorthogonally conjugated drug" Nano Letters (2019). DOI: 10.1021/acs.nanolett.8b03837

Costa SA*, Simon JR*, Amiram M, Tang L, Zauscher S, Brustad EM, Isaacs FJ, Chilkoti A. "Photocrosslinkable unnatural amino acids enable facile synthesis of thermoresponsive nano- to micro-gels of intrinsically disordered polypeptides" Advanced Materials (2018) DOI: 10.1002/adma.201704878

Costa SA, Chandramohan V, Bigner DD, Chilkoti A. "A sustained-release biopolymer-immunotoxin fusion for treatment of brain tumors" (2018) U.S. Patent Pending 62/647,199.

Mozhdehi DM, Luginbuhl K, Dzuricky M, **Costa SA**, Xiong, S, Huang, F, Lewis M, Zelenetz S, Colby C, Chilkoti A. "Genetically Encoded Cholesterol-Modified Polypeptides" Journal of American Chemical Society (2019) DOI: 10.1021/jacs.8b10687

Yousefpour, P, Ahn L, Tewksbury J, Saha SS, **Costa SA**, Bellucci JJ, Li X, Chilkoti A. "Conjugate of Doxorubicin to Albumin Binding Peptide Outperforms Aldoxorubicin" Small (2019). DOI: 10.1002/sml.201804452

Roberts SR, **Costa SA**, Schaal JL, Simon JR, Dzuricky M, Quiroz FG, Chilkoti A. "Elastin-like polypeptides " Comprehensive Biomaterials II (2017) 90-108.

Manzari MT, Anderson GR, Lin KH, Soderquist R Cakir M, Zhang M, Moore CE, Skelton RN, Fevre M, Li X, Bellucci JJ, Wardell SE, **Costa SA**, Wood KC, Chilkoti A. "Genomically informed small molecule drugs overcome resistance to sustained release formulation of an engineered death receptor agonist." Under review in Science Advances (2019).

Roberts SR, Miao V, **Costa SA**, Simon JR, Chilkoti A. "Complex Microparticle Architectures from Stimuli-Responsive Intrinsically Disordered Polypeptides" In preparation.